学位論文

Search for Heavy Higgs Bosons Decaying to a Pair of τ Leptons in Proton-Proton Collisions at $\sqrt{s} = 13\,\mathrm{TeV}$

(重心系エネルギー13TeVの陽子陽子衝突における
タウ粒子対へ崩壊する重いヒッグス粒子の探索)

平成28年12月博士 (理学) 申請

東京大学理学系研究科
物理学専攻

森永 真央

Ph.D Thesis

Search for Heavy Higgs Bosons Decaying to a Pair of τ Leptons in Proton-Proton Collisions at $\sqrt{s} = 13\,\mathbf{TeV}$

December 2016

Depertment of Physics, Faculty of Sience
The University of Tokyo

Masahiro Morinaga

Abstract

This thesis presents the search for the heavy Higgs bosons decaying into a pair of τ's at proton-proton collisions with a center-of-mass energy $\sqrt{s} = 13$ TeV at the Large Hadron Collider (LHC). After the discovery of the new scalar boson with a mass of 125 GeV, several problems of the Standard Model still remain. An extended Higgs boson which expected from several physics beyond the Standard Model provides solutions for such given problems. The Minimal Supersymmetric Standard Model (MSSM) is one of simplest extension of the Standard Model based on supersymmetry. The Higgs bosons are extended into five physical particles h, H, A and $H^{\pm}$. The hMSSM scenario is recently developed and the new 125 GeV boson is treated as the neutral Higgs boson h, other neutral H and A are heavier than 125 GeV. A decay mode of final state with a pair of τ-leptons has a large part of branching fraction in possible decay modes. A search for such decay mode is most promising experimental content and one of the first priorities of experimental particle physics programs.

An integrated luminosities of $28\,\mathrm{fb}^{-1}$ is used in this thesis. This analysis is focused on the di-τ events in final states characterised by one isolated high p_{T} light lepton, one hadronically decaying τ-lepton and a large missing transverse energy ($E_{\mathrm{T}}^{\mathrm{miss}}$) corresponding to three neutrinos from τ-lepton decays.

The search covers following achievements: establishment of a data-driven way to model a background with mis-identified hadronic-τ objects, and an improvement of search sensitivity for wider mass range by using the $E_{\mathrm{T}}^{\mathrm{miss}}$ information. The background estimation method which developed in this thesis improves understanding of the mis-identified hadronic-τ background. The analysis sensitivity is imporved using the $E_{\mathrm{T}}^{\mathrm{miss}}$ based analysis categorisation by 25-50% at heavy signal hypotheses. Using the obtained samples, no obvious excess is observed and the exclusion limits for on the hMSSM is set to $\tan\beta > 36.8$ at $m_{\mathrm{A}} = 1$ TeV.

Acknowledgements

This thesis has been written with the help of my supervisor Prof. Shoji Asai at the University of Tokyo. During the four years of Ph.D I received great support from
Dr. Junichi Tanaka, Dr. Yuji Enari, Dr. Takashi Yamanaka and Dr. Takuya Nobe.
I benefited from working in close collaboration with Dr. Nikolaos Rompotis and Dr. Lei Zhang.

Contents

1 Introduction

To get and understand insight into the constitutions of matter and their interactions are one of the oldest questions in fundamental science. There are three forces in the elementary particle physics, the weak, electromagnetic and strong force. A unified theoretical explanation of the electromagnetic and weak interactions was established by Glashow, Salam and Weinberg. They introduced the gauge symmetry which forms the core of the theoretical foundation for the description of the structure of the Standard Model. The Standard Model (SM) is the modern description of elementary particles and interactions together with a model of the strong interaction. A consistent quantum theory with the gravity has not yet established. The Standard Model describes particle interactions very accurately for the last 40 years. The missing part in the Standard Model was the Higgs boson, which have been discovered in July 2012.

In spite of the success of the Standard Model in describing many experimental results, the Higgs boson mass is subject to large radiative corrections. It means a huge difference between the Higgs mass parameter and the measured Higgs boson mass $m_H \simeq 125$ GeV. Without further explanation of this, we have to accept unnatural difference. Furthermore the Standard Model does not provide a particle that could make up dark matter which was established by the WMAP and Planck satellite missions.

In order to address these problems, the Standard Model need to be extended. Supersymmetry is a symmetry between bosons and fermions. A superpartner is introduced for every SM particle with half integer different spin. Two-Higgs-doublets which produce five physical Higgs bosons are introduced in the Minimal Supersymmetric Standard Model (MSSM). The five physical state consists of three electrically neutral Higgs bosons and two electrically charged Higgs bosons. Three neutral Higgs bosons have different state of CP-even h and H, CP-odd A, while the two charged Higgs are same quantum state with electrically different charge $H^{\pm}$. The decays of H/A into down-type fermions is enhanced and the $\tau\tau$ decay mode provides a particular sensitivity to the MSSM models.

Energy of colliding particles is crucial to prove a new physics beyond the Standard Model (BSM). Large Hadron Collider (LHC) was operated with a center-mass-energy $\sqrt{s} = 7$ TeV in first physics run 2011. A center-mass-energy was increased up to $\sqrt{s} = 8$ TeV after the first year run and discovered the Higgs boson in 2012. The Standard Model was tested with recorded data and also several searches for BSM physics were performed. From 2013 to 2014, the LHC have been upgraded its proton beam energy up to 6.5 TeV. The LHC has started again with a center-mass-energy of $\sqrt{s} = 13$ TeV from 2015 spring. New particles expected from the BSM are produced at higher rates in $\sqrt{s} = 13$ TeV.

There are four large detectors within the LHC proton ling. Two general purpose experiments ATLAS[1] and CMS[2] perform searches for new physics and measurements of the SM particle properties. The LHC provided the integrated luminosities of up to $3.3\,\mathrm{fb}^{-1}$ in 2015 data-taking and $24.7\,\mathrm{fb}^{-1}$ until August 2016 data-taking periods at the ATLAS detector.

[1] A Toroidal LHC ApparatuS
[2] Compact Muon Solenoid

In this thesis a search for the neutral Higgs bosons A and H in the decay mode of $H/A \to \tau\tau \to \tau_\ell\tau_{\text{had}}$ is performed, where τ_{had} and τ_ℓ denotes a tau lepton hadronically and laconically decay respectively. The search is based on recorded data with the ATLAS detector during 2015 to 2016 summer technical shutdown. The $\tau_\ell\tau_{\text{had}}$ decay channel includes approximately 45% of all events in the $H/A \to \tau\tau$ mode. The search with $\tau_\ell\tau_{\text{had}}$ chanel is clean and simple compared to other two decay channels. As a trigger is important component of the experiments at the LHC, the $\tau_\ell\tau_{\text{had}}$ channel has one electron and muon which gives clear signature in terms of triggering. Electron and muon can suppress background events from the QCD multijets process which is largest part of interactions in proton-proton collisions. The $\tau_\ell\tau_{\text{had}}$ channel tends to have larger transverse missing energy ($E_{\text{T}}^{\text{miss}}$) which is made up from three neutrinos produced in di-τ decays. A new analysis strategy focused on events with a large transverse missing energy are introduced and it significantly improves experimental sensitivity. In addition, a method to estimate background events containing mimicking τ_{had} is newly developed and performed.

A brief review of the Standard Model is given together with an introduction to the concepts of supersymmetry focused on the MSSM in Chapter 2. An overview of the method used to calculate event rates and differential distributions for several physics production processes including backgrounds and signal processes is described in this chapter. In addition, a short review of a benchmark signal model is also given. The LHC and the ATLAS experiment are described in Chapter 4. The reconstruction and identification procedures of particle objects and event kinematics based on output from the ATLAS detector is given in Chapter 5. Details of the search for heavy Higgs bosons decaying into a pair of τ leptons is given in Chapter 6. An experimental signatures of heavy Higgs bosons production and decay is described. Event selection criteria and event categorisations to separate signal from background events is also given. Estimating background process of a mis-identified τ_{had} play an important role in the search, detailed description is also given in Chapter 6 including other background processes. The statistical methods used to interpret results of the analysis and its results is presented in Chapter 7.

2 Theoretical Overview

The theoretical concepts relevant for this search are introduced in this chapter. A brief overview of the Standard Model is given in Section 2.1 based on reference [1]. Among the extension of the Standard Model, the Minimal Supersymmetric Standard Model (MSSM) is most promising. The MSSM is introduced in Section 2.2 with emphasis on the Higgs boson sector based on reference [2, 3]. A brief summary of the search for the neutral MSSM Higgs boson is given in Section 2.3. Phenomenology of the heavy Higgs bosons are described in Chapter 3.

2.1 The Standard Model of Particle Physics

The Standard Model (SM) is the established theoretical framework that describes properties of elementary particles and their interactions. The Standard Model was developed in 20th century, and was confirmed by the discovery of $W^{\pm}$ and Z bosons in 1983. In addition, the SM predicts the existence of a Higgs boson. In 2012 a new boson was found by the ATLAS[1] and CMS[2] experiments [4, 5]. A new boson seems to be consistent with the SM Higgs boson A general description of the SM is based on reference [6]. A brief overview is given below.

Interactions between particles can be associated with three forces, the electromagnetic, weak and strong force. The gravitational interaction is not described by the Standard Model. The effects of the gravitational force can usually be neglected in particle physics. The model is based on the gauge symmetry assumption in $\mathrm{SU(2)_L} \times \mathrm{SU(3)_C} \times \mathrm{U(1)_Y}$ group which has 12 generators and gauge field. The electromagnetic and weak interactions [7–9] are described by the $\mathrm{SU(2)_L} \times \mathrm{U(1)_Y}$ symmetry group, while $\mathrm{SU(3)_C}$ is the group of the strong colour forces of Quantum Chromodynamics (QCD) [10]. Eight gluons are associated to the $\mathrm{SU(3)_C}$ colour group, while four gauge bosons, $W^{\pm}, Z$ and γ, are associated to the electroweak symmetry $\mathrm{SU(2)_L} \times \mathrm{U(1)_Y}$. Gluons and photons are massless while the remaining weak gauge bosons have mass. The spontaneous symmetry breaking [11–14] give a mass to these gauge bosons without spoiling the electroweak gauge symmetry. An additional complex scalar field is required and lead up to a new scalar particle, the Higgs boson, which interacts with particles with a strength proportional to their masses.

Quarks are subject to all three SM interactions. Each quark flavour is a colour triplet and carries electroweak charge including electric charges of +2/3 and -1/3 for up-type and down-type quarks respectively. Leptons are colourless but have electroweak charges. Electrons, muons and τ leptons carry unit electric charge -1, while the associated neutrinos ν_e, ν_μ and ν_τ are electrically neutral. The respective anti-leptons carry opposite sign electric charge. Quarks and leptons group in three generations with equal charge quantum numbers but different masses. If the type of the charge is not

[1] A Toroidal LHC ApparatuS
[2] Compact Muon Solenoid

explicitly specified, charge refers to the electric charge.

2.1.1 The Higgs Mechanism in the Standard Model

All fermions have masses, and the $W^{\pm}$ and Z are massive and masses of

$$m_{W^{\pm}} = 80.385 \pm 0.015\,\text{GeV} \tag{2.1}$$
$$m_{Z} = 91.1876 \pm 0.0021\,\text{GeV} \tag{2.2}$$

have been measured [15], while photon is massless. The neutrino flavour oscillations strongly predicts neutrinos are massive.

Masses can be generated with the spontaneous symmetry breaking of a gauge symmetry. The Higgs mechanism introduces a SU(2) doublet. The Higgs potential

$$V(\phi) = \mu^2\phi^{\dagger}\phi + \lambda(\phi^{\dagger}\phi)^2 \tag{2.3}$$

where $\phi = (\phi_1, \phi_2)^T$, and ϕ_1 and ϕ_2 is a complex scalar field, μ is a mass parameter. A self coupling parameter λ is invariant under $\text{SU}(2)_L \times \text{U}(1)_Y$ symmetry transformations. A SU(2) doublet is assigned weak hypercharge $Y = +1$.

For $\mu^2 < 0$ and $\lambda > 0$ the potential of the Higgs field V, has minimum at

$$v = |\phi_0| = \sqrt{\frac{-\mu^2}{2\lambda}}, \text{ with values } V(\phi_0) = -\frac{\mu^4}{4\lambda} = -\lambda\frac{v^4}{4} \tag{2.4}$$

When the neutral complex scalar field ϕ has non-zero for vaccum expectation, the $\text{SU}(2)_L \times \text{U}(1)_Y$ symmetry is spontaneously broken with the electromagnetic gauge symmetry $\text{U}(1)_{EM}$ remaining as a symmetry of the ground state. Three degrees of freedom of the scalar field are absorbed as longtitudinal polarisation states of the $W^{\pm}$ and Z bosons, which in this way acquire their masses, while photon remains massless. The remaining degree of freedom corresponds to a physical scalar particle, i.e. the Higgs boson. The masses of the fermions can be generated via so-called, the Yukawa interaction term [16].

2.1.2 Unsolved Problem on Particle Physics

In the last decades the SM has been proven by amount of experiments and has widely accepted. However, there are some experimetal aspects that cannot be explained by the SM which is usually referred to as *physics beyond the Standard Model (BSM)*. A overview of unsolved problems are briefly reviewed in following.

Dark Matter and Dark Energy

The WMAP [17] and Plank [18] satellite have measured the spectrum of the cosmic microwave background (CMB). The CMB is the radiation from the period of recombination when temperture dropped to below the hydrogen ionisation temperture. The multipole spectrum is fitted by a six-parameter cosmological model, ΛCDM [19]. The results of a fit with the model predicts that the fraction of baryonic matter contributes only 4.9% to the total matter and energy distribution. Dark matter and dark energy contributes 68.3% and 26.8% respectively. The Standard Model cannot provide an explanation for dark energy or a candidate particle for dark matter.

Baryon Asymmetry and CP violation

Universe seems to be completely dominated by matter, Sakharov's three conditions [20] need to be filled. One of three conditions requires baryon number violation, which is absent from perturbative

descriptions of the Standard Model. The baryon number is conserved in the Standard Model. CP violation which is induced from the CKM matrix is too small to explain the baryon number asymmetry within the Standard Model framework. In order to explain this a further source of CP violation form the physics beyond the Standard Model is necessary.

Neutrino Masses

When neutrinos have mass, it can oscillate between three flavour eignestates. Th first hint of neutrino flavour oscillation was the solar neutrino problem(ν_e) [21, 22]. The anti-neutrinos from reactors $\bar{\nu}_e$ [23] and atmospheric (anti-) neutrinos $\nu_\mu, \bar{\nu}_\mu$ [24] were observed disapperance effects as the same as ν_3. Experiments of appearance of ν_τ [25] observed the oscillations as well, which uses beams of neutrinos created in their muonic interaction state. The neutrino oscillation predicted by extensions of the Standard Model in which neutrinos are massive particles. The oscillation probabilities $P(\nu_\ell \to \nu_{\ell'})$ depends on the mass difference between two neutrnis states $\Delta m^2_{\ell,\ell'}$ and the ratio between the distance and energy $L/2E$ of the system. The fit of the experimental data imply

$$|\Delta m^2_{21}| \simeq 7.5 \times 10^{-5}\text{eV}^2, \tag{2.5}$$

$$|\Delta m^2_{31}| \simeq 2.5 \times 10^{-3}\text{eV}^2, \tag{2.6}$$

$$|\Delta m^2_{21}|/|\Delta m^2_{31}| \simeq 0.03. \tag{2.7}$$

Hierarchy and Fine-tuning Problem

The bare mass parameter for the Higgs boson is corrected by loop contributions to obtain the observed mass due to the renormalisation procedure. The loop contributoions are proportional to Λ^2_{UV}, where Λ_{UV} is the ultraviolet momentum cut-off scale. As the contributions to the source of Higgs boson mass after the renormalisation from fermion - anti-fermion loops are $\mathcal{O}(30)$ of magnitude larger than the observed Higgs boson mass. Therefore, the bare mass has to be fine-tuned to cancel out between the fundamental and quantum corrections. Hierarchy problem problems are connected to fine-tuning and problem of naturalness.

Above many extensions of the Standard Model, supersymmetry is theoretically favoured as it provides natural solutions to problems on the Standard Model. Supersymmetry can solve the hierarchy problem, provide a stable dark matter candidate and predict unification of the three SM gauge couplings at the GUT scale.

2.2 Supersymmetry and The Minimal Supersymmetric Standard Model

Supersymmetry (SUSY) [26–28] is a symmetry that relates bosons and fermions. An overview of the Minimal Supersymmetric Standard Model (MSSM) is given based on References [2, 29].

One superpartner has to be introduced for every Standard Model particle. The superpartner of the boson states are the Winos, Bino, gluinos and the Higgsinos. The superpartner of fermions are called squarks and sleptons for quarks and leptons respectively. All supersymmetric particles are referred to as sparticles, the superpartners of the gauge bosons are referred to as gauginos. The SUSY generators $\mathcal{Q}$ transform fermions into bosons and vice versa :

$$\mathcal{Q}\,|\text{Fermion}\rangle = |\text{Boson}\rangle\,, \mathcal{Q}\,|\text{Boson}\rangle = |\text{Fermion}\rangle\,, \tag{2.8}$$

2.2.1 The Higgs Sector of the MSSM

An overview of the MSSM Higgs sector is given based on Reference [30] in this section. The MSSM requires the complex Higgs doublets H_u and H_d to provide masses for up-type and down-type fermions via the spontaneous breaking of the $\mathrm{SU(2)_L \times U(1)_Y}$ gauge symmetry. Two complex Higgs doublets implies the existence of five Higgs bosons, i.e. two charged Higgs bosons, $H^{\pm}$, and three neutral Higgs bosons: a CP-odd (pseudoscalar) state A, and two CP-even (scalar) states, h and H, with $m_h < m_H$. The masses of these five Higgs bosons and their mixing can be written by the gauge boson masses m_W and m_Z with two additional parameters, the pseudoscalar mass m_{A} and the ratio of the vacuum expectation values of the neutral components of the two Higgs doublets $\tan\beta$,

$$\tan\beta = \frac{\langle H_u^0 \rangle}{\langle H_d^0 \rangle} = \frac{v_u}{v_d}, \tag{2.9}$$

where v_u and v_d need to be satisfied $(v_u^2 + v_d^2)^{1/2} \sim 246$ GeV. The tree-level mass of charged Higgs states is given by $m_{H^\pm}^2 = m_A^2 + m_W^2$, the mass matrix for the neutral CP-even states is given by

$$\mathcal{M}^2_{\mathrm{tree}} = \begin{pmatrix} m_{\mathrm{A}}^2 \sin^2\beta + m_Z^2 \cos^2\beta & -(m_{\mathrm{A}}^2 + m_Z^2)\sin\beta\cos\beta \\ -(m_{\mathrm{A}}^2 + m_Z^2)\sin\beta\cos\beta & m_{\mathrm{A}}^2 \cos^2\beta + m_Z^2 \sin^2\beta \end{pmatrix} \tag{2.10}$$

This matrix is diagonalized by an angle α, and the mass eigenvalues are given by :

$$\tan\alpha = \frac{-(m_{\mathrm{A}}^2 + m_Z^2)\sin 2\beta}{(m_Z^2 - m_{\mathrm{A}}^2)\cos 2\beta + \sqrt{(m_{\mathrm{A}}^2 + m_Z^2)^2 - 4m_{\mathrm{A}}^2 m_Z^2 \cos^2 2\beta}}. \tag{2.11}$$

$$m_{h,H}^2 = \frac{1}{2}\left(m_{\mathrm{A}}^2 + m_Z^2 \mp \sqrt{(m_{\mathrm{A}}^2 + m_Z^2)^2 - 4m_{\mathrm{A}}^2 m_Z^2 \cos^2 2\beta} \right). \tag{2.12}$$

The role of the SM Higgs boson is shared between the scalars h and H in the MSSM. The relative coupling to the corresponding SM of the neutral scalars to pairs of massive vector bosons and fermions are summarised in Table 2.1

	g_{VV}	g_{uu}	$g_{dd,\ell\ell}$
H	$\cos(\beta-\alpha)$	$\sin\alpha/\sin\beta$	$\cos\alpha/\cos\beta$
h	$\sin(\beta-\alpha)$	$\cos\alpha/\sin\beta$	$-\sin\alpha/\cos\beta$
A	0	$\cot\beta\ \tan\beta$	

Table 2.1: The relative coupling to massive boson pairs and the SM fermions to the SM couplings. In addition to these couplings, there are non-SM couplings of the neutral scalars to ZA and to $W^\pm H^\mp$. These are proportional to $\cos(\beta-\alpha)$ for h and to $\sin(\beta-\alpha)$ for H. The ZAA coupling vanishes and the $W^\pm H^\mp A$ coupling does not depends on α or β.

The decoupling limit

Figure 2.1 shows the tree-level mass of m_H, m_h and $m_{H^\pm}$ as a function of m_{A}. The mixing angle in the CP-even sector can be simplified as $\alpha \sim \beta - \pi/2$ in the *decoupling limit* ($m_{\mathrm{A}} > m_Z$). As a consequence of the decoupling limit, the masses of the neutral scalar h becomes approximately constant value, $m_h \sim m_Z|\cos\beta|$, and its coupling become similar to the SM Higgs boson. The masses of H and $H^\pm$ are approximately degenerated with m_{A}, the coupling of H to the massive gauge bosons vanish and to up-type (down-type) SM fermions are also suppressed (enhanced) for higher $\tan\beta$. A

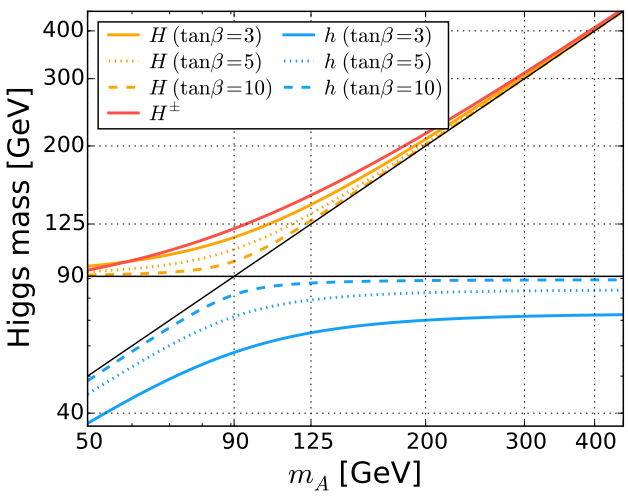

Figure 2.1: Tree-level values masses of the charged scalar, $m_{H^\pm}$ and of the neutral scalars m_H and m_h as a function of the pseudoscalar mass m_A. Orange (blue) curves are for the H and h respectively.

heavy and mass-degenerate multiplet $(H, A, H^\pm)$ with vanishing couplings to massive gauge bosons is shown in this limit.

The Radiative Corrections

Tree-level masses of the MSSM Higgs bosons are affected by the radiative corrections. Loops of top quark and top squarks (stops) are dominant contributions to the lightest-scalar mass. In the decoupling limit it takes the approximated form

$$\Delta m_h^2 \sim \frac{3m_t^4}{2\pi^2 v^2}\left(\log\frac{m_\mathrm{SUSY}^2}{m_t^2} + \frac{X_t^2}{m_\mathrm{SUSY}^2} - \frac{X_t^4}{12m_\mathrm{SUSY}^4}\right), \tag{2.13}$$

where $m_\mathrm{SUSY} = (m_{\tilde{t}_1} m_{\tilde{t}_2})^{1/2}$ is an average scale for the stop mass, and $X_t = A_t - \mu\cot\beta$ is the stop mixing term, where A_t is the soft SUSY-breaking Higgs-stop coupling and μ is the higgsino mass parameter. The one-loop top/stop contributions can be maximised if m_SUSY is large and for the maximal mixing condition $|X_t| = \sqrt{6} m_\mathrm{SUSY}$. A smaller negative contribution from sbottom loops can be relevant for only large $\tan\beta$. Full one-loop calculation of the MSSM Higgs mass is available with partial two-loop corrections and the leading three-loop corrections.

2.2.2 MSSM Benchmark Scenarios

Several constraints on the parameter space of the MSSM can be taken into account after the LHC Run1 :

- The discovery of a scalar particle with a mass of 125.09 ± 0.24 GeV [31–33].
- Measured values of couplings are consistent with the predictions for the SM Higgs boson with accuracy of $\pm \sim 20\%$ [34, 35].
- No observation of additional neutral or charged Higgs bosons n direct searches [36–39].
- No observation of SUSY particles.

The Higgs boson that have been discovered in the LHC is interpreted a the lightest neutral scalar h in the MSSM. The lightest scalar mass is usually treated as a constraint on unknown SUSY parameters, with $m_h = 125 \pm 3$ GeV. ± 3 GeV variation corresponds to theoretical uncertainty of the MSSM prediction for m_h due to unknown effects of higher-order corrections [40, 41].

Tree-level mass of h is constrained the bound $m_h < m_Z$, so that the $m_{\rm SUSY}$ which is around ~ 1 TeV need to reproduce the observed m_h in the case of $\tan\beta \gtrsim 10$ and the decoupling region of $m_{\rm A}$. A few TeV stop masses are necessary for smaller X_t. A strong constraint has been obtained by direct searches by ATLAS and CMS in the ($m_{\rm A}$, $\tan\beta$) plane.

The heavy Higgs bosons are not yet excluded by direct searches at the LHC where $m_{\rm A}$ are less than 200 GeV in the case of low $\tan\beta$. The heavy Higgs bosons whose mass is lighter than 200 GeV has not been excluded for low $\tan\beta$ case. Decay modes of $H \to WW, H \to ZZ, H \to hh$ and $A \to Zh$ still have significant branching fraction in the lower-$\tan\beta$ region, especially below the threshold for decaying to a top-quark pair.

The hMSSM Approach

Lower $\tan\beta$ case implies a lower tree-level mass of h, and require larger $m_{\rm SUSY}$ with the radiative corrections to satisfy the mass constraint ($m_h = 125 \pm 3$ GeV). The hMSSM approach [42–44] is the phenomenological approach under assumptions with treating m_h as input for the calculation of the radiative corrections and used to predict masses and couplings of the remaining MSSM Higgs bosons. The Higgs sector of the MSSM is described in terms of the parameters entering the tree-level expressions for masses and mixing with the experimental m_h value. The hMSSM approach can be considered as model independent, because the predictions for the MSSM Higgs bosons does not depend on details of the un-observed SUSY sector. The mass matrix for the neutral CP-even states can be expanded by

$$\mathcal{M}^2 = \mathcal{M}^2_{\rm tree} + \begin{pmatrix} \Delta\mathcal{M}^2_{11} & \Delta\mathcal{M}^2_{12} \\ \Delta\mathcal{M}^2_{12} & \Delta\mathcal{M}^2_{22} \end{pmatrix}, \tag{2.14}$$

where the tree-level matrix $\mathcal{M}^2_{\rm tree}$ is given by Eq. 2.10 and $\Delta\mathcal{M}^2_{ij} (i, j = 1 \text{ or } 2)$ are the radiative corrections. The hMSSM approach is based on the following assumptions

- The observed Higgs boson is the light-scalar h.
- Only the element $\Delta\mathcal{M}^2_{22}$, which contains the leading logarithmic terms from top-stop loops, needs to be taken into account.
- All SUSY particles are heavy enough to escape detection at the LHC, and it can be neglected for the Higgs sector.

With these assumptions $\Delta\mathcal{M}^2_{22}$ can be calculated by inverting the relation in Eq. 2.14 as

$$\Delta\mathcal{M}^2_{22} = \frac{m_h^2(m_{\rm A}^2 + m_Z^2 - m_h^2) - m_{\rm A}^2 m_Z^2 \cos^2 2\beta}{m_Z^2 \cos^2\beta + m_{\rm A}^2 \sin^2\beta - m_h^2}. \tag{2.15}$$

The heavy-scalar mass and the mixing angle can also be written as

$$m_H^2 = \frac{(m_{\rm A}^2 + m_Z^2 - m_h^2)(m_Z^2 \cos^2\beta + m_{\rm A}^2 \sin^2\beta) - m_{\rm A}^2 m_Z^2 \cos^2 2\beta}{m_Z^2 \cos^2\beta + m_{\rm A}^2 \sin^2\beta - m_h^2}, \tag{2.16}$$

$$\tan\alpha = \frac{(m_{\rm A}^2 + m_Z^2)\cos\beta\sin\beta}{m_Z^2 \cos^2\beta + m_{\rm A}^2 \sin^2\beta - m_h^2}. \tag{2.17}$$

The mass of the charged Higgs scalar coincides with the tree-level value, i.e. $m_{H^\pm} = m_{\rm A}^2 + m_W^2$ in this approach.

The production cross sections and the decay branching fractions of all the MSSM Higgs bosons depend on only $m_{\rm A}$ and $\tan\beta$ for a fixed m_h, under the assumptions that characterise the hMSSM.

There is a minimum value of $m_{\rm A}$ ($m_{\rm A}^{\rm min}$) which it is not possible to reproduce the desired m_h with only a correction to $\mathcal{M}_{22}^2$ for any given value of $\tan\beta$. For large $\tan\beta$ case, it has $m_{\rm A}^{\rm min} \sim m_h$, while for the low $\tan\beta$ case the minimum value of $m_{\rm A}$ increases up to $m_{\rm A}^{\rm min} = (m_h^2 - m_Z^2)^{1/2}$. It is discussed about the validity of the assumption of neglecting $\mathcal{M}_{11}^2$ and $\mathcal{M}_{12}^2$ on References [43, 44]. The dominant contributions from top-stop loops shows that the $\mathcal{M}_{11}^2$ and $\mathcal{M}_{12}^2$ are proportional to powers of the ratio term $\mu X_t/m_{\rm SUSY}^2$. $m_{\rm SUSY}$ is a few TeVin the hMSSM scenarios, the full one-loop and the known two-loop contributions does not changed this assumption. A numerical comparison between the predictions for m_H and α obtained from the codes `SuSpect` [45] and FeynHiggs [40, 46–49] and the hMSSM approximations in References [43, 44]. A comparison with the EFT have been also studied in Reference [30].

2.3 Experimental Status of Heavy Higgs Bosons Searches

Searches for the heavy Higgs bosons with 2HDMs and MSSM are reviewed. Direct searches using collider have been tested by several experiments. A brief review of direct searches at LEP, Tevatron and LHC are described.

2.3.1 Direct Searches for the Neutral MSSM Higgs Bosons

Direct searches have been performed at LEP, Tevatron and LHC. Figure 2.2 shows a summary

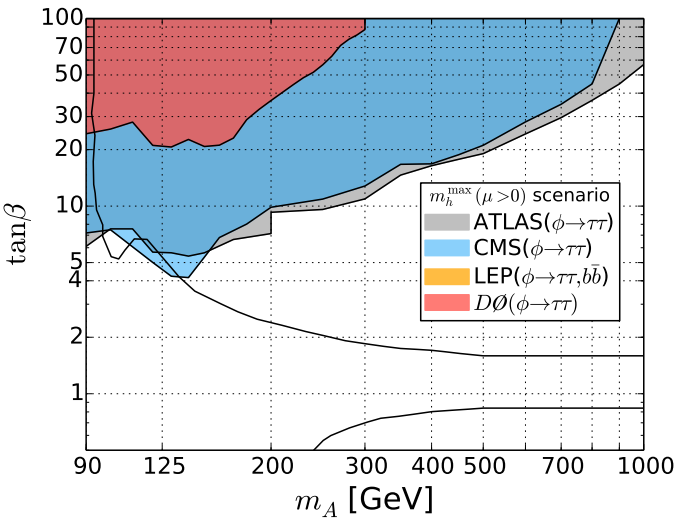

Figure 2.2: Observed exclusion limits at the 95% confidence level for the $m_h^{\rm max}$ benchmark scenarios on (mA, $\tan\beta$) plane with four independent search results from LEP, *DØ*, ATLAS and CMS (taken from Reference [37, 50, 51] and [36] respectively).

for the searches. Several exclusion limits has been set by $\phi \to \tau\tau$ and $\phi \to b\bar{b}$ decay modes. The *DØ* result was performed by $\phi \to \tau\tau, b\bar{b}$ with integrated luminosities of 5.2-7.3 fb^{-1}. The results of the ATLAS and CMS collaboration have obtained by Run1 with $\sqrt{s} = 7, 8$ TeV using integrated luminosities of 19.5-20.3 fb^{-1} and 24.6 fb^{-1} respectively. Before the discovery of SM Higgs boson at $m_h \sim 125$ GeV, the $m_h^{\rm max}$ scenario was used for a benchmark to search for the MSSM Higgs bosons.

Searches for the Neutral MSSM Higgs Bosons at LEP

Direct searches for the neutral heavy Higgs bosons were performed by the LEP experiments, ALEPH, DELPHI, L3 and OPAL [50]. LEP was electron-positron collider, so that the experimental signature was $e^-e^+ \to hZ$ mode. There are two Higgs boson decay modes of $b\bar{b}$ and $\tau^-\tau^+$ with Z boson decaying to $q\bar{q}, \nu\bar{\nu}, e^-e^+, \mu^-\mu^+, \tau^-\tau^+$ and $q\bar{q}, \nu\bar{\nu}, \tau^-\tau^+$ respectively. The region filled with green in Figure 2.2 shows the 95% confidence level exclusion limits on the ($m_{\rm A}$, $\tan\beta$) plane.

Searches for the Neutral MSSM Higgs Bosons at the Tevatron

The neutral MSSM Higgs bosons have been searched by the CDF and $D\emptyset$ collaborations with $\sqrt{s} = 1.96$ TeV. A combined result by the CDF and $D\emptyset$ were reported in Reference [52], but the $D\emptyset$ collaboration has updated results in Reference [51] as shown in Figure 2.2. They searched $\phi \to \tau\tau$ and $\phi \to b\bar{b}$ decay modes for the $m_h^{\rm max}$ with $\mu > 0$ scenario using integrated luminosities of 5.2-7.3 $\rm fb^{-1}$. They considered only $\tau_\mu \tau_{\rm had}$ decay channel as a final state. In addition to an algorithm of tagging hadronic τ-lepton decay products, b-quarks are also identified using the b-jet tagging technique. This leads analysis sensitivity even better at high-tan β region which enhance b-quark couplings. This technique have been also used in experiments in LHC.

Searches for the Neutral MSSM Higgs Bosons at the LHC

Since a center-of-mass energy of LHC is highest among above collider , the production cross section of the heavy Higgs bosons are highest. The analysis sensitivity for the heavy Higgs bosons have been significantly improved at high-tan β region even wider $m_{\rm A}$ range. In Figure 2.2, gray (ATLAS [37]) and blue (CMS [36]) region presents the observed exclusion limits at the 95% confidence level for $m_h^{\rm max}$ ($\mu > 0$) scenario using $\phi \to \tau\tau$ decay mode with $\sqrt{s} = 7, 8$ TeV. Reconstruction technique of an invariant mass of di-τ system have been developed at searches for the SM Higgs boson at the Tevatron [53]. This technique improved a $m_{\tau\tau}$ resolution typically 20-30% at $m_h \sim 125$ GeV. Results at both experiments used three decay channels ($\tau_\ell \tau_\ell$, $\tau_\ell \tau_{\rm had}$, $\tau_{\rm had} \tau_{\rm had}$) and the b-jet tagging to identify the bottom annihilation production process. Besides $\phi \to \tau\tau$ decay mode, several other decay mode like $H \to VV$ have been also developed [54] can be seen in Figure 3.11. As discussed in Section 3.2.3 $\phi \to \tau\tau$ decay mode is most important experimental searches.

3 Phenomenology of Proton-Proton Collisions

The Lagrangian of the Standard Model or MSSM are not directly observable. The process of deriving physical observable, like the interaction rate for given physical process, and the simulation of hadron collisions are evaluated by the Monte Carlo simulation. A review of the simulation of such physics process is given in Section 3.1 based on References [55–57] Phenomenology of heavy Higgs bosons production and decay are briefly described in Section 3.2 based on reference [58].

3.1 Simulation of Hadron Collisions and Calculation of Cross-Section

Number of some physics processes, N_{int}, is determined by the cross-section σ, and the integrated luminosity $\int \mathcal{L}dt$. An instantaneous luminosity $\mathcal{L}$ is given approximately by :

$$N_{\text{int}} = \sigma \int \mathcal{L}dt, \quad \mathcal{L} = \frac{f N_1 N_2}{2\pi \Sigma_x \Sigma_y}, \tag{3.1}$$

where f is the frequency of collision, N_1 and N_2 are the number of protons per bunch for both beam, Σ_x and Σ_y are the horizontal and vertical convoluted beam width [59] under the assumption of a Gaussian density profile of beam. The integrated luminosity depends on the machine parameters and the length of the data-taking only, but the cross-section for hard scattering events are independent on the machine parameters.

Figure 3.1 shows a schematic overview of a proton-proton collision.

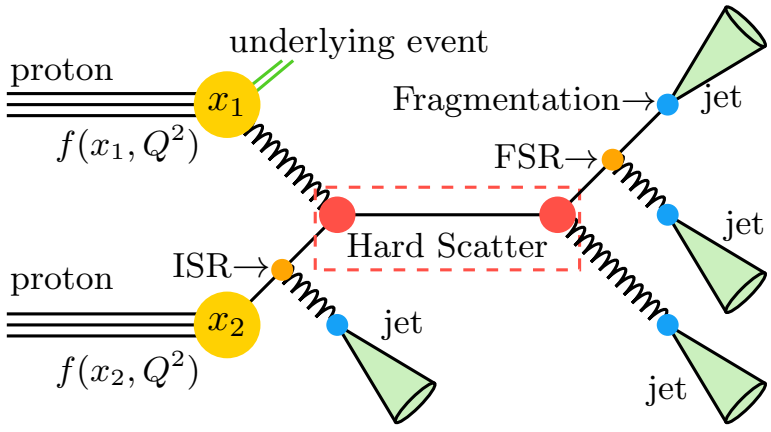

Figure 3.1: Illustration of the perturbative and non-perturbative subprocesses for the simulation of hadron collisions. The momentum of two initial state partons are described by the PDFs, the hard scatter event is described by a matrix element calculated perturbation theory followed by phenomenological models for soft QCD effects as parton showering and hadronisation (fragmentation).

Phenomenological models of non-perturbative effects must interplay with theoretical predictions for

the hard scattering process. The remnants of proton-proton collision undergo a series of low-energy interactions, denoted as *underlying event*. The initial and final state particles at the hard scatter carry colour and electric charge. Additional interactions, denoted as the initial (*ISR*) state radiation and final state radiation (*FSR*) can happen. A jet consists of a narrow cone of the colour neutral hadrons which is hadronised from the colour charged final-state partons The instrumental detector effects should be accounted to compare experimental data with theoretical predictions. A detailed detector simulation including accurately models the particle matter interaction in the sub-detectors of ATLAS. A brief review of the chain of various methods to simulate of proton-proton collisions is described in following sub-sections.

3.1.1 The Factorisation Theorem, Parton Distribution and Fragmentation Functions

It is impossible to calculate the cross-section of hard-process directly from proton-proton collision, since low-energy QCD effects govern the parton structure. While it is possible to factorise the effects that can be described by perturbation theory from non-perturbative low-energy effects.

The factorisation theorem make it possible to approximately calculate from the convolution of a low-energy, long-range function and a high-energy, short-range function. This scale is called as the factorisation scale μ_F that is used to distinguish low- and high-energy effects. Details of factorisation theorem can be found in Reference [60]. The factorisation scale is not a physical parameter, so that it is not expected that the physical value of an observable depends on the factorisation scale. It is conventionally checked a variation of varying it with a certain range and its variation is treated as a systematic uncertainty. The factorisation scale is employed for the parton distribution functions (PDF) and the process of hadronisation described in Section 3.1.4.

Quarks and gluons, i.e. partons, can be treated as the point-like constituents of hadrons. According to the factorisation theorem the differential cross-section for a physical observable $\mathcal{O}$ in a collision of hadrons $h_{1,2}$ can be written as

$$\frac{d\sigma}{d\mathcal{O}} = \sum_{a,b} \int_0^1 \mathrm{d}x_a \int_0^1 \mathrm{d}x_b \sum_F \mathrm{d}\Phi_F f_a^{h_1}(x_a, \mu_F) f_b^{h_2}(x_a, \mu_F) \frac{\mathrm{d}\hat{\sigma}_{ab\to F}}{\mathrm{d}\hat{\mathcal{O}}} D_F\left(\hat{\mathcal{O}} \to \mathcal{O}, \mu_F\right), \tag{3.2}$$

where a and b in the outer sum runs over all partonic constituents of a hadrons h_1 and h_2. The inner sum includes all possible final states of F in the processes $ab \to F$ with phase space Φ_F. The functions $f_a^{h_1}(x_a, \mu_F)$ and $f_a^{h_2}(x_b, \mu_F)$ are the non-perturbative parton distribution functions. $\hat{\sigma}$ is the perturbative partonic cross-section and $D_F(\hat{\mathcal{O}} \to \mathcal{O}, \mu_F)$ is a non-perturbative fragmentation function, which describes the transition from the quantity $\hat{\mathcal{O}}$ based on the partons from final state F to the observable $\mathcal{O}$. The parton distribution function $f_a^{h_1}(x_a, \mu_F)$ implies the probability to find a parton of type a with a fraction of momentum to original hadron h_1 momentum, x_a. The value of the parton distribution and the fragmentation function at a scale Q'^2 can be achieved from the value at Q^2, where Q denotes an energy scale of the hard interaction. This evolution is described by the Dokshitzer–Gribov–Lipatov–Altarelli–Parisi (DGLAP) evolution equations [62–64]. Since the parton distribution functions cannot be calculated in the perturbative QCD, so that it needs to be extracted from an experimental data, mainly from deep inelastic scattering experiments. Several collaborations have performed combined fits to dataset, with small differences in the exact choice of input data and the chosen parameterization of the parton-density functions. The following sets recently provide results: PDF4LHC [65], NNPDF [66], CT14 [67], MSTW [61] and AZNLO [68]. The major uncertainties on the PDF fits are experimental uncertainties of the input data, uncertainties on the strong coupling α_S and the functional form used as parameterization. Figure 3.2 shows the parton density as a function of x as provided by the MSTW2008 PDF set and its uncertainty at two different momentum transfer scales.

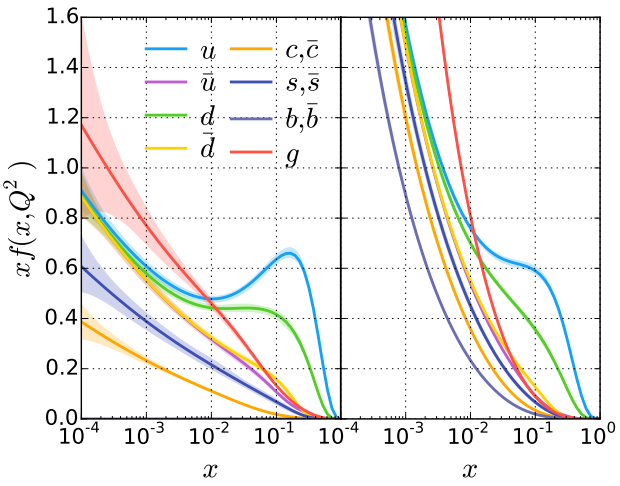

Figure 3.2: MSTW 2008 parton distribution functions at $Q^2 = 10$ GeV^2 (left) and $Q^2 = 10^4$ GeV^2 (right) with 68% confidence level uncertainty bands. The products of the proton momentum fraction of quarks or gluon, x, and the parton distribution function $f(x, Q^2)$ are shown. The parton distribution function for gluons are scaled down by a factor of 10 (made from References [61]).

3.1.2 Partonic Cross-Section and Event Generation

When the energy scale of the hard scatter is large enough to allow for a perturbative treatment of QCD, the partonic differential cross-section for an inclusive production of a final state F can be expanded in powers of the strong coupling constants:

$$\frac{\mathrm{d}\sigma_{ab\to F}}{\mathrm{d}\hat{\mathcal{O}}} = \int \mathrm{d}\Phi_F |\mathcal{M}_F|^2 \delta\left(\hat{\mathcal{O}} - \hat{\mathcal{O}}(\Phi_F)\right) = \sum_{k=0}^{\infty} \int \mathrm{d}\Phi_{F+k} \left|\sum_{l=0}^{\infty} \mathcal{M}^l_{F+k}\right|^2 \delta\left(\hat{\mathcal{O}} - \hat{\mathcal{O}}(\Phi_F)\right), \tag{3.3}$$

where $\mathcal{M}_F$ is the matrix element for the production of the final state F with phase space Φ_F. The matrix element is perturbatively expanded in α_S. The sum over k runs over additional partons in the final state, which are real emissions from QCD interactions. The sum over l runs over virtual corrections, which are loops from QCD interactions.

$\mathcal{M}^l_{F+k}$ is the matrix element for the final state F with real emissions k, loops l and phase space Φ_{F+k}. If the sum includes only the term for $k = 0, l = 0$, the result is the leading order of α_S approximation (conventionally called as LO), for $k = n, l = 0$ the result is the leading order of α_S approximation for $F + n$ jets if all real emissions are quarks or gluons (LO). Finally in the case of $k + l \leq n$, the result is N^{n-1}LO approximation. The processes used for the matrix element can be calculated by the Feynman rules. Practical calculations can be also additionally included the Feynman diagrams with the leading logarithmic divergences (LL) of a higher order. A detailed explanation of the Feynman rules can be found in References [6, 55].

If observable $\mathcal{O}$ is calculated at fixed order in α_S with perturbation theory, it is still possible that the result is divergent due to loop effects. It is not possible to calculate all orders in the perturbation theory, the divergences are removed by normalising the theory.

In the renormalization, the charges, masses and fields in the Lagrangian (*bare quantities*) are replaced by observable quantities that formally include divergences. This divergences would cancel out with loop-induced divergences of the bare quantities, so that the observable quantities are finite. An unnatural scale μ_R is introduced, which is similar to the factorisation scale in the renormalization theorem. It is also conventionally varied and a variation of results is used to be as a systematic uncertainty. A detailed overview of the renormalization can be found in Reference [6].

It is important to understand effects of detector's acceptance and experimental efficiency. A measurement of differential distributions is necessary to compare a multi-dimensional phase space of experimental data and theoretical estimation. *Monte Carlo Event Generators* perform the numerical integrations and generate sets of four-momentum of the final state particles.

3.1.3 The Partonic Process Simulation and Parton Shower Matching

The initial state partons for the hard process (F) are chosen by the parton distribution functions. The final state partons and the corresponding four-momenta are produced with probability density functions that are proportional to the differential cross-sections based on fixed-order calculations. For the final state $F+n$ jets, the additional partons are required to have a minimum transverse momentum p_{T} and minimum angular separation ΔR, so that soft and collinear divergences are avoided in the NLO generators calculation. Other partons are generated by the parton shower algorithm. The parton shower algorithms are complementary to the simulation of partonic process. All orders of perturbative calculation are included in the parton shower algorithm to avoid the divergences, which is based on the resummation of the leading collinear and soft logarithms. A relation of the differential cross-section for ax final state with n partons and the differential cross-section of a final state with $n+1$ partons are also built by the parton shower algorithm :

$$\mathrm{d}\sigma_{n+1} = \sigma_n \sum_{i\to jk} \frac{\alpha_S}{2\pi} \frac{\mathrm{d}\theta^2}{\theta^2} \mathrm{d}z P_{i\to jk}(z,\phi)\mathrm{d}\phi, \tag{3.4}$$

where z is the energy fraction between a parton k and its parent parton i, θ is an opening angle between the partons k and i, ϕ is an azimuthal angle of a parton j around an axis defined by the parton i and the sum accordingly $i \to jk$ runs over possible splitting pars to j, k. $P_{i\to jk}(z,\phi)$ are the spin averaged splitting functions [57] defined by :

$$P_{q\to qg} = C_F \frac{1+z^2}{1-z}, P_{q\to gq} = C_F \frac{1+(1-z)^2}{z}, \tag{3.5}$$

$$P_{g\to gg} = C_A \frac{z^4+a+(1-z)^4}{z(1-z)}, P_{g\to q\bar{q}} = T_R(z^2+(1-z)^2, \tag{3.6}$$

with

$$C_F = \frac{N_C^2-c}{2N_C}, C_A = N_C \text{ and } \frac{\mathrm{d}\theta^2}{\theta^2} = \frac{\mathrm{d}q^2}{q^2} = \frac{\mathrm{d}k_{\mathrm{T}}^2}{k_{\mathrm{T}}^2}, \tag{3.7}$$

$$q^2 = z(1-z)\theta^2E^2, \quad k_{\mathrm{T}}^2 = z^2(1-z)^2\theta^2E^2, \tag{3.8}$$

where N_C is the number of colours, q is the virtuality of the propagator and k_{T} is the transverse momentum of the parton k with respect to the parton i, T_R is a colour factor that is fixed only convention, $T_R = 1/2$. $P_{q\to qg}, P_{q\to gq}, P_{g\to gg}$ and $P_{g\to q\bar{q}}$ correspond to the splittings $q \to qg, q \to gq, g \to gg$ and $g \to q\bar{q}$ respectively[1]. The parton shower algorithm are implemented as successive parton splittings with a probability (so called Sudakov form factor) proportional to the differential cross-section as a function of k_{T} or θ. The parton splitting is stopped at q which is below a cut-off that corresponds to the hadronisation scale for virtuality-ordered parton showers. For other implementation, e.g. SHERPA [69] and PYTHIA8 [70], is built on the Catani-Seymour dipole factorisation [2].
If the parton showers are used together with generators for NLO or LO $F+n$ jets production, a phase space overlap between jets created by the partons shower and the fixed-order generator. The overlap are removed with following matching algorithms.

[1] A fifth splittings function $P_{q\to\bar{q}q}$ corresponding to $g \to \bar{q}q$ is equal to $P_{g\to q\bar{q}}$
[2] see References [71]

CKKW algorithm

CKKW [72, 73] algorithm is based on a resolution of the k_{T} jet algorithm [74]. Two jets i and j are resolved when the distance parameter y_{ij} is greater than the resolution parameter y_{cut},

$$y_{ij} = 2\min(E_i^2, E_j^2)(1 - \cos\theta_{ij})/Q^2 > y_{\mathrm{cut}}, \tag{3.9}$$

where E_i is the energy of jet i, θ_{ij} is an angular difference between jet i and j. y_{cut} is the pre-defined resolution and Q^2 is the scale of the interaction [75]. The fixed-order calculation is used for the parton splittings with $y_{ij} > y_{\mathrm{cut}}$ and the parton showers for $y_{ij} < y_{\mathrm{cut}}$. An event with $F + n$ jets production is generated and the resolution parameters y_{cut} to obtain $2, 3, \cdots, n$ jets are determined. A backward parton shower is performed in a clustering process. Only particle combinations that can result from a parton splitting are clustered.

The Sudakov form factor [76] introduces a cut-off scale for the parton shower evolution. It depends on a variable whcih describes the parton shower evolution. It ensures that partons are only generated with values of the evolution higher than the marging scale by the fixed-order generators. The parton shower emissions are only produced below the cut-off scale for the parton shower evolution variable. The CKKW algorithm is used in the `SHERPA`.

MLM algorithm

MLM algorithm [77] is an alternative algorithm. A hard scattering event based on a fixed-order calculation is generated with partons with a minimum transverse momentum , $p_{\mathrm{T,min}}$ and a minimum angular distance ΔR_{min}. Dividing event samples into two categories with events $\geq n$ partons, are called as inclusive sample, and with all other events are called as exclusive samples. A parton shower is evaluated and a jet clustering algorithm (k_{T} algorithm) with a distance parameter $\Delta R_{\mathrm{cluster}}$ is applied to obtain jets with $p_{\mathrm{T}} > p_{\mathrm{T,cluster}}$ which are matched to the partons from the fixed-order generator within $\Delta R < 1.5\Delta R_{\mathrm{cluster}}$. If two partons are matched to the same jet, the jet is selected. Otherwise a jet is rejected.

3.1.4 Hadronisation

Hadronisation is a transition of a parton event with colour-charged quarks and gluons into an event with colour-neutral hadrons. The most common model is the Lund-String-Model [75] which are used in `Pythia`. An overview is given in the following, a more detail can be found in Reference [57].

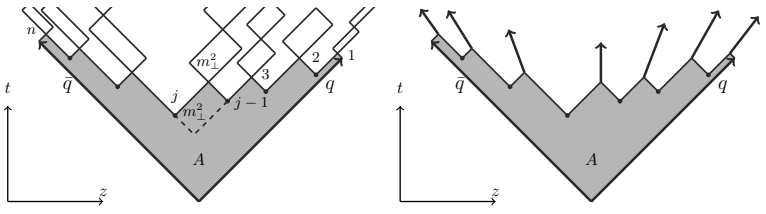

(a) High-energy string break-up **(b)** Fragmentation

Figure 3.5: (a):The break-up in space-time of a Lund string into n hadrons. The fragmentation area is denoted by A. (b):A sketch of the fragmentation of a one-dimensional $q\bar{q}$-string.

The model is based on a few general assumptions :

- Final state particles originate from a break-up of a string-like force field spanned between the coloured constituents.
- There is causality and Lorentz invariant.
- The production of the particles can be described in terms of a stochastic process which obeys a saturation assumption.
- The force field is considered as a massless relativistic string with a pair of quark at the end-points.

- Gluons are treated as internal excitations on the string field which behaves a constant force field with $\kappa \sim 1$ GeV/fm corresponding to a linear potential spanned between an original pair

The string is split into two pieces after a new pair is created. The production probability of a pair is given by following :

$$P(m_\perp) = \exp\left(-\frac{\pi m_\perp^2}{\kappa}\right), \tag{3.10}$$

where $m_\perp = \sqrt{\mu^2 + k_{\mathrm{T}}^2}$ with transverse momentum k_{T}. The final state mesons in the Lund-String-Model correspond to isolated string pieces containing a q from one break-up vertex and a $\bar{q}$ from the adjacent vertex together with the produced transverse momentum and the field energy. Figure 3.5(a) shows the break-up of the string. The procedure of string breaking are summarised following:

- Generate $q\bar{q}$ with $u\bar{u}$: $d\bar{d}$: $s\bar{s}$: $c\bar{c}$ = 1: 1: 0.3: 10^{-11} corresponding to be probability Equation 3.10.
- Set transverse momentum with Gaussian momentum (Fermi motion).
- Select the hadron state ($L = 0, S = 0$ or 1 for mesons), which has dynamical effect should be taken account by experimental data.

3.1.5 Underlying Event and Multiple Parton Interaction

The underlying event is a hadronic activity from a collision between partons of colliding hadrons not contribute to a hard process. The underlying event includes effects from the hadronisation of beam remnants and multiple $2 \to 2$ parton interactions. An accurate model of the underlying event is of the highest interest, since soft particles from the underlying have impacts on the performance of momentum measurements significantly, like for instance jet-energy calibrations and the determination of $E_{\mathrm{T}}^{\mathrm{miss}}$ (see Section 5.7). There are several models and implemented in common multi-purpose Monte Carlo event generators. Usually these models include various parameters, which can be tuned with experimentally accessible observable like the charged particle multiplicity [78, 79].

3.1.6 Pile-up Events Simulation

In addition to the underlying event, another origin of soft QCD interactions exist, so-called *pile-up*. The pile-up is caused by multiple proton-proton interactions per bunch crossing and a major issue in the high luminosity environment of the LHC. From 2015 LHC proton-proton collisions, bunch trains rise up to 10^{11} protons with a transverse size of roughly 16 μm. During the 2016 data taking period, the number of interactions per bunch crossing is expected to $20 \sim 40$. In order to save a lot of time and simulation resources for a full simulation with pile-up activity, the interactions is modelled by generating an inclusive proton-proton collision event samples and by overlaying them to the hard scatter event samples. To model conditions in real data as precise as possible, the number of overlaid event is varied and reweighted to match actual distributions of the number of interactions per bunch crossing.

3.1.7 Detector Simulation

The ATLAS detector is an extremely complex detector, consisting of multiple sub-detectors and more than 100 millions of read-out channels. The detector description is given in Chapter 4. A detailed description can be found in References [80, 81]. Generated events including non-perturbative corrections like the parton shower, hadronisation and pile-up activity are passed through a detailed detector simulation. The simulation is based on `Geant4` [82] which performs all interaction between

particles and materials. After `Geant4` simulation event samples need to pass a digitisation, which simulates electrical response in sub-detectors. It is ensured that the simulated event samples can be used same output format as the actual experimental data.

3.2 Phenomenology of Heavy Higgs Bosons

The production and decay of Higgs bosons are described for the MSSM benchmark scenario in this section. The cross-sections and decay branching fraction are shown for the MSSM Higgs boson in proton-proton collisions at $\sqrt{s} = 13$ TeV.

3.2.1 Production of Heavy Higgs bosons in Benchmark Scenario

The cross-section for a production of the neutral Higgs bosons $\phi \equiv (h, H, A)$ via gluon-fusion ($gg \to \phi$) and bottom-annihilation ($b\bar{b} \to \phi$) have been computed with the code `SusHi 1.5.0` [83]. The SM input parameters for `SusHi` have been chosen to the values listed in Table 3.1 in calculation of the production cross-section. The renormalization scale μ_R and the factorisation scale μ_F have been

Parameter	`SusHi 1.5.0`	`HDECAY 6.42`
PDF(NLO)	`MSTW2008nlo68cl`	-
PDF(NNLO)	`MSTW2008nnlo68cl`	-
$\alpha_S(m_Z)$	0.119	0.119
$m_c(m_c)^{\overline{\rm MS}}$	1.28 GeV	1.28 GeV
$m_b(m_b)^{\overline{\rm MS}}$	4.16 GeV	4.16 GeV
$m_c^{\rm pole}$	-	1.42 GeV (1-loop value)
$m_b^{\rm pole}$	4.75 GeV	4.49 GeV (1-loop value)
$m_t^{\rm pole}$	172.5 GeV	172.5 GeV
G_F	1.16637×10^{-5} GeV^{-2}	1.16637×10^{-5} GeV^{-2}
m_Z	91.1876 GeV	91.15349 GeV (Complex mass scheme)
m_W	-	80.36951 GeV (Complex mass scheme)
Γ_Z	-	2.49581 GeV (Derived NLO)
Γ_W	-	2.08856 GeV (Derived NLO)
$\alpha_{\rm EW}^{-1}(m_Z)$	127.67	(value to obtain m_W =80.398 GeV)

Table 3.1: SM parameters used for the calculation of the Higgs production cross-section and branching ratio with the code `SusHi 1.5.0` and `HDECAY 6.40`. The listed value of $\alpha_S(m_Z)$ is used for RG evolution and passed to `FeynHiggs` for the calculation of the Higgs boson masses and mixing, whereas the corss section calculation use the values of α_S associated to the PDFs.

fixed as $\mu_R = \mu_F = m_\phi/2$ in the case of the gluon-fusion and as $\mu_R = 4\mu_F = m_\phi$, in the case of the bottom-annihilation(see in Reference [30]). Uncertainties on these scales have been obtained from the envelope of seven independent variation of μ_R and μ_F by factor 2 within the constraint $1/2 \leq \mu_R/\mu_F \leq 2$ in the case of the gluon-fusion, and $2 \leq \mu_R/\mu_F \leq 8$ in the case of the bottom-annihilation. The `MSTW2008` parton distribution function set has been used, and residual uncertainties on the parton distribution functions and on the strong coupling constant α_S have been obtained by proposed method in Reference [65].

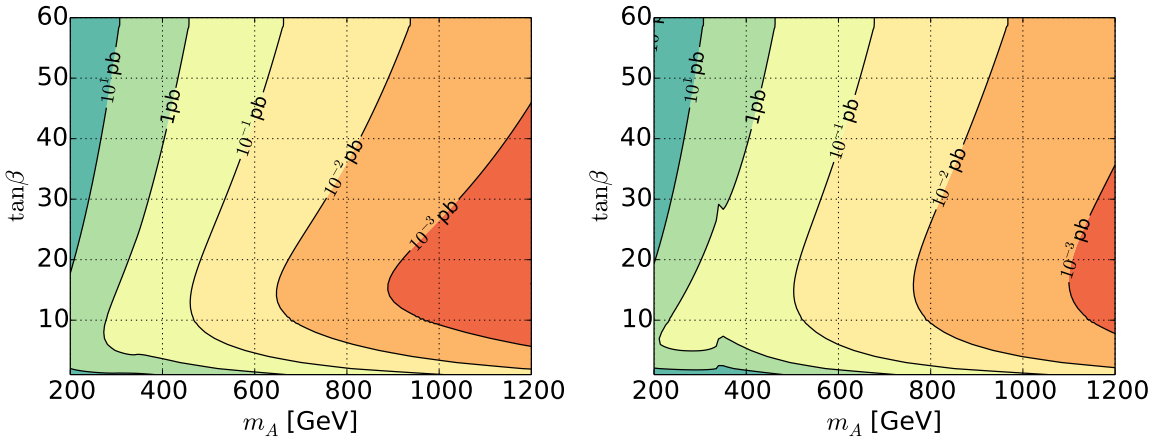

(a) CP-even Higgs, H **(b)** CP-odd Higgs, A

Figure 3.6: The production cross-section for the Higgs bosons with the gluon-fusion process in (m_{A}, $\tan\beta$) plane. Left(right) shows the cross-section of the CP-even(odd) Higgs, $gg \to H(A)$.

Gluon-Fusion Production Cross-Section

The code implements top- and bottom-loop contributions at NLO [84, 85], NNLO top contributions in the heavy-top limit from [86–90] and electroweak contributions by light quarks [91, 92]. There are no contributions from squark loops since consistency with the assumption. Figure 3.6 shows the production cross-section for $gg \to \phi$ in (m_{A}, $\tan\beta$) plane.

Bottom-Annihilation Production Cross-Section

`SusHi` implements the NNLO results in the five-flavour scheme from Reference [93]. The amplitude for the production of the SM Higgs boson mass m_ϕ is re-weighted with the effective coupling g_{dd} given in equation in Table. 2.1. In addition to the five-flavour scheme, the four-flavour scheme cross-

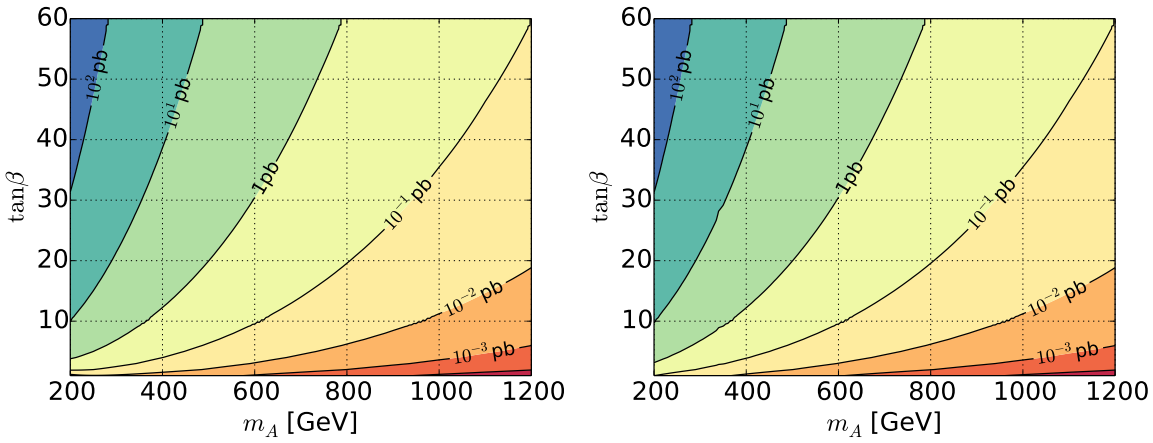

(a) CP-even Higgs, H **(b)** CP-odd Higgs, A

Figure 3.7: The production cross-section for the Higgs bosons with the Bottom-Annihilation process in (m_{A}, $\tan\beta$) plane. Left(right) shows the cross-section of the CP-even(odd) Higgs, $bb \to H(A)$.

section ($gg \to b\bar{b}\phi$) [94, 95] is combined by the "Santander matching method" [96]. The production cross-section with the Santander matching for the CP-even and CP-odd Higgs bosons are presented

in Figure 3.7.

Comparison of Two Production Cross-Section

Since down-type fermions are strongly enhanced at higher-tan β it is important to compare two production cross-sections. Figure 3.8 shows ratios for the bottom-annihilation and the gluon-fusion

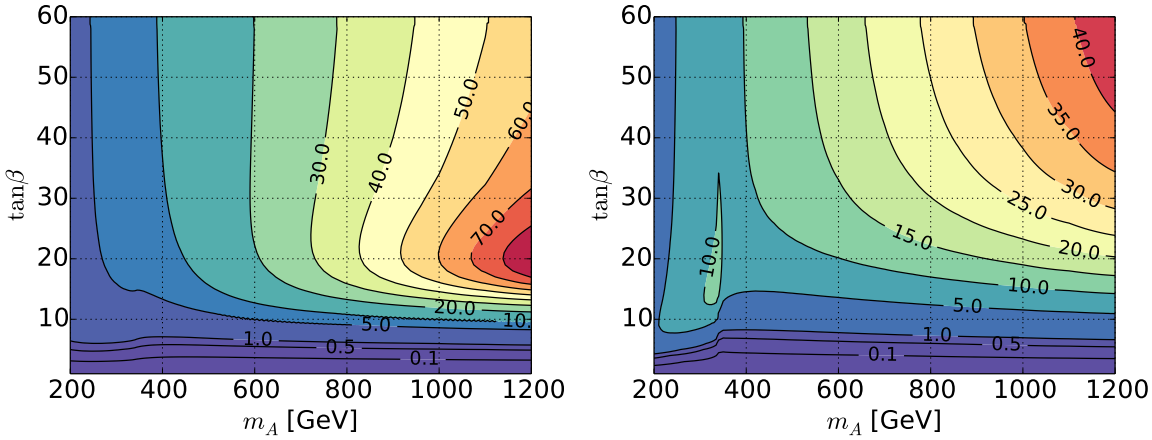

(a) CP-even Higgs, H **(b)** CP-odd Higgs, A

Figure 3.8: Ratio of the production cross-section the bottom-annihilation process and the gluon-fusion (bbA/ggF) in (m_{A}, tan β) plane. Left(right) shows the cross-section of the CP-even(odd) Higgs.

production process in (m_{A}, tan β) plane for the CP-even Higgs (a) and the CP-odd Higgs (b). As expected from the down-type fermion enhancement, tan $\beta \gtrsim 15$ the bottom-annihilation cross-section is larger than the gluon-fustion by a factor of $\simeq 10(80)$ for CP-even Higgs (CP-odd Higgs). Identification of b-quarks is important which is described in Section 5.3.3.

3.2.2 Decay of Heavy Higgs bosons in Benchmark Scenario

The branching fraction have been calculated with the code `HDECAY` [97, 98] which can take m_h as input and obtain m_H and mixing angle α from the hMSSM prescriptions in Eq. (2.11) and (2.13). The value of the SM input parameters are summarised in Table 3.1. The hMSSM mode of `HDECAY` implements: N^{4}LO-QCD corrections to the decays to a pair of quarks [99–111]; LO results are used for the decays to lepton pairs and for the decays involving massive gauge bosons. Figure 3.9 shows the branching fraction of several decay modes which can be searched at the LHC for both CP-even and CP-odd Higgs bosons. For the CP-odd Higgs the WW and ZZ couplings are vanished. The $\phi \to \tau\tau$ decay mode shows relatively larger branching fraction for tan $\beta = 3$ and 30 compared with other decay modes in the CP-even and CP-odd Higgs bosons. The $b\bar{b}$ mode has larger branching fraction than the $\phi \to \tau\tau$ mode, however $\phi \to b\bar{b}$ mode is experimentally difficult at the LHC due to difficulty of triggering only b-quarks (or including other light-flavour). The CP-even Higgs boson have $\phi \to WW/zZ$ decay modes. Leptonic decay of $Z/W^{\pm}$ are useful for triggering and suppression of backgrounds, but branching fraction is suppressed. Figure 3.10 shows the branching fraction of the $\phi \to \tau\tau$ decay mode in (m_{A}, tan β) plane ($\mathrm{Br}^H_{\tau\tau}$, $\mathrm{Br}^A_{\tau\tau}$). Figure 3.10 (b) shows "edge" around $m_{\mathrm{A}} \sim 350$ GeV and tan $\beta < 10$ due to decay mode opens to $A \to t\bar{t}$ channel. For tan $\beta \geq 10$ both $\mathrm{Br}^H_{\tau\tau}$ and $\mathrm{Br}^A_{\tau\tau}$ has greater than 10% branch and less dependency against tan β.

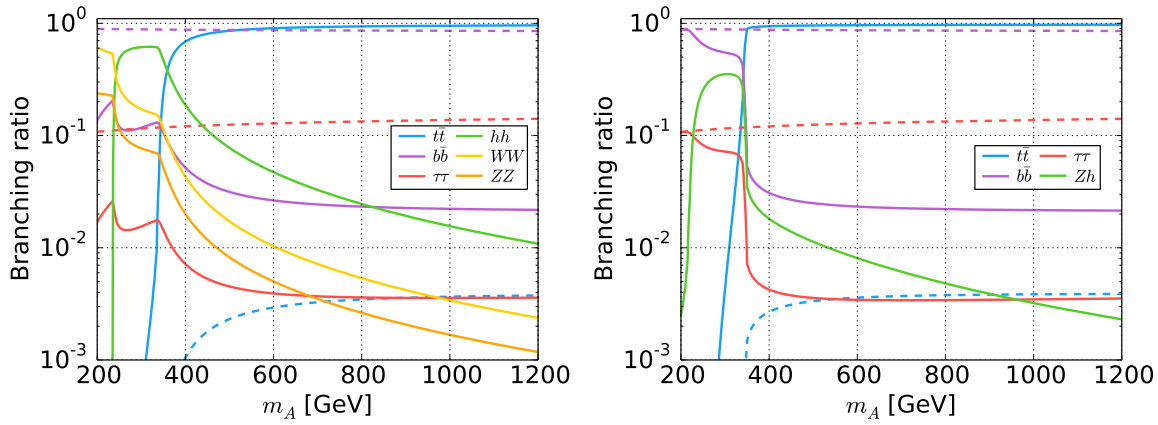

(a) CP-even Higgs, H **(b)** CP-odd Higgs, A

Figure 3.9: Branching ratios for CP-even and CP-odd Higgs bosons as a function of the pseudoscalar mass m_{A} with two different $\tan\beta$ values in log-scale. All solid(dashed) lines correspond to $\tan\beta = 3(30)$. Only decay modes which has $> 10^{-3}$ are presented in both $\tan\beta$ values.

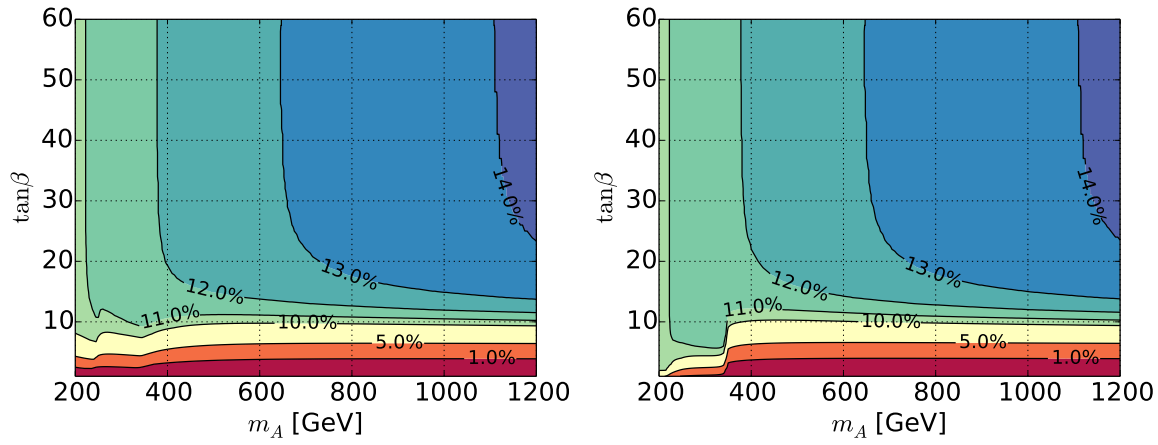

(a) CP-even Higgs, H **(b)** CP-odd Higgs, A

Figure 3.10: The branching ratios of $\phi \to \tau\tau$ for CP-even and CP-odd Higgs bosons in (m_{A}, $\tan\beta$) plane.

3.2.3 Experimental Search Channels

Searches for heavy Higgs bosons is one of important BSM physics search in experiments at the LHC. Only several combinations of production and decay mode are accessible due to experimental considerations because of triggering or signal-background separation. Because of $\tan\beta$ enhancement and suppression, any experimental signature cannot cover whole region on (m_{A}, $\tan\beta$) plane, so that several experimental signatures are need to search entire region of (m_{A}, $\tan\beta$). Experimentally searching the neutral Higgs bosons (H/A) are well established and tested so far. Searches for the neutral Higgs bosons can be separated in two groups, which is sensitive at high- or low-$\tan\beta$. Figure 3.11 shows direct and indirect exclusion limit for the hMSSM scenario in (m_{A}, $\tan\beta$) plane. At low $\tan\beta$, $H \to ZZ, H \to W^{\pm}W^{\mp}, H \to hh, A \to Zh$ and $H/A \to t\bar{t}$ dominate sensitivities due to $\tan\beta$ suppression. Diboson modes are suppressed above $m_{\mathrm{A}} \gtrsim 350$ GeV due to the branching fraction open to $H \to t\bar{t}$ mode, and the branching fraction at higher $\tan\beta$ are strongly decreased. Diboson decay modes are sensitive only region of $(m_{\mathrm{A}}, \tan\beta) \lesssim (350\ \mathrm{GeV}, 5)$. The indirect exclusion

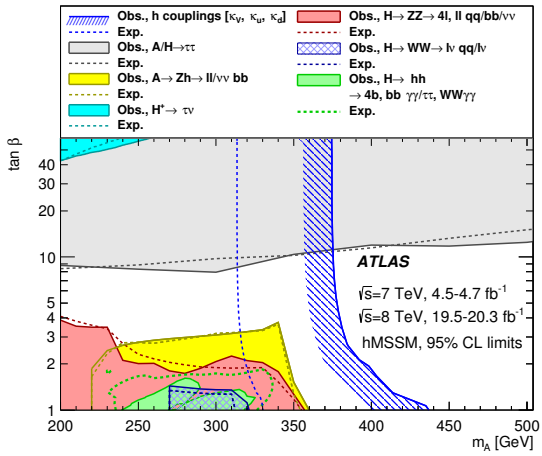

Figure 3.11: Regions of the (m_{A}, $\tan\beta$) plane excluded in the hMSSM scenario via direct searches for heavy Higgs bosons and fits of the measured rate of observed Higgs boson production and decays. The observed (expected) exclusion region is indicated by the hashed (dashed) line. (taken from Reference [112], detailed description can be found in Reference [54])

limit from the SM Higgs boson measurements is expected even higher than ~ 375 GeV for most of $\tan\beta$ region (blue hashed and line as shown in Figure 3.11). While $H \to t\bar{t}$ mode has large branching fraction at $m_{\mathrm{A}} > 350$ GeV and low-$\tan\beta$, but difficulty of separation against the SM $t\bar{t}$ processes are crucial to search them. There is also an interference effect between $H \to t\bar{t}$ and the SM $t\bar{t}$, estimation of the effect recently developed [113] and its sensitivity is not yet fully optimised. On the other hand, at high-$\tan\beta$ two decay mode are promising, $H/A \to b\bar{b}$ and $H/A \to \tau\tau$. Since the LHC is proton-proton collider, the QCD multijet (dijet) process is dominated its event rate (cross-section is $\mathcal{O}$(mb)). $H/A \to b\bar{b}$ has only b-quarks (or gluons) in the final state, this leads hard situation to trigger its event, the ATLAS single jet (or b-jet) trigger tends to have large jet p_{T} threshold of about $p_{\mathrm{T}} \gtrsim 400$ (150) GeV. In addition to trigger, background-to-signal ratio is poor due to large contributions from the QCD multijets and SM $t\bar{t}$ processes. $H/A \to \tau\tau$ have relatively large branching ratio at wider range of m_{A} and $\tan\beta > 10$. In terms of triggering $H/A \to \tau\tau$ has an unique final state with leptons ($\ell = e, \mu$) and hadronic τ-lepton decay products. Accordingly the branching fraction

channel	final state	BR (%)	trigger	background	search range
$\tau_\ell\tau_\ell$	$\ell + \ell + 4\nu$	12.4	leptons,	very clean	low mass
$\tau_\ell\tau_{\mathrm{had}}$	$\ell + \tau_{\mathrm{had}} + 3\nu$	45.1	lepton, had. τ,$E_{\mathrm{T}}^{\mathrm{miss}}$	clean	low/ high mass
$\tau_{\mathrm{had}}\tau_{\mathrm{had}}$	$\tau_{\mathrm{had}} + \tau_{\mathrm{had}} + 2\nu$	40.1	hadronic-τ	relatively high	high mass

Table 3.2: Summary of decay channels of $H/A \to \tau\tau$ mode with final states particles, branching ratio, accessible triggers, background cleanness and search range on m_{A}.

of τ-lepton, $H/A \to \tau\tau$ are grouped three decay channels, $\tau_{\mathrm{had}}\tau_{\mathrm{had}}$, $\tau_\ell\tau_{\mathrm{had}}$ and $\tau_\ell\tau_\ell$ has two hadronic τ-lepton products, one leptonic τ-lepton decay products and one hadronic τ-lepton products and two leptonic τ-lepton decay products respectively. Three decay channels are summarised in Table 3.2. In the sense of trigger, $\tau_\ell\tau_{\mathrm{had}}$ channel has several choices and their total trigger efficiency is nearly 100%. While $\tau_{\mathrm{had}}\tau_{\mathrm{had}}$ channel has only hadronic-τ triggers and its trigger threshold is already $p_{\mathrm{T}}^{\tau_{\mathrm{had}}} \gtrsim 100$ GeV at the beginning of the Run2[3] commissioning phase. The single-lepton-trigger[4] are still kept its threshold about $p_{\mathrm{T}}^{\ell} \gtrsim 25$ GeV. The $\tau_\ell\tau_{\mathrm{had}}$ channel are also characterised as large $E_{\mathrm{T}}^{\mathrm{miss}}$ compared to other two channels. Neutrinos emitted from di-τ are relatively balanced in the $\tau_{\mathrm{had}}\tau_{\mathrm{had}}$ and $\ell^+\ell^-$.

[3] The Run2 started from 2015 and will continue 2018 with $\sqrt{s} = 13$ TeV. The instantaneous luminosities will go up-to $2.0 \times 10^{34}\mathrm{cm}^{-2}\,\mathrm{s}^{-1}$.

[4] Trigger decision with only one lepton signature, details are given in Chapter 5.

4 The ATLAS Experiment at the LHC

The ATLAS experiment [114] is one of the four large experiments at the Large Hadron Collider (LHC) [115]. The detector is located at the European Organisation for Nuclear Reserch (CERN) in Geneva, Swizerland. The accelerator complex is used to accelerate and collide particles in the LHC is introduced in Section 4.1, As well as an overview of the ATLAS experiment and its detector concept is described in Section 4.2.1. A run condition during data-taking periods in 2015 and 2016 is summarised in Section 4.3.

4.1 The Large Hadron Collider

The Large Hadron Collider(LHC) is the most powerful particle accelerator ever built. It was first conceived in the 1980s a facility to find the Higgs boson and physics beyond our current understanding. The LHC accelerator is designed as a proton-proton collider at a center-of-mass energy of $\sqrt{s} = 14\,\text{TeV}$ with a high instantaneous luminosity of $10^{34}\,\text{cm}^{-2}\,\text{s}^{-1}$. This performance can be achieved with an injector complex and the following 27 km LHC main ring as summarised in Figure 4.1.

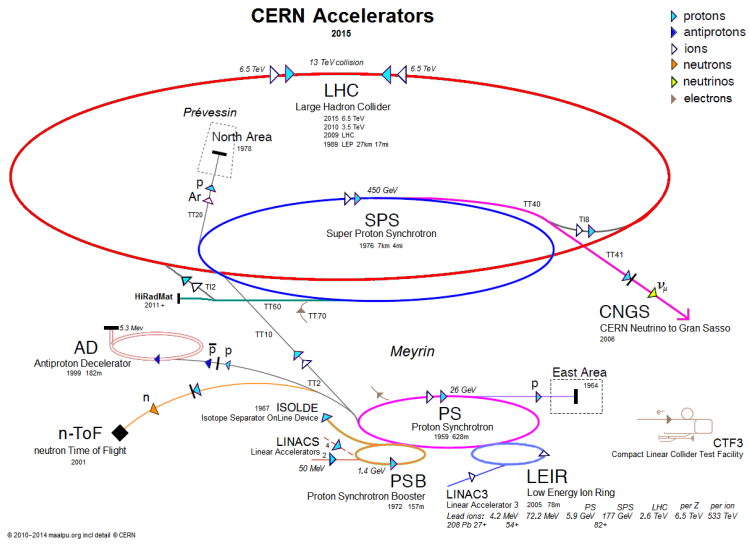

Figure 4.1: Schematic view of the CERN accelerator complex including the LHC injection chain consisting of the accelerators, LINAC2, PS and SPS.

The injector system consists of a series of accelerators, the LINAC2, Proton Synchrotron Booster (PSB), Proton Synchrotron (PS) and Super Proton Synchrotoron (SPS), which boost protons from 50 MeV (after LINAC2) to 450 GeV. The LHC is designed to accelerate protons from injected energy up to 7 TeV by oscillating radio-frequency (RF) electric fields[1]. Superconducting coils are operated in a superfluid

[1]The RF is delivered to all the system, not only to the accelerator apparatus but also to the detector system, so that

helium at 1.9 K in order to generate 8.33 Tesla to bend the 7 TeV proton beams in the LHC main ring. The LHC is composed of octant 2.45 km arcs and 1232 bending magnets are aligned along beam lines.

In total, 39 bunch trains[2] are filled into the LHC in a design conditions, so that 2808 bunches per beam are brought to collision in the LHC. Each bunch contains about 10^{11} protons. A peak luminosity of $\mathcal{L} = 10^{34}\text{cm}^{-2}\,\text{s}^{-1}$ is achieved at a beam crossing angle of 285 mrad. The two general purpose detectors ATLAS and CMS [116] reside at these points. LHC beam parameters are summarised in Table 4.1. Besides ATLAS and CMS the LHC has two other large detectors, the ALICE[3] and LHCb[4]

	Design
Length of the rings	26.7 km
Magnetic field of dipoles	8.33 Tesla
Current	11.85 kA
Beam energy	14 TeV
Luminosity	$10^{34}\,\text{cm}^{-2}\,\text{s}^{-1}$
Number of bunches	2808
Number of protons per bunch	1.15×10^{11}
Time between collisions	25 ns
Beam radius at IP ($\sigma_{x,y}$)	16.6 μm
Beam length at IP (σ_z)	7.55 mm
Full crossing angle	$\approx 0.3\,\mu$rad

Table 4.1: LHC beam parameters

.

In addition to the four large experiments, several experiments dedicated to important physics are located at the LHC. LHCf[5] and TOTEM[6] and MODEL[7].

4.2 The ATLAS Detector

ATLAS is a general-purpose detector covering a solid angle of nearly 4π. It provides an excellent resolution of physical objects and reconstructs hard scatter events and detects a physical phenomenon beyond the Standard Model without failing if it exists. To satisfy that, the following performances are provided :

- Good spatial resolution in vertex reconstruction for efficient identification of secondary vertices from b hadron and τ lepton decays, an identification of the primary interaction vertex.
- Fine transverse segmentation of the electromagnetic calorimeter for distinction of $\pi^0 \to \gamma\gamma$ decays from primary photons and good angular resolution in photon and electron reconstruction.

the operation coherent to the LHC operation is achieved.

[2] Protons are bunched together with 115 billion protons and 72 bunches are grouped into a bunch train

[3] A Large Ion Collider Experiment detector [117] which have been built for the heavy ion experiment of the LHC

[4] Large Hadron Collider beauty detector [118] which are an asymmetric detector with extremely good vertex detector for studying rare b-hadron decays.

[5] Large Hadron Collider forward experiment [119] is a far forward detector intended to study physics of cosmic ray and to deepen the understanding of forward scattering

[6] Total Cross-Section, Elastic Scattering and Diffraction Dissociation [120] measure the total elastic and diffractive cross-section of proton-proton collisions which cannot be calculated by perturbative approaches.

[7] Monopole and Exotics Detector at the LHC [121] is an experiment searching for exotic particle like magnetic monopoles

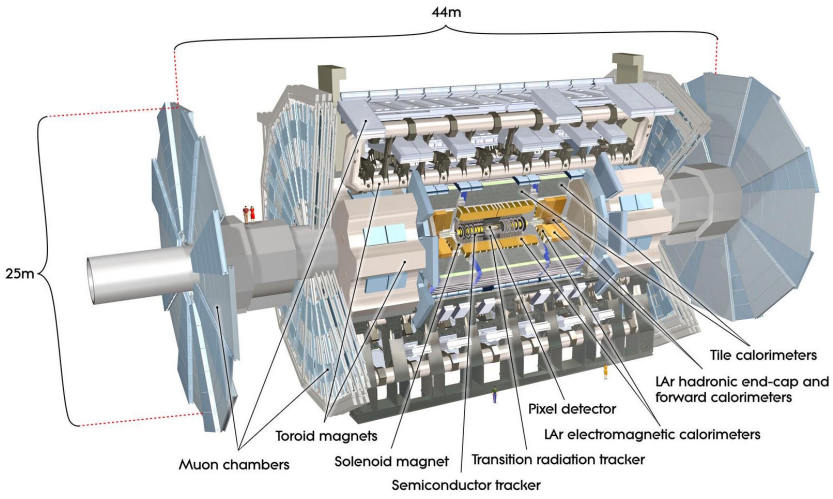

Figure 4.2: The ATLAS detector consists of tracking detectors, calorimeters, and the muon spectrometers. It is 25 m in height and 45 m in length. The overall weight of the detector is approximately 7000 tons.

- High geometrical coverage to maximise a total detector acceptance.
- High energy resolution for the electromagnetic and the hadronic calorimeter for electron, photon and hadronic jet energy measurements and a precise reconstruction of missing transverse energy.
- High muon momentum resolution over a wide range of momenta.
- Efficient and extremely fast triggering algorithm to cope with high luminosities delivered by the LHC.

Figure 4.2 shows a schematic view of the ATLAS detector consisting of the inner detectors, calorimeter systems, and the muon spectrometers. The detector is constructed as a symmetric detector system in terms of forward-backward direction. The detector contains a solenoid as well as three toroidal magnets to measure charged particle momentum. The superconducting solenoid provides a 2 T magnetic field to measure charged particle momentum by the inner detectors. It is hosted in the same cryostat as the barrel electromagnetic calorimeter. The electromagnetic calorimeter is sampling calorimeter fulfilled with liquid Ar. The hadronic calorimeter is placed after the electromagnetic calorimeter. Three toroidal magnets provide a magnetic field for additional bending of muon trajectories for a precision measurement in the muon spectrometers. The sub-detector and triggering systems are briefly introduced based on References [122, 123] in the following subsections.

4.2.1 Coordinate System

The ATLAS coordinate system is a right-handed Cartesian system. Its z-axis points along the beam pipe, the x-axis to center of the LHC ring and y-axis as well upward direction. Spherical coordinates are better to describe rotational invariant properties and it is suited to collider experiments. The (r, ϕ, θ) coordinate is defined by $r = \sqrt{x^2 + y^2}, \phi = \arctan(y/x)$ and $\theta = -\ln\tan(r/z)$. The pseudorapidity, η is used instead of the polar angle θ where $\eta = -\ln\tan(\theta/2)$. The pseudorapidity coincide with the rapidity y for the massless limit of particles. Since rapidity differences Δy are Lorentz-invariant, so η provides a physically better measurement than the polar angle. Table 4.2 summarise kinematical quantities based on the ATLAS coordinate system.

4.2.2 The Inner Detector

In the ATLAS detector, the tracking system usually means the inner detectors (ID) without outermost muon spectrometers (MS). The inner detectors consist of three different detectors as shown in Figure 4.3. It reconstructs tracks of charged particles with a coverage of $|\eta| < 2.5$.

Variable	Description	Definition
$\vec{p}$	Momentum	$p_\mu = (E, p_x, p_y, p_z)$
p_T	Transverse momentum	$p_\mathrm{T} = \sqrt{p_x^2 + p_y^2}$
ϕ	Azimuthal angle	$\phi = \arctan(p_y/p_y)$
θ	Polar angle	$\theta = \arctan(p_\mathrm{T}/p_z)$
y	Rapidity	$y = \frac{1}{2}\ln\frac{E+p_z}{E-p_z}$
η	Pseudorapidity	$\eta = -\ln(\tan\frac{\theta}{2})$
$\Delta\phi$	Opening angle in ϕ	$\Delta\phi_{ij} = \min(\lvert\phi_i - \phi_j\rvert, \pi - \lvert\phi_i - \phi_j\rvert)$
$\Delta\eta$	Difference angle in η	$\Delta\eta_{ij} = \lvert\eta_i - \eta_j\rvert$
ΔR	Opening in (η, ϕ) space	$\Delta R_{ij} = \sqrt{\Delta\phi_{ij}^2 + \Delta\eta_{ij}^2}$

Table 4.2: Definitions of commonly used variables in the description of particle and event properties in the ATLAS coordinate system.

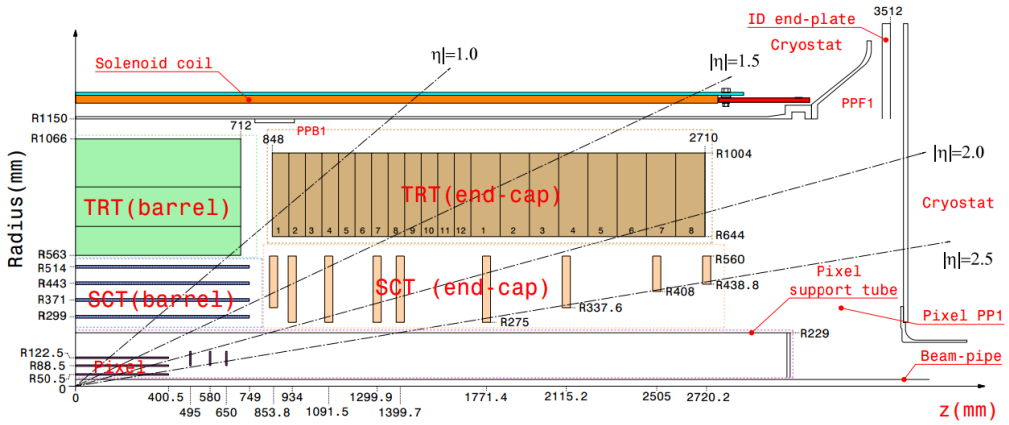

Figure 4.3: Schematic view of the tracking system. In the barrel pseudorapidity region, from inner layer it consists of the pixel, semiconductor detectors and transition radiation tracker. In the End-cap region, semiconductor detectors and transition radiation trackers stands in.

The Pixel Detector

The silicon *Pixel detector* is the closet detector component to the interaction vertex and made up of four cylindrical layers located between 31 mm–120 mm in radial distance from the beam pipe. The innermost layer is often referred to as *Insertable B-Layer (IBL)*, as it is a crucial detector component for secondary vertexing for b-hadron decay reconstruction. The IBL is one of a new detector installed during a 2 years shutdown after the LHC Run1. The three outer layers are referred to as *B-Layer, Layer-1 and 2*. Three disks provide a coverage up to $|\eta| < 2.5$ in the forward region. In total, the pixel detector consists of 6.2 and 80.4 million pixels for the IBL and three outer layers with a nominal size of 50×250 and 50×400 $\mu\mathrm{m}^2$ respectively. A charged particle produces four hits on an average, with an intrinsic resolution of 4 μm in the $R - \phi$ plane and 115 μm along the z-axis. The pixel are operated at a temperature of 0 °C in order to suppress an electronic noise.

The Silicon Microstrip Tracker

The Silicon Microstrip Tracker (SCT) is a silicon strip detector made up of four cylindrical layers in the barrel region and two endcaps with nine disks. In total, the SCT provides an active are $63\,\mathrm{m}^2$ to measure four space-points over the full inner detector coverage. Two sensors are mounted back-to-back on the modules titled against each other by a small stereo angle of 40 mrad. A sensor contains 768 active strips with $285\,\mu$m thick and a strip pitch of $80\,\mu$m. This angle breaks a degeneracy along the z-direction. It allows to measure three-dimensional space-points with an accuracy of $17\,\mu$m in the $R-\phi$ plane, $580\,\mu$m along the z-axis for the barrel region. The endcap disks are built from inner, middle and outer wheel modules with slightly different geometry. The sensors are single sided p-in-n silicon detectors with an applied bias voltage of about 150 V. The SCT is operated at a temperature of $-10\,^{\circ}$C to $-5\,^{\circ}$C to suppress electronic noise.

Transition Radiation Tracker

The concept of the TRT is based on a transition radiation, which is emitted by charged particles passing a boundary of two di-electric materials. It is make of polymide drift tubes with a diameter of 4 mm and a length of 144 cm and interleaved with polyproyplen/polyethylen fibres. Each tube is filled by a xenon-based gas mixture and contains a gold plated tungsten wire to collect the charge from the gas ionisation. Two type of hits of high- and low-threshold are considered. The low-threshold is optimised to detect an ionisation from primary traversing particles, while the high-threshold hits indicate a transition radiation. The intensity of a transition radiation is proportional to the Lorentz factor γ of particles. So the TRT can provide a particle identification, especially $e^{\pm}/\pi^{\pm}$ separation over a wide momentum range 0.5 GeV to 150 GeV by counting the number of high-threshold hits along the path of flight. Although the accuracy per hit is quite poor, the TRT can provide valuable information for a track reconstruction given that each particle provides about 36 hits in the TRT easing pattern recognition. The TRT covers pseudorapidity of $|\eta| < 2$.

4.2.3 The Calorimeter System

The calorimeter system is intended to provide an accurate measurement of particle energies by absorbing them and measuring shower properties, which also helps particle identification. The electromagnetic calorimeter is designed to fully absorb and precisely measure the energies of electromagnetic cascades of subsequent e^+ e^- pair production and Bremsstrahlung processes initiated from electrons and photons from a hard scatter. The hadronic calorimeter fully absorbs hadronic showers which cannot be detected at the electromagnetic calorimeter. The calorimeter system covers a region of $|\eta| < 4.9$. The detector is build as a sampling calorimeter with alternating samples of passive and active material to detect secondary particles. An accurate spatial resolution is required for a precise reconstruction of photon and electron, so that the calorimeter system is finely segmented to both longitudinal and azimuthal direction. It is also important for a reconstruction of the missing transverse energy. The three-dimensional shower position can be reconstructed using topological clustering algorithm as described in Section 5.2. Figure 4.4 (a) shows the different calorimeter sub-system in a cut-away view.

The Electromagnetic Calorimeter

The electromagnetic (EM) calorimeter is a finely segmented sampling calorimeter. It consists of two components, the central barrel and endcap calorimeter covering pseudorapidity up to $|\eta| < 1.4$ with a small gap of 4 mm at $|z| = 0$ and $|\eta| < 3.2$ respectively. The cylindrical barrel has inner and outer diameters of r =2.8 m and 4 m, respectively and covers full azimuthal angle. The endcaps calorimeter covers from r =0.33 m to 2.1 m with respect to the beam pipe.

The EM calorimeter is constructed as a liquid argon (LAr) sampling calorimeter with a lead

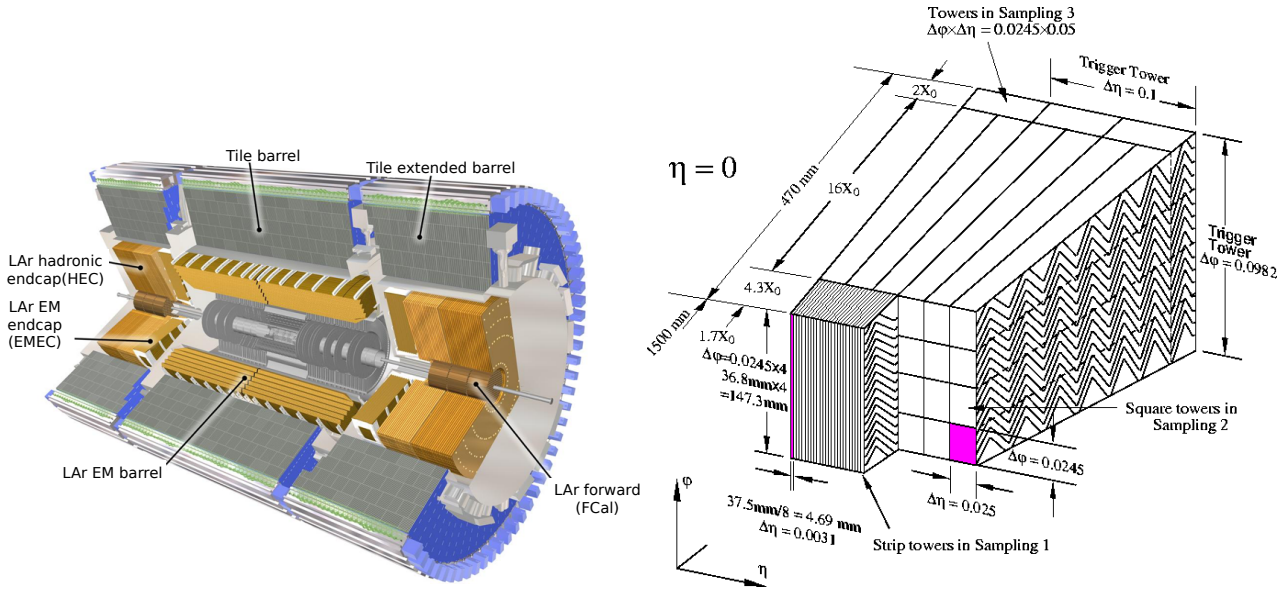

Figure 4.4: Cut away view of the ATLAS calorimeter system. From innermost, the LAr calorimeter stands and the hadronic calorimeter is placed after the EM calorimeter. (b) shows an overview of the EM LAr calorimeter barrel module. The first layer is referred to as *strip layer* with a granularity of $\Delta\eta \times \Delta\phi = 0.0031 \times 0.098$ to allow an excellent identification of $\pi^0 \to \gamma\gamma$ decays as one important background to primary photons. The second layer has a granularity of $\Delta\eta \times \Delta\phi = 0.025 \times 0.0245$ and is the thickest layer with 16 radiation length X_0. The third layer measures the tails of electromagnetic showers and can therefore be used to distinguish from hadronic deposits.

absorber plate. It is built with an accordion shaped in Figure 4.4 (b) in order to reduce insensible region. The LAr calorimeter provides a good energy resolution of approximately $\sigma_E/E = 10\%/\sqrt{E/\text{ GeV}} \oplus 0.7\%$. A thickness of the lead plate is 1.13 mm to 1.53 mm depending on modules. Three copper layers are used as readout electrodes in the gaps. A high voltage is applied to the gaps between each absorber materials. The inner plate is a readout using capacitive coupling. The charge drift time is approximately 450 ns. Fine angular resolution and full shower containment are obtained by three different layers.

The layered structure provides additional information about the shower development referred to as shower shapes like the longitudinal depth of the shower. The first layer of the barrel module is referred to as *strip layer* with a granularity of $\Delta\eta \times \Delta\phi = 0.0031 \times 0.098$. It allows an excellent identification of the primary photon from $\pi^0 \to \gamma\gamma$ decays. The second layer is the thickest layer with 16 radiation length X_0 with a granularity of $\Delta\eta \times \Delta\phi = 0.025 \times 0.0245$. The third layer measures the tails of electromagnetic showers and can be used to distinguish e/γ from hadrons.

Each endcap calorimeter consists the inner and outer wheel with a spacing of about 3 mm in between. The layout of the endcaps follows the barrel geometry. Three layers are used between $1.5 < |\eta| < 2.5$ including a strip layer, while only two layers of a coarser granularity are used in the outermost part of the outer and inner wheel.

Since the electromagnetic calorimeter is a sampling calorimeter, a deposit energy is measured by a bipolar pulse shape transfer. When the pile-up activity overlaps over signal, it should be subtracted. The subtraction is performed for all signals in the calorimeter, so that there is a negative energy signal after plus shaping. This is corrected by dedicated algorithm and event cleaning criteria as shown in Chapter 5.

The Hadronic Calorimeter

As the hadronic calorimeter, there are the hadronic tile, the hadronic endcap and the liquid argon forward calorimeter for different pseudorapidity regions. All hadronic calorimeters are sampling calorimeters. The typical jet energy resolution of the hadronic barrel and endcap calorimeter is $\sigma_E/E = 50\%/\sqrt{E/\text{ GeV}} \oplus 3\%$, while it is about $\sigma_E/E = 100\%/\sqrt{E/\text{ GeV}} \oplus 10\%$ for the forward calorimeter. Steel and a scintillating tile is used as the absorber and active material of the tile barrel calorimeter. A photo-multiplier tube is used as a readout of the scintillating tile at the tile edges by wavelength shifting fibers.

The tile calorimeter is cylindrically build around the EM calorimeter with an inner radius of $r = 2.3\,\text{m}$ and an outer radius of 4.3 m. It is divided into the central barrel with length of 5.8 m and two extended barrel parts with length of 2.6 m covering pseudorapidity of up to $|\eta| < 1.7$ as shown in Figure 4.4. There are service cables between the central and extended barrel for the inner detector and LAr pipes are mounted, so that a gap of 60 cm exists.

All barrel parts consist of three layer. The granularity of the hadronic calorimeter is coarser than the EM calorimeter due to hadronic showers tend to become wider than EM showers. The cell granularity of the tile barrel is $\Delta\eta \times \Delta\phi = 0.1 \times 0.1$ in the first two layers, while $\Delta\eta \times \Delta\phi = 0.1 \times 0.2$ in the third layer.

The hadronic endcap is built by copper and liquid-argon sampling calorimeter and consists of two disks for the forward and backward region covering $1.5 < |\eta| < 3.2$. The size of disk cell is 0.1×0.1 and 0.2×0.2 for $1.5|\eta| < 2.5$ and $2.5|\eta| < 3.2$ respectively.

The LAr forward calorimeter is a combined electromagnetic and hadronic calorimeter and consists of three layers. A copper is used as the absorber material in the first layer to absorb electromagnetic interactions. While a tungsten is used in the second and third layer to absorb hadronic showers. The far forward region of $3.1 < |\eta| < 4.9$ is covered by the LAr forward calorimeter. There are significant overlaps with the hadronic endcap calorimeters, this is because of a smooth transition between the endcap and LAr forward calorimeter. Liquid argon is used as an active material and is filled in small gaps which are drilled inside the absorber material. It is hosted in the same cryostat structure as the electromagnetic endcap and the hadronic endcap calorimeters.

4.2.4 The Muon Spectrometer

The outermost part of the ATLAS detector is the muon spectrometer (MS) consisting of carious sub-detectors to detect muons efficiently and measure their momentum over a broad range. The MS consists of different types of subdetectors, the Monitored Drift Tubes (MDT), the Cascade Strip Chambers (CSC), the Resistive Plate Chambers (RPC) and the Thin Gap Chambers (TGC). Schematic view of the ATLAS Muon Spectrometer and its components are shown in Figure 4.5. It provides an overall acceptance up to $|\eta| < 2.7$ and measures momenta ranging from 3 GeV to a few TeV. At design specifications, it offers a relative momentum resolution of 10% for muons at $p_{\text{T}} = 1\,\text{TeV}$. Three air-core toroidal magnets provide the magnetic field to bend the muon trajectories; covering the barrel ($|\eta| < 1.7$) and the two endcap region ($1.6 < |\eta| < 2.7$). Each toroidal consists of eight coils. The integrated field strength $\int B_\perp d_\perp$ ranges from 1.5 Tm to 5.5 Tm in the barrel and between 1.0 Tm to 7.5 Tm in the endcaps.

MDT provides precision measurements for muons with $|\eta| < 2.7$. 1150 chambers with 354,000 channels are installed which consist of two batches of three or four layers of drift tubes. The individual drift tubes are built from aluminium tubes with a diameter of 3 cm and length of 0.9 m to 6.2 m. The drift tubes are strained a tungsten-rhenium wire at a potential of 3 080 V and pressurised with a mixture gas of Ar and CO_2 (93%/7%). This leads to a gas gain of 2×10^4 and a maximum drift time from the wall of the tubes to the wire take about 700 ns.

MDT cannot be operated a hit rates above $150\,\text{cm}^{-1}\,\text{s}^{-1}$. This rate are expected in the first endcap

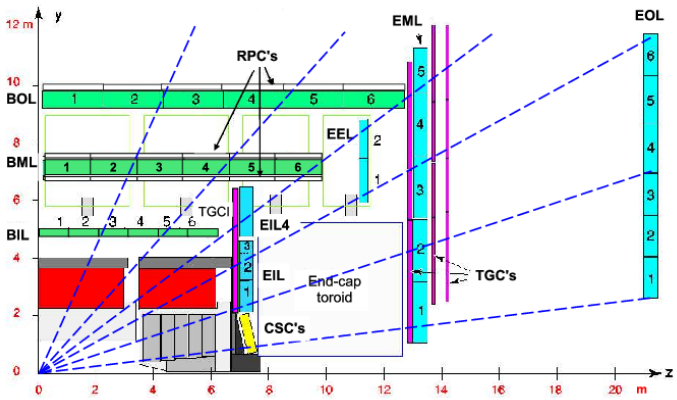

Figure 4.5: Schematic cross section view of the ATLAS Muon Spectrometer system. Precision muon track measurements are provided by the MDT in the barrel (BIL, BML, BOL) and the endcap (EIL, EEL, EML, EL) and the CSC. Triggering are provided the RPC in the barrel and the TGC in the endcap (taken from Reference [114]).

wheel at $|z| = 7.4\,\text{m}$ for $|\eta| > 2$, where CSC are installed with 32 modules with 31,000 channels up-to $|\eta| < 2.7$. CSC is multi-wire proportional chambers which are placed in radial direction and two cathodes, so that one cathode is segmented parallel and one cathode perpendicular to the wires applied a potential of 1 900 V. chambers are filled with a mixture gas of Ar and CO_2 (80%/20%) that provides an average gain of 6×10^4 and a drift time is about 30 ns.

RPC is used for triggering in the barrel, which consists of 606 modules with 373,00 channels. RPC is a gaseous resistive parallel plate detectors which are segmented at a distance of 2 mm from each other with the electric field of $4.9\,\text{kV mm}^{-1}$, so that one plate can measure the ϕ direction and the other plate η. Time resolution of RPC is less than 2 ns.

In the forward region with $1.05 < |\eta| < 2.4$, a total 3588 of the TGC are mounted with 318,000 channels for the trigger detectors. TGC are a multi-wire proportional chamber with a gain of $\times 10^5$ for a wire potential of 2 900 V. One coordinate is measured by the wire and a second coordinate can be inferred from pickup strips that are perpendicular to the wires. TGC provides triggers within 5 ns. 3

4.2.5 The Luminosity and Forward Detectors

The integrated luminosity is determined by the LUCID[8] and ALFA[9] detectors. LUCID is placed at 17 m away from the interaction point in the the beam axis direction for both side of the ATLAS detector. It consists of an array of 20 Cerenkov tubes and provides an online determination of luminosity values by counting the number of charged particles in the far forward area from inelastic proton-proton interactions. The ALFA detector is located 240 m from the interaction point to measure the elastic scattering amplitude at extremely small scattering angles, which can be related to the total cross-section using the optical theorem. The luminosity detectors have been calibrated using *van der Meer* scans [124, 125], which measure the beam spread in the vertical and horizontal planes.

4.2.6 The Trigger System and Data Acquisition System

The extremely high collision rate of 40 MHz does not allow to readout of the full signal of all detectors due to the limitation of bandwidth in data storage infrastructures and computing resources. A dedicated trigger system picks up events of interesting, predefined physical topologies to reduce the event rate. The trigger and data acquisition system (TDAQ) consists of a hardware-based level 1 trigger (L1) and a single software-based high-level trigger (HLT). This two-stage system can reduce the event rate to 100 kHz at L1 and to an average recording rate of 1 kHz at the HLT. A detailed

[8] LUminosity measurement using Cerenkov Integrating Detector
[9] Absolute Luminosity for ATLAS

description of the ATLAS trigger system can be found in Reference [126].

Fast electronics are employed to find region of interest (RoI) using the calorimeter and muon Spectrometer with coarse information within a latency of 2.5 μs at L1. L1 trigger consists of L1 calorimeter system (L1Calo), L1 muon trigger system (L1Muon), L1 topological trigger modules (L1Top) [127] and Central Trigger Processors (CTP) [128]. L1 trigger selects muons, electromagnetic clusters (used as electrons and photons), jets, hadronic τ-lepton decays, $E_{\mathrm{T}}^{\mathrm{miss}}$ and sum of the transverse energy in all calorimeter cells. L1Calo reads out 7000 projective trigger towers[10] which are coarse granularity of $\Delta\eta \times \Phi = 0.1 \times 0.1$ to allow for a fast readout. The energy which is readout from the trigger tower is calibrated to the full expected energy by a special procedure. L1 electrons and photons are 2×2 trigger tower clusters in the EM calorimeter with an isolation-window which consists of the surrounding twelve trigger towers for vetoing a fake signal. L1 hadronic τ-leptons are made up with same trigger tower size as L1 electrons and photons with only the hadronic calorimeter. L1 jet are identified using sums of E_{T} within windows consisting of $2 \times 2, 3 \times 3$ and 4×4 trigger towers in the EM and hadronic calorimeters. L1 muon trigger is based on coincidence requirements between different trigger chambers using predefined look-up-table. In addition, L1 calculates the scalar and vectorial sum of the energy deposits to provide the L1 missing transverse energy trigger (L1XE).

At HLT, fast algorithm accessing signals around a RoI defined at L1, or offline-like algorithm using the full event information performs on a unique PC farmware within a processing time of 0.2 s on an average. The event that is triggered by the HLT is subsequently sent to event storage infrastructures. Event reconstruction is applied by data Acquisition system (DAQ).

Efficiencies of each triggers are measured by data as well as simulated samples and corrections are applied to the simulated sample. Details of trigger efficiencies are described in Chapter 5 including its systematic uncertainty.

4.3 Data Taking During LHC Run2

The first run period of the LHC at $\sqrt{s} = 13$ TeV was successfully completed in 2015. Since November 2009, proton-proton collisions with energy of protons have been risen to 450 GeV to 6.5 TeV. During the Run1, the beam energy was $\sqrt{s} = 7$ TeV in 2011 and 8 TeV in 2012 respectively. The bunch spacing was 50 ns which is doubled compared to the design specifications of the LHC. The achieved peak luminosity was $7.73 \times 10^{33}\mathrm{cm}^{-2}\,\mathrm{s}^{-1}$ which is close to the design value of 1×10^{34} $\mathrm{cm}^{-2}\,\mathrm{s}^{-1}$. Figure 4.6 (a) shows the integrated and peak luminosity as a function of data-taking date. An integrated Luminosity of 3.38 fb^{-1} was delivered by the LHC, of which ATLAS recorded 3.21 fb^{-1} in 2015 run. Part of 2016 data-taking period is used in this thesis, which have the integrated luminosity of 26.07 (24.8) fb^{-1} delivered from LHC (recorded by ATLAS). The peak luminosity was $1.2 \times 10^{34}\mathrm{cm}^{-2}\,\mathrm{s}^{-1}$ The number of interactions per bunch-crossing was increased due to the larger luminosity. The presence multiple proton-proton collisions in a single bunch-crossing will be denoted as *pile-up* (PU). Besides the direct impact of pile-up on the event reconstruction or trigger decision, a secondary effect impacts the object reconstruction performance and the trigger performance. *In-time pile-up* is proton-proton collisions occurring in the same bunch crossing as the collision of interest. *Out-of-time pile-up* is additional collisions occurring in bunch crossings before and after the collision of interest. The measured mean number of interaction per bunch-crossing is shown in Figure 4.6 (b) for 2015 and 2016 data-taking periods analysed in this thesis.

All detector subsystems permanently monitor their performance during data-taking with automatically and dedicated shifts check data quality in order to ensure that no faulty detector affecting the performance. If there are large defects like offline subsystem, such information are recorded in a data

[10] Energy deposits in the calorimeter are gathered into one output as input to trigger decision, which is called as trigger tower.

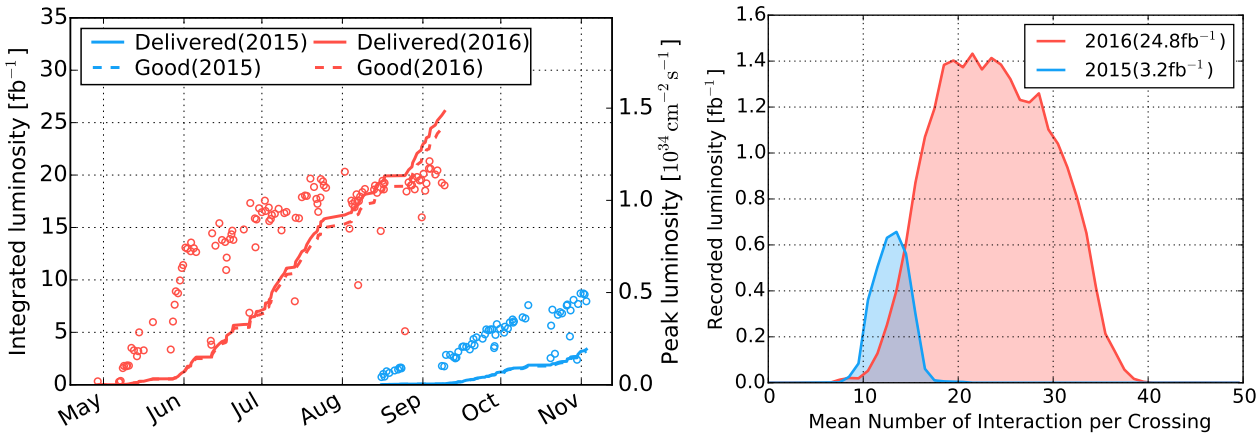

(a) Luminosity **(b)** Pile-up

Figure 4.6: (a): The integrated luminosity and the maximum instantaneous luminosity per run delivered to ATLAS as a function of the date for both 2015 and 2016. (b) : Luminosity-weighted distribution of the mean number of interactions per bunch-crossing for 2015(blue) and 2016(red) data. The mean number of interactions per cross is the mean of the Poisson distribution of the number of interactions per crossing calculated for each bunch.

quality database. This database is so-called *Good Runs Lists* (GRL) which can define later the run available for physics analyses.

5 Physics Object Reconstruction and Particle Identification

The object reconstruction and identification processes are important steps to convert experimental detector-level information into physical information like particle four-momentum. For data events passing the online trigger requirements and simulated events, the raw detector data signals are recorded for further processing and event reconstruction. The object reconstruction and identification are based on higher-level detector information such as reconstructed tracks instead of hits in the tracking detectors. Besides the reconstructed four-momentum of the particle candidate, additional useful variables for physics analyses are computed. Dedicated reconstruction and identification algorithms are implemented in the `Athena` software framework [129], which can be used for data and simulated events. The purpose of the reconstruction algorithm is an accurate reconstruction of the object four-momentum vector with higher efficiency. The identification algorithm reduces the mis-reconstructed objects while keeps a high identification efficiency.

An overview and performance of the reconstruction and Identification method used in the search for $H/A \to \tau\tau$ decay are given used in the data-taking in 2015 and 2016. A brief overview of tracks and cluster of energy deposit which are the most common higher-level detector object are given in Section 5.1 and 5.2. The Reconstruction of the jets, electrons, muons and hadronic τ-lepton decays are introduced in the Section 5.3–5.6. As neutrinos cannot be detected with ATLAS due to small interaction rate with matter, transverse missing energy ($E_{\mathrm{T}}^{\mathrm{miss}}$) plays a important role in constraining the momentum of escaped neutrinos. The $E_{\mathrm{T}}^{\mathrm{miss}}$ reconstruction is described in Section 5.7.

5.1 Tracks and Vertices

Reconstructed tracks originating from charged particles passing the inner detector are one of the most important basic objects for further physics object reconstruction and identification. In this analysis, extremely high momentum τ-lepton's decays introduce strongly collinear set of the charged pions. It makes difficult to reconstruct each track because of sharing hits with each other charged pions. A brief overview is given based on Reference [130] in this section.

In the Pixel detector each hit equates to one space-point while the SCT detector hits from both sides of a strip layer must be combined to obtain a three-dimensional measurement. The measured charge in a pixel sensor is often collected by multiple pixels. The total charge is determined by the incident angle of the particle with respect to the sensor. A connected component analysis [131] makes clusters. The cluster is a set of hits in the detector, which is expected from one charged particle. The charged particle's intersection point to the sensor is determined from the cluster pixel content using a linear approximation with a charge interpolation technique. To identify the cluster is merged or not, An artificial neural network (NN) [132] is used to determine the cluster is originated from one

charged particle or more than two particles. The cluster is splitted into two or three clusters if the NN judges that it is merged cluster[1].

The primary track reconstruction algorithm (track seed finding) works iteratively after cluster making. A staged pattern recognition approach is used. Seeds consists of sets of three space-points. The perigee parameters of a track seed are estimated by assuming a perfect trajectory in a uniform magnetic field. Four possible pattern of combinations can be made from the pixel detector and SCT detector space-points. To reduce mis-reconstructed seeds it is considered starting with SCT-only then Pixel-only seeds. Purity can be improved by requiring one additional space-point to be compatible with the seed. After iterative seed-finding a combinatorial Klakman filter [133] is used to build track candidate from the seed. The filter creates multiple track candidates per seed if more than one compatible space-point extension exist on the same layer. New reconstruction algorithm is recently developed to improve the track reconstruction efficiency in the dense environment with multiple collinear tracks. New algorithm is called as *Tracking In Dense Environment* (TIDE) [130]. Figure 5.1 shows the track reconstruction efficiency in $\rho \to \pi^{\pm}\pi^{\mp}$ (a) and $\tau \to 3\pi^{\pm} + \nu_{\tau}$ (b) events

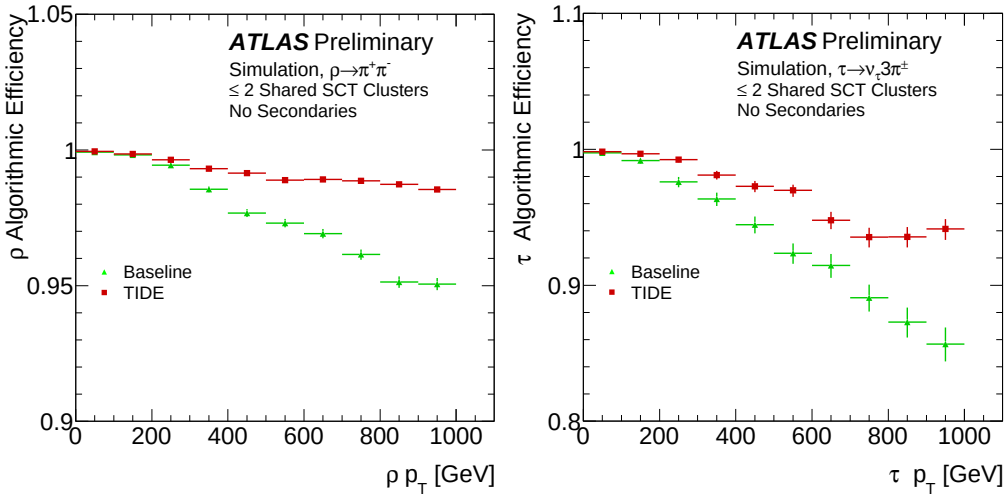

(a) Luminosity **(b)** Pile-up

Figure 5.1: Efficiency to reconstruct all decay products from a ρ meson or τ-lepton decay in events (taken from Reference [130]). Green (red) points present baseline(TIDE) algorithm efficiency.

as a function of the transverse momentum. The reconstruction efficiency of complex charged particle groups is improved at high p_{T}. After the reconstruction a set of track quality selection is applied, which is summarised in the following:

- $p_{\mathrm{T}} > 400$ MeV and $|\eta| < 2.5$
- number of silicon hits ≥ 9 and 11 for $|\eta| \leq 1.65$ and > 1.65 respectively.
- number of shared[2] modules ≤ 1
- number of silicon holes[3] ≤ 1 and no holes in pixel, one IBL or next innermost pixel layer hit.

[1] Merged cluster is referred as a cluster which overlaps with other particle detections, and it is reconstructed as one cluster.

[2] A pixel detector with a hit used by more than one tracks and SCT with two hits in the same SCT layer used by more than none tracks are referred to as shared modules

[3] Holes are defined as intersection of the track trajectory with no hits in detector which is caused by inactive modules or region such as edge ares.

Vertices are reconstructed using the distribution of z coordinates of reconstructed tracks along the beamline. A vertex candidate is reconstructed by *Iterative Vertex Finding* procedure [134, 135]. The tracks are extrapolated to the point of closest approach to the beam spot center. The algorithm finds the maximum of the distribution of extrapolated z-coordinates. Vertex position is determined using the *adaptive vertex fitting* algorithm [136] which is based on a robust χ^2 fitting. Tracks are refitted under the assumption that they produced from this vertex candidate. The procedure is repeated until all tracks are associated to some vertices. Vertices with less than two associated tracks are discard. Event have more than one vertices, so that the primary vertex is chosen as the vertex with the largest sum of squared transverse momentum of the associated tracks ($\sum p_{\mathrm{T}}^2$).

5.2 Topological Clustering

The topological cluster (TopCluster or just TC) is used as seeds of jet and hadronic τ-lepton decay reconstruction. The topological cluster algorithm aims at grouping deposits at the calorimeter into each particle shower and suppressing the calorimeter noise. The energy collection of the calorimeter cell signals into one topo-cluster follows signal-significance patterns generated by particle showers. The basic observable for making the topp-cluster is the cell signal significance $\varsigma_{\mathrm{cell}}^{\mathrm{EM}}$ which is defined by

$$\varsigma_{\mathrm{cell}}^{\mathrm{EM}} = \frac{E_{\mathrm{cell}}^{\mathrm{EM}}}{\sigma_{\mathrm{noise,cell}}^{\mathrm{EM}}}, \tag{5.1}$$

where the cell signal $E_{\mathrm{cell}}^{\mathrm{EM}}$ and $\sigma_{\mathrm{noise,cell}}^{\mathrm{EM}}$ are measured in the electromagnetic (EM) energy scale. $E_{\mathrm{cell}}^{\mathrm{EM}}$ is energy measured in the cell at the EM scale, $\sigma_{\mathrm{noise,cell}}^{\mathrm{EM}}$ is a noise level of the cell. The EM scale is defined by calibration constants derived in test-beam measurements using ATLAS calorimeter prototype [137]. Topo-cluster are formed by a highly significant seed. The seeding, growth and

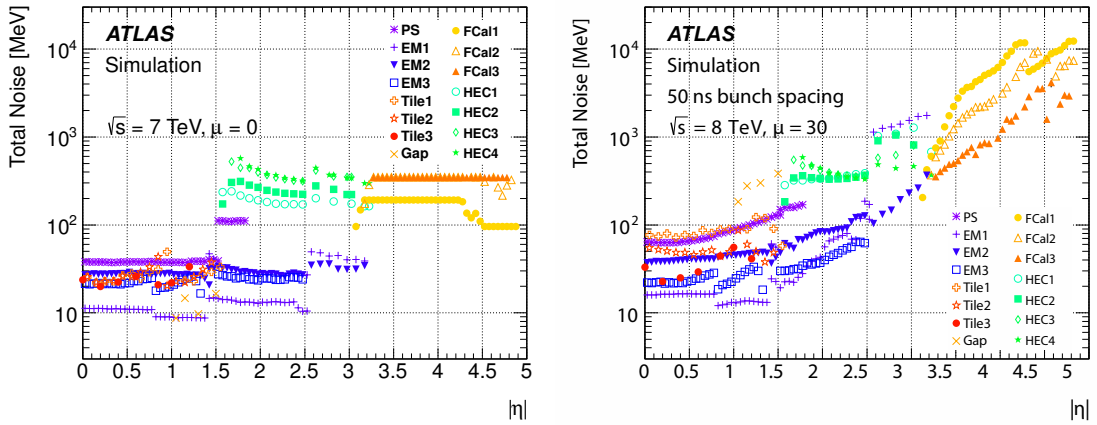

(a) $\langle\mu\rangle = 0$ **(b)** $\langle\mu\rangle = 30$

Figure 5.2: Expected noise level per cell in the different calorimeter subdetectors for two different luminosity conditions. (a) plot shows the only the electric noise, while (b) plot includes energy deposits from multiple proton-proton collisions at instantaneous luminosity of $10^{34}\,\mathrm{cm}^{-2}\,\mathrm{s}^{-1}$ (taken from Reference [138]).

boundary feature of topo-cluster are controlled by the three parameters S,N,P, which defines signal thresholds in terms of $\sigma_{\mathrm{noise,cell}}^{\mathrm{EM}}$. Selection is applied based on $\varsigma_{\mathrm{cell}}^{\mathrm{EM}}$. The default values of (S,N,P) is (4,2,0) which are derived from optimizations of the response of cluster energy and the relative energy

resolution for charged pions with the test-beam [137]. Figure 5.2 shows the expected noise in the different calorimeter sub-systems for two different pile-up profiles.

After constructing seeds, the *collect* step starts. These *seed* and *collect* steps are repeated until all clusters topologically connected cells passing the criteria given in $\varsigma^{\mathrm{EM}}_{\mathrm{cell}} > S, N$ and their neighbours satisfying the $\varsigma^{\mathrm{EM}}_{\mathrm{cell}} > P$. The algorithm starts by selecting cells with $\varsigma^{\mathrm{EM}}_{\mathrm{cell}} > S$ and ordering in decreasing $\varsigma^{\mathrm{EM}}_{\mathrm{cell}}$. Neighbouring cells are subsequently merged into the seed if they satisfy $\varsigma^{\mathrm{EM}}_{\mathrm{cell}} > N$. In the case of a cell is a neighbour to two potential clusters, the clusters are merged. This procedure is iteratively applied until the last set of neighbouring cells with passing $\varsigma^{\mathrm{EM}}_{\mathrm{cell}} > P$.

Finally the cluster splitting step identifies and isolates local energy maxima in the clusters. The clusters with two or more local maxima are splitted into corresponding signal peaks in all three dimensions. A local signal maxima is defined by $E^{\mathrm{EM}}_{\mathrm{cell}} > 500$ MeV. In addition to the topological requirements, it is required to have at least four neighbours and none of the neighbours with larger signal. This step can find cells which are neighbours to two or more signal maxima. The cell is assigned to the two highest-energy clusters after splitting of the original topo-cluster in this case. Each topo-cluster with at least three cells with $E^{\mathrm{EM}}_{\mathrm{cell}} > 0$ has a full set of geometrical moments. Simple (η, ϕ) direction and a center of weighted moment points are calculated as a geometrical moment. They has the EM scale and Local Cluster Weighting (LCW or just LC) calibration [139, 140] for energy scale. This calibration is based on comparison between the reconstructed and their true energy of simulated charged and neutral pions energy. The corrections are applied using the shower classification observable p^{EM}[4]. Jets built from local calibrated topo-cluster can be improved energy resolution with respect to the EM scale. Both jets and hadronic τ-lepton are reconstructed using calibrated topo-clusters with the EM scale and the LCW scale respectively in this analysis.

5.3 Jets

Jets are narrow clustering of particles (quarks or gluons) reconstructed from topo-clusters and tracks by jet reconstructing algorithm. Jets are used for selecting the bottom-annihilation production process. A brief overview of the reconstruction algorithm is given in Section 5.3.1. Energy calibration and resolution are shown in Section 5.3.2. The flavour tagging, so-called b-tagging, and the pile-up suppression are described in Section 5.3.3 and 5.3.8. Reconstruction of the hadronic τ-lepton decays is an important role of this analysis. Hadronic-τ objects is reconstructed based on jet seeds. Details of the hadronic-τ reconstruction is given in Section 5.6.

5.3.1 Jet Reconstruction

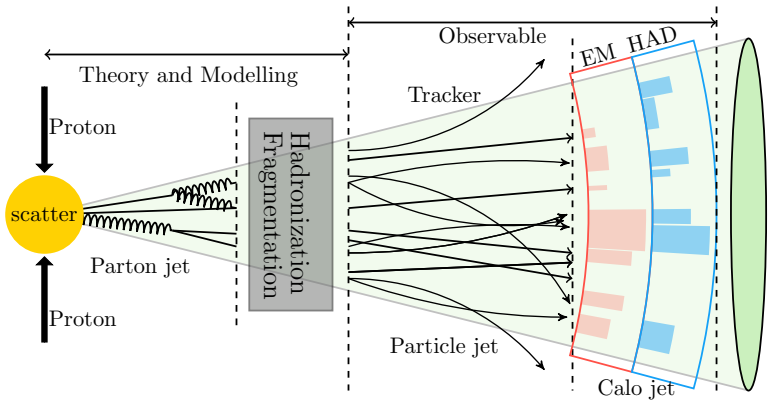

Figure 5.3: Illustration of simple example of an event showing the point of collision, the fragmentation and hadronisation of the quarks and gluons and the resulting jet found through the detection of the stable particle.

[4] A probability to be of hadronic or electromagnetic origin based on the cluster shower shape.

Coloured particles in the final state of a hard scatter are hadronised at typical scales of the strong interactions. Secondary particles are collimated due to highly boosted partons with colour neutral particles like pions or kaons. Jet properties like the particle multiplicity, energy profile and other spatial distributions cannot be predicted from first principle because the hadronisation is a non-perturbative effect. Special care needs to take into account in terms of the definition of jets. It allows a fair comparison between *parton jets* in parton-level calculation (perturbative QCD, pQCD) and *calo jets* reconstructed from topo-clusters in the calorimeter. Figure 5.3 shows a sketch of these different level jets. The jet reconstruction algorithm should satisfy stability criteria, i.e. should be stable against additional collinear and infrared radiation of additional partons and invariant under boost transformation along the z-axis. Collinear and infrared safety are important properties to ensure the applicability of the algorithm at parton-level due to soft and collinear radiations dominate in the parton shower. The anti-k_{T} algorithm [141] is mostly used for jet reconstruction is implemented in the `FastJet` package [142]. The following measures are defined with object i and j :

$$d_{i,j} = \min\left(p_{\mathrm{T},i}^{-2}, p_{\mathrm{T},j}^{-2}\right)\frac{\Delta R_{i,j}^2}{r^2}, \tag{5.2}$$

$$d_{i,B} = p_{\mathrm{T},i}^{-2}, \tag{5.3}$$

where $\Delta R_{i,j}^2$ is the distance between topo-clusters i and j in the $\eta - \phi$ plane r is a size parameter of the algorithm. $r = 0.4$ is used in this analysis. The algorithm calculates the $d_{i,j}$ and $d_{i,B}$ for all input topo-clusters and finds the minimum among these quantities. The topo-cluster i and j are merged into a single one until the minimum one becomes $d_{i,B}$, This cluster is considered as a jet removed from the list of input topo-clusters. The algorithm repeats this steps until no more input clusters are left over the list. The algorithm reduces circular jets in the $\eta - \phi$ plane with the radius of r. A detailed description of this algorithm can be found in Reference [143]. Truth jets are reconstructed by the anti-k_{T} algorithm as well, using truth particles in the simulated events. Truth jets are used as references of the jet energy calibration, as shown in Section 5.3.2.

5.3.2 Jet Energy Calibration and Resolution

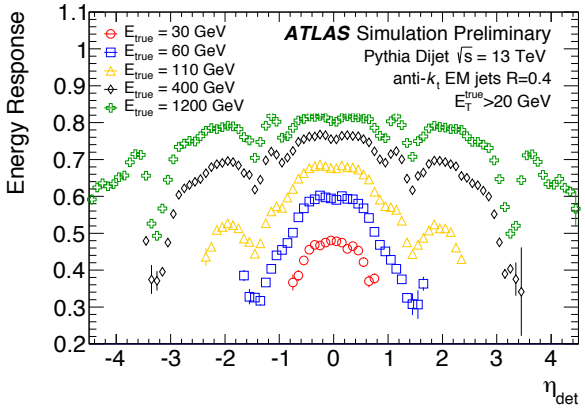

Figure 5.4: Energy response as a function of η before calibration for EM scale anti-k_{T}, $r = 0.4$.All pile-up correction have been applied (taken from Reference [144]).

As mentioned above, an additional jet calibration is applied to correct for effects not accounted for in the local cluster calibration. The pile-up correction is also applied using the jet are dependent correction [145]. The average jet p_{T} response(*jet energy response*) is defined by:

$$R = \left\langle p_{\mathrm{T}}^{\mathrm{jet}} / p_{\mathrm{T}}^{\mathrm{truth}} \right\rangle, \tag{5.4}$$

where $p_{\mathrm{T}}^{\mathrm{jet}}$ and $p_{\mathrm{T}}^{\mathrm{truth}}$ is the transverse momentum of calo-jet and truth jet respectively. The average

is taken from a Gaussian fit to the $p_{\mathrm{T}}^{\mathrm{jet}}/p_{\mathrm{T}}^{\mathrm{truth}}$ distribution within a range of $1.6\,\sigma$ from its mean value. Before applying the response correction, the effects of pile-up on jet calibration are subtracted using an area-based subtraction method [146].

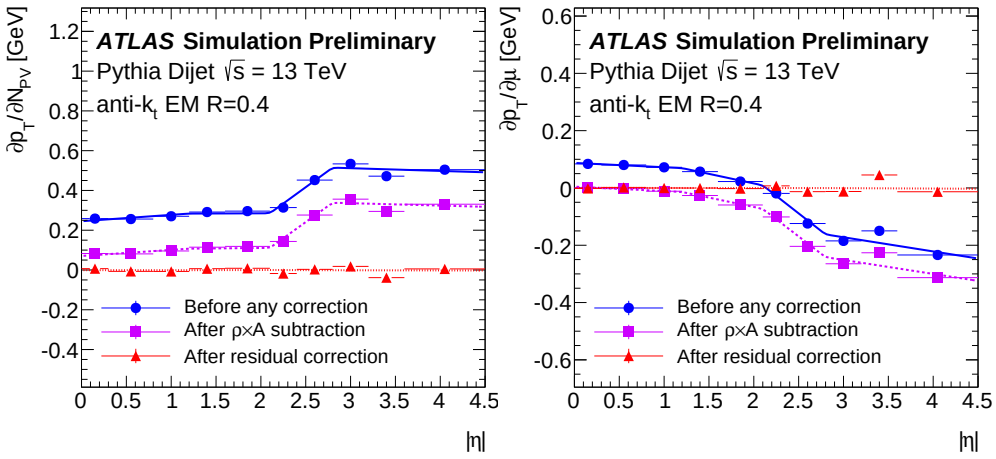

(a) in-time pile-up correction **(b)** out-of-time pile-up correction

Figure 5.5: Dependence of the reconstructed jet p_{T} on in-time pile-up(a) and out-of-time (b) pile-up as a function of jet η with three correction stages (taken from Reference [144]).

The jet are [147] is based on "ghost" particle[5] association technique implemented in `FaseJet` package. It assumes that the pile-up activities provide an uniform density distribution n the detector and they are included in the jet clustering. The jet ares of the jet j which is belonged by the ghost g is given by $A_j = N_g^j/\nu_g$, where N_g^j is the number of ghosts contained in jet j, ν_g is the number of ghosts per unit are. The jet are provides an estimate of a jet's sensitivity to pile-up effects. The median p_{T} density ρ is defined by $\rho = \mathrm{median}\ \{p_{\mathrm{T}}^{\mathrm{jet},j}/A_j^{\mathrm{jet}}\}$ which the index j enumerates the jets found with the k_{T} algorithm [148, 149]. Effects of hard scatters can be reduced by taking the median to estimate the pile-up effects. The use of the k_{T} algorithm for the ρ calculation is motivated by its sensitivity to soft radiation [145]. The pile-up subtracted p_{T} based on residual correction is given by:

$$p_{\mathrm{T}}^{\mathrm{corr}} = p_{\mathrm{T}}^{\mathrm{EM}} - \rho \times A - \alpha \times (N_{\mathrm{PV}} - 1) - \beta \times \langle \mu \rangle \,, \tag{5.5}$$

where α and β are parameters for residual correction for additional pile-up effects which are denoted by in-time and out-of-time pile-up, N_{PV} is the number of primary vertex in events and $\langle \mu \rangle$ is an average of the number of interaction per bunch crossing. Figure 5.5 shows the correction factor of in-time and out-of-time pile-up as a function of jet pseudorapidity. A set of data-driven corrections is applied to correct the jet response differences between the simulated and real calorimeter [144]. These corrections are derived by comparing the jet energy to that reference object like a Z boson or jet system. The direct balance with respect to well calibrated objects (electrons, muons and photons) is used for absolute scale, di-jet balance allows to reduce systematic uncertainties. In addition to these uncertainties, various systematical source of uncertainties need to be taken account like flavour compositions. Full systematic uncertainty variations are shown in Figure 5.6 (a).

The resolution of the reconstructed jet is measured by the dijet balance technique. The dijet balance technique measures the asymmetry A between the transverse momenta $p_{\mathrm{T}}^{j_1}, p_{\mathrm{T}}^{j_2}$ of the dijet system. The asymmetry A is defined by $A = (p_{\mathrm{T}}^{j_1} - p_{\mathrm{T}}^{j_2})/(p_{\mathrm{T}}^{j_1} + p_{\mathrm{T}}^{j_2})$. Its standard deviation σ_A gives

[5] Neutral and infinitesimally soft ($p_{\mathrm{T}} \sim 10^{-100}$ GeV) particle

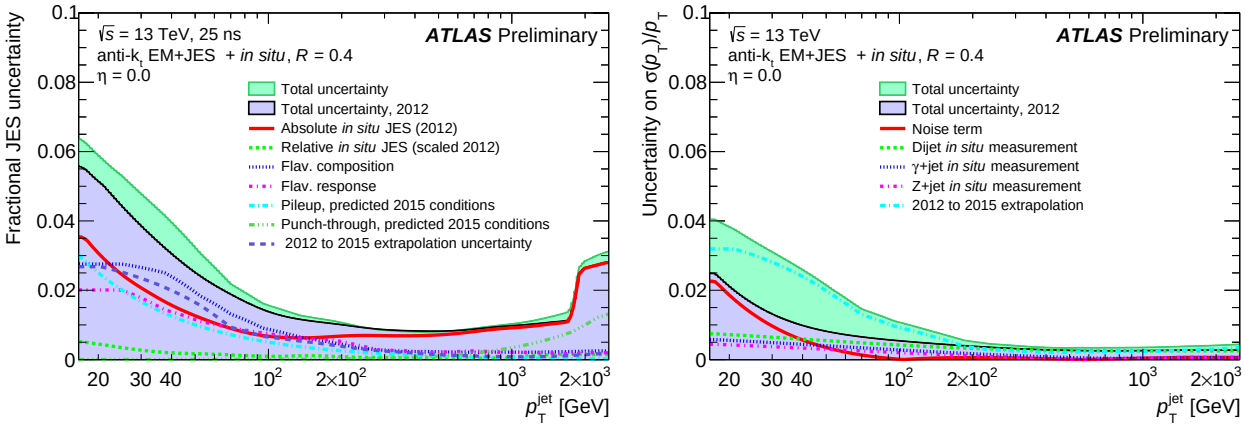

(a) Energy scale uncertainty **(b)** Energy resolution uncertainty

Figure 5.6: Jet energy resolution and scale uncertainties as a function of jet ($\eta = 0$) p_{T} (taken from Reference [144]).

the resolution by taking approximation of

$$\sigma = \frac{\sqrt{(p_{\mathrm{T}}^{j_1})^2 + (p_{\mathrm{T}}^{j_2})^2}}{\left\langle p_{\mathrm{T}}^{j_1} + p_{\mathrm{T}}^{j_2} \right\rangle} \simeq \frac{1}{\sqrt{2}} \frac{\sigma_{p_{\mathrm{T}}}}{p_{\mathrm{T}}}. \tag{5.6}$$

The jet energy resolution is also measured by Z+jets and γ+jets events using same technique. It is about 20% at $p_{\mathrm{T}} = 30$ GeV, 10% at $p_{\mathrm{T}} = 100$ GeV. The systematic uncertainties on the jet energy resolution is shown in Figure 5.6 (b).

5.3.3 Jet Flavour Identification and Pile-up Suppression

An overview of the b-tagging or flavour-tagging [150, 151] is given in this section. The flavour tagging is a key part in many physics analyses, for example in the b-jet multiplicity in $t\bar{t}$ decays. The identification of b-quark induced jets in ATLAS is based on unique strategies with three basic b-tagging algorithms. The results of three algorithm are combined using a multivariate discriminant. A brief overview are given in the following.

5.3.4 IP2D and IP3D: The Impact Parameter based Algorithm

The long lifetime of hadrons containing a b-quark ($c\tau \sim 450\,\mu$m) can be used to build lifetime-based algorithms. The transverse (longitudinal) impact parameter (IP) d_0 ($z_0 \sin\theta$) is defined as the distance of closet approach in the r-ϕ plane of the track to the primary vertex. Tracks from b-hadrons tend to generate large impact parameters. The IP2D and IP3D tagger are based on a log-likelihood ratio (LLR) between three jet-flavour hypothesis ($b, c,$ light). Probability density function (PDF) obtained from Monte Carlo simulation based on impact parameters with certain categorisation. The IP2D tagger uses of the transverse Impact parameter significance d_0/σ_{d_0} as discriminating variable while the IP3D tagger uses both the longitudinal and transverse impact parameters. The LLR discriminant is computed as the sum of the per-track combination, $\sum \log p_b/p_u$, the sum run over all track candidates. p_b and p_u are probability for the b- and light-flavour jet hypotheses respectively. No correlation is assumed among the tracks contributions to the sum. Figure 5.7 shows the LLR distributions for three jet-flavour using $t\bar{t}$ Monte Carlo simulation.

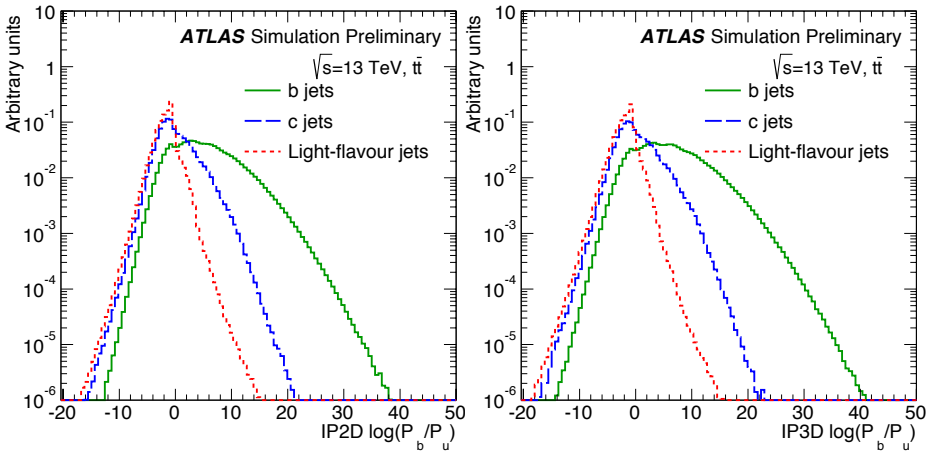

(a) IP2D distribution **(b)** IP3D distribution

Figure 5.7: The log-likelihood ratio for the IP2D (a) and IP3D (b) b-tagging algorithm for b- (solid green), c- (dashed blue) and light-flavour (dotted red) jets in $t\bar{t}$ events (taken from Reference [150]). If no tracks in the jet, a large negative value is assigned as output.

5.3.5 Secondary Vertex Finding Algorithm : SV

The secondary vertex finding algorithm [152] reconstructs an inclusive displaced secondary vertex within the jet from all tracks in the jet. All track pairs are tested for a two-track vertex hypotheses and rejected if they were to originate from the decay of a long-lived particle decay (K_s or Λ), photon conversions or hadronic interaction with a material. The track candidate is selected by certain criteria [150]. Each track pair should have a significant distance between the track and the primary vertex, $\Delta R(\mathrm{PV}, \mathrm{trk}) > 2$. The sum of the two impact parameter significance of the tracks in the track pair vertex should be higher than 2. In addition the χ^2 of the fitted track pair should be less than 4.5 and an invariant mass of the track pair should be less than 6 GeV to remove tracks from b- or c-hadron decays. Figure 5.8 shows properties of the secondary vertex reconstructed by the SV

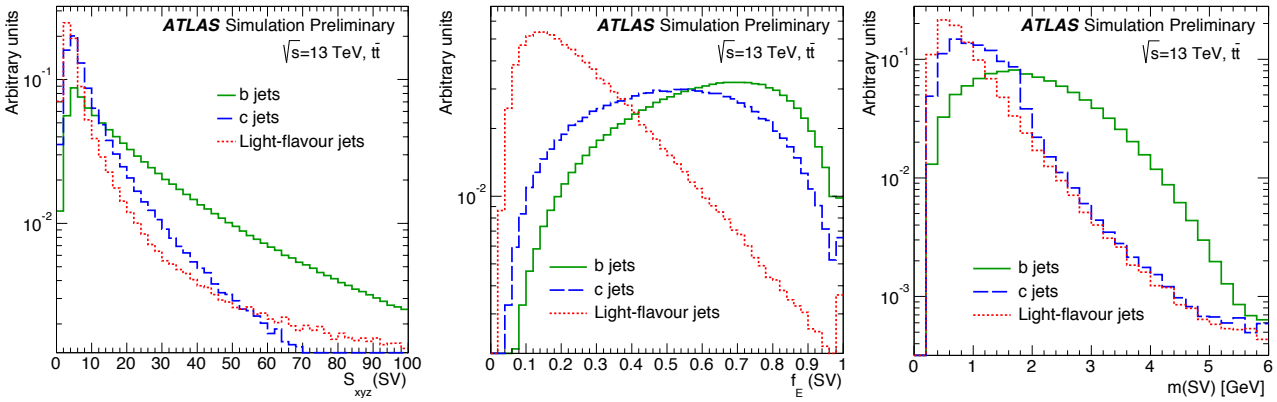

(a) The 3D decay length significance **(b)** The energy fraction **(c)** The invariant mass

Figure 5.8: Properties of secondary vertices reconstructed by the SV algorithm for b- (solid green), c- (dashed blue) and light-flavour (dotted red) jets in $t\bar{t}$ events (taken from Reference [150]). Note that: the energy fraction (b) is defined as a fraction of the tracks in the displaced vertex and all tracks reconstructed within the jet.

algorithm. These properties are inputs for the final multivariate discriminator.

5.3.6 Decay Chain Multi-Vertex Algorithm : JetFitter

The `JetFitter` algorithm [153] can reconstruct multiple vertices in the jet. The full b-hadron decay chain can be reconstructed. Kalman filter is used to find a common decay line from the primary vertex into bottom and charm vertices with b-hadron decay in flight constraint. The `JetFitter` uses

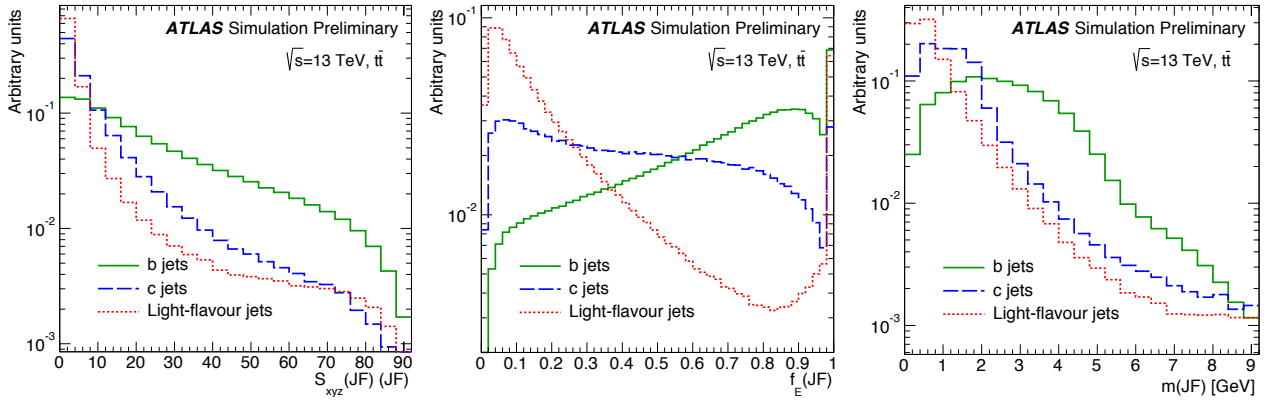

(a) The 3D decay length significance **(b)** The energy fraction **(c)** The invariant mass

Figure 5.9: Properties of secondary vertices reconstructed by the JetFitter algorithm for b- (solid green), c- (dashed blue) and light-flavour (dotted red) jets in $t\bar{t}$ events (taken from Reference [150]). Note that: the energy fraction (b) is defined as a fraction of the tracks in the displaced vertex and all tracks reconstructed within the jet.

kinematical constraints in the fit. Figure 5.9 shows properties of the secondary vertex reconstructed by the JetFitter algorithm. These properties are inputs for the final multivariate discriminator.

5.3.7 Multivariate Algorithm : MV2

The input variables obtained from the three basic algorithms are combined using a boosted decision tree (BDT) to discriminate the b-quark from c-quark and light-flavour quark jets. The training is performed on a few million $t\bar{t}$ Monte Carlo simulation events. The `MV2c20`(`MV2c10`,`MV2c00`) algorithm is defined as the output of BDT with the training performed b-jets as signal and mixture of 80% (93%,100%) light-flavour jets and 20% (7%,0%) c-jets as a background. A detailed description of the MV2 algorithm can be found in Reference [151]. Figure 5.10 shows the output score distribution of the MV2c20 and its rejection power to the c- and light-flavour jets with two different background mixture hypotheses. In this thesis, The MV2c10 tagger is used with a working point is chosen to achieve 77% efficiency to the b-jet tagging while the c-jet rejection rate is 6 and light-flavour jet is 134. To evaluate systematic uncertainties, several validations are performed by different training configuration and alternative background samples with observed data($t\bar{t} \to e\mu + bb$ sample). It is assigned of roughly $5 \sim 10\%$ for inclusive $|\eta|$ region over $p_{\mathrm{T}}^{b} = 20$ GeV ~ 300 GeV [151].

5.3.8 Tagging and Suppression of Pile-up Jets

Further subtraction of the pile-up activity in addition to the jet area method is important to improve accuracy of missing transverse energy reconstruction. The *Jet Vertex Tagger* algorithm is used [154] which consist of the JVF and $R_{p_{\mathrm{T}}}$ variable. The *Jet Vertex Fraction (JVF)* and $E_{p_{\mathrm{T}}}$is

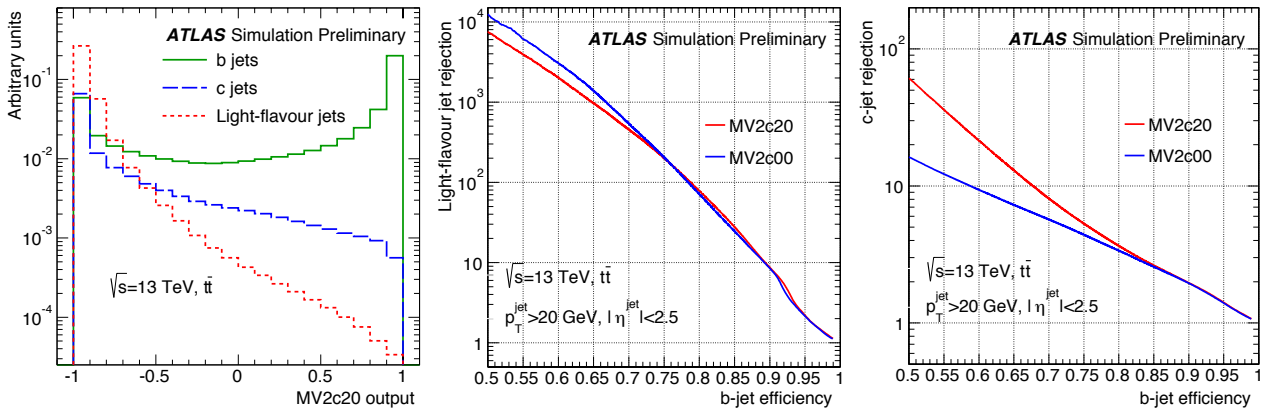

(a) The MV2c20 output distribution **(b)** The light-flavour rejection efficiency **(c)** The c-jet rejection efficiency

Figure 5.10: The MV2 algorithm output distribution (a) and its rejection efficiency comparison between MV2c20 and MVc00 for light-flavour (b) and c-jet (c) (taken from Reference [150]).

defined as following:

$$\mathrm{JVF} = \frac{\sum_k p_{\mathrm{T}}^{\mathrm{trk}_k}(\mathrm{PV}_0)}{\sum_l p_{\mathrm{T}}^{\mathrm{trk}_l}(\mathrm{PV}_0) + \frac{\sum_{n\geq l}\sum_l p_{\mathrm{T}}^{\mathrm{trk}_k}(\mathrm{PV}_n)}{(\kappa \cdot n_{\mathrm{trk}}^{\mathrm{PU}})}}, \quad R_{p_{\mathrm{T}}} = \frac{\sum_k p_{\mathrm{T}}^{\mathrm{trk}_k}(\mathrm{PV}_0)}{p_{\mathrm{T}}^{\mathrm{jet}}}. \tag{5.7}$$

where PV_0 is the hard-scatter vertex (HS) and $\mathrm{PV}_j, j \geq 1$ corresponds to primary vertices due to the in-time pile-up interaction. $n_{\mathrm{trk}}^{\mathrm{PU}}$ is the total number of pile-up tracks per event with the scaling factor $\kappa = 0.01$ determined by correlation with $\left\langle \sum_{n\geq l}\sum_l p_{\mathrm{T}}^{\mathrm{trk}_k}(\mathrm{PV}_n) \right\rangle$ and $n_{\mathrm{trk}}^{\mathrm{PU}}$. It measures the fractional p_{T} from tracks associated with the hard-scatter vertex. The $R_{p_{\mathrm{T}}}$ is defined as the scalar p_{T} sum of the tracks associated with the jet from the HS vertex divided by the fully calibrated jet p_{T} : The JVT is constructed using JVF and $R_{p_{\mathrm{T}}}$ as a two dimensional likelihood based on a k-nearest neighbour (kNN) algorithm. The JVT is defined by only jets with $20 < p_{\mathrm{T}} < 60$ GeV and $|\eta| < 2.4$ since the PU jets tend to have low p_{T}. The likelihood is a ratio of the number of signal local neighbourhood and the number of signal + background local neighbourhood. The local neighbourhood is defined as the 100 nearest neighbours around the (JVF, $R_{p_{\mathrm{T}}}$) point using a Euclidean metric. Figure 5.11 shows the JVF, $R_{p_{\mathrm{T}}}$ and JVT distribution for the HS and PU jets with certain jet p_{T} range. Both JVF and JVT = -1 events imply no-track candidate within the jet. a cut of JVT > 0.59 is used for suppressing the pile-up jets. Figure 5.12 shows the selection efficiency for the simulated events and data. The efficiency is measured using $Z \to \mu\mu$+jets events. If the jet is balanced to $Z \to \mu\mu$ system then it comes from the HS, while not balanced to $Z \to \mu\mu$, then it is likely from the PU. The systematic uncertainties are evaluated by changing selection criteria, muon momentum variations and jet energy scale uncertainty. The systematic uncertainty is a few percent level.

5.4 Electrons

Electron is an important experimental signature for many physics analyses, because it can be reconstructed and measured with high precision and purity. This is obtained by combined measurements and reconstructions with the tracking detectors and electromagnetic calorimeters. Electron also provides a clean signature at the trigger level, so single electron trigger items are used in this

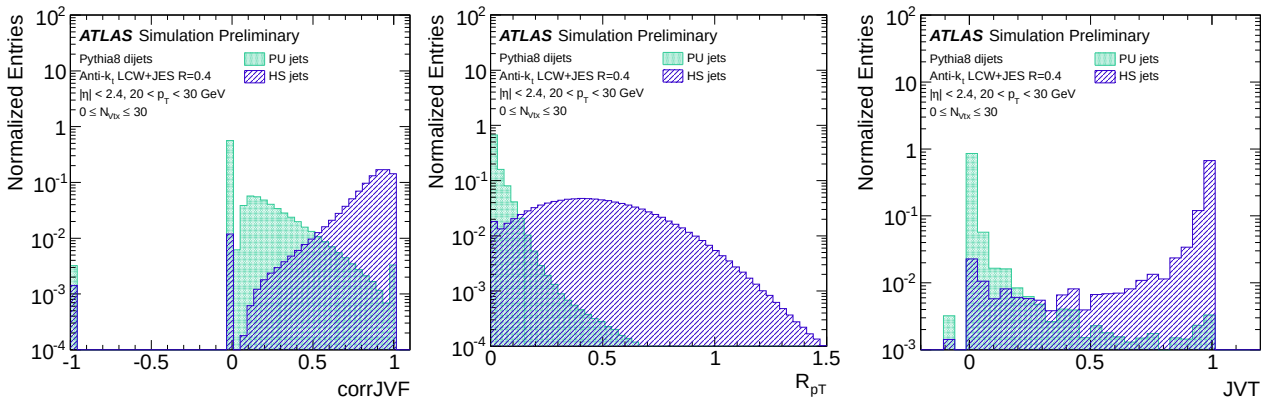

(a) JVF distribution **(b)** $R_{p_{\mathrm{T}}}$ distribution **(c)** JVT distribution

Figure 5.11: Distribution of the JVF, $R_{p_{\mathrm{T}}}$ and JVT for HS and PU jets with $20 < p_{\mathrm{T}} < 30\,\mathrm{GeV}$ (taken from Reference [155]).

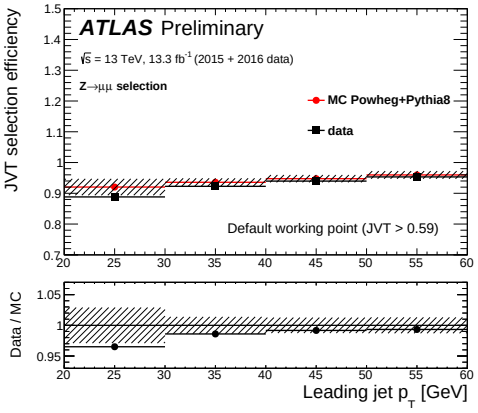

Figure 5.12: The hard-scatter jet selection efficiency for Monte Carlo and observed data (2015+2016) of JVT > 0.59 cut with $Z \to \mu\mu$ events. Overall systematic uncertainties are obtained from data-driven way and it shows less than 5% in lowest jet p_{T} bin, at highest jet p_{T} bin it is roughly 1% level.

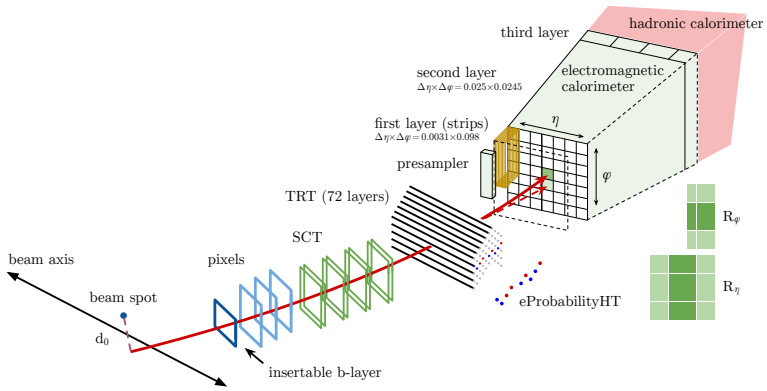

Figure 5.13: Schematic view of the electron reconstruction and identification (taken from Reference [156]). Electron is reconstructed by full information using the inner detector including the TRT hit probability likelihood information and the EM calorimeter cluster shower shapes.

analysis. Figure 5.13 shows a schematic view of the electron reconstruction and identification, which described in Section 5.4.1 and 5.4.3 respectively. An overview of the energy calibration, resolution and its uncertainty measurements are given in Section 5.4.2. In addition, an electron isolation is a key item to reduce mis-identification objects originated from hadronic jets. An brief overview of an isolation selection is given in Section 5.4.4. A description of the electron trigger is also given in Section 5.4.5

5.4.1 Electron Reconstruction

The electron reconstruction in the central region of the ATLAS detector ($|\eta| < 2.46$) is given by following procedure. A detailed description can be found in Reference [156].

- **Seed-cluster reconstruction** : Electron seed clusters are reconstructed by a sliding window with a size of 3×5 (unit is 0.025×0.025) in $\eta \times \phi$ by the EM calorimeter. A seed clustering efficiency ranges from 95% at $E_{\mathrm{T}} = 7\,\mathrm{GeV}$ to more than 99% above $E_{\mathrm{T}} = 15\,\mathrm{GeV}$.

- **Track reconstruction** : A pattern recognition and track fit are performed for electron track seeds. In order to take into account the Bremsstrahlung the pattern recognition algorithm allows up to 30% energy loss at each intersection of the track assuming the pion hypothesis. After that a second pattern recognition is performed by an electron hypothesis. The ATLAS Global χ^2 Track Fitter [157] is used to fit track candidates with firstly the pion hypothesis and if it fails then refitted with the electron hypothesis.

- **Gaussian Sum Filter** : The obtained tracks are required to natch with the EM clusters using a distance in $\eta - \phi$ considering energy loss due to the Bremsstrahlung. Tracks are refitted using Gaussian Sum Filter (GSF) [158] which can take into account non-linear Bremsstrahlung effects.

- **Electron reconstruction** : A matching of the track candidate and the cluster seed is performed finally. If several tracks satisfy matching criteria, one "primary" track is chosen based on an algorithm using the cluster-track distance R calculated with a different momentum hypothesis. The number of pixel hits and the presence of hits in the first layer of the silicon detectors are used [159].

The four-momentum of electron is calculated using information from both the calibrated energy cluster[6] and the best track matched to the original seed cluster. The energy is given by the calibrated cluster, while the η and ϕ direction are from the corresponding track parameter with respect to the primary vertex of a hard scatter. Figure 5.14 reconstruction efficiencies using $Z \to ee$ events for

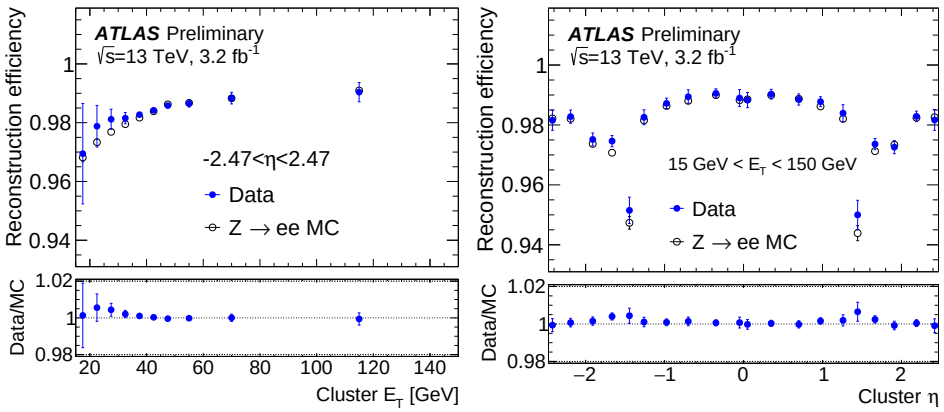

(a) Efficiency (E_{T}) **(b)** Efficiency (η)

Figure 5.14: Efficiencies and scale factors fro the electron reconstruction as a function of electron transverse momentum (left) and pseudorapidity (left) using $Z \to ee$ events(taken from Reference [156]). Markers with closed (open) circle shows real (simulated) data in upper panels, while the scale factors in represented in the bottom panels.

simulated and experimental data. Differences between simulated and experimental data should be

[6] Based on multivariate technique, details can be found in Reference [160]

taken account by correction factors (*scale factors, SF*). The scale factor have been evaluated using $Z \to ee$ tag-&-probe method [156] in this analysis.

5.4.2 Electron Energy Calibration and Resolution

A detailed description about the electron calibration is found in Reference [161]. There are several different steps in the procedure to calibrate the energy response of electrons for simulated and experimental data. The procedure can be split up to 5 $\sim$ 4 steps. Starting from the EM cluster energy, a MC-based e/γ energy calibration is applied for the simulated and real data. The longitudinal calorimeter layer inter-calibration is applied for only real data. The MC-based e/γ energy calibration is based on a multivariate technique. Uniformity corrections are applied for only real data to correct the energy response difference of ϕ-angle plane. Then the $Z \to ee$ resolution smearing and scale calibration is applied for the simulated and real data. The calibrated electron energy scale is validated with electron candidates from $J/\psi \to ee$ and $Z \to e^+e^-$ events in real data. The electron

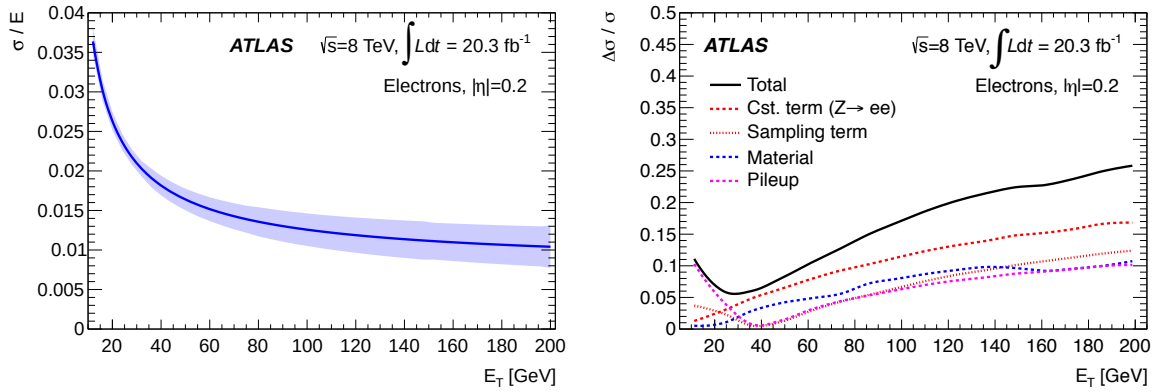

(a) Energy resolution **(b)** Resolution uncertainty

Figure 5.15: Resolution curve and its uncertainty as a function of electron E_{T} (left) and its enveloped with different systematical uncertainties source (right) (taken from Reference [161]).

energy resolution is defined by the following:

$$\frac{\sigma_E}{E} = \frac{1}{\sqrt{E}} \oplus \frac{b}{E} \oplus c, \tag{5.8}$$

where a, b and c are η-dependent parameter: a is the sampling term, b is the noise term and c is constant term. The sampling term is derived from the calorimeter intrinsic resolution. It is obtained from detector simulation and its systematic uncertainties is assumed as 10% from test-beam studies [162]. The pile-up and electric noise of the EM calorimeter are a source of he noise term. The constant term is measured by $Z \to ee$ events assuming $\langle {E_{\mathrm{T}}}^e \rangle \simeq 40$ GeV in $Z \to ee$ event. Figure 5.15 shows the electron energy resolution and its systematics uncertinties as a function of the electron E_{T}. In addition to three terms above, systematic uncertainties of a material in calorimeter is obtained by alternative simulations. The relative energy resolution at $E_{\mathrm{T}} = 40$ GeV is about 2% with relatively 7% uncertainty.

5.4.3 Electron Identification

In order to reduce mis-identified hadronic jets and converted photons, an algorithm for electron identification (ID) is constructed by using properties of reconstructed electrons. The electron ID algorithm is based on a likelihood (LH) technique with the signal and background probability density

function (PDF) given by :

$$d_{\mathcal{L}} = \frac{\mathcal{L}_S}{\mathcal{L}_S + \mathcal{L}_B}, \ \mathcal{L}_X(\vec{x}) = \prod_{i=1}^{n} P_{X,i}(x_i), \tag{5.9}$$

where $\vec{x}$ is the vector of discriminating variables and $P_{X,i}(x_i)$ is the value of the signal or background PDF of the variable x_i. The input variable list is summarised in Reference [156]. For example the shower shape of the topo-cluster and information of hit in TRT are used in the electron ID algorithm. The PDFs for the signal and background are obtained from simulated samples of $Z \to ee$ and dijet respectively. The electron ID has three different working point, `Loose`, `Medium` and `Tight`. The

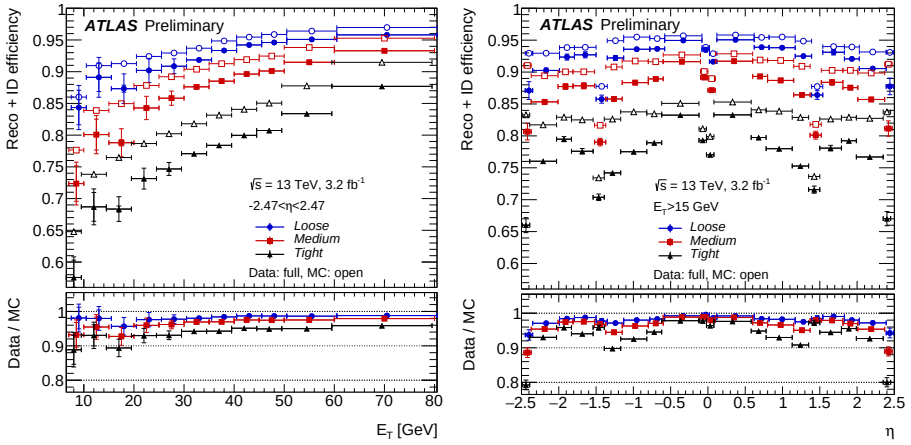

(a) E_{T} **(b)** η

Figure 5.16: The efficiency and scale factor of the electron LH ID including reconstruction efficiency as a function of electron transverse momentum (left) and pseudorapidity (left) using $Z \to ee$ events with three different ID working points (Loose, Medium and Tight) (taken from Reference [156]).

working points are constructed for different identification efficiencies. At $E_{\mathrm{T}} = 40\%$ efficiencies of `Loose`, `Medium` and `Tight` correspond to about 78%, 87% and 97% for signal electrons in real data. The `Medium` working point is used for default electron ID and its scale factors is derived by $Z \to ee$ tag-&-probe method. Figure 5.16 shows the efficiency of the electron ID for the signal electrons using $Z \to ee$ events in simulated and real data. The systematic uncertainties are derived in data-driven ways and also alternative detector simulations using different condition of the `Genat4` simulation. Besides identification of electron, the LH ID is used for the hadronic τ-lepton identification which described in Section 5.6.3.

5.4.4 Electron Isolation

In addition to the identification, an isolation requirement is useful to further distinguish the signal and background. The isolation variable quantify the energy of the particles produced around the electron candidate. Two discriminating variables are used for this purpose.

- **Calorimeter isolation** $E_{\mathrm{T}}^{\mathrm{cone0.2}}$: defined as the sum of transverse energies of topo-clusters calibrated at the EM scale within a cone of $\Delta R = 0.2$ around the electron candidate. An (E_{T}, η) dependent correction is applied to take into account the electron energy leakage outside cluster and pile-up. Underlying effects is also corrected on event-by-event [145]

- **Track isolation** $p_{\mathrm{T}}^{\mathrm{varcone0.2}}$: defined as the sum of transverse momenta of all tracks which satisfy certain track selection criteria within cone of $\Delta R = \min(0.2, 10\,\mathrm{GeV}/E_{\mathrm{T}})$ around the candidate

electron track [156].

Several working points are constructed for the isolation selection, in this thesis analysis `Gradient` working point has been chosen as a default isolation selection. In addition to `Gradient` working point, the `Tight` and `FixedCutLoose` are used in the electron trigger (Section 5.4.5) and background estimations (description is in Section 6.5.1). It is two-dimensional selection using $E_{\mathrm{T}}^{\mathrm{cone0.2}}$ and $p_{\mathrm{T}}^{\mathrm{varcone0.2}}$. Selection cut values depend on the transverse momentum correspondingly satisfying efficiency of $\min\left((0.1143 \times E_{\mathrm{T}} + 92.14)\%, 99\%\right)$. The total efficiencies are 90 (99)% at 25 (60) GeV of electron E_{T}. Figure 5.17 shows the efficiency and scale factors of the electron isolation selection with

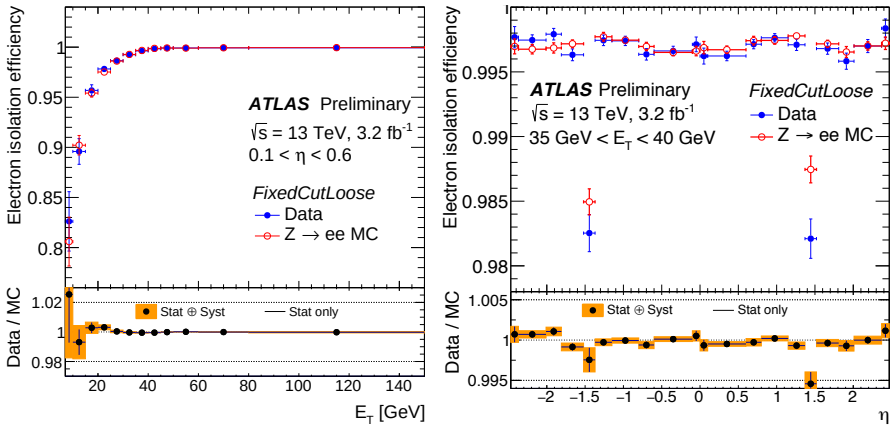

(a) E_{T} **(b)** η

Figure 5.17: The efficiency and scale factor of the electron isolation selection (`FixedCutLoose`) as a function of electron transverse momentum (left) and pseudorapidity (left) using $Z \to ee$ events (taken from Reference [156]). The `FixedCutLoose` requires $E_{\mathrm{T}}^{\mathrm{cone0.2}}/E_{\mathrm{T}} < 0.2$ and $p_{\mathrm{T}}^{\mathrm{varcone0.2}}/E_{\mathrm{T}} < 0.15$.

`FixedCutLoose` working point. The total uncertainties are within $2 \sim 3\%$ level at low E_{T} region. In this analysis the electron is required $E_{\mathrm{T}} > 30$ GeV so its uncertainties are about less than 1% level.

5.4.5 Electron Trigger

As discussed in Section 4.2.6, at each stage of the ATLAS trigger system the identification and isolation algorithm are used. At the L1 RoIs, the identification and isolation using a sliding window algorithm on calorimeter trigger towers with a granularity of $\Delta\eta \times \Delta\phi = 0.1 \times 0.1$ are required using a dedicated electronics. HLT uses the full granularity from the RoIs (L1EM items) with combining the calorimeter clusters and tracks, which is close to the offline-like algorithm. The trigger items used in the analysis are called as *single-electron-trigger*, requiring the presence of one electron candidate above a certain p_{T} threshold, identification and isolation criteria. In this analysis, six single-

Year	p_{T}	identification
2015	24, 60, 120(20) GeV for HLT (L1)	medium, medium, loose
2016	26, 60, 140(22) GeV for HLT (L1)	tight, medium, loose

Table 5.1: The single-electron-trigger items used in this analysis for 2015 and 2016 data-taking.

electron-trigger items are used corresponding to data-taking periods and its p_{T} thresholds based on Reference [163]. Table 5.1 summarise the single-electron-trigger which used in this analysis. Three different p_{T} threshold menus are taking OR-ing to reduce uncertainties and suppress online isolation

inefficiency. Figure 5.18 shows the trigger efficiency of the 2015 lowest-p_{T} single-electron-trigger for

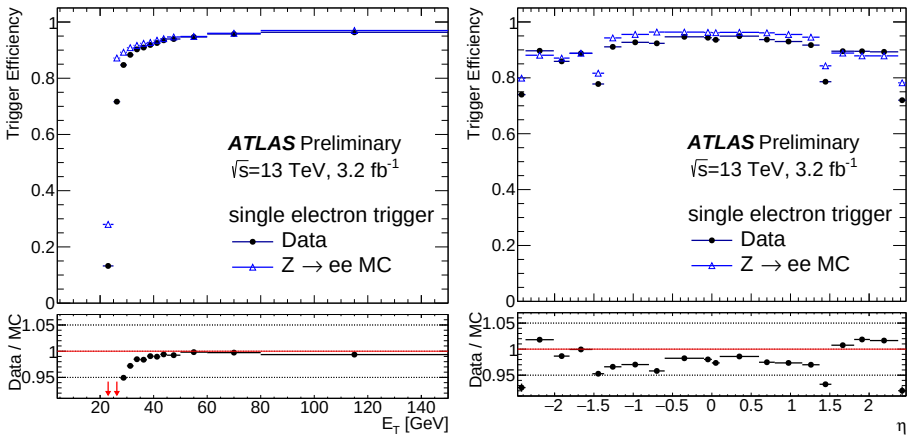

(a) E_{T} **(b)** η

Figure 5.18: The efficiency and scale factor of the single-electron-trigger of 2015 p_{T} threshold of 24 GeV as a function of electron transverse momentum (a) and pseudorapidity (b) using $Z \to ee$ events (taken from Reference [156]).

simulated and experimental data using $Z \to ee$ tag-&-probe method. (a) shows the trigger efficiency as a function of the offline electron p_{T}. Small drop in low p_{T} region can be seen. In this analysis $p_{\mathrm{T}} > 30$ GeV is required, so the efficiency in all range of p_{T} has greater than 80%. (b) shows the trigger efficiency as a function of the offline electron η. There are non-negligible efficiency drop in $|\eta| \sim 1.5$, this region is so-called *crack-region* due to a large amount of dead-material (service cable of the inner detectors). In this analysis electrons which pointed in $1.37 < |\eta| < 1.52$ are vetoed.

5.5 Muons

Muon is a minimal ionised particle (MIP), so energy deposit in the calorimeter is extremely small. The ATLAS detector has dedicated muon spectrometers outside of the hadronic calorimeter, which can measure its momentum. The muon spectrometers are located inside a magnetic field of a average field strength of 0.5 T providing a bending power to ensure a high momentum resolution for muon up to 1 TeV. Thanks to low mis-identification rate of backgrounds and the precise momentum measurement, muons provide an excellent trigger signature. Explanation of the muon reconstruction and its identification are given in Section 5.5.1 A brief overview of the muon momentum calibration and isolation is described in Section 5.5.2. and 5.5.3. The muon signature trigger used in the analysis is shown in Section 5.5.4.

5.5.1 Muon Reconstruction and Identification

Muon reconstruction is performed independently in the inner detector (ID) and muon spectrometer (MS). Muons are reconstructed as described in Section 5.1 in the inner detector. The muon reconstruction in the MS and its combination are focused in this section.

In each MDT chamber and other trigger chamber, a Hough transform [164] is used to find hits aligned on the bending plane of the detector. For example, MDT segments are reconstructed by performing a straight-line fit to the hits found in each layer. Muon track candidates are built by fitting together the segments from in the different layers. At least two matching segments are required to build a muon track, except in the barrel-endcap transition region. The different track candidates

can initially share the same segment. The hits associated with each track candidates are fitted to minimise a global χ^2. A track candidate is selected by certain criteria using the χ^2 of the fit. The fit is repeated until no additional hits are found around the track candidates.

The combined ID-MS muon reconstruction is performed according to various algorithm based on the information provided by the ID, MS and calorimeter. Following four-types are defined depending on which subdetectors are used in reconstruction:

- **Combined muon (CB)** : The muon are first reconstructed in MS, then the outside-in pattern recognition extrapolates the MS track into the inner detector to find corresponding a ID track. The inside-out pattern recognition is used to find a MS track matched with the ID track.

- **Segment-tagged muons (ST)** : In order to recover the efficiency to low p_{T} muons, a track in the inner detector is classified as a muon if it can be extrapolated to MS. Because the low p_{T} track has only one segment hit in muon chambers, the ID track is required at least one track segment.

- **Calorimeter-tagged muons (CT)** : Tracks in the inner detector is identified as a muon if it can be matched to an energy deposit in the calorimeter is compatible with a MIP. CT muon has the lowest purity of all the muon types. CT muon can recover acceptance in the region where the ATLAS MS is only partially installed for cabling and services to the calorimeter and inner detector. The identification criteria is optimised for region of $|\eta| < 0.1$ where other reconstruction algorithm efficiency drops.

- **Extrapolated muons (ME)** : This type consists of a muon track based on only a MS track. Loose matching with originating the interaction point is required. ME muons are mainly used to recover an acceptance for a muon in the region of $2.5 < |\eta| < 2.7$ where there are no inner detectors.

`Chain 3rd` algorithm is used in this analysis as described in Reference [165]. The chain 3rd algorithm takes OR of existing tracks and removes overlapped tracks.

In addition to muon reconstruction, identification selection is applied using three variables listed in below:

- q/p **significance** : defined as the absolute value of the difference of the ratio of the charge to its momentum. It is divided by the quadrature sum of its uncertainties.

- ρ' : defined as the absolute value of the difference between the transverse momentum in the ID and MS. It is also divided by the p_{T} of the combined track.

- χ^2 : defined as normalised χ^2 of the combined track fit.

Four muon identification working points are defined. The `Medium` working point is used as a default in this analysis. The `Medium` working point requires the muon tracks reconstructed by only the CB tracks. It has greater than three hits in at least two MDT layers, except for tracks in the $|\eta| < 0.1$ region, where there is only one MDT layer. No more than one MDT hole are allowed. The q/p significance should be less than seven and ρ' is required by a loose compatibility selection. Figure 5.19 shows the reconstruction and identification efficiency for the `medium` working point using $Z \to \mu\mu$ and $J/\psi \to \mu\mu$ tag-&-probe method. The efficiency is $\geq 98\%$ for a muon with $20 < p_{\mathrm{T}} < 100$ GeV. While the efficiency of fake muons from hadrons is less than 0.2%. The total uncertainties are less than 3% level at hole range of the muon p_{T} and also muon η.

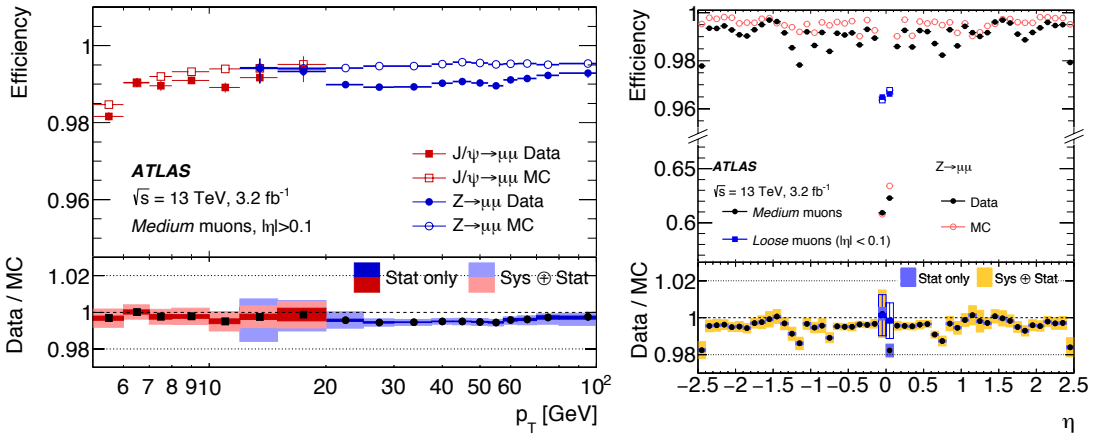

(a) p_{T} **(b)** η

Figure 5.19: Reconstruction efficiency for the `medium` working point as a function of p_{T} (a) and η (b) measured by $Z \to \mu\mu$ and $J/\psi \to \mu\mu$ tag-&-probe method for simulated and experimental data (taken from Reference [166]). The error band on top (bottom) panel indicate the statistical (statistical plus systematical) error.

5.5.2 Muon Momentum Calibration and Resolution

The muon momentum calibration is defined as corrections to the simulated muon transverse momenta reconstructed in the ID and MS to reproduce the experimental data. It corrects the ID and MS components of the CB track. The corrected transverse momentum $p_{\mathrm{T}}^{\mathrm{corr,det}}$ (det = ID,MC) is defined by following :

$$p_{\mathrm{T}}^{\mathrm{corr,det}} = \frac{p_{\mathrm{T}}^{\mathrm{MC,det}} + \sum_{n=0} 1s_n^{\mathrm{det}}(\eta,\phi)(p_{\mathrm{T}}^{\mathrm{MC,det}})^n}{1 + \sum_{m=0}^{2} \Delta r_m^{\mathrm{det}}(\eta,\phi)(p_{\mathrm{T}}^{\mathrm{MC,det}})^{m-1} g_m}, \tag{5.10}$$

where $p_{\mathrm{T}}^{\mathrm{MC,det}}$ is the un-corrected p_{T} in the simulated samples, g_m is random Gaussian distribution with zero mean and unit width. The term of $\Delta r_m^{\mathrm{det}}(\eta,\phi)$ and $s_n^{\mathrm{det}}(\eta,\phi)$ represents the momentum resolution smearing and scale correction factors respectively. Detailed values of the resolution smearing and scale correction can be found in Reference [165]. The correction factors are obtained from the observed $Z \to \mu\mu$ and $J/\psi \to \mu\mu$ line shape with fitting the momentum scale and smearing, which are shown in Figure 5.20 On m_Z shapes, total uncertainties are estimated to about $2 \sim 5\%$ in range of $20 < p_{\mathrm{T}} < 100\,\mathrm{GeV}$.

5.5.3 Muon Isolation

The muon isolation selection is also applied to reduce the fake background coming from semi-leptonic decay of B-meson or other hadrons. The track and calorimeter based isolation are defined as well as the electron isolation. The definition of the muon isolation requirement is similar to the electron. The correction against pile-up effects are slightly different but it is not relevant to explain in this thesis [165]. The `Gradient` isolation selection working point of the muon is also used which is same definition as the electron. Figure 5.21 shows the efficiency of the isolation selection as a function of the transverse momentum. The efficiency is measured to about 92% for low p_{T} muons, while ¿ 99% is achieved for high p_{T} muons. The systematic uncertainty is derived by uncertainty of background subtractions, muon momentum and Identification. It is estimated as less than 1% in wider p_{T} range.

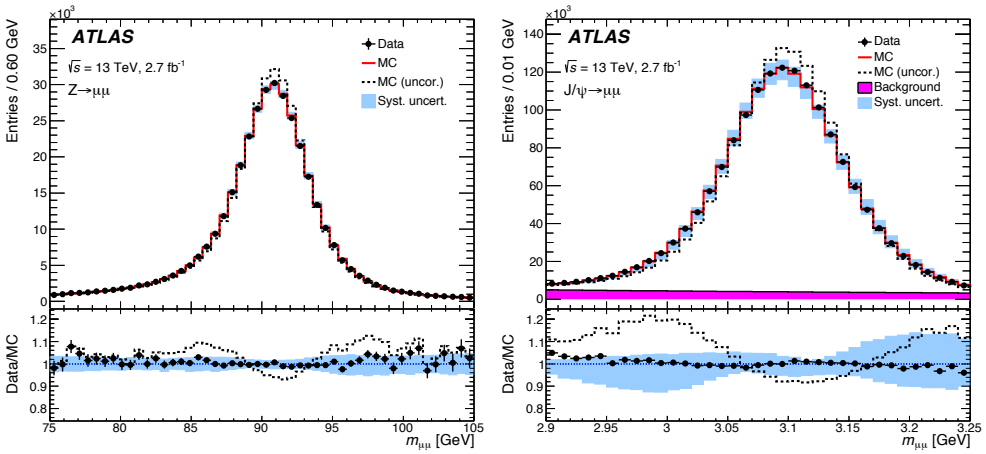

(a) $Z \to \mu^+\mu^-$ **(b)** $J/\psi \to \mu\mu$

Figure 5.20: Dimuon invariant mass distribution of $Z \to \mu\mu$ (a) and $J/\psi \to \mu\mu$ candidate events (taken from Reference [166]). Solid (dashed) histograms present before (after) applying momentum corrections. The lower panels shows the ratio between the MC simulation and experimental data. Good agreements can be seen after the corrections.

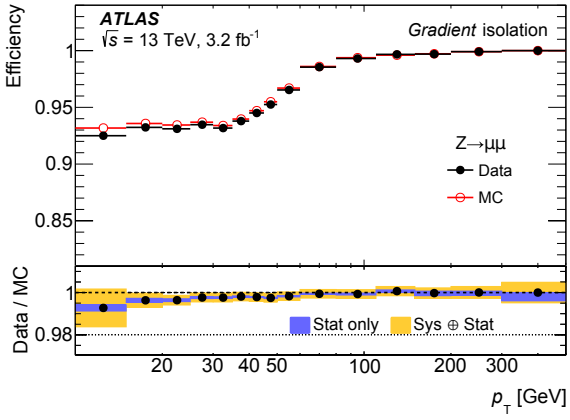

Figure 5.21: Isolation efficiency for the `Gradient` working point (taken from Reference [166]). The efficiency is shown as a function of the muon p_{T} by $Z \to \mu\mu$ events. The closed (open) markers indicate the efficiency measured in data (simulation) samples. The error bands shown on the efficiency are statistical only. The bottom panel shows the ratio between efficiency measured in data and simulation, as well as the statistical and systematic uncertainties.

5.5.4 Muon Trigger

The ATLAS muon trigger follows the two-level design of the ATLAS trigger system. The L1 trigger takes a decision based on coincident signals in the muon trigger chambers. RPC work in barrel-region ($|\eta| < 10.5$) and TGC work in the endcap region ($1.05 < |\eta| < 2.4$). The L1 send the RoIs information to the central trigger processor to make the HLT decision. The HLT used by offline-like muons using full detector information from RoIs also has option of HLT level full scan of muons. Three single-muon-triggers are used in this analysis. An OR of single-muon-triggers with p_{T} threshold of 20 GeV (with loose isolation selection) and 50 GeV is used for the 2015 data. While p_{T} threshold of 26 GeV (with medium isolation selection) and 50 GeV are used for the 2016 data.

The single-muon-trigger has extremely good resolution on both the L1 and HLT items. Figure 5.22 shows the muon trigger efficiency as a function of offline muon p_{T} and ϕ for the barrel and endcap region. An inefficiency can be seen at the L1 trigger (`mu15`) due to inefficiencies of RPC chambers in the barrel region. There are also efficiency drop around $\phi \sim= -1.2 \sim -2.0$, due to huge materials of the toroidal magnet arms. While in the endcap region, the L1 has $> 90\%$ efficiency at the plateau region. The HLT efficiency with regard to the L1 is greater than 90% for both the barrel and endcap region. The total efficiency of the single-muon-trigger is 70 (85)% in the barrel (endcap) region.

The inefficiency in the barrel region is not negligible. So the $E_{\mathrm{T}}^{\mathrm{miss}}$ trigger is introduced in this

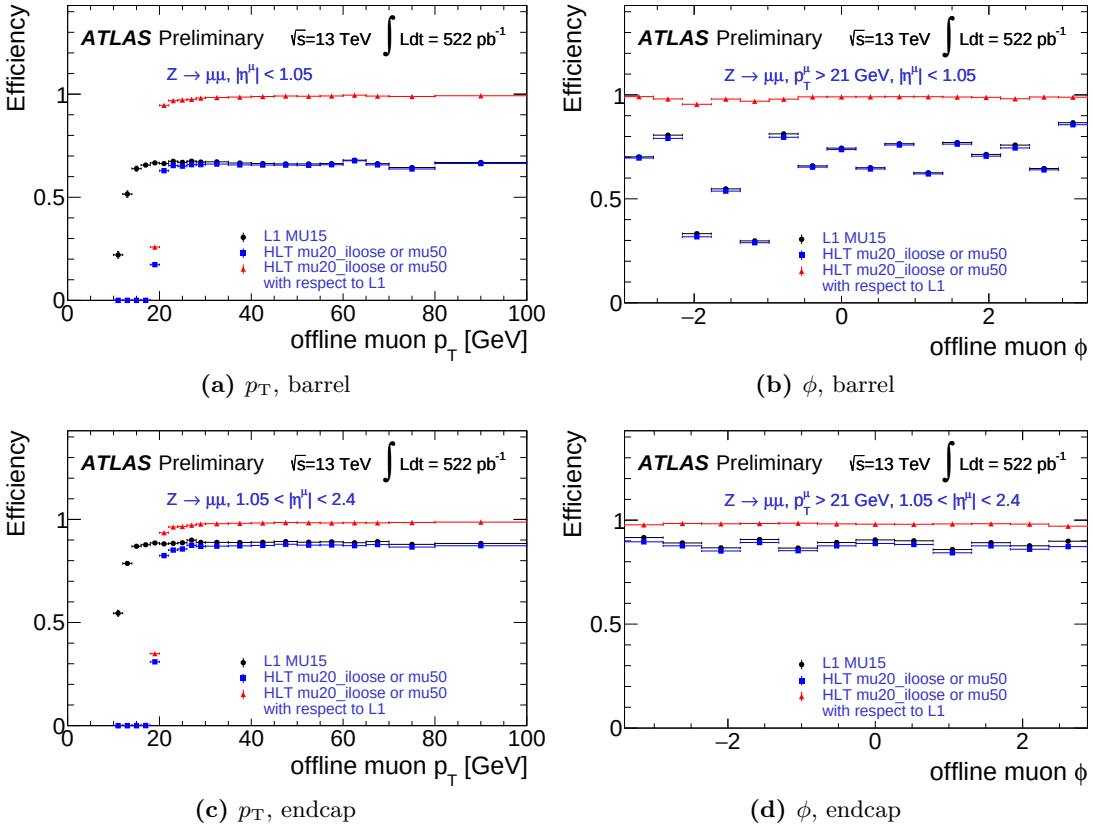

(a) p_{T}, barrel **(b)** ϕ, barrel

(c) p_{T}, endcap **(d)** ϕ, endcap

Figure 5.22: Efficiency of the single-muon-trigger (`mu20_iloose_L1MU15 or mu50`) for the barrel and endcap region as a function of offline muon p_{T} (a,c) and ϕ (b,d) (taken from Reference [167]). The efficiency is measured by using a $Z \to \mu\mu$ tag & probe method.

analysis to recover them. Detailed description is given in Section 5.7.3. The scale factor are obtained by experimental data using $Z \to \mu\mu$ and $J/\psi \to \mu\mu$ tag-&-probe method. The uncertainties of the single-muon-trigger are obtained from the $Z \to \mu\mu$ tag-&-probe method. Variation of `Geant4` simulation parameterization is taken into account as an additional systematic uncertainty. It is ranges $1 \sim 5\%$ on inclusive muon p_{T} range.

5.6 Hadronic Tau Decays

The τ-lepton is the heaviest lepton with a mass of $m_\tau = 1776.86 \pm 0.12$ MeV [168]. The τ-leptons decay with a mean lifetime of $\tau = (290.4 \pm 0.5) \times 10^{-15}$s via weak charged current interactions into hadrons or light leptons (electron or muon). Table 5.2 summarises decay modes for leptonic (τ_ℓ) and hadronic (τ_{had}) decay[7]. The main leptonic modes decays into one charged lepton and two neutrinos. In addition to these modes very rare decay with multiple charged leptons exist below the branching fraction of $< 2.8 \times 10^{-5}$. Since in the ATLAS detector lepton from the τ-leptonic decay cannot be identified, our target of an identification of the τ-lepton decay is to distinguish hadronically decaying τ from the τ-lepton hadronic decay.

In the decay products of the hadronic decay mode should contain an odd number of charged

[7]The symbol τ_ℓ and τ_{had} is used to denote both a leptonically and hadronically decay. In addition to this τ_{vis} is used to its reconstructed visible decay products without neutrinos.

hadrons for the charge conservation. The 1- or 3-prong decay modes dominate its branching fractions of hadronic τ-lepton decays. The main process for the 1- or 3-prong modes can be seen in Table 5.2[8]. The difference of the number of neutral hadrons are not taken into account in this analysis[9]. In the future this technique will be important in precision measurement of the SM Higgs boson.

decay mode	final state	main decay mode	BR (%)	Total (%)
leptonic	e	$e^- + \bar{\nu}_e + \nu_\tau$	17.82	35.21
	μ	$\mu^- + \bar{\nu}_\mu + \nu_\tau$	17.39	
1prong	$1\pi^\mp + 0\pi^0$	$\pi^- + \nu_\tau$	10.82	48.90
	$1\pi^\mp + 1\pi^0$	$\rho^- \to \pi^- + \pi^0$	25.93	
	$1\pi^\mp + 2\pi^0$	$a_1 \to \rho^- + \pi^0$	12.15	
3prong	$3\pi^\mp + 0\pi^0$	$a_1^- \to \rho^0 + \pi^-$	9.8	15.09
	$3\pi^\mp + 1\pi^0$	$\omega + \rho^0$	5.29	

Table 5.2: Main decay modes, the corresponding branching ratio, its main decay process. The branching fractions are the result of a combined fit to several experimental data, taken from Reference [168].

The hadronic-τ decay products are highly collimated, because typical momenta of the τ-leptons produced in electroweak interactions are larger than its mass. This collimated hadrons can be reconstructed as a narrower jet compared with jets from quark or gluon hadronisation. The reconstruction procedures are described in Section 5.6.1. The number of reconstructed tracks and cluster shower shape profiles are used to distinguish hadronic-τ from hadronic jets. Besides hadronic jets, electrons provide similar signature to the 1-prong decay when an electron track is accidentally combined with hadronic calorimeter activity. A dedicated set of identification criterion is used to suppress electrons mis-identified as hadronic-τ objects. The identification algorithm including separation of electrons are described in Section 5.6.3. A specific energy momentum calibration is performed to the visible τ_{had} objects. This calibration procedure is described in Section 5.6.2.

5.6.1 Hadronic-τ Reconstruction

The visible hadronic-τ[10] reconstruction algorithm have been developed and tested during the Run1 data-taking [170, 171]. Several improvements have been implemented as in Reference [169] from the Run2. As an input for seeds of the hadronic-τ reconstruction, hadronic jets reconstructed by the anti-k_{T} with a distance $\Delta R = 0.4$. Seed jets are calibrated by the local hadronic topo-cluster scale (LC). The seed jets are required to selection criteria of $p_{\text{T}} > 10$ GeV and $|\eta| < 2.5$. Topo-clusters in the core region ($\Delta R < 0.2$) are used to reconstruct kinematic of hadronic-τ, while those in the isolation region ($0.2 < \Delta R < 0.4$) are used to suppress the background. The topo-cluster is reconstructed with the hadronic calorimeter and the last layer of the EM calorimeter. Other layers of the EM calorimeter are used for referring the energy deposit in the EM calorimeter.

Vertex Association and Track Selection

The seed jet is required to have ID tracks within the core region, which satisfy:

- $p_{\text{T}} > 1$ GeV

[8] in addition to the pion mode, there are non-negligible Kaon decay process, but the ATLAS detector cannot separate them, so only the pion decay mode are summarised.

[9] The ATLAS collaboration have already developed an algorithm to distinguish this "substructure of hadronic decay" in Reference [169] by using a particle flow algorithm.

[10] "visible" means only hadronic components without neutrino, same argument visible-τ is also used in this thesis.

- Number of pixel + IBL hits ≥ 2 and number of pixel + SCT hits ≥ 7
- $|d_0| < 1.0$mm and $|z_0 \sin\theta| < 1.5$mm

where d_0 (z_0) is the distance of closest approach of the track to the vertex in the transverse (longitudinal) plane. These two impact parameter selections should be robust against high pile-up environment. The 1-prong decay consists of only one charged tracks (or, and neutral π^0 activity). So the track-to-vertex association is important to reconstruct the 1-prong hadronic-τ. Usually the track-to-vertex association is performed using d_0 and $|z_0 \sin\theta|$. This association becomes difficult under the high pile-up environment. The primary vertex (PV) is chosen as the highest sum of transverse momentum ($\sum_{\text{trk}}^{\in\text{vtx}}(p_{\text{T}}^{\text{trk}})^2$) vertex. The `Tau Vertex association (TV)` algorithm [155] chooses the vertex using the fraction of the sum p_{T} between all tracks in the jet and tracks associated to the vertex defined by following :

$$f_{\text{TV}}^{\text{vtx}} = \frac{\sum_{\text{trk}}^{\in\text{vtx}} p_{\text{T}}^{\text{trk}}}{\sum_{\text{trk}}^{\in\text{jet}} p_{\text{T}}^{\text{trk}}}, \tag{5.11}$$

where the vertex association selection is optimised for the 1-prong and 3-prong separately. Figure 5.23 shows the efficiency of the TV and the default PV selection. The TV algorithm improves its association efficiency for the 1-prong τ. The number of tracks associated with the TV is shown in Figure 5.23 (c). Most of the 1- and 3-prong are reconstructed as correct decay mode. Figure 5.24 shows the efficiency of the reconstruction of visible-τ objects and its systematic uncertainties. The reconstruction efficiency is about 70% on an average. The efficiency to the 3-prong visible-τ objects slightly drop at higher-p_{T}, because multiple charged tracks cover each other and one of them cannot be reconstructed at the track reconstruction. Leading systematic uncertainty is the pile-up effect using MC-based estimation for both decay mode. At lower-p_{T} region (20-30 GeV) the total uncertainty is about 4.5%.

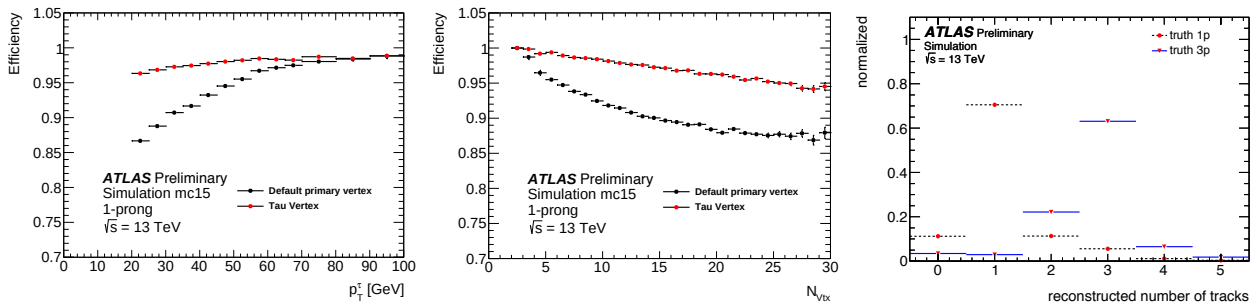

(a) Efficiency (p_{T}) **(b)** Efficiency (N_{PV}) **(c)** The number of tracks

Figure 5.23: Efficiency for correct production vertex association in 1-prong hadronic-τ with default (black circle) PV and TV (red circle) as a function of visible-τ p_{T} (a) and the number of reconstructed vertices (b) using MC simulation. Plot (c) shows the number of track associated with the selected TV for the 1- and 3-prong visible-τ objects (taken from Reference [171]).

5.6.2 Hadronic-τ Energy Calibration and Resolution

The energy of the visible-τ candidate is calibrated at the LC scale using only calorimeter information after the reconstruction. The visible-τ energy scale (so-called TES) is corrected from measured energy into the true visible energy (E_{true}). The four-momentum of the visible-τ is determined in the calorimeter assuming that it is massless. The energy contributed from pile-up interaction is subtracted by the similar way to the jet energy calibration. A response correction is applied to account for decay

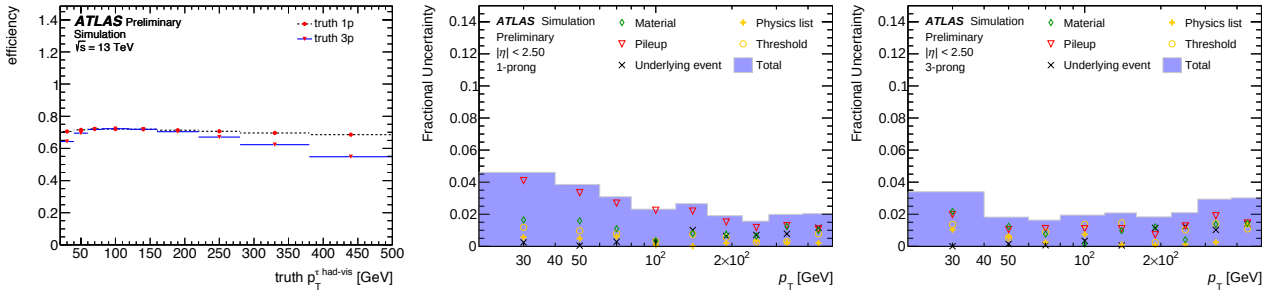

(a) Efficiency **(b)** Uncertainty,1-prong **(c)** Uncertainty,3-prong

Figure 5.24: Efficiency for reconstructing the same number of tracks as decay products as a function of visible-τ p_{T} (a). Relative systematic uncertainties on the efficiency for the reconstruction of visible-τ objects with same number of tracks as the number of charged decay products of the τ-lepton as a function of the visible-τ p_{T} for the 1-prong (b) and 3-prong (c). The individual sources of systematic uncertainties are in plots and total systematic are shown in blue filled histograms (taken from Reference [171]).

products not detected the calorimeter. The corrected energy of the visible-τ is described as:

$$E_{\mathrm{corr}} = E_{\mathrm{LC}} - A \times (N_{\mathrm{PV}} - \langle N_{\mathrm{PV}} \rangle), \quad E_{\mathrm{calib}} = \frac{E_{\mathrm{corr}}}{R(E_{\mathrm{corr}}, |\eta|, n_{\mathrm{prong}})}, \tag{5.12}$$

where A is a correction factor with regard to pile-up effects which is shown in Figure 5.25 (a), R is a response function, E_{LC} is the visible-τ energy with the LC scale. The pile-up correction factor A

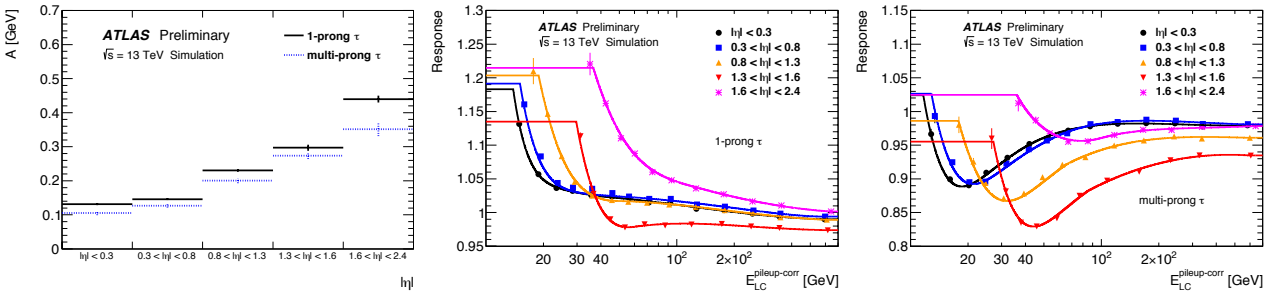

(a) Pile-up correction factor **(b)** Response, 1-prong **(c)** Response, 3-prong

Figure 5.25: Pile-up correction factor (a) as a function of visible-τ pseudorapidity and number of reconstructed tracks and detector response R as a function of the visible-τ energy with the pile-up correction for 1-prong (b) and multi-prong (c) decay mode (taken from Reference [171]).

corresponds to the average contribution per vertex to the visible-τ energy. The average number of primary vertex is calculated as $\langle N_{\mathrm{PV}} \rangle \sim 14$ in MC simulation. The response R is obtained from the Gaussian mean of the $E_{\mathrm{corr}}/E_{\mathrm{true}}$ distribution depending $|\eta|$ and n-prong.

The resolution of the visible-τ objects is derived as the Gaussian width of the $E_{\mathrm{calib}}/E_{\mathrm{true}}$ distribution. The resolution is estimated in several $|\eta|$ and n-prong as shown in Figure 5.26 which follows a usual parameterization :

$$\frac{\sigma_E}{E} = \frac{a}{\sqrt{E}} \oplus \frac{b}{E} \oplus c, \tag{5.13}$$

where a, b and c are the sampling, noise and constant term respectively. The systematic uncertainty of the tau energy scale (TES) are evaluated from the simulation using the alternative MC samples.

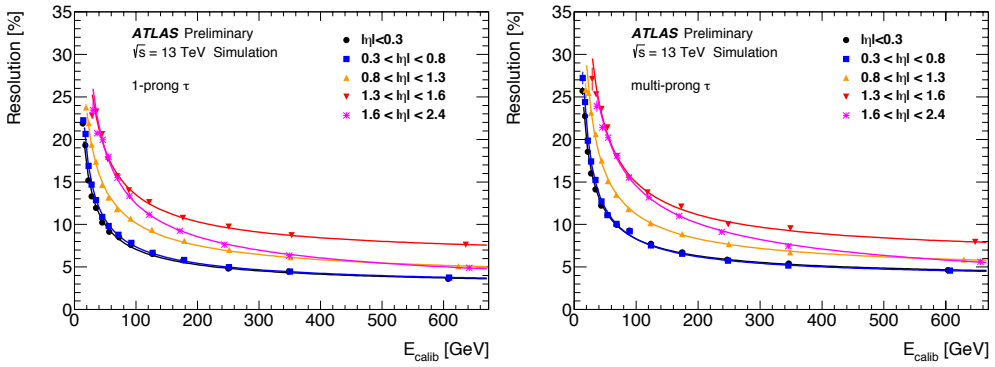

(a) Resolution, 1-prong **(b)** Resolution, 3-prong

Figure 5.26: Resolution on the visible-τ energy after calibration for reconstructed 1-prong (a) and 3-prong (b) modes. Each curve are fitted by parameterization from Equation (5.13) (taken from Reference [171]).

Individual sources of systematic uncertainties are shown in Figure 5.27, which are summarised in below:

- **Pile-up** : defined as difference between default simulated samples and alternative samples with different pile-up parameterization. Several checks of the out-of-time pile-up effects are performed and obtained its effects less than 1%. In addition to the out-of-time pile-up, the residual dependence with respect to the in-time pile-up is also taken into account to this uncertainty.
- **Underlying** : different tuning of the underlying event is checked, and its impact is negligible.
- **Material** : the amount of materials in front of the calorimeter is varied, and its difference is taken into account.
- **Physics list** : alternative `Geant4` hadronic shower model is used to estimate uncertainty on the response function. Different shower model can affect the clustering of the energetic cells into topo-clusters. The topo-cluster calibration is affected in this variation.
- **Threshold** : The noise suppression threshold variations estimates a modelling of response in the calorimeter calibration.
- **Closure** : The shift in the Gaussian mean of $E_{\text{corr}}/E_{\text{true}}$ distribution using the alternative samples from the nominal samples. Corresponding to deviations from unity of that same Gaussian mean. this is taken into account for the closure uncertainty.
- **Single-particle response** : This is the largest uncertainty, In the Run1, the *particle deconvolution method* [172] was used to estimate single-pion response measurement in low-μ data-taking and test beam data. This method is not yet used for this analysis. The other MC-based response uncertainties covers the components entering the single-particle response uncertainty, As the detector has not dramatically changed since the Run1, so that this uncertainty has been included as an additional systematic uncertainty inflated by a safety factor of 2.

The total uncertainty is obtained by symmetrizing each systematic uncertainty and summing up them in quadrature. Uncertainties vary in the 2-6% range depending on visible-τ p_{T} and $|\eta|$. The single-particle response is always important component, Additional contribution from the calorimeter calibration becomes relevant at low-p_{T}. The `Geant4` shower model contribution is also significant in the central region.

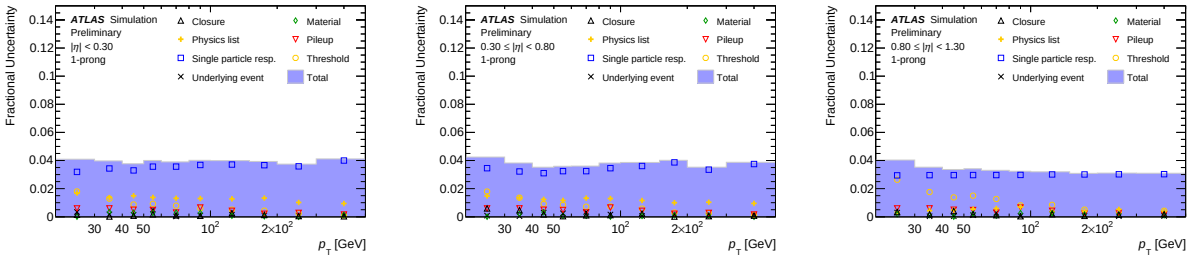

(a) 1-prong, $|\eta| < 0.3$ **(b)** 1-prong, $0.3 < |\eta| < 0.8$ **(c)** 1-prong, $0.8 < |\eta| < 1.3$

(d) 1-prong, $1.3 < |\eta| < 1.6$ **(e)** 1-prong, $1.6 < |\eta| < 2.4$

(f) 3-prong, $|\eta| < 0.3$ **(g)** 3-prong, $0.3 < |\eta| < 0.8$ **(h)** 3-prong, $0.8 < |\eta| < 1.3$

(i) 3-prong, $1.3 < |\eta| < 1.6$ **(j)** 3-prong, $1.6 < |\eta| < 2.4$

Figure 5.27: Systematic uncertainties on the visible-τ energy after calibration for 1- and 3-prong tau decays. The individual uncertainties as well as their quadratic sum are shown as a function of the visible-τ p_{T} for five different η binning (taken from Reference [171]).

5.6.3 Hadronic-τ Identification

An additional τ identification algorithm is introduced to suppress mis-identified jet (or electron) objects. Rejection against jets is provided by a multivariate technique using the track and topo-cluster information found in the core and isolation region around the visible-τ candidate. Rejection against electrons is constructed using the electron LH discriminant as shown in Section 5.4.3.

Identification for jets separation

The identification to discriminate hadronic jets from the visible-τ candidates is performed by the Boosted Decision Trees (BDT) [173]. The BDT is trained separately for the 1-prong and 3-prong visible-τ objects using $Z/\gamma^* \to \tau\tau$ as a signal and di-jet events as a background. The BDT input variables are different for the 1-prong and 3-prong as shown in Table 5.3. Definitions of each variable

variable	f_{cent}	$f^{-1}_{\text{lead trk}}$	$f^{\text{trk}}_{\text{iso}}$	$f^{\text{trk-HAD}}_{\text{EM}}$	$f^{\text{EM}}_{\text{trk}}$	$p_{\text{T}}^{\text{EM+trk}}/p_{\text{T}}$
1-prong	✓	✓	✓	✓	✓	✓
3-prong	✓	✓	✗	✓	✓	✓
variable	$R^{0.2}_{\text{trk}}$	ΔR_{max}	$\lvert S_{\text{lead trk}}\rvert$	$S^{\text{flight}}_{\text{T}}$	m_{trk}	$m_{\text{EM+trk}}$
1-prong	✓	✗	✓	✗	✗	✓
3-prong	✓	✓	✗	✓	✓	✓

Table 5.3: Discriminating variables used as input in the tau BDT identification for 1-prong and 3-prong respectively.

is listed below and detailed distributions can be found in Reference [174]:

- **Central energy fraction (f_{cent})** : Fraction of the calorimeter transverse energy deposit in the region of $\Delta R < 0.1$ with respect to all energy in the region of $\Delta R < 0.2$ around the visible-τ candidate. Energy deposit is calculated by summing up the energies of topo-clusters calibrated in the EM-scale.

- **Leading track momentum fraction ($f^{-1}_{\text{lead trk}}$)** : Fraction between the transverse energy of the EM-scale topo-cluster in the core region and the transverse momentum of the highest-p_{T} charged particle in the core region.

- **Fraction of tracks p_{T} in the isolation region ($f^{\text{trk}}_{\text{iso}}$)** : Scalar sum of the track p_{T} associated with the visible-τ candidate in the isolation region divided by scalar sum of all tracks p_{T} associated with the visible-τ candidate.

- **Fraction of EM energy from charged pions ($f^{\text{trk-HAD}}_{\text{EM}}$)** : Fraction of energy deposit in the EM calorimeter to charged tracks in the core region. The denominator is the sum of the topo-cluster energy in the EM calorimeter associated to the visible-τ candidate. The numerator is difference between the sum of the track momentum in the core region, and the sum of topo-cluster energies in the hadronic calorimeter. All topo-clusters are calibrated in the LC-scale.

- **Ratio of EM energy to track momentum ($f^{\text{EM}}_{\text{trk}}$)** : Fraction of the sum of energy in the EM calorimeter part of topo-cluster associated with the candidate and the sum of the track momentum in the core region. All topo-cluster are calibrated at the LC-scale.

- **Ratio of track+EM-system to p_{T} ($p_{\text{T}}^{\text{EM+trk}}/p_{\text{T}}$)** : Ratio of the visible-τ p_{T} estimated by the vector sum of track momentum and two highest energetic EM clusters in the core region to the calorimeter measured visible-τ p_{T}.

- **Track radius ($R^{0.2}_{\text{trk}}$)** : p_{T} weighted track ΔR associated in the core region to the τ direction.

- **Maximum ΔR (ΔR_{max})** : The maximum ΔR between the track associated with the visible-τ candidate in the core region and the visible-τ object direction.

- **Leading track IP significance ($|S_{\text{lead trk}}|$)** : Absolute value of the transverse impact parameter of the highest-p_{T} track in the core region with respect to the TV divided by its uncertainty.
- **Transverse flight path significance ($S_{\text{T}}^{\text{flight}}$)** : The transverse decay length of the secondary vertex reconstructed from the tracks associated with the core region with respect to the TV divided by its uncertainty
- **Track mass (m_{trk})** : Invariant mass calculated from the vectorial sum of the all track four-momentum in the core and isolation regions, assuming each track is pion (mass of tracks are assumed $m_{\pi^{\pm}}$).
- **Track+EM-system mass ($m_{\text{EM+trk}}$)** : Invariant mass of the tracks and two highest energetic EM clusters in the core region, The mass of topo-cluster is set to zero and topo-cluster seed direction is used as the four-momentum.

To ensure the pile-up robustness, a correction is applied to each input variable, which depends linearly on the average number of interaction per bunch crossing ($\langle\mu\rangle$) calculating from the instantaneous luminosity. The usage of $\langle\mu\rangle$ instead of the number of reconstructed primary vertices gives compatibility with the HLT-tau trigger, which cannot use the primary vertex. The BDT score distri-

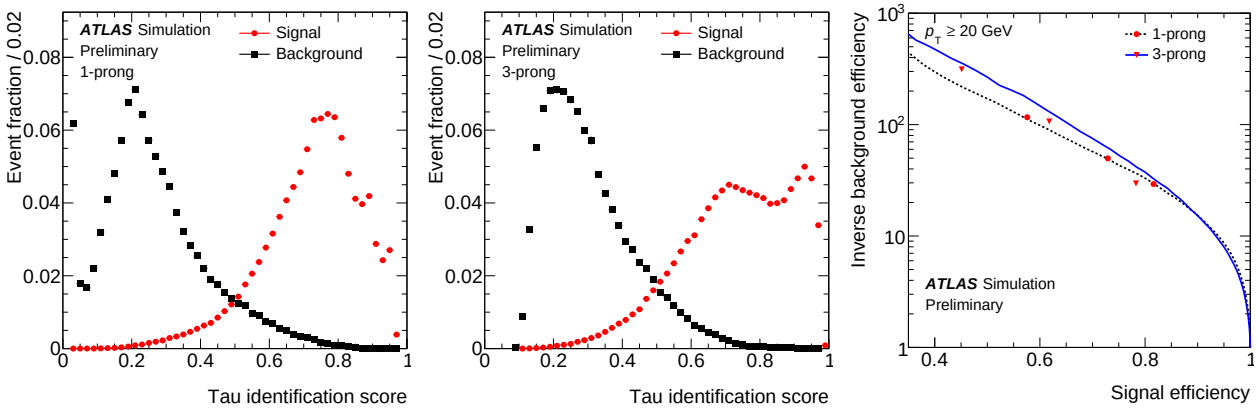

(a) 1-prong **(b)** 3-prong **(c)** Rejection power

Figure 5.28: BDT score distribution for visible-τ candidate for 1-prong (a) and 3-prong (b) with signal (red circles) and background (black squares). Inverse of the efficiency for mis-identified hadronic jets as a function of thee identification efficiency for true visible-τ candidates (c). Two lines refer to 1-prong and 3-prong respectively. Each point(circles and triangles) present three working point (Loose, Medium, Tight) (taken from Reference [174]).

bution of the signal and background is shown in Figure 5.28 for 1-prong (a) and 3-prong (b) modes. Three working points, *Loose, Medium* and *Tight* are defined. The threshold of each working point depends on the visible-τ p_{T} to achieve a constant efficiency. Simplified cut values are about 0.675, 0.725 and 0.75 for the 1-prong loose, medium and tight working points, corresponding the 3-prong loose, medium and tight are about 0.75, 0.8 and 0.85. The dependence of the combined reconstruction and identification efficiency as a function of p_{T} and $\langle\mu\rangle$ is significantly reduced as shown in Figure 5.29 after the tuning of the p_{T}-dependent cut values and the pile-up corrections. The identification scale factor is set to equal 1 with MC-based systematic uncertainty [171]. Due to a lack of data statistics, the scale factor for the τ-ID is not evaluated. The scale factor obtained in the Run1 is applied with additional systematic uncertainties in this analysis. The medium working point is used. Its combined reconstruction and identification efficiency is about 55% for 1-prong and 39% for 3-prong modes.

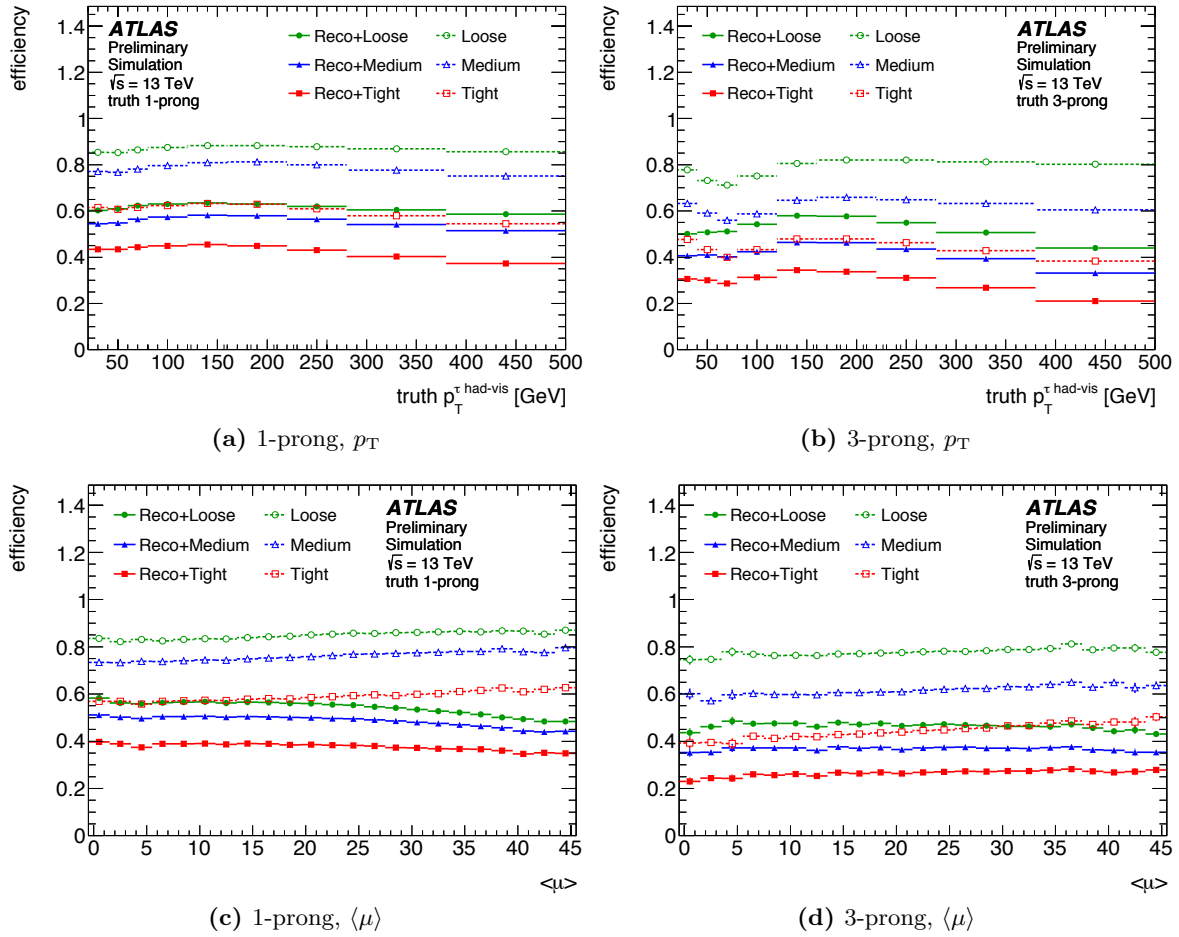

(a) 1-prong, p_{T} **(b)** 3-prong, p_{T}

(c) 1-prong, $\langle\mu\rangle$ **(d)** 3-prong, $\langle\mu\rangle$

Figure 5.29: Efficiency for the visible-τ identification (open symbols) and combined reconstruction and identification efficiency (filled symbols) as a function of the visible-τ and the average number of interaction per bunch crossing for 1-prong (a,c) and 3-prong (b,d) (taken from Reference [174]).

Difference between the 1-prong and 3-prong arise from track reconstruction. Systematic uncertainties on the identification efficiency are evaluated using alternative simulated samples with different configurations as discussed in Section 5.6.1. The result for the medium working point are shown in Figure 5.30 for the 1-prong and 3-prong with different $|\eta|$ bins. The calorimeter calibration and performance uncertainty is the highest contribution at $p_{\mathrm{T}} < 100$ GeV, which is variation in shapes of calorimeter-based and tracking-based input variables. It has up to 16% for the 3-prong decay in central region. At higher-p_{T}, the pile-up uncertainty is dominant due to the impact parameter resolution can change the $|S_{leaddaggerrk}|$ distribution. This uncertainty is one of dominant source of uncertainties on signal strength in this analysis as discussed in Chapter 7.

Identification for electrons separation (e-veto)

To suppress electron background, it is useful to use same discriminant as used in the electron identification discussed in Section 5.4.3. The electron likelihood (electron LH) is constructed by shower shape information from the calorimeter and track information from the inner detectors. In terms of separation between electrons and charged pions, TRT plays an important role, which can measure two operating points for optimising electron and charged pion detection using ionisation threshold information. The electron-veto procedure is simple compared to the jet-discriminant. First it finds the electron objects around the visible-τ objects with $\Delta R < 0.4$, here electron objects should

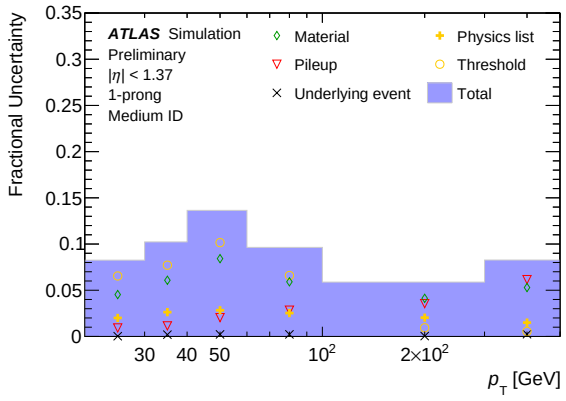

(a) 1-prong, $|\eta| < 1.52$

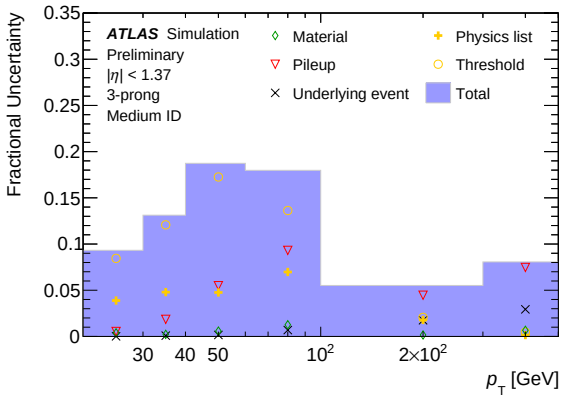

(b) 3-prong, $|\eta| < 1.52$

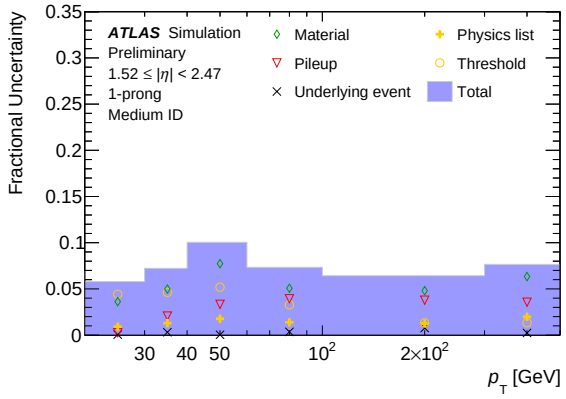

(c) 1-prong, $|\eta| > 1.52$

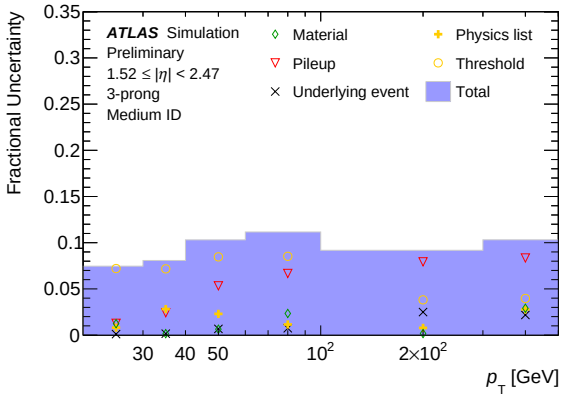

(d) 3-prong, $|\eta| > 1.52$

Figure 5.30: Relative uncertainties on the identification efficiency for the medium working point as a function of the visible-τ p_{T} for 1-prong (a,c) and 3-prong (b,d) in the central $|\eta| < 1.52$ region and forward region $|\eta| > 1.52$ (taken from Reference [174]).

satisfy loose identification criteria and $p_{\mathrm{T}} > 5$ GeV. If it is found, the visible-τ objects are vetoed. If there are no such electrons, it finds the electron candidate is required by $p_{\mathrm{T}} > 5$ GeV and failing the loose identification. If electron candidate is found, the electron LH score is examined. This electron faking the visible-τ objects, called "$e \to \tau$ fake", rises from $Z/\gamma^* \to ee$ process in the di-τ final state analysis. Figure 5.31 (a) shows the electron LH score distribution for the signal and background. The default working point for the e-veto is set to achieve the signal efficiency is 95%, the background rejection capability are shown in Figure 5.31 (b) for several different pseudorapidity regions. The scale factor of the e-veto identification for electrons is measured as shown in Figure 5.31 (c). The scale factors are measured using $Z/\gamma^* \to ee$ tag-&-probe method with 3.2 fb^{-1} 2015 data. The systematic uncertinty is obtained by evaluating the τ-ID and electron ID systematic uncertinties. In addition to them, additional systematic uncertinty corresponding the electron and tau energy scale. In the most forward bin ($|\eta| \sim 2.45$), there are no TRT detector, so the electron LH consists of different shower shape information. This leads significant mis-modelling as shown in Figure 5.31 (c). Therefore in this thesis, the visible-τ objects are selected by $|\eta| < 2.3$. The scale factors of the e-veto identification for true hadronic-τ objects is not yet measured due to a lack of data statistics.

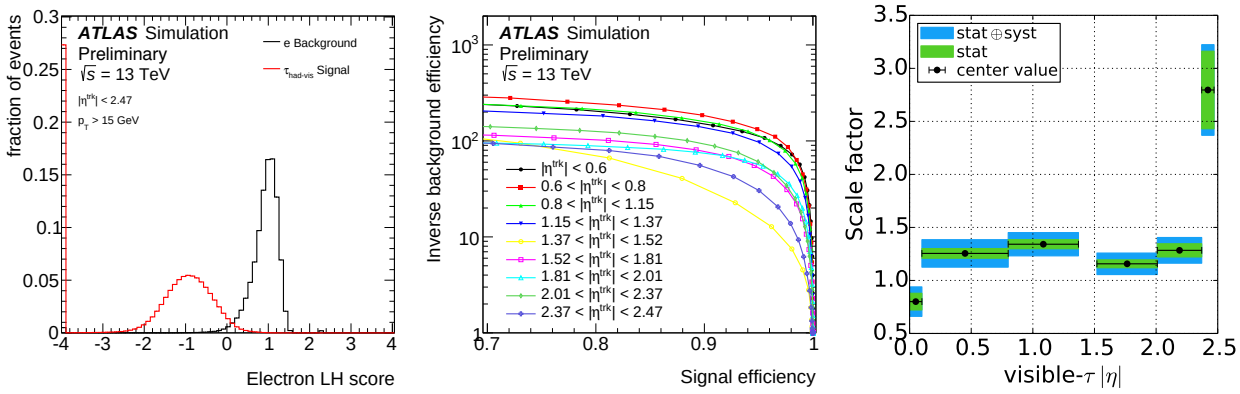

(a) Electron LH score **(b)** Inverse background efficiency **(c)** Scale factor

Figure 5.31: Electron likelihood score distribution for the visible-τ and electron candidate from signal ($Z/\gamma^* \to \tau\tau$) and background ($Z/\gamma^* \to ee$). (v) : Inverse background efficiency as a function of the signal efficiency for different $|\eta|$ region (taken from Reference [174]). Events with score equal to -4 has no electron candidates within $\Delta R < 0.4$. (c) : Scale factors for the e-veto identification selection of true electrons using $Z/\gamma^* \to ee$ tag-&-probe method. Black circles show center values, green (blue) region shows statistical (systematic) uncertainties for this measurements.

5.7 Missing Transverse Energy ($E_{\mathrm{T}}^{\mathrm{miss}}$)

Tau leptons decaying into leptons (e, μ) or hadrons and at least one neutrino. In order to reconstruct $H/A \to \tau\tau$ event topology, reconstruction of such neutrinos is essential and crucial. Neutrino cannot be detected at the ATLAS detector, so that additional assumption is necessary to obtain neutrino momentum. Since the LHC is proton-proton collider, initial parton momentum always changes and conservation of momentum is validated only transverse plane to the beam axis. The missing transverse momentum ($E_{\mathrm{T}}^{\mathrm{miss}}$) is be measured as an imbalance in the sum of visible transverse momentum. It is important to reconstruct efficiently hard objects which come from the primary vertex. Due to extremely high pile-up condition of the LHC, dedicated algorithm is applied to catch up hard objects only from such interaction point. In addition to hard objects, there are soft particles which cannot be reconstructed as any physics objects, for example underlying activity with lower-p_{T} than the threshold of the hadronic jet reconstruction. This should be taken into account as a "soft term". The soft term is one of the difficult objects to correctly obtain, due to mis-identification of the pile-up activity. A detailed reconstruction procedure of the $E_{\mathrm{T}}^{\mathrm{miss}}$ is given based on Reference [175] in Section 5.7.1. The $E_{\mathrm{T}}^{\mathrm{miss}}$ reconstruction performance and its systematic uncertainty is described in Section 5.7.2. A trigger related to the $E_{\mathrm{T}}^{\mathrm{miss}}$ is briefly described in Section 5.7.3.

5.7.1 $E_{\mathrm{T}}^{\mathrm{miss}}$ Reconstruction

The $E_{\mathrm{T}}^{\mathrm{miss}}$ is calculated by the calibrated and reconstructed objects. The input objects consists of charged leptons, photons, visible-τ and hadronic jets. In addition to these physics objects, the soft

term is also calculated by the tracks not associated with any physics objects.

$$E_{x,y}^{\mathrm{miss}} = E_{x,y}^{\mathrm{miss,e}} + E_{x,y}^{\mathrm{miss},\gamma} + E_{x,y}^{\mathrm{miss},\tau} + E_{x,y}^{\mathrm{miss},\mu} + E_{x,y}^{\mathrm{miss,jet}} + E_{x,y}^{\mathrm{miss,soft}}, \tag{5.14}$$

$$E_{\mathrm{T}}^{\mathrm{miss}} = \sqrt{(E_x^{\mathrm{miss}})^2 + \left(E_y^{\mathrm{miss}}\right)^2}, \tag{5.15}$$

$$\phi^{\mathrm{miss}} = \arctan(E_y^{\mathrm{miss}}/E_x^{\mathrm{miss}}), \tag{5.16}$$

$$\sum E_{\mathrm{T}} = \sum p_{\mathrm{T}}^{e} + \sum p_{\mathrm{T}}^{\gamma} + \sum p_{\mathrm{T}}^{\tau} + \sum p_{\mathrm{T}}^{\mu} + \sum p_{\mathrm{T}}^{\mathrm{jet}} + \sum p_{\mathrm{T}}^{\mathrm{soft}}, \tag{5.17}$$

The term for jets, electrons (e), muons (μ), visible-τs (τ) and photons (γ) are the negative vectorial sum of the momentum. The $\sum E_{\mathrm{T}}$ is the scalar sum of transverse momentum of all input objects. The reconstruction procedure is so-called as *Track Soft Term (TST)* [175][11]. In addition to the default (tight) track selection as shown in Section 5.1, several selections are applied to ensure track-to-vertex association. Tracks must satisfy the transverse and longitudinal impact parameters of $d_0 < 2$mm and $z_0 \sin\theta < 3$mm with respect to the primary vertex. The primary vertex is selected by the vertex which has the largest value of $\sum p_{\mathrm{T}}^2$, where scalar sum run over all tracks associated with that vertex.

Before summing up all hard objects and the soft term, geometrical overlap between hard objects should be solved (*overlap removal(OLR)*). Selection using the geometrical distance of $\Delta R(i,j)$ for object i and j is performed. Starting from muons, all hard objects (obj $= e, \gamma, \tau$ and jets) are removed if $\Delta R(\mu, \mathrm{obj}) < 0.2$. Then same OLR are performed with order of $e \to \gamma \to \tau$ with $\Delta R = 0.1, 0.2, 0.2$. For jets and tracks special treatment is applied, because partial internal overlaps can happen with clusters and tracks between jets and others. The JVT selection is applied for jets to ensure production from hard collision. If the calibrated jet p_{T} is greater than 20 GeV and a unique fraction[12] is greater than 0.5, the jet is added to a list of $E_{x,y}^{\mathrm{miss,jet}}$. Otherwise, jets are treated as the soft term with track momentum. Before constructing the soft term, the OLR and a cleaning process is applied to all track candidates which described following:

- Tracks within $\Delta R < 0.05$ are removed between tracks and electron/photon cluster.
- Tracks within $\Delta R < 0.2$ are removed between tracks and visible-τ.
- Tracks associated with jets using the ghost-association technique are removed.
- Tracks associated to combined or segment-tagged muons are replaced with the combined ID+MS tracks.
- high-p_{T} (($p_{\mathrm{T}} > 200$ GeV and $|\eta| < 1.5$) or ($p_{\mathrm{T}} > 120$ GeV and $|\eta| > 1.5$)) non-isolated ($p_{\mathrm{T}}^{\mathrm{cone\ 0.2}}/p_{\mathrm{T}} > 0.1$) tracks are removed if satisfy following:

$$\frac{E_{\mathrm{T}}^{\mathrm{cone\ 0.2}}}{p_{\mathrm{T}} + p_{\mathrm{T}}^{\mathrm{cone\ 0.2}}} < 0.6, \quad \text{and} \quad \frac{p_{\mathrm{T}}^{\mathrm{cone\ 0.2}}}{p_{\mathrm{T}} + p_{\mathrm{T}}^{\mathrm{cone\ 0.2}}} > 0.6. \tag{5.18}$$

- Tracks has its track momentum uncertainties larger than 40% are removed.

Association to the primary vertex is relatively sensitive to pile-up effects.

[11] There is another procedure using calorimeter clusters as input of the soft term, *Cluster Soft Term (CST)*. Track $E_{\mathrm{T}}^{\mathrm{miss}}$ consist of only tracks without any hard objects The resolution of CST and Track $E_{\mathrm{T}}^{\mathrm{miss}}$ is even worse than the TST's.

[12] Fraction of jet energy between calorimeter measured scale and constituents scale.

5.7.2 $E_{\mathrm{T}}^{\mathrm{miss}}$ Performance and Uncertainty

Since $Z \to \mu\mu$ events have small background and muon can be precisely measured, $Z \to \mu\mu$ events provide an ideal final state to evaluate of $E_{\mathrm{T}}^{\mathrm{miss}}$ performance. In $Z \to \mu\mu$ events neutrinos are produced only by heavy-flavour meson decay, so it can be negligible. In addition to $Z \to \mu\mu$ events, $W \to \mu\nu$ events is a good candidate to measure the $E_{\mathrm{T}}^{\mathrm{miss}}$ from one true neutrino. Performance and resolution measurement by $Z \to \mu\mu$ and $W \to \mu\nu$ events is evaluated in and details can be found in Reference [175, 176]. Only results and its uncertainties are given based on these Reference in this thesis. In terms of the $E_{\mathrm{T}}^{\mathrm{miss}}$ performance, the $E_{\mathrm{T}}^{\mathrm{miss}}$ response, linearity and resolution are usually considered. The $E_{\mathrm{T}}^{\mathrm{miss}}$ response is defined as a projection to the axis of the p_{T} of the Z boson. It is sensitive to balance between leptons and the soft hadronic recoil. Definition of the $E_{\mathrm{T}}^{\mathrm{miss}}$ response R and linearity L are defined by following :

$$R = \left\langle \vec{E}_{\mathrm{T}}^{\mathrm{miss}} \cdot \frac{\vec{p_{\mathrm{T}}}^{\ell^+} + \vec{p_{\mathrm{T}}}^{\ell^-}}{p_{\mathrm{T}}^{\ell^+} + p_{\mathrm{T}}^{\ell^-}} \right\rangle, \tag{5.19}$$

$$L = \left\langle \frac{E_{\mathrm{T}}^{\mathrm{miss}} - E_{\mathrm{T}}^{\mathrm{miss,true}}}{E_{\mathrm{T}}^{\mathrm{miss,true}}} \right\rangle \tag{5.20}$$

where $\vec{p_{\mathrm{T}}}^{\ell^\pm}$ are the transverse momentum of leptons from the Z boson decay. Figure 5.32 shows the $E_{\mathrm{T}}^{\mathrm{miss}}$ response, linearity and resolution. For the $E_{\mathrm{T}}^{\mathrm{miss}}$ response, perfect balance of leptons against

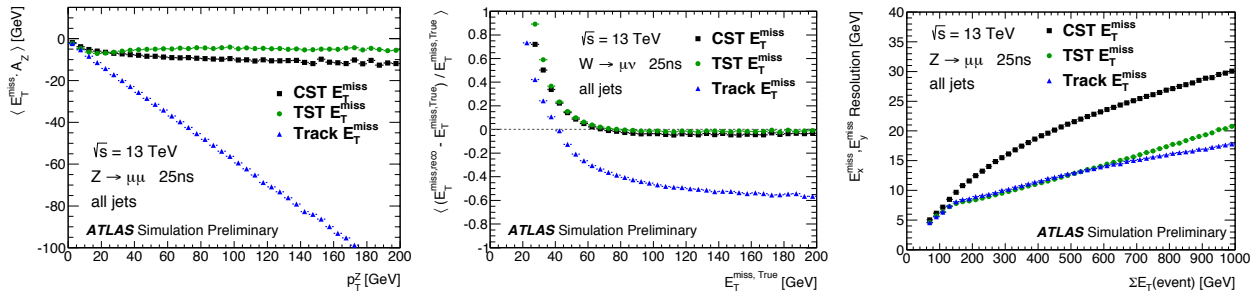

(a) $E_{\mathrm{T}}^{\mathrm{miss}}$ response **(b)** $E_{\mathrm{T}}^{\mathrm{miss}}$ linearity **(c)** $E_{\mathrm{T}}^{\mathrm{miss}}$ resolution

Figure 5.32: Performance of the $E_{\mathrm{T}}^{\mathrm{miss}}$ reconstruction using $Z \to \mu\mu$ (a,c) and $W \to \mu\nu$ (b) simulated samples. Plots includes results of three $E_{\mathrm{T}}^{\mathrm{miss}}$ reconstruction algorithm, in this thesis only TST (green circle) is used. (a) : the $E_{\mathrm{T}}^{\mathrm{miss}}$ response R as a function of the transverse momentum of the Z boson. (b) : the $E_{\mathrm{T}}^{\mathrm{miss}}$ linearity L as a function of the true $E_{\mathrm{T}}^{\mathrm{miss}}$ from $W \to \mu\nu$decay. (c) : the $E_{\mathrm{T}}^{\mathrm{miss}}$ resolution as a function of the sum E_{T} (taken from Reference [176]).

the soft recoil $R = 0$ would expected. A good response are shown in Figure 5.32 (a) for the $E_{\mathrm{T}}^{\mathrm{miss}}$ TST. The $E_{\mathrm{T}}^{\mathrm{miss}}$ linearity is almost flat above $E_{\mathrm{T}}^{\mathrm{miss,true}} \gtrsim 60$ GeV for the $E_{\mathrm{T}}^{\mathrm{miss}}$ TST as shown in Figure 5.32 (b). The $E_{\mathrm{T}}^{\mathrm{miss}}$ resolution as shown in (c) is typically 10 GeV at $\sum E_{\mathrm{T}} \sim 400$ GeV and 15 GeV at $\sum E_{\mathrm{T}} \sim 650$ GeV. An comparison between data and MC simulation is also shown in Figure 5.33. A good agreement is obtained for both the $E_{\mathrm{T}}^{\mathrm{miss}}$ response and resolution.

For uncertainties related to the $E_{\mathrm{T}}^{\mathrm{miss}}$ reconstruction, only the soft term is taken into account. Because other hard objects can handle via each reconstruction, identification or energy calibration procedures. To derive the soft term systematic uncertainties, $\vec{p_{\mathrm{T}}}^{\mathrm{hard}}$ is defined as the vector sum of the transverse momenta of the hard objects in the event. As the track soft term systematic uncertainty, difference between different simulated samples are taken into account (details for MC generators is described in Reference [176]). Systematic uncertainties are calculated by projecting the soft term components onto the transverse and longitudinal of the $\vec{p_{\mathrm{T}}}^{\mathrm{hard}}$. The soft term scale longitudinal to

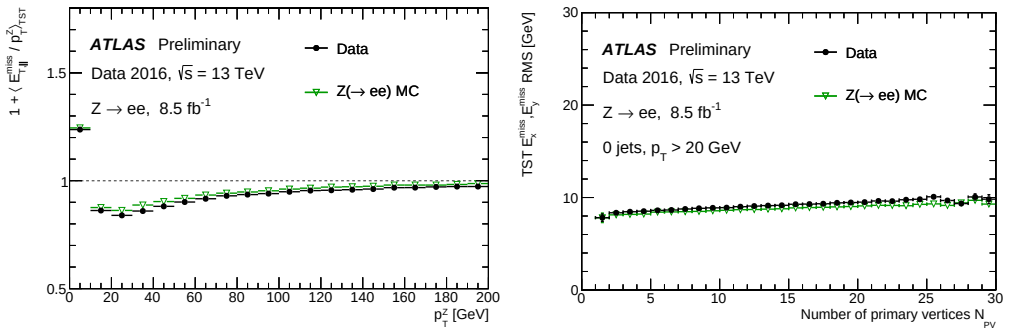

(a) $E_{\mathrm{T}}^{\mathrm{miss}}$ response **(b)** $E_{\mathrm{T}}^{\mathrm{miss}}$ resolution

Figure 5.33: $E_{\mathrm{T}}^{\mathrm{miss}}$ response and resolution using $Z \to ee$ events of simulated and experimental data. Black (green) circles show data and $Z \to ee$ simulation respectively (taken from Reference [177]).

$\vec{p_{\mathrm{T}}}^{\mathrm{hard}}$ is sensitive to the modelling of the hadronic recoil. The one σ of the systematic uncertainty is obtained from the variation between nominal MC samples and two alternative samples with checking a Kolmogorov-Smirnov test to avoid statistical fluctuations. An additional uncertainty is assigned if there is 5% or smaller probability of a KS-test. In addition to this generator difference systematic uncertainty, an alternative simulation with different detector material budget condition are evaluated. Total systematic uncertainty is shown in Figure 5.33. As shown in plot, relatively larger uncertainty

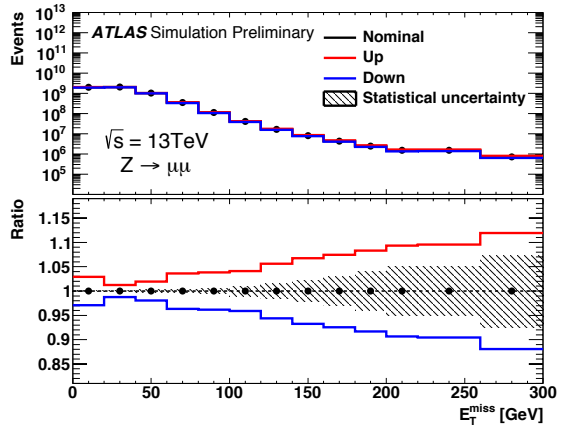

Figure 5.34: Total $E_{\mathrm{T}}^{\mathrm{miss}}$ systematic uncertainty as a function of the reconstructed $E_{\mathrm{T}}^{\mathrm{miss}}$ magnitude (take from Reference [177]). In the ratio, the hatched band shows the statistical uncertainty, red (blue) lines shows $+1\sigma$ (-1σ) variation of the systematic uncertainty including the statistical uncertainty.

is expected for higher-$E_{\mathrm{T}}^{\mathrm{miss}}$ events, typically $\pm 10\%$ at $E_{\mathrm{T}}^{\mathrm{miss}} \sim 250$ GeV.

5.7.3 $E_{\mathrm{T}}^{\mathrm{miss}}$ Trigger

Since the single-lepton-trigger efficiency is not perfect, the $E_{\mathrm{T}}^{\mathrm{miss}}$ trigger is good item to include in the search for heavy Higgs bosons. The $\tau_\ell\tau_{\mathrm{had}}$ channel has larger $E_{\mathrm{T}}^{\mathrm{miss}}$ compared with other two channels. Events with large $E_{\mathrm{T}}^{\mathrm{miss}}$ is interesting because the most of background processes doesn't have such large $E_{\mathrm{T}}^{\mathrm{miss}}$. The $E_{\mathrm{T}}^{\mathrm{miss}}$ trigger is introduced for the first time in this analysis.

As described in Section 4.2.6, the ATLAS trigger is two steps pipe-line system. At the L1, the $E_{\mathrm{T}}^{\mathrm{miss}}$ is roughly reconstructed by the L1 calorimeter RoIs, so-called *L1XE*. The level 1 trigger is hardware-based trigger which cannot precisely measure energy or transverse momentum[13]. The level 1 muon trigger processor is separated from other L1 trigger processors, so that in the L1XE calculation muons are not taken into account. These feature leads that L1XE trigger resolution become coarse, typically $\sim 30 - 40$ GeV.

[13] The L1EM has only 0.5 GeV step at hardware level, L1Calo is coarser than the L1EM.

After L1XE decision, the HLT $E_{\mathrm{T}}^{\mathrm{miss}}$ trigger (so-called `HLT_xe`) is evaluated using offline-like algorithm. The vertex reconstruction cannot be performed during the HLT processing. So the same soft-term cannot be obtained, this leads that the pile-up effect becomes crucial to the HLT $E_{\mathrm{T}}^{\mathrm{miss}}$ trigger. To suppress the pile-up effects, there are several algorithm related to how to calculate the soft term components [178]. Three algorithm are used in this analysis described in following:

- **Cell-based algorithm (`xe`)** : In each LAr and Tile calorimeter cell, contributions are calculated by the sum of each cell $p_{x,y}^{i} = E_i \cos\theta_i \sin\phi_i, E_i \cos\theta_i \sin\phi_i$. To suppress noise, the cells with energy $|E_i| > 2\sigma_i$ and $E_i > -5\sigma_i$ are considered, where σ_i is the noise threshold significance. $E_{\mathrm{T}}^{\mathrm{miss}}$ is calculated by taking the negative vector sum of all active cells.

- **Jet-based algorithm (`xe_tc_mht`)** : $E_{\mathrm{T}}^{\mathrm{miss}}$ is calculated directly from the negative vector sum of the transverse momentum from all jets reconstructed by the jet trigger algorithm, which have been applied correction for the pile-up contribution as shown in Section 5.3, but the JVT selection is not applied.

- **Topo-cluster-based algorithm (`xe_tc_lcw`)** : $E_{\mathrm{T}}^{\mathrm{miss}}$ is calculated from topo-clusters calibrated with the LC-scale of the entire calorimeter. Each topo-cluster is calculated with massless particle assumption. The $E_{\mathrm{T}}^{\mathrm{miss}}$ is reconstructed from the negative vector sum of topo-clusters.

The $E_{\mathrm{T}}^{\mathrm{miss}}$ trigger is sensitive to the instantaneous luminosity. The $E_{\mathrm{T}}^{\mathrm{miss}}$ trigger threshold was changed many times during data-taking period. Table 5.4 summarised the $E_{\mathrm{T}}^{\mathrm{miss}}$ trigger items used in this analysis. During 2015 data-taking threshold and algorithm has not been changed. While

Period	peak lumi.	integrated lumi.	trigger items
2015 All	$0.50 \times 10^{34}\,\mathrm{cm}^{-2}\,\mathrm{s}^{-1}$	3193.6 pb^{-1}	`xe70` or `xe70_mht` or `xe70_tc_lcw`
2016 A-C	$0.88 \times 10^{34}\,\mathrm{cm}^{-2}\,\mathrm{s}^{-1}$	5380.2 pb^{-1}	`xe80_tc_lcw` or `xe90_mht`
2016 D1-D3	$0.99 \times 10^{34}\,\mathrm{cm}^{-2}\,\mathrm{s}^{-1}$	736.2 pb^{-1}	`xe90_mht`
2016 D4-F1	$1.03 \times 10^{34}\,\mathrm{cm}^{-2}\,\mathrm{s}^{-1}$	6545.3 pb^{-1}	`xe100_mht` or `xe110_mht`
2016 F2-	$1.21 \times 10^{34}\,\mathrm{cm}^{-2}\,\mathrm{s}^{-1}$	12138.0 pb^{-1}	`xe110_mht`

Table 5.4: The $E_{\mathrm{T}}^{\mathrm{miss}}$ trigger items used in this analysis for 2015 and 2016 data-taking.

during 2016 data-taking, the $E_{\mathrm{T}}^{\mathrm{miss}}$ trigger threshold was increased as the peak luminosities increases up. Unexpectedly non-linear trigger rate ascent was observed for the topo-cluster-based algorithm (`xe_tc_lcw`). So from 2016 period D1 this trigger threshold was rose up to 130 GeV. While, jet-based algorithm (`xe_tc_mht`) have kept its trigger threshold. During 2016 period D4-F1, at start of higher luminosity runs `xe100_mht` was pre-scaled[14], so taking OR with `xe110_mht` is required.

The efficiency of the $E_{\mathrm{T}}^{\mathrm{miss}}$ trigger strongly depends on event topology, i.e. the efficiency depends on the source of $E_{\mathrm{T}}^{\mathrm{miss}}$ source, from real $E_{\mathrm{T}}^{\mathrm{miss}}$ (from neutrinos) and fake $E_{\mathrm{T}}^{\mathrm{miss}}$ originated by the pile-up activity. Detailed of measurement are discussed in Section 6.3.

[14] pre-scaled means that trigger is vetoed with certain rate. For example, the pre-scaled is 0.5, 50% of events fired this trigger is recorded.

6 Search for the MSSM Higgs Bosons in the $\tau_\ell\tau_{\text{had}}$ Final State

The search for $H/A \to \tau\tau$ decays in $\tau_\ell\tau_{\text{had}}$ final state is discussed, which is developed, implemented and performed in the course of this thesis. It is based on a mass bump hunting to discriminate the signal from background events. Three event categories are defined, optimised for the gluon-fusion and bottom-annihilation signal production mechanisms. A maximum-likelihood fit to a mass distributions and to additional control regions is performed to estimate the parameter of the combined signal and background model and to extract a measurement of the product of signal cross-section and decay branching fraction. The experimental signature of the signal processes and comparison of the main background processes is introduced in Section 6.1. The analysed data samples, as well as simulated event samples used in this analysis are described in Section 6.2 and 6.3 respectively. The event selection and categorisation is given in Section 6.4. To establish a potential excess of data over the expected SM background, a reliable model of the background processes is necessary. The background modelling is described in Section 6.5 and comparisons between the observed data and background are also given. The systematic uncertainties and their propagation to the final observable is explained in Section 6.6. An important role of the analysis is a construction of the profiled likelihood model. The profiled likelihood fit is used to estimate the number of expected events yields for the signal and background with nuisance parameters. A concept of the profiled likelihood and other statistical analysis is described in Chapter 7.

6.1 Experimental Signature of $H/A \to \tau_\ell\tau_{\text{had}}$ Decays

The experimental signature of $H/A \to \tau\tau$ signal depends on the decays of the τ leptons, as well as on the Higgs boson production mechanism. The $\tau_\ell\tau_{\text{had}}$ channel consists of a single electron or muon, denoted as ℓ, two neutrinos from the leptonic τ decay, and one reconstructed visible-τ object and one neutrino from the hadronically decaying τ-lepton. The lepton and the visible-τ object carry opposite electric charge. Neutrinos, which escape from direct detection, lead to a significant amount of the missing transverse energy which can be used to complement the information from the reconstructed decay products. The event selection criteria discussed in Section 6.4 are constructed based on these final state objects. The kinematic properties of the signal processes as well as dominant background processes are described in the following.

6.1.1 Signal Processes

Figure 6.1 shows the Feynman diagrams of the two main Higgs boson production mechanisms considered in this analysis. The bottom-annihilation process is dominant in terms of the experimental sensitivity as shown in Section 3.2.2. The bottom-annihilation process has two leading order diagram

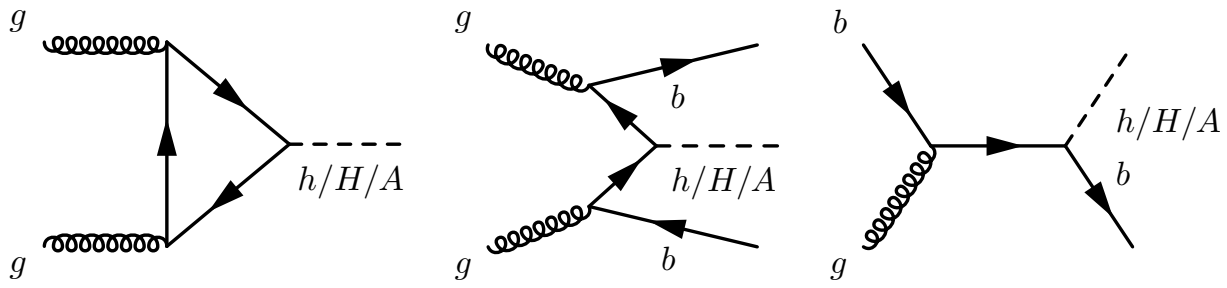

(a) Gluon fusion **(b)** Bottom annihilation (4FS) **(c)** Bottom annihilation (5FS)

Figure 6.1: Feynman diagrams of the three main production diagrams of H/A bosons at the LHC. Only leading diagram is shown for each process.

as shown in Figures 6.1 (b) and (c). There are at least one b-quark in the final state, but the transverse momentum of the b-quark tends to be small. It is difficult to model the transverse momentum of the Higgs bosons, so the analysis does not actively use information related to them. This leads that an event topology of signal becomes back-to-back in terms of two decay products of the heavy Higgs bosons.

Since the di-τ system originates from the intermediate resonant state, the combined four-momentum of all the decay products allows to reconstruct information about the Higgs boson four-momentum. A crucial property of the di-τ system is the invariant di-τ mass $m_{\tau\tau}$. $Z/\gamma^* \to \tau\tau$ process has similar kinematical properties to the signal process. So the mass difference between Z and Higgs bosons provides a powerful discriminating property these two processes. The event cannot directly reconstructed due to the multiple neutrinos though away. A brief overview of those observable definitions is given in Section 6.1.3.

6.1.2 Dominant Background Processes

Background processes contributing to the final state can be grouped. One is processes with a real hadronically decaying τ-lepton and lepton, Other processes have either a hadronic jet or a lepton is mis-identified as a $\tau_{\text{vis-had}}$ object[1] and mis-identified as a lepton (e, μ)[2]. The estimation of the second group are complicated. Because the τ_{had} mis-identification probability is not well modelled in simulation. The major background with real τ_{had} is $Z/\gamma^* \to \tau\tau$ and $t\bar{t} \to b\bar{b}\tau\tau\nu\bar{\nu}$. $Z/\gamma^* \to \tau\tau$

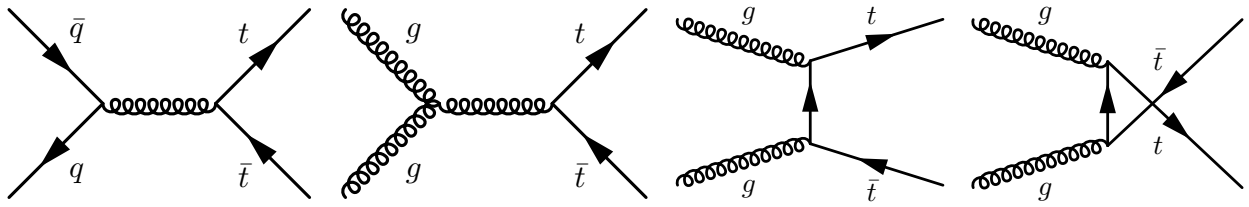

Figure 6.2: Feynman diagrams of $t\bar{t}$ production at the LHC. Only leading diagram is shown.

process is irreducible with the gluon-fusion signal processes in terms of di-τ decay products and hadronic jets production. Figure 6.2 shows the $t\bar{t}$ production diagrams. In the case of $t\bar{t}$ events with di-leptonic decay of two $W^\pm$ bosons, additional two b-quark can be seen. So $t\bar{t} \to b\bar{b}\tau\tau\nu\bar{\nu}$ process has similar final state with the bottom-annihilation signal process in terms of di-τ decay

[1] referred to as "fake τ_{had}"
[2] referred as to "fake lepton".

products and b-quark production. Besides these two background processes, other processes become background. The production cross-sections of such processes is small compared to $Zzero/\gamma^* \to \tau\tau$ and $t\bar{t} \to b\bar{b}\tau\tau\nu\bar{\nu}$ processes. Such background processes are estimated by the MC simulations with data-driven corrections.

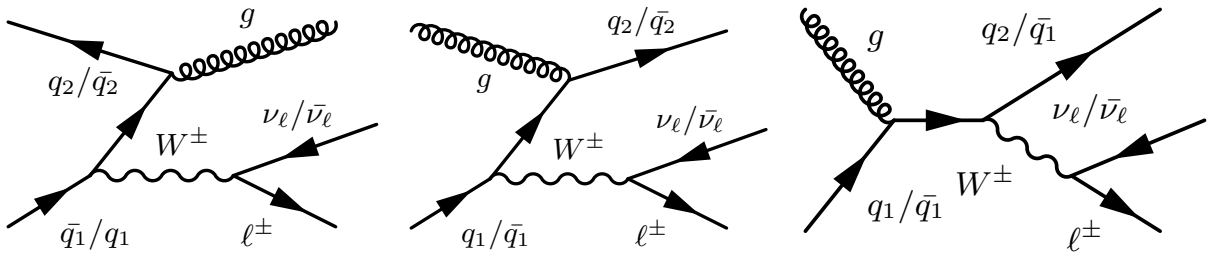

Figure 6.3: Feynman diagrams of W+jets production with one jet at the LHC. Only leading diagram is shown.

Background with mis-identified $\tau_{\rm had}$ objects mainly consists of four physical processes, W+jets, $t\bar{t} \to b\bar{b}\ell$+jets $Z \to \ell\ell$, and the QCD multijets. Origin of mis-identified $\tau_{\rm had}$ objects should be considered. The fake $j \to \tau_{\rm had}$ and $\ell \to \tau_{\rm had}$ objects originate from hadronic jets and leptons respectively. The dominant process of $j \to \tau_{\rm had}$ is W+jets, $t\bar{t}$ and the QCD multijet processes. In addition to the fake hadronic-τ, the QCD process has the fake lepton ($j \to \ell$).

W+jets process has additional hadronic jets which become the fake τ. An origin of additional jets is practically quarks as shown in Figure 6.3. A probability of the $j \to \tau_{\rm had}$ fake is not large, but the production cross-section of W+jets is large enough to observe in this analysis. The other fake τ background comes from the $t\bar{t}$ process is semi-leptonic channel. It has one real lepton from $W^\pm$ decay and the fake τ from mainly quarks. The transverse mass $m_{\rm T}^W$ is useful to distinguish events with or without $W^\pm \to \ell^\pm\nu_\ell$ process:

$$m_{\rm T}^W = \sqrt{2p_{\rm T}^\ell E_{\rm T}^{\rm miss}(1 - \cos\Delta\phi_{\ell,E_{\rm T}^{\rm miss}})}, \tag{6.1}$$

where $p_{\rm T}^\ell$ is the transverse momentum of charged lepton, $\Delta\phi_{\ell,E_{\rm T}^{\rm miss}}$ is an angle difference between the lepton and $E_{\rm T}^{\rm miss}$ direction in the transverse plane. The $m_{\rm T}^W$ has a unique peak at around $W^\pm$ boson mass.

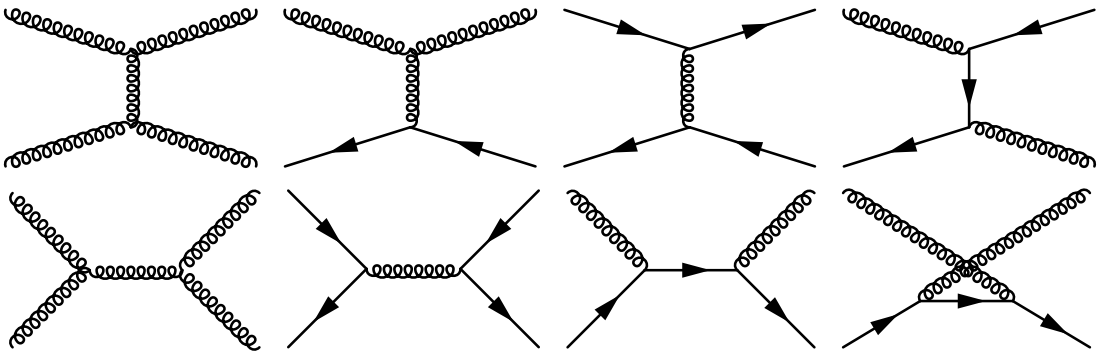

Figure 6.4: Feynman diagrams of the QCD multijets process at the LHC. Only leading diagram is shown.

The QCD multijets process has the fake τ and the fake lepton as well. As shown in Figure 6.4 the QCD multijets process has more gluons in the final state compared to W+jets and $t\bar{t}$.

The q/g fraction[3] is an important feature in terms of the $j \to \tau_{\text{had}}$ fake probability. In general gluon jet instantly spreads geometrically wider than quarks. Typically probability of gluon to τ_{had} fake object become smaller than quark one. The QCD multijets has the fake lepton, probability of $j \to \ell$ is smaller than $j \to \tau_{\text{had}}$ at a factor of $\lesssim 1\%$. A detailed description of the fake τ estimation including the fake lepton is given in Section 6.5.1.

$Z/\gamma^* \to \ell\ell$ + jets is also background. It has two kind of the fake τ, one is event with a charged lepton and the $j \to \tau_{\text{had}}$ fake, i.e. the other lepton fails to identify. Such event rate is not so large and it is possible to estimate them together with above three fake backgrounds. In addition to its rate, the q/g fraction is similar to W+jets, so it is estimated by together with W+jets.

Another component is one real lepton and one $\ell \to \tau_{\text{had}}$ fake. $e \to \tau_{\text{had}}$ fake is dominant in practice. $Z \to ee$ process is main source of the $e \to \tau_{\text{had}}$ fake background. It is suppressed by dedicated identification criteria as described in Section 5.6.3. It is estimated by data-driven technique as described in Section 6.5.1. Other processes like diboson and single-top production, its production cross-section is small. So it is reasonable to use simulated event samples with correction factors.

6.1.3 $m_{\tau\tau}$ Reconstruction

The invariant mass of di-τ system is one of the most important event properties in the search. Since multiple neutrinos are emitted, some assumptions is necessary. There are several techniques with regards to a type of assumption.

Visible Mass, m_{vis}

Most simple definition is ignoring such missing neutrinos, it is called as "visible mass" m_{vis} and defined as :

$$m_{\text{vis}} = \sqrt{(E_\ell + E_{\tau_{\text{vis-had}}})^2 - (\vec{p}_{\text{T}}^{\,\ell} + \vec{p}_{\text{T}}^{\,\tau_{\text{vis-had}}})^2}. \tag{6.2}$$

As the neutrinos carry a large fraction of the τ-lepton momenta, the visible mass distribution is shifted to lower value with respect to true $m_{\tau\tau}$ value. The visible mass is often used to validate kinematical modelling of lepton and hadronic-τ.

Total transverse mass, $m_{\text{T}}^{\text{tot}}$

The total transverse mass $m_{\text{T}}^{\text{tot}}$ is the sum of transverse mass between two visible-τ objects and the $E_{\text{T}}^{\text{miss}}$ defined as following :

$$m_{\text{T}}(i,j) = \sqrt{2 p_{\text{T},i} p_{\text{T},j} (1 - \cos\Delta\phi_{i,j})}, \tag{6.3}$$

$$m_{\text{T}}^{\text{tot}} = \sqrt{m_{\text{T}}(\ell, \tau_{\text{had}})^2 + m_{\text{T}}(\ell, E_{\text{T}}^{\text{miss}})^2 + m_{\text{T}}(\tau_{\text{had}}, E_{\text{T}}^{\text{miss}})^2}. \tag{6.4}$$

The total transverse mass has softer for The QCD multijets has softer distribution compare to other background processes. The total transverse mass is used in this analysis as a final discriminant.

6.2 Simulated Event Samples

Various simulated event samples are used in the analysis to model differential distributions of signal and background processes. Even through the background estimation is performed by data-driven ways, simulated event samples are used in the design and validation of such methods, as well as in the development of background-suppression strategies. An overview of the various simulated

[3] The fraction of a jet origin, it is usually defined as the ratio between quark jets and gluon jets.

event samples of signal and background processes is given In the following subsections.

6.2.1 Signal Processes

Simulated events for heavy neutral MSSM Higgs bosons signal is generated by PowHeg-Box v2 [179–181][4] and MadGraph5_aMC@NLO 2.1.2 [182, 183] programs for the gluon-fusion and the bottom-annihilation process respectively. For the gluon-fusion process, the CT10[184] is used as a PDF set and pythia8 (version is 8.210). The AZNLO [68] tuning is applied for the parton shower, underlying event and hadronisation. For the bottom-annihilation process, the CT10nlo_nf4 [67] and the Pythia8 (version is 8.210) with the A14 [185] tuned parameters us used as well for the parton shower and underlying event and hadronisation. EvtGen v1.2.0 [186][5] is used to revise the heavy flavour quark production and decay in the parton shower. This leads that improvements of b-tagging, provides a common efficiency reference across all generators and extrapolation to non-calibrated regions. I is assumed that the difference between CP-even and CP-odd Higgs bosons is negligible at all reconstructed object level. The reconstructed $m_{\tau\tau}$ resolution is not compatible to a generated mass width of Higgs bosons, so an effects of mass width difference is neglected. Each signal is normalised to the sum of cross-section with the CP-even plus the CP-odd. The signal samples are produced at the pseudoscalar mass of $m_{\mathrm{A}} = 200$, 300, 350, 400, 500, 600, 700, 800, 1000, 1200 GeV. Pythia 8.186 is used to overlay the minimum-bias[6] events on each generated event in order to model the pile-up for all simulated samples including the background processes,

6.2.2 Backgrounds Processes

Background process except the QCD multijets are generated for major processes summarised in Table 6.1 W+jets and Z+jets samples are generated by PowhegBox v2 interfaced to Pythia 8.186

Process	Generator (PDF set)	Shower (tune,PDF set)	Order	σ[pb]
Z+jets	Powheg-v2 (CT10)	Pythia8(AZNLO,CTQ6L1)	NNLO	1950
$W^{\pm} \to \ell^{\pm}\nu$	Powheg-v2 (CT10)	Pythia8(AZNLO,CTQ6L1)	NNLO	20079
$t\bar{t}$	Powheg-v2 (CT10)	Pythia6(P2012,CTQ6L1)	NNLO	993.8
single-$t/\bar{t}$, t-channel	Powheg-v1 (CT10f4)	Pythia6(P2012,CTQ6L1)	NNLO	216.95
single-$t/\bar{t}$, Wt-channel	Powheg-v2 (CT10)	Pythia6(P2012,CTQ6L1)	NNLO	75.57
single-$t/\bar{t}$, s-channel	Powheg-v2 (CT10)	Pythia6(P2012,CTQ6L1)	NNLO	10.32
Diboson	Sherpa (CT10)	-	NLO	45.42

Table 6.1: Description of Monte Carlo samples used in this analysis for background modelling.

with the AZNLO tune [68]. Photos++ v3.52 [188, 189] is used for photon radiations from electroweak vertices ad charged leptons. All W/Z+jets samples are normalised to the next-to-next-to-leading-order (NNLO) cross section calculated by FEWZ [190–192]. $t\bar{t}$ and single-top production except single-top t-channel are generated by Powheg-Box v2 with CT10 PDF set. Single-top t-channel is generated with Powheg-Box v1 jointing the four-flavour scheme for the NLO matrix element calculations to ether with the fixed four-flavour scheme PDF set CT10f4. Top-quark decay is simulated with MadSpin [193]. For all top-quark production, the spin correlations are preserved and the partons shower, fragmentation and underlying event are simulated Pythia 6.428 [194] with the CTQ6L1 PDF

[4] The PowHeg is a generator with the matrix element (ME) at NLO in QCD.
[5] EvtGen is an "afterburner" which runs after the Standard MC generation has taken place. EvtGen perform "re-decay" them with more accurate lifetime and decay table.
[6] The minimum-bias samples are generated with Pyhia8 using the A2 tune [187] and the MSTW2008LO PDF set.

set corresponding to Perugia 2012(P2012) tuning [78]. The $t\bar{t}$ production sample is normalised to the NNLO cross section including soft-gluon resummation to next-to-next-leading-logarithm accuracy [195]. The single-top samples are also normalised to an approximated NNLO calculation [196–198]. Diboson sample are generated by Sherpa 2.1.1 with the CT10 PDF set, up to one additional parton at NLO (depending on the process) and up to three additional parton at LO are calculated. The diboson samples are normalised to their NLO cross sections as computed by Sherpa.

6.3 Data Samples and Trigger Selection

The data sample analysed in this analysis was recorded during the data-taking periods in 2015 and 2016. Basic data quality criteria are applied to ensure that the detector worked well condition as shown in Section 4.3. An integrated luminosities of 3.2 fb^{-1} and 24.8 fb^{-1} for 2015 and 2016 are used for the search after this data quality selection. The luminosity calibration is obtained from van-der-Meer scans with uncertainties of $\pm 2.8\%$ for the 2015 and $\pm 5\%$ for 2016 data-taking period. The peak instantaneous luminosity increased significantly to $1.2 \times 10^{34}\text{cm}^{-2}\,\text{s}^{-1}$ in the 2016 data-taking, while $0.5 \times 10^{34}\text{cm}^{-2}\,\text{s}^{-1}$ in the 2015 data-taking.

Events are collected using the single-electron-trigger, single-muon-trigger and the missing transverse energy triggers. As the instantaneous luminosity varied during data-taking periods, the online threshold of these trigger items were adjusted several times to cope with the limited bandwidth available for data storage. Three different electron trigger items are used for the 2015 data samples with p_{T} threshold of 24, 60, 120 GeV in the 2015 data, 26, 60, 140 GeV for the 2016 data-taking respectively. Three different muon trigger items are used with p_{T} threshold of 20, 26, 50 GeV for the 2015 and 2016 data-taking. The online threshold of the $E_{\text{T}}^{\text{miss}}$ trigger items in the 2015 data-taking is 70 GeV. While during the 2016 data-taking period, the threshold were varied between 80 - 110 GeV.

6.3.1 Trigger Selection

Since this analysis has two decay channel, the $e\tau_{\text{had}}$ and $\mu\tau_{\text{had}}$ channels, the trigger selection is performed corresponding to the channel. The single-electron and $E_{\text{T}}^{\text{miss}}$ trigger are used in the $e\tau_{\text{had}}$ channel, as well as the single-muon and $E_{\text{T}}^{\text{miss}}$ trigger are used in the $\mu\tau_{\text{had}}$ channel. To avoid unexpected effects, the matching criteria between online trigger objects and offline[7] objects are considered. For the single-lepton-trigger(SLT), it is required that the transverse momentum of the offline lepton is greater than the online p_{T} threshold. All leptons are required $p_{\text{T}} > 30$ GeV, which reaches a stable efficiency of offline triggers. In addition to the p_{T} requirement, a geometrical matching is taken into account between the online and offline leptons. This is performed by using a cone matching criterion, $\Delta R(\text{offline}, \text{online}) < 0.1$.

A resolution of the online $E_{\text{T}}^{\text{miss}}$ is poor compared to the lepton triggers. The trigger selection for the $E_{\text{T}}^{\text{miss}}$ trigger is discussed together with its efficiency measurements in next subsection.

6.3.2 Measurement of the $E_{\text{T}}^{\text{miss}}$ Trigger Efficiency

In order to recover the trigger efficiency of the single-lepton-trigger, the $E_{\text{T}}^{\text{miss}}$ trigger is introduced in $H/A \to \tau\tau$ searches for the first time in this analysis. Since a simulation of the $E_{\text{T}}^{\text{miss}}$ trigger is difficult, so that for the simulated samples including the signal samples, simulated results does not used. Instead of using simulated results, the $E_{\text{T}}^{\text{miss}}$ trigger efficiency is measured in data. The efficiency of the $E_{\text{T}}^{\text{miss}}$ trigger is measured using the tag-&-prove method. $E_{\text{T}}^{\text{miss}} > 150$ GeV is used for an offline trigger threshold requirement. As a tag-trigger, the SLT is used and the efficiency is

[7] Usually a trigger and analysis level are called “online” and “offline” respectively.

measured by data. The trigger efficiency is evaluated by following fitting curve :

$$f = p_0 \left[1 + \mathrm{erf}\left(\frac{x - p_1}{p_2}\right)\right] + p_3, \tag{6.5}$$

where p_0, p_1, p_2 and p_3 are plateau, half, scale and offset parameters. Figure 6.5 shows the fitted curves for $e\tau_{\mathrm{had}}$ and $\mu\tau_{\mathrm{had}}$ respectively[8]. Figures containing five data-taking periods, three different selection stages are listed in Appendix A Figure A.1. A region filled by several colour represents one

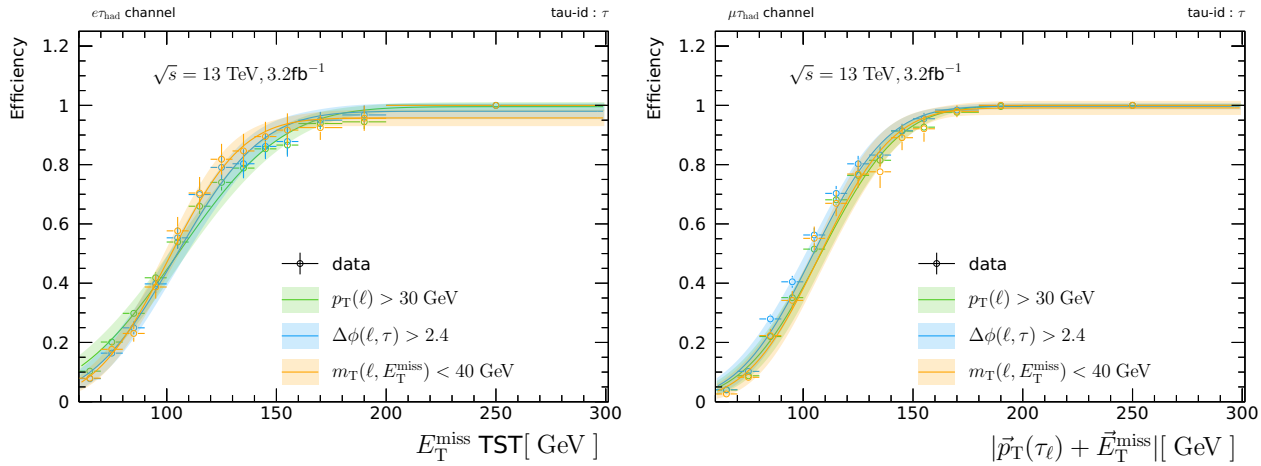

(a) $e\tau_{\mathrm{had}}$ **(b)** $\mu\tau_{\mathrm{had}}$

Figure 6.5: Efficiency for the $E_{\mathrm{T}}^{\mathrm{miss}}$ trigger of $e\tau_{\mathrm{had}}$ (a) and $\mu\tau_{\mathrm{had}}$ (b) channel with 2015 data-taking period as a function of $E_{\mathrm{T}}^{\mathrm{miss}}$ (a) $|\vec{E}_{\mathrm{T}}^{\mathrm{miss}} + \vec{p}_{\mathrm{T}}(\mu)|$ (b). Each plots have three different curves, after the preselection ($p_{\mathrm{T}}(\ell) >$ 30 GeV), $\Delta\phi(\ell, \tau_{\mathrm{vis}}) > 2.4$ and $m_{\mathrm{T}}(\ell, E_{\mathrm{T}}^{\mathrm{miss}}) < 40$ GeV.

sigma error from the fitting results. The 90% efficiency is achieved at $E_{\mathrm{T}}^{\mathrm{miss}} > 150$ GeV and this threshold is used as a trigger selection.

6.4 Event Selection and Categorisation

Event selection criteria are used to define phase-space regions of special interest. Basic requirements are applied to select events with the final state objects, called as "preselection". The trigger requirements and kinematical selection are applied to enhance the signal processes and suppress the background events after the preselection. The definition of the preselection is given in Section 6.4.1. The signal region is described in Section 6.4.2.

6.4.1 Object Definitions and Event Preselection

An overview of definition of the physics objects is summarised in Table 6.2. The physics object is selected independently to each other. The overlap removal solves overlaps between each objects to avoid double-counting. The overlap removal procedure is described in the following :

step 1 : Remove electron, hadronic-τ and jet if $\Delta R(\mu, e/\tau_{\mathrm{had}}/\mathrm{jet}) < 0.2/0.2/0.4$.

step 2 : Remove hadronic-τ and jet if $\Delta R(e, \tau_{\mathrm{had}}/\mathrm{jet}) < 0.2/0.4$ after the step 1

[8] Muons is not taken into account in the trigger decision, so the vector sum of the $E_{\mathrm{T}}^{\mathrm{miss}}$ and muon p_{T} is used as a online-$E_{\mathrm{T}}^{\mathrm{miss}}$.

physics object	muon	electron	hadronic-τ	jet
identification	medium	medium	medium	JVT
p_{T}	30 GeV	30 GeV	25 GeV	20 GeV
η range	$\lvert\eta\rvert < 2.5$	$\lvert\eta\rvert < 2.47$*	$\lvert\eta\rvert < 2.3$*	$\lvert\eta\rvert < 2.5$
isolation	gradient WP	gradient WP	-	-
other	ID requirements	-	1 or 3 tracks charge $= \pm 1$ ℓ-veto	jet cleaning

Table 6.2: Definitions of physics objects for the event selection. The mark "*" present $|\eta|$ require except $1.37 < |\eta| < 1.52$ addition to it.

step 3 : Remove hadronic-τ if $\Delta R(\tau_{\mathrm{had}}, \text{loose } \mu/e) < 0.2$ after the step 2

step 4 : Remove jet if $\Delta R(\tau_{\mathrm{had}}, \text{jet}) < 0.4$ after the step 3

where loose e and μ is selected using same selection criteria but with the loose ID requirement, no-isolation selection and $p_{\mathrm{T}} > 20$ GeV. After the overlap removal, it requires the number of survived leptons is exactly one. An opposite sign with regard to electric charge between lepton and visible-τ objects are required. The trigger requirement is described in Section 6.4.2.

6.4.2 Categorisation and Event Selection

Event selection and categorisation are applied to selected events after the preselection. Figure 6.6

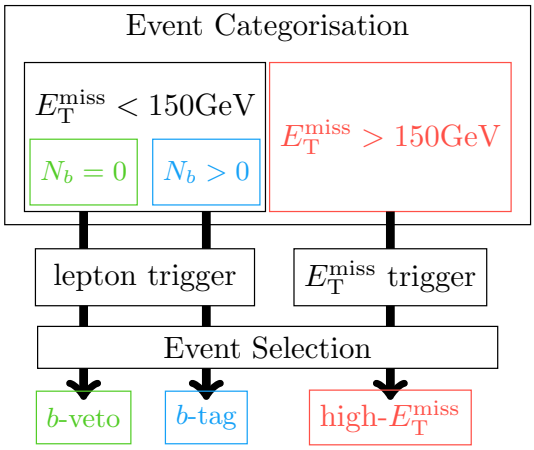

Figure 6.6: Flow chart of analysis categorisation, triggering and event selection. Events failed trigger or event selections are rejected from analysis.

shows a flow chart of analysis categorisation, trigger and event selection. The event categorisation separates events into three categories to improve analysis sensitivity. The event selection distinguishes the signals from background events. The regions passing all event selection are called as "signal regions (SRs)". There are several regions dominated by background processes called as "control regions (CRs)". Details of the control regions are described in Section 6.5.

Event Categorisation

There are three categories, the high-$E_{\mathrm{T}}^{\mathrm{miss}}$, b-tag and b-veto categories. One of major improvement of this thesis's work is taking closer notice of the $E_{\mathrm{T}}^{\mathrm{miss}}$ of signal processes. The heavy Higgs bosons have larger $E_{\mathrm{T}}^{\mathrm{miss}}$ than background processes. In order to enhance the heavy Higgs bosons signal, an event categorisation firstly separates events using $E_{\mathrm{T}}^{\mathrm{miss}} > 150GeV$ (high-$E_{\mathrm{T}}^{\mathrm{miss}}$ category). Muon is

not taken into account in the $E_{\mathrm{T}}^{\mathrm{miss}}$ trigger calculation. So instead of $E_{\mathrm{T}}^{\mathrm{miss}}$, $p_{\mathrm{T}}(\mu) + E_{\mathrm{T}}^{\mathrm{miss}}$ is used in the $\mu\tau_{\mathrm{had}}$ channel, i.e. $p_{\mathrm{T}}(\mu) + E_{\mathrm{T}}^{\mathrm{miss}} > 150$ GeV for the $\mu\tau_{\mathrm{had}}$ channel. A comparison of the reconstructed $E_{\mathrm{T}}^{\mathrm{miss}}$ is shown in Figure 6.7 (a). Events with $E_{\mathrm{T}}^{\mathrm{miss}} < 150$ GeV (low $E_{\mathrm{T}}^{\mathrm{miss}}$ category)

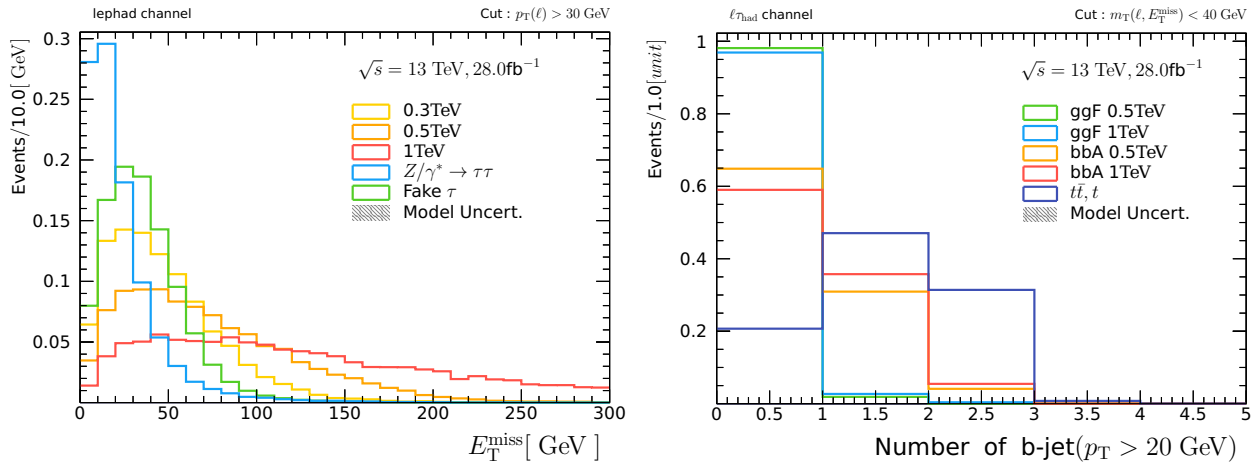

(a) $E_{\mathrm{T}}^{\mathrm{miss}}$ **(b)** The number of b-jet

Figure 6.7: Distributions of the $E_{\mathrm{T}}^{\mathrm{miss}}$ and number of b-jet for the signal processes and major backgrounds processes.

are separated correspondingly the number of b-jets (N_b). The b-tag category requires at least one b-jet to enhance sensitivity for the bottom-annihilation production. Events without b-jet are categorised as the b-veto category to enhance the gluon-fusion process. The number of b-jet distribution is shown in Figure 6.7 (b). The $E_{\mathrm{T}}^{\mathrm{miss}}$ trigger is used for the high-$E_{\mathrm{T}}^{\mathrm{miss}}$ category as described in Section 6.3.1. The single-lepton-trigger is are used for the b-tag and b-veto categories corresponding channel.

Event Selection

Same event selections are applied for three categories. Event selection criteria consists of two common selections corresponding to event kinematics, $\Delta\phi(\tau_\ell, \tau_{\mathrm{had}}) > 2.4$ and $m_{\mathrm{T}}(\tau_\ell, E_{\mathrm{T}}^{\mathrm{miss}}) < 40$ GeV. Figure 6.8 shows event kinematic variables used in the event selection. Three different signal mass hypothesis are included and $Z \to \tau\tau$ and fake τ_{vis} processes are shown as a background process. The signal tends to have $\Delta\phi \sim \pi$. The signal processes have lower m_{T} values, while the fake τ has a peak around $m_{\mathrm{T}} \sim 80$ GeV. In order to suppress $e \to \tau_{\mathrm{had}}$ fake events from $Z \to ee$ process, events are rejected when a visible mass is within $80 < m_{vis} < 100$ GeV for only $e\tau_{\mathrm{had}}$ channel.

6.5 Backgrounds Model

The description of methodology to model the background processes is given in this section. The fake τ_{vis} background contributes significantly on the tail of $Z/\gamma^* \to \tau\tau$ distributions as discussed in Section 6.1.2. Major contribution of the fake τ_{vis} is the W+jets process, but also the multijets, $t\bar{t}$ and Z+jets processes contributes. These multiple source process are estimated by "combined fake factor method" as described in Section 6.5.1. Other background like a $Z/\gamma^* \to \tau\tau$ and $t\bar{t}$ with real lepton and real τ_{vis} process are described in Section 6.5.2. A validation of estimated background processes is given in Section 6.7.

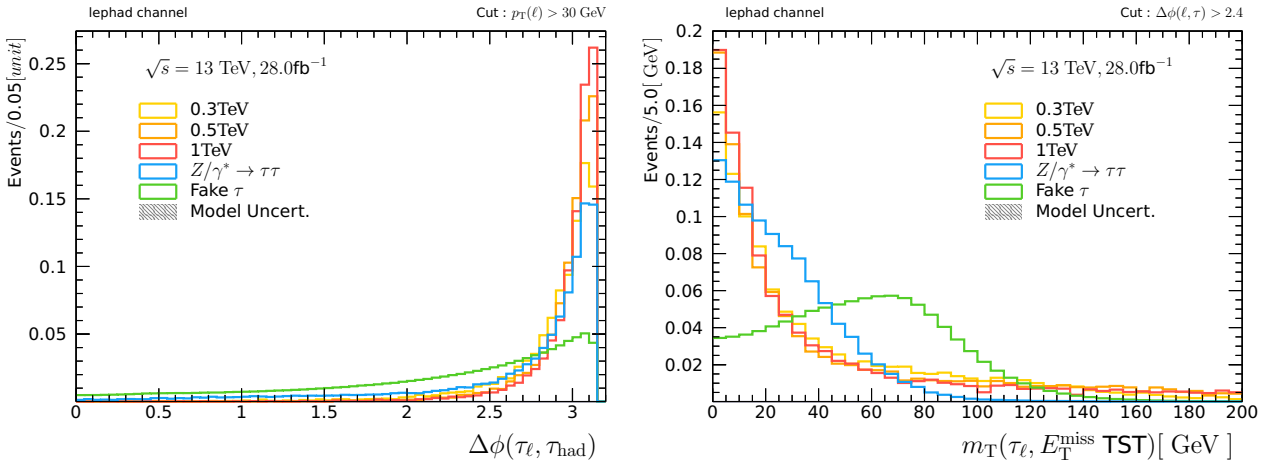

(a) $\Delta\phi(\tau_\ell, \tau_{\rm had})$ **(b)** $m_{\rm T}(\tau_\ell, E_{\rm T}^{\rm miss})$

Figure 6.8: Event kinematic variables using in event selections, (a) and (b) show a shape of $\Delta\phi(\tau_\ell, \tau_{\rm had})$ and $m_{\rm T}(\tau_\ell, E_{\rm T}^{\rm miss})$ respectively. (a) is after the preselection, while (b) is after $\Delta\phi(\tau_\ell, \tau_{\rm had}) > 2.4$. Both plots three different signal mass samples (300 GeV, 500 GeV, 1 TeV) and two major backgrounds with arbitrary scale.

6.5.1 Estimation of Background Events with Misidentified $\tau_{\rm had}$ Objects

Background events with mis-identified $\tau_{\rm vis}$ objects are hard to simulate by several reason. The identification algorithms deployed to suppress fake $\tau_{\rm vis}$ objects relies on various kind of shower shape variables describing the evolution of the hadronic and electromagnetic showers of the charged and neutral pions. Hadronic shower evolution consists of a large amount of random components, it needs that a large set of simulated events. Since hadronic jets are hadronised from gluons and quarks, a crucial aspect in the simulation is the modelling of the q/g fraction within samples of jets. Gluons have larger effective colour charge than quarks, this leads that gluons tend to hadronise into wider jets than quarks. The $\tau_{\rm vis}$ mis-identification probability of gluons differs significantly from quark's one. It is focused on an estimation of the $j \to \tau_{\rm had}$ fake and also the $e \to \tau_{\rm had}$ fake is given in most part of this section.

The Fake Factor Method

The fake factor method was first developed in the Tevatraon analysis and further improvements was applied at the ATLAS analysis Reference [199]. The fake factor method extrapolates the event yields from the control region into the signal regions by using the fake factor (FF) defined as following :

$$N_{\rm pass}^{\rm SR} = N_{\rm fail}^{\rm SR} \times \underbrace{\frac{N_{\rm pass}^{\rm CR}}{N_{\rm fail}^{\rm CR}}}_{FF}, \tag{6.6}$$

where the "pass" and "fail" means that event with passing and failing an identification selection to control fake probability, for example the τ identification is used in the fake $\tau_{\rm vis}$ estimation. The $N_{\rm pass}^{\rm SR}$ and $N_{\rm fail}^{\rm SR}$ has exactly same event kinematics but only an identification condition is different. The physics meaning of the fake factor is a probability of transition from the failed into passed events.

The fake $\tau_{\rm vis}$ background contributing in the signal regions consists of the QCD multijets, $t\bar{t}$ and W/Z+jets. As a numerator default τ identification (`medium WP`) is used. While as a denominator events with `not loose and BDT score>0.35` is defined. This denominator is so-called "anti-id τ ($\bar{\tau}$

)". Evens yields of the fake τ_{vis} would be expected following :

$$N^{\text{SR}}_{\text{fake}} = N^{\text{SR}}_{\text{fake,q}} + N^{\text{SR}}_{\text{fake},W} + N^{\text{SR}}_{\text{fake},t\bar{t}} + N^{\text{SR}}_{\text{fake},Z}, \tag{6.7}$$

where q, W and Z means the QCD multijets, W+jets and Z+jets respectively. Equation (6.7) can be transformed into Equation (6.8) using Equation (6.6):

$$\begin{aligned} N^{\text{SR}}_{\text{fake}} &= FF^{\text{q}}_{\bar{\tau}\to\tau} \times N^{\text{SR}}_{\bar{\tau},q} + FF^{W}_{\bar{\tau}\to\tau} \times N^{\text{SR}}_{\bar{\tau},W} + FF^{t\bar{t}}_{\bar{\tau}\to\tau} \times N^{\text{SR}}_{\bar{\tau},t\bar{t}} + FF^{Z}_{\bar{\tau}\to\tau} \times N^{\text{SR}}_{\bar{\tau},Z}, & (6.8)\\ &= N^{\text{SR}}_{\bar{\tau}} \times \sum_i FF^{i}_{\bar{\tau}\to\tau} \times \frac{N^{\text{SR}}_{\bar{\tau},i}}{N^{\text{SR}}_{\bar{\tau}}}, & (6.9)\\ &= N^{\text{SR}}_{\bar{\tau}} \times FF^{\text{comb}}_{\bar{\tau}\to\tau} & (6.10)\\ FF^{\text{comb}}_{\bar{\tau}\to\tau} &= \sum_i FF^{i}_{\bar{\tau}\to\tau} \times r_i. & (6.11) \end{aligned}$$

where the sum runs over the background processes, r_i is a ratio of background i and the sum of all backgrounds, $FF^{\text{comb}}_{\bar{\tau}\to\tau}$ is the combined fake factor. In order to simplify the combined fake factor, the dedicated fake factors for each background processes can be merged into two groups. Here again, the quark and gluon fraction is most influential parameter to decide the fake probability. So processes which has similar q/g fraction can be merged. The Z+jets production diagrams are almost same as the W+jets, so an origin of their jets is also similar. In terms of the number of quarks in the final state, the $t\bar{t}$ with semi-leptonic channel is dominated with quarks, gluons contribute only initial or final state radiation. As shown in Figure 6.4 the QCD multijets process has the larger number of gluons in final state than other three EW processes. As a result of this simplification, the combined fake factor is simplified as the following :

$$\begin{aligned} FF^{\text{comb}}_{\bar{\tau}\to\tau} &\simeq r_q \times FF^{q}_{\bar{\tau}\to\tau} + r_{\text{EW}} \times FF^{\text{EW}}_{\bar{\tau}\to\tau}, & (6.12)\\ &= r_q \times FF^{q}_{\bar{\tau}\to\tau} + (1 - r_q) \times FF^{\text{EW}}_{\bar{\tau}\to\tau}. & (6.13) \end{aligned}$$

where the EW denotes the W/Z+jets and $t\bar{t}$ processes, and $r_q + r_{\text{EW}} = 1$ is assumed. To estimate the fake τ_{vis} background, three variables need to be obtained, $FF^{q}_{\bar{\tau}\to\tau}$, $FF^{EW}_{\bar{\tau}\to\tau}$ and r_q. The $FF^{q}_{\bar{\tau}\to\tau}$ and $FF^{EW}_{\bar{\tau}\to\tau}$ are measured at dedicated control regions. A measurement of the r_q is synonymous with an estimation of the QCD multijets process, so that the QCD multijets estimation is described in next sub-subsection.

Estimation of r_q :The Lepton Fake Factor Method

The r_q is defined as a ratio of the QCD multijets contribution and the QCD plus EW process. In order to measure the r_q , the QCD multijets contributions in the SR with anti-id τ objects is estimated. In a past study, there are several way to measure the r_q , the simplest way is just using the simulated samples with assuming there are no additional source of the fake τ_{vis}. This leads that $r_q = 1 - r_{\text{EW}}$ where $r_{\text{EW}} = N_{\text{EW}}/(N_{\text{total}} - N_{\text{real}})$. A large systematic uncertainties should be taken into account. The QCD multijets processes have two fake objects, the fake τ_{vis} and the fake lepton. To estimate the fake lepton, a similar method is used called as the lepton fake factor method. The lepton isolation criteria suppress the fake lepton, so the lepton isolation is used as a control variable.

$$N^{\text{SR}}_{\ell,\bar{\tau}} = N^{\text{SR}}_{\bar{\ell},\bar{\tau}} \times \underbrace{\frac{N^{\text{SR}}_{\ell,\bar{\tau}}}{N^{\text{SR}}_{\bar{\ell},\bar{\tau}}}}_{FF_{\bar{\ell}\to\ell}}, \tag{6.14}$$

where $FF^{q}_{\bar{\ell}\to\ell}$ is the lepton fake factor, $N^{\mathrm{SR}}_{\ell,\bar{\tau}}$ the number of events in the signal region with isolated lepton (ℓ) and anti-id τ_{vis}. $N^{\mathrm{SR}}_{\bar{\ell},\bar{\tau}}$ is the number of events in the signal region with anti-isolated lepton ($\bar{\ell}$) and anti-id τ_{vis}. The anti-isolated lepton is a lepton with failing default isolation selection. The lepton fake factor is measured in the region where has more jet-like τ_{vis} fake. The jet-like τ_{vis} is defined by `BDT score<0.35` called as loose-anti-id τ_{vis} ($\bar{\tau}'$). Before proceeding to actual estimations, definition of dedicated control regions is given in Figure 6.9. The signal region is same condition as

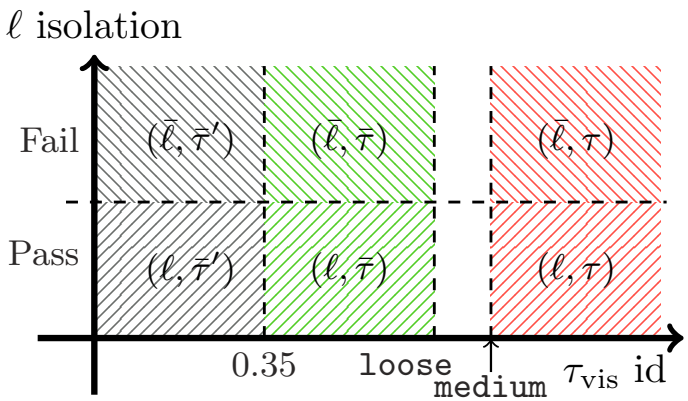

Figure 6.9: Description of the region for controlling the fake background. There are six dedicated regions for τ identification and lepton isolation conditions. Bottom column is isolated-lepton (ℓ) region, while top column is non-isolated-lepton ($\bar{\ell}$) region. From right side the id-τ (τ), anti-id τ ($\bar{\tau}$) and loose-anti-id τ ($\bar{\tau}'$) regions lie.

the (ℓ,τ) region, other regions are used for the fake background estimation. The fake factor $FF^{\mathrm{EW}}_{\bar{\tau}\to\tau}$ is defined as a fraction between the region of $(\ell,\bar{\tau})$ and (ℓ,τ). $FF^{q}_{\bar{\tau}\to\tau}$ is derived as a fraction between the region $(\bar{\ell},\bar{\tau})$ and $(\bar{\ell},\tau)$. While the lepton fake factor $FF^{q}_{\bar{\ell}\to\ell}$ is defined as a fraction between the region of $(\bar{\ell},\bar{\tau}')$ and $(\ell,\bar{\tau}')$.

As there are several backgrounds in the control region of the lepton fake factors, a numerator need to subtract such non-QCD multijets background, mainly the W+jets process. A modelling of such simulated visible-τ objects is not well performed as discussed, so some kind of correction is necessary to use the simulated samples. Figure 6.10 shows the transverse mass distributions for

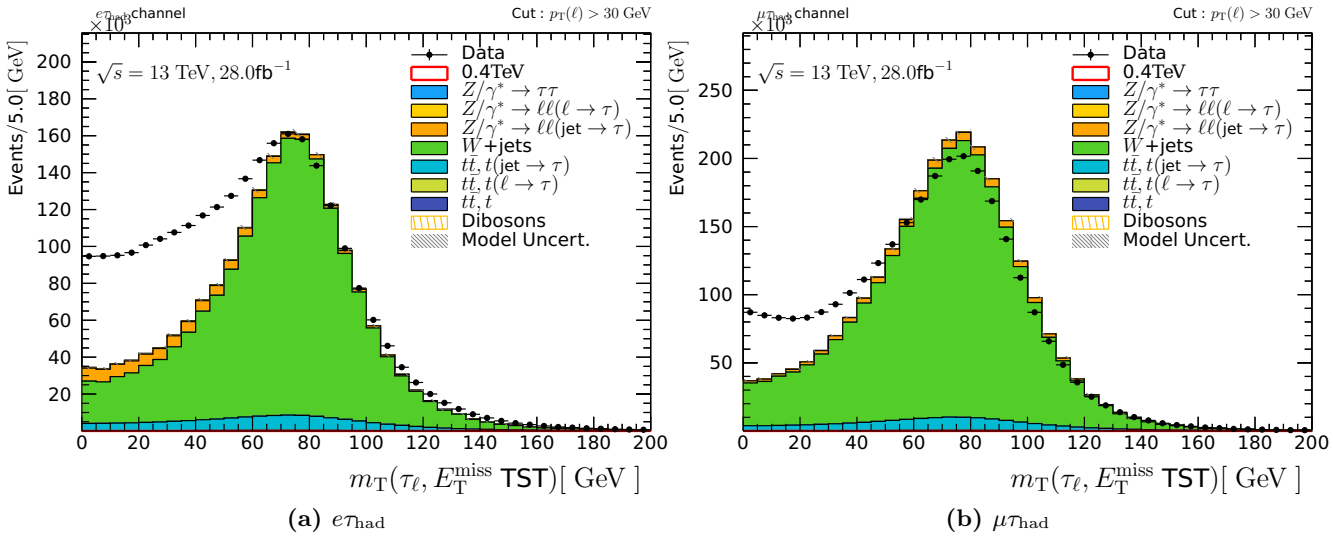

(a) $e\tau_{\mathrm{had}}$ **(b)** $\mu\tau_{\mathrm{had}}$

Figure 6.10: The transverse mass distribution in the region of $(\ell,\bar{\tau}')$ for $e\tau_{\mathrm{had}}$ (a) and $\mu\tau_{\mathrm{had}}$ (b) channels after the preselection.

$e\tau_{\mathrm{had}}$ (a) and $\mu\tau_{\mathrm{had}}$ (b) channels in the $(\ell,\bar{\tau}')$ region after the preselection. As expected there are a large amount of excess at lower m_{T} region, this would come from the QCD multijets fake process. An important feature is a difference of a $j \to \ell$ fake probability between electrons and muons as shown in

Figure 6.10, there are a larger fake electrons than muon. To obtain correction for the simulated fake τ_{vis}, a dedicated control region is defined. The W+jets has a unique peak around m_W GeV, so it is natural to use a window of $60 < m_{\text{T}}(\ell, E_{\text{T}}^{\text{miss}}) < 120$ GeV as a control region for the W+jets (WCR). Along the m_{T} window cut, default selection of $m_{\text{T}} < 40$ GeV is replaced. In addition to the m_{T} window, $E_{\text{T}}^{\text{miss}} > 40$ GeV is also applied to suppress the QCD multijets contaminations. In the WCR

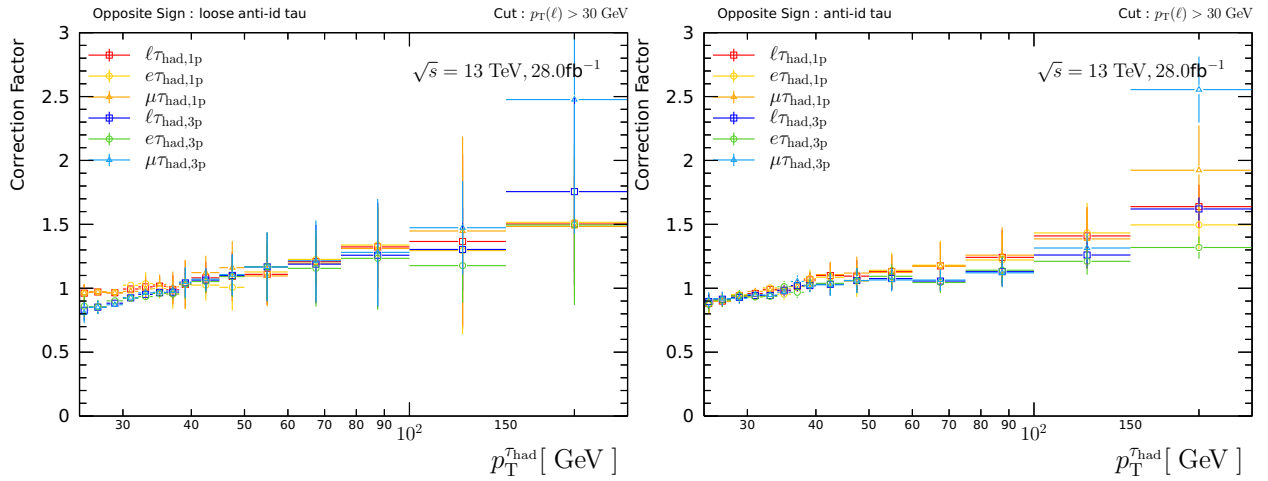

(a) correction in $(\bar{\ell}, \bar{\tau}')$ **(b)** correction in $(\ell, \bar{\tau})$

Figure 6.11: Correction factors for the simulated τ_{vis} fake objects as a function of the transverse momentum of τ_{vis}. Plot show six variations for $e\tau_{\text{had}}$ and $\mu\tau_{\text{had}}$ channel with 1, 3-prong and inclusively. Error bars include its statistical and systematic uncertainties, systematic uncertainty is obtained from a q/g fraction difference between the WCR and the SR as described in later. (a) and (b) shows the correction factor in the $(\bar{\ell}, \bar{\tau}')$ and $(\ell, \bar{\tau})$ respectively.

a correction factor is obtained as a function of the visible-τ p_{T} as shown in Figure 6.11 (a). The correction factors depends only n-prong. This correction factors does not change event yields but its shapes. For the overall scale corrections are performed with independently for $e\tau_{\text{had}}$, $\mu\tau_{\text{had}}$ and n-prong decay channels. As an extrapolation bias check the q/g fraction difference between the WCR and SR is evaluated by simulated samples. Figure 6.12 shows comparisons of the q/g fraction and shape difference between the WCR and the SR as a function of the τ_{had} p_{T}. Each content is the ratio of fraction and shape between the WCR and SR. Overall uncertainties are less than 5 % at low-p_{T} and about 10% at higher p_{T} region. The error band is directly used as an extrapolation uncertainty of this correction. As expected from origin of the fake lepton, there are non-negligible dependencies on events has more quarks or not. The lepton fake factor is splitted to the b-tag and b-veto events. Figure 6.13 shows the lepton fake factors and reweighting factors. The lepton fake factor $FF_{\bar{\ell}\to\ell}$ is defined as a function of lepton p_{T}. Two reweighting factors for $e\tau_{\text{had}}$ channels are also given as a function absolute values of lepton pseudorapidity (c) and angle difference between direction of lepton and $E_{\text{T}}^{\text{miss}}$ (d) in the transverse plane. These reweighting factors correct a kind of calculation difference between the isolated- and non-isolated lepton. The $R_{\bar{\ell}}(|\eta|))$ corrects difference of the electron identification criteria among pseudorapidity regions[9] as discussed in Section 5.4.3. The $R_{\bar{\ell}}(\Delta\phi))$ corrects difference of the $E_{\text{T}}^{\text{miss}}$ reconstruction procedure in terms of the soft term subtraction[10]. As a result of the QCD multijets, the r_q is measured in the $(\ell, \bar{\tau})$ region. Since the r_q is a fraction of the QCD multijets components in the $(\ell, \bar{\tau})$ region, so other components in that region should be understood. To ensure

[9] The electron identification likelihood has strong dependency against pseudorapidity due to the TRT detector components are different.

[10] The isolated-electron, tracks around electrons are calculated as the soft term, while tracks around the non-isolated lepton are account as EM cluster or electron itself.

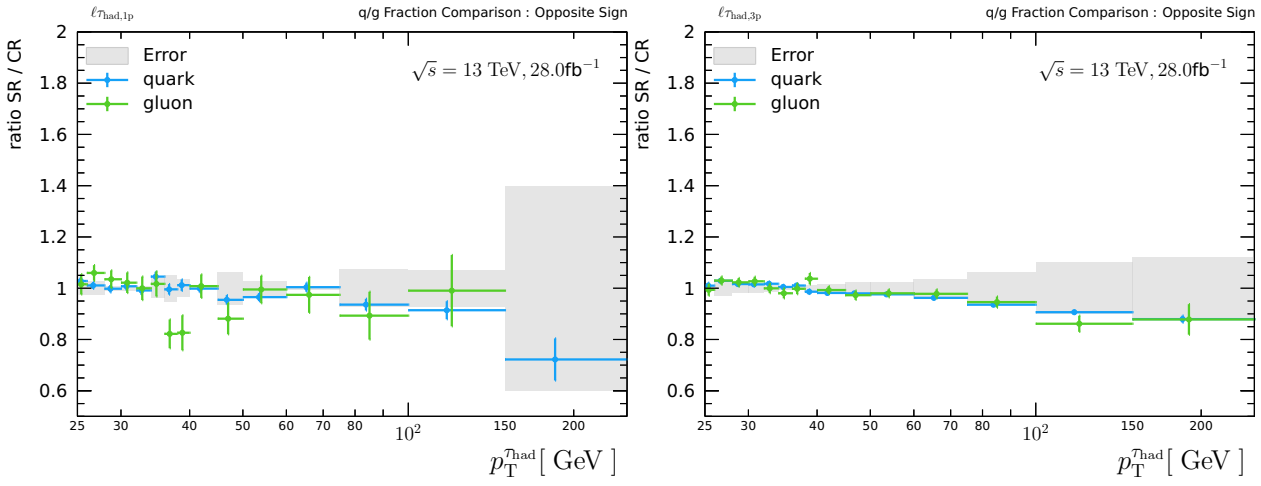

(a) $\tau_{\rm had}^{\rm 1p}$ **(b)** $\tau_{\rm had}^{\rm 3p}$

Figure 6.12: Comparison of the q/g fraction and shape difference between the WCR and the SR as a function of the transverse momentum of $\tau_{\rm vis}$ objects.

other component, the WCR is used and correction factors is obtained by similar way in the WCR. Figure 6.11 (b) shows the correction factors for the $\bar{\tau}$ events from the WCR including statistical and systematic uncertainties obtained from comparison of the q/g fraction difference between the WCR and the SR as shown in Figure 6.14. Uncertainty are a few % order at lower $p_{\rm T}$ region, while at higher $p_{\rm T}$ region, it is up to 30% level due to non-negligible difference of the q/g shapes. The scale correction of each fake component is performed by fitting the transverse momentum of lepton in the WCR and they are extrapolated into the SR. The fit is performed by floating only the fake $\tau_{\rm vis}$ sources, the W+jets, $t\bar{t}$ and Z+jets, other processes including the QCD multijets are fixed. The systematic uncertainties with respect to this fit are taken into account from fitting results, typically it is $3 \sim 5\%$ level.

The r_q is measured in each SR with $(\ell, \bar{\tau})$ regions after the scale and shape corrections, As a systematic uncertainty, several source is considered, statistical and systematic uncertainties related to the lepton fake factor, the scale and shape correction. Figure 6.15 shows the measured r_q as a function of the transverse momentum of the fake $\tau_{\rm vis}$ objects. For the value greater than 1.0 are constrained with $r_q = 1.0$ with additional 5% uncertainty. As shown in plots, the $e\tau_{\rm had}$ and $\mu\tau_{\rm had}$ channel show different trends at higher $p_{\rm T}$ region, the $e\tau_{\rm had}$ channel lower than $\mu\tau_{\rm had}$ channel. The r_q is extrapolated by same values as 200 GeV with additional 10% uncertainty for $p_{\rm T} > 200$ GeV. In addition to the low-$E_{\rm T}^{\rm miss}$ category, the high-$E_{\rm T}^{\rm miss}$ category is checked. The QCD multijets process has no $E_{\rm T}^{\rm miss}$ source except neutrinos from hadronic jets, so that the met is powerful variable to suppress them. Since the high-$E_{\rm T}^{\rm miss}$ category is already applied $E_{\rm T}^{\rm miss} > 150$ GeV, so the fake lepton is extremely small. Figure 6.16 shows the transverse mass distributions for the high-$E_{\rm T}^{\rm miss}$ $(\ell, \bar{\tau})$ region. The background expectation agrees well with observed data within uncertainties. The fake leptons are extremely small, they are less than 0.1% of total background expectation. The systematic uncertainty is considered from difference in Figure 6.16 between data and background expectation. The systematic uncertainty, hence, is estimated ±7% and ±12% for $e\tau_{\rm had}$ and $\mu\tau_{\rm had}$ channel respectively.

Measurements of The QCD Fake Factors : $FF^{q}_{\bar{\tau}\to\tau}$

The QCD fake factor $FF^{q}_{\bar{\tau}\to\tau}$ is measured in the QCD CR with condition of $(\bar{\ell}, \bar{\tau})$ amd $(\bar{\ell}, \tau)$ which are inverted the lepton isolation criteria. The QCD multijets processes dominates in that region, so a subtraction of other EW processes is negligible for the QCD fake factor. It is necessary to consider

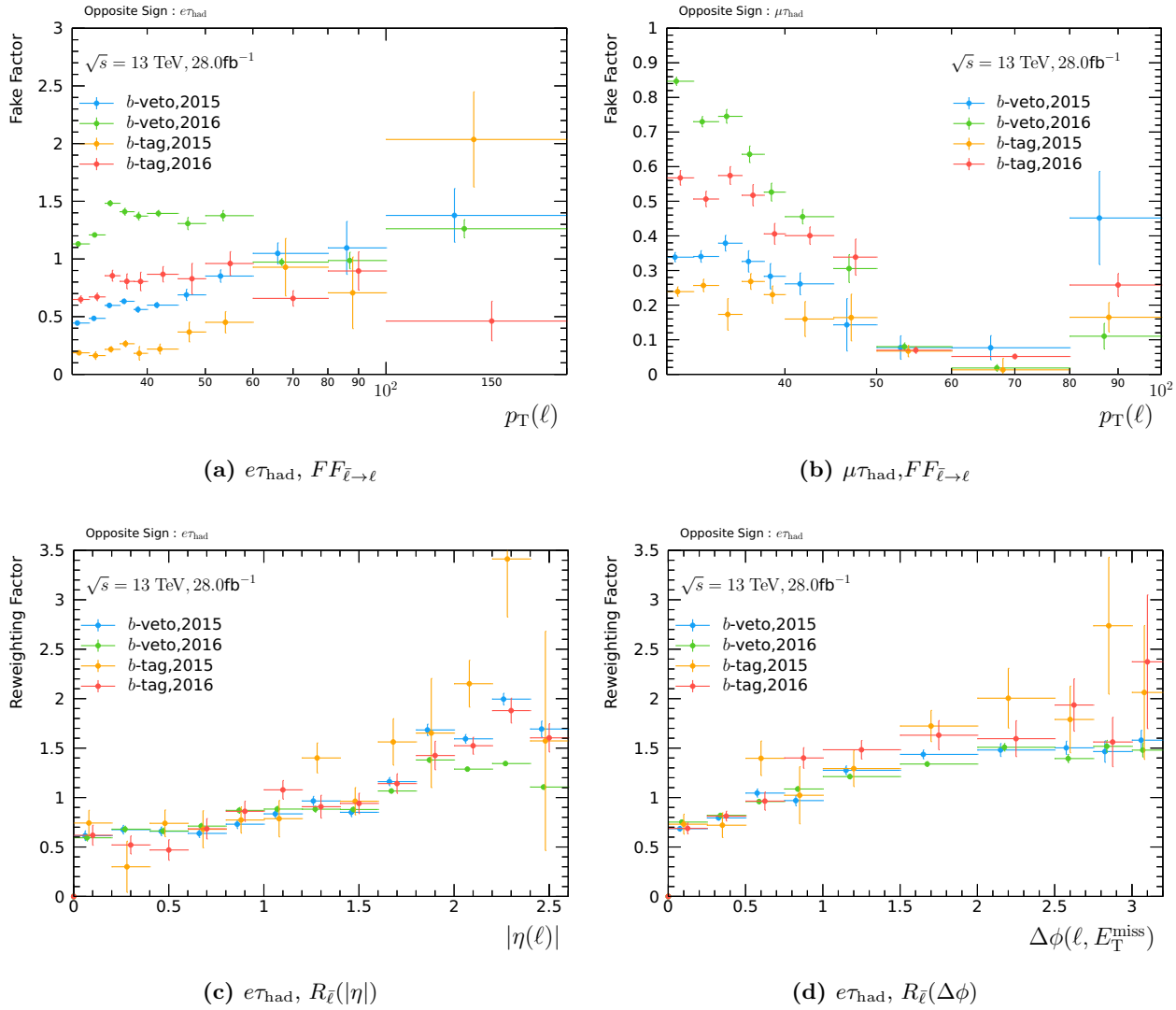

(a) $e\tau_{\text{had}}$, $FF_{\bar{\ell}\to\ell}$ **(b)** $\mu\tau_{\text{had}}$,$FF_{\bar{\ell}\to\ell}$

(c) $e\tau_{\text{had}}$, $R_{\bar{\ell}}(|\eta|)$ **(d)** $e\tau_{\text{had}}$, $R_{\bar{\ell}}(\Delta\phi)$

Figure 6.13: The lepton fake factors for electrons (a) and muons (b) as a function of the lepton p_{T}. And reweighting factors for $e\tau_{\text{had}}$ channel as a function of $\Delta\phi(\ell, E_{\text{T}}^{\text{miss}})$ (c) and $|\eta(\ell)|$ (d). For all plots, it is separated with b-tagged or b-veto events and 2015 or 2016 data-taking period.

an extrapolation bias as a systematic uncertainty. It is evaluated by checking difference of the fake factor between default QCD CR and modified QCD CR. The modified QCD CR has slightly closer condition to the SR in terms of the lepton isolation criteria, which fails the `gradient` working point but passes the `loose` WP. The pile-up effects is also evaluated as the systematic uncertainty. In order to check the pile-up effects, two fake factors with lower and higher pile-up condition are compared using the average number of interactions per bunch crossing $\langle\mu\rangle$. It is estimated by $1 \sim 4\%$ on the QCD fake factor. Figure 6.17 shows the QCD fake factor for the 1-prong and 3-prong decay channels with four different events, data-taking period and the number of b-tagged jets.

Measurements of The EW Fake Factors : $FF_{\bar{\tau}\to\tau}^{\text{EW}}$

The EW fake factor $FF_{\bar{\tau}\to\tau}^{\text{EW}}$ is measured in the WCR with condition of (ℓ, τ) and $(\ell, \bar{\tau})$. The WCR is defined as $60 < m_{\text{T}} < 110$ GeV. The other components from real hadronic-τ is subtracted from denominator and numerator of the fake factors. As the real visible-τ subtraction simulated samples

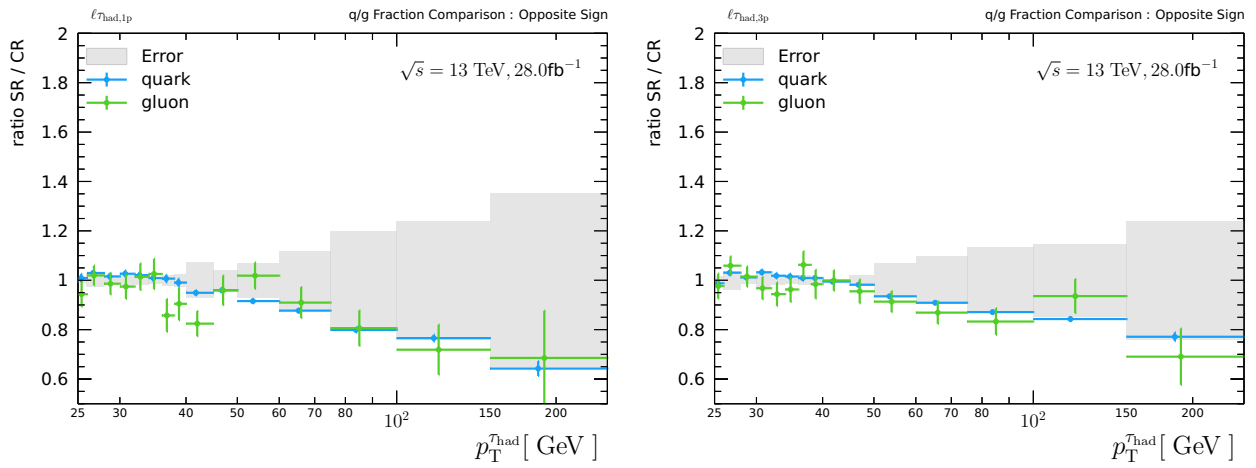

(a) $\tau_{\text{had}}^{\text{1p}}$ **(b)** $\tau_{\text{had}}^{\text{3p}}$

Figure 6.14: Comparison of the q/g fraction and shape difference between the WCR and the SR as a function of the transverse momentum of τ_{vis} objects.

is used and it is evaluated as less than 5%. As a other systematic uncertainty, an extrapolation bias is obtained by using the simulated q/g fraction comparison. The pile-up effect is also estimated by same way as doing for the QCD fake factors, it is less than 1%. Figure 6.18 shows the EW fake factor for the 1-prong and 3-prong channels with four different events, data-taking period and the number of b-tagged jets. For the high-$E_{\text{T}}^{\text{miss}}$ category same fake factors are used due to a lack of data statistics to estimate. Potential differences of the EW fake factor between the low-$E_{\text{T}}^{\text{miss}}$ and high=$E_{\text{T}}^{\text{miss}}$ events are obtained by the simulated samples, it is estimated as $3 \sim 8\%$. This differences are taken into account as an additional systematic uncertainty for only the high-$E_{\text{T}}^{\text{miss}}$ category.

Corrections on $\Delta\phi(\tau, E_{\text{T}}^{\text{miss}}$

Since the fake factor method extrapolates from $\bar{\tau}$ region, a correction is applied correspondingly difference of the $E_{\text{T}}^{\text{miss}}$ reconstruction procedure between the id-τ and $\bar{\tau}$ regions. This is similar correction to the lepton fake factor method, an affected term is the τ term of the $E_{\text{T}}^{\text{miss}}$ reconstruction. An angle difference between visible-τ and $E_{\text{T}}^{\text{miss}}$ $\Delta\phi(\tau, E_{\text{T}}^{\text{miss}})$ is used as correction target. The correction factor on $\Delta\phi(\tau, E_{\text{T}}^{\text{miss}})$ is defined as a ratio between the id-τ and $\bar{\tau}$ region, as shown in Figure 6.19. The correction factor is interpolated using the PCHIP algorithm[11] to obtain smooth lines. No significant difference between those event categorisation was found, so the correction factors is used inclusively. Only statistical error on the denominator and numerator is propagated as a systematic uncertainty.

Background with $e \to \tau_{\text{had}}$ Fake

Other source of fake τ_{had} need to be taken account, in $Z/\gamma^* \to ee$ events one electron is identified as electron, another electron mimicking into τ_{had} objects. They dominates in $e\tau_{\text{had}}$ 1-prong channel, the 3-prong fake $e \to \tau_{\text{had}}$ can be negligible. The electron LH identification criteria is used to estimate

[11] The Piecewise Cubic Hermite Interpolating Polynomial technique, which can perform more stable than other algorithm like the cubic interpolation.

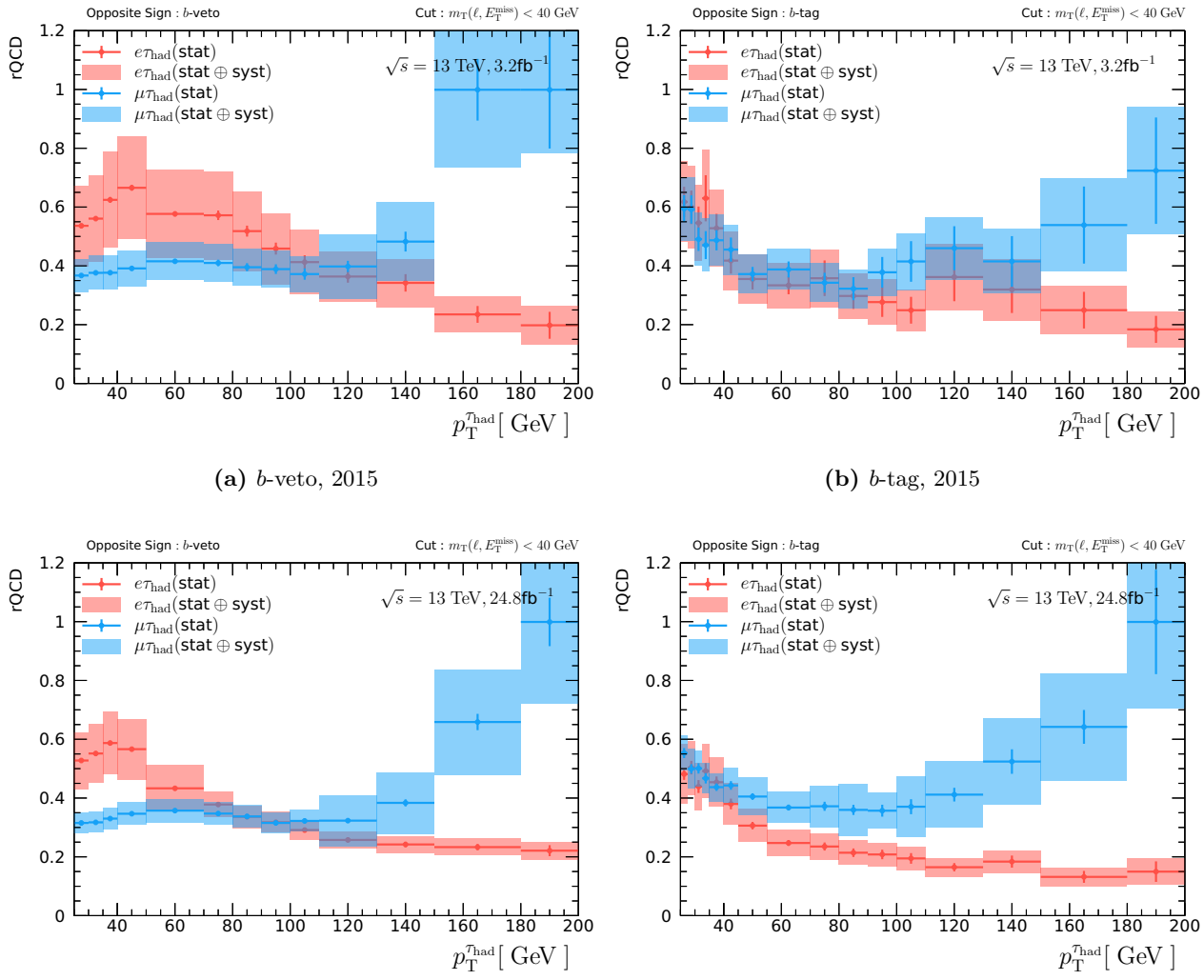

(a) b-veto, 2015 **(b)** b-tag, 2015

(c) b-veto, 2016 **(d)** b-tag, 2016

Figure 6.15: The measured r_q for b-tag and b-veto splitting 2015 and 2016 data-taking period as a function of the τ_{vis} p_{T}. All plots show $e\tau_{\text{had}}$ (red) and $\mu\tau_{\text{had}}$ (blue) points with statistical uncertainty and filled regions with quadratic sum of statistical and systematic uncertainty.

the $e \to \tau_{\text{had}}$ fake events using the fake factor method:

$$N^{\text{SR}}_{e\to\tau_{\text{had}}} = N^{\text{SR}}_{\text{fail eLH}} \times \underbrace{\frac{N^{\text{CR}}_{\text{pass eLH}}}{N^{\text{CR}}_{\text{fail eLH}}}}_{FF_{e\to\tau_{\text{had}}}}, \tag{6.15}$$

where the CR is inside a window of $80 < m_{vis} < 110$ GeV, the eLH is the electron likelihood identification selection. Figure 6.20 shows the $e \to \tau_{\text{had}}$ fake factor for $e\tau_{\text{had}}$ 1-prong channel as a function of the visible-τ p_{T}. For the b-tag and high-$E_{\text{T}}^{\text{miss}}$ categories, extremely small contribution from $Z \to ee$ process is expected, so that the $e \to \tau_{\text{had}}$ fake process can be neglected.

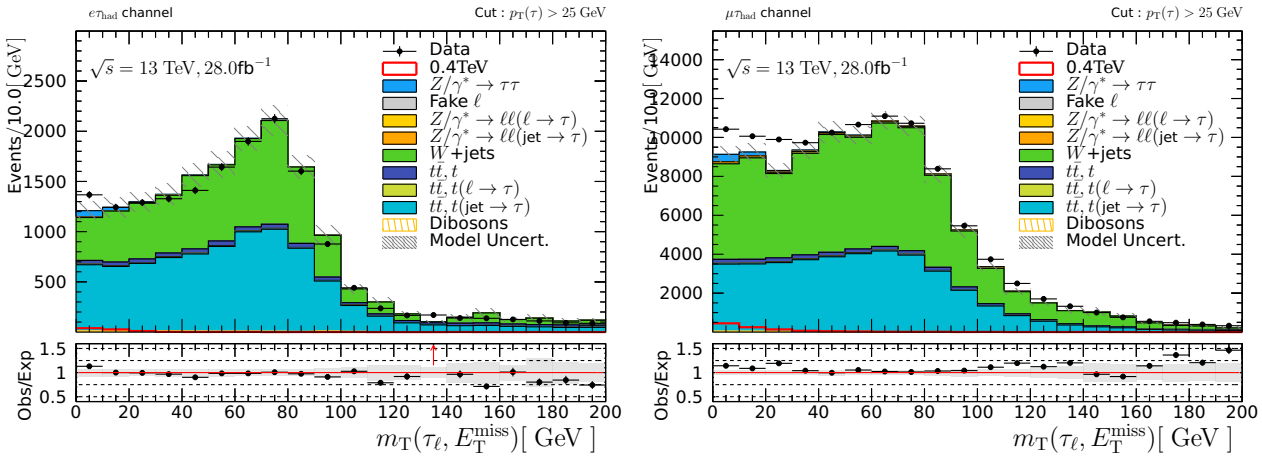

(a) $e\tau_{\rm had}$ **(b)** $\mu\tau_{\rm had}$

Figure 6.16: Transverse mass distributions at the high-$E_{\rm T}^{\rm miss}$ category for $e\tau_{\rm had}$ (a) and $\mu\tau_{\rm had}$ (b) channels in the $(\ell, \bar{\tau})$ region.

6.5.2 Modelling Additional Background Processes

Additional background processes are validated and corrected using dedicated control regions. The $Z \to \tau\tau$ CR (ZCR) is defined as applying same selections of the signal region and $m_{vis} < 80$ GeV, since this region does not impact on any signal. The $t\bar{t} \to \ell\tau_{\rm had}$ CR (TCR) is defined as applying same selections of the signal region but applied $m_{\rm T} > 120$ GeV. The TCR is defined in the high-$E_{\rm T}^{\rm miss}$ and b-tag SR, not for the b-veto SR. The W+jets CR (WCR) is defined as same selections of the signal region but applied $70 < m_{\rm T} < 110$ GeV. The WCR is defined in the high-$E_{\rm T}^{\rm miss}$ and b-veto SR. The same sign CR (SSCR) which have large QCD contributions are defined as the all SRs but required $q_\ell \times q_{\tau_{\rm had}} > 0$. Table 6.3 summarises the result of validation of each background process. In the WCR

CR		$e\tau_{\rm had}^{\rm 1p}$	$e\tau_{\rm had}^{\rm 3p}$	$\mu\tau_{\rm had}^{\rm 1p}$	$\mu\tau_{\rm had}^{\rm 3p}$
high-$E_{\rm T}^{\rm miss}$	TCR	$0.920\pm < 0.01$	0.855 ± 0.04	0.896 ± 0.03	0.827 ± 0.08
	ZCR	$1.192\pm < 0.01$	1.024 ± 0.04	1.264 ± 0.03	$1.112\pm < 0.01$
	WCR	0.885 ± 0.07	0.779 ± 0.04	0.938 ± 0.02	0.865 ± 0.05
	SSCR	0.613 ± 0.06	1.062 ± 0.05	$0.955\pm < 0.01$	0.921 ± 0.05
b-tag	TCR	$0.830\pm < 0.01$	$1.019\pm < 0.01$	$0.984\pm < 0.01$	$0.944\pm < 0.01$
	ZCR	0.795 ± 0.07	0.990 ± 0.02	1.255 ± 0.14	1.591 ± 0.06
	SSCR	$1.010\pm < 0.01$	1.089 ± 0.03	$1.028\pm < 0.01$	1.196 ± 0.03
b-veto	WCR	$1.011 < 0.01$	$0.944 < 0.01$	$0.967 < 0.01$	$0.923\pm < 0.01$
	ZCR	$1.045 < 0.01$	$0.961 < 0.01$	$0.934 < 0.01$	$0.983\pm < 0.01$
	SSCR	$1.249 < 0.01$	$1.070 < 0.01$	$0.987 < 0.01$	0.987 ± 0.02

Table 6.3: Scale factors measured in several CRs.

and SSCR, a validations of the fake $\tau_{\rm had}$ is performed for the EW and QCD components respectively. A residual is taken into account as an additional non-closure systematic uncertainty. In the low-$E_{\rm T}^{\rm miss}$ categories, results of the TCR are propagated into b-veto regions. The result from the WCR in the b-veto is not used for correcting the fake $\tau_{\rm had}$ background. It is used for validation of the fake $\tau_{\rm had}$

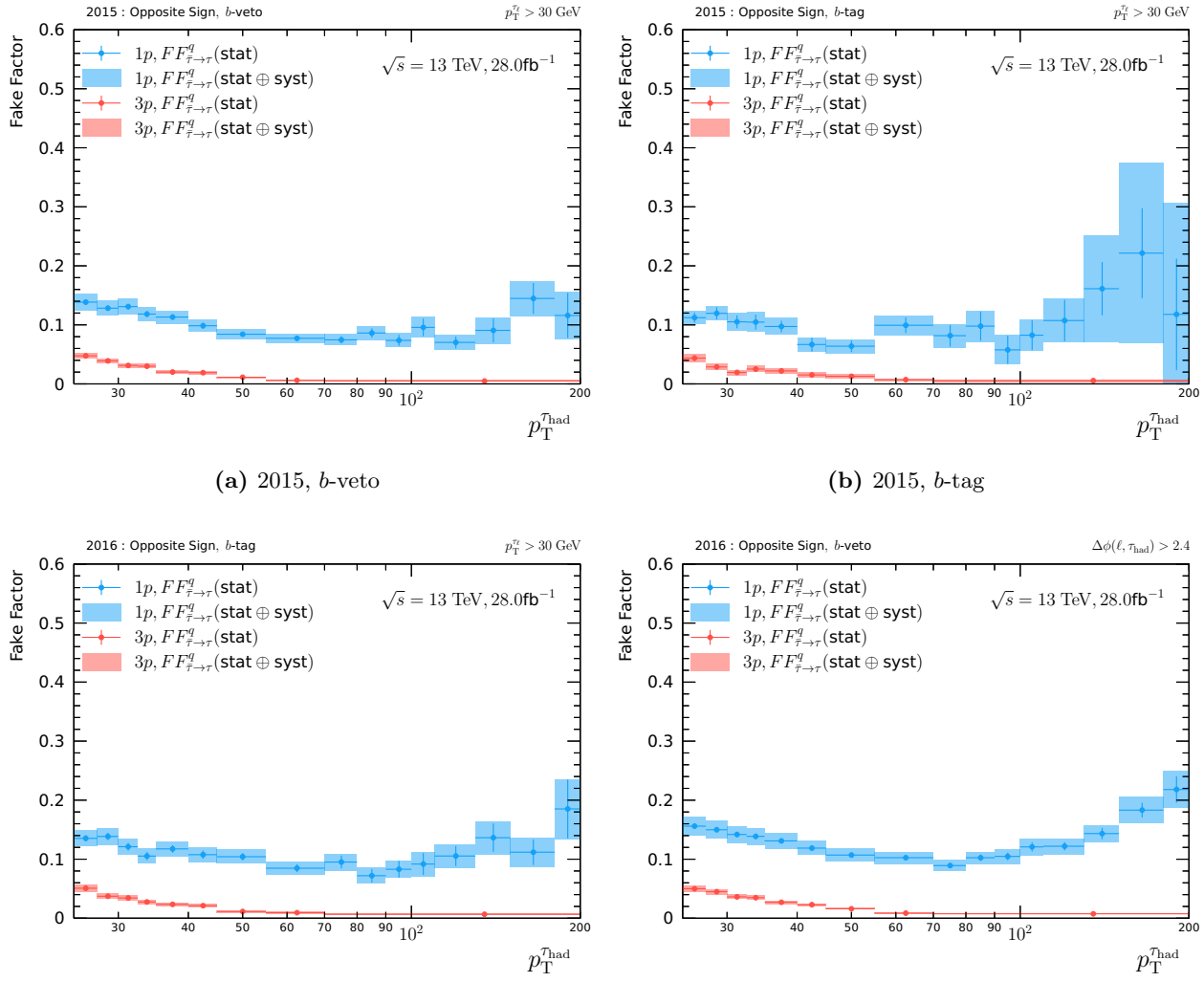

(a) 2015, *b*-veto **(b)** 2015, *b*-tag

(c) 2016, *b*-veto **(d)** 2016, *b*-tag

Figure 6.17: The fake factors for the QCD components, $FF^{q}_{\tau\to\tau}$ as a function of visible-τ p_{T} for 1-prong (blue) and 3-prong (red). Plots (a,b) and (c,d) shows the fake factors of 2015 and 2016 data-taking period respectively. The fake factors are splitted events with *b*-veto (a,c) and *b*-tag (b,d) respectively. In each plots, points with marker present center values and its statistical uncertainty, while filled regions present total uncertainty including all systematic uncertainties.

background and assigning an additional uncertainty as a non-closure systematic uncertainty. Diboson process is too small to validate its accuracy and there are no regions which can measure them.

6.6 Systematic Uncertainties

To extract experimental results, various systematic uncertainties are taken into account together with the statistical uncertainty. There are various systematic uncertainties on the physics object reconstruction and calibration. The theoretical modelling of signal and background processes, as well as on the background modelling are considered.

It affects the number of expected signal and background events in the analysis regions. The systematic uncertainties is splitted into two type of systematic uncertainties, “acceptance” and “shape”

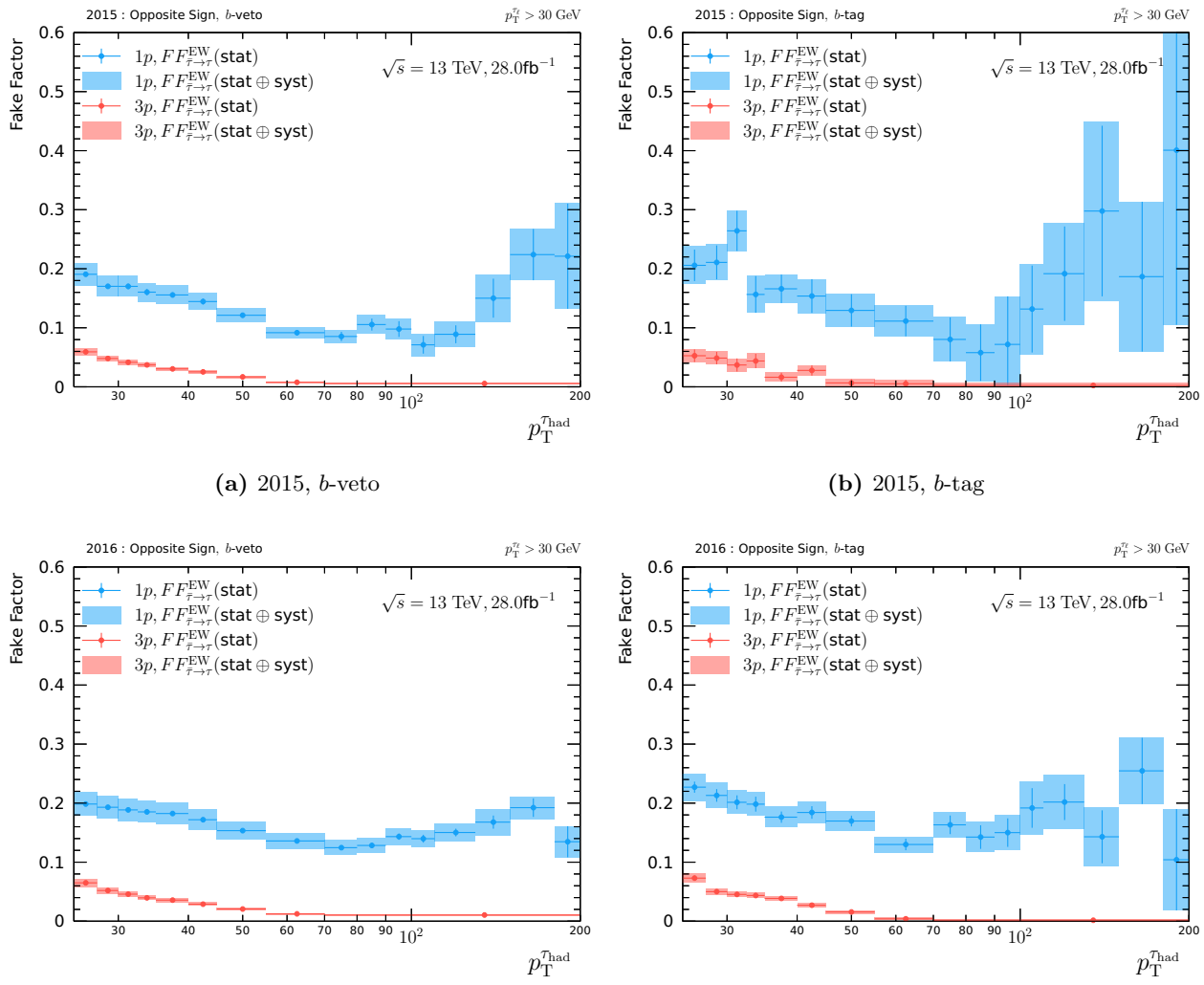

(a) 2015, *b*-veto **(b)** 2015, *b*-tag

(c) 2016, *b*-veto **(d)** 2016, *b*-tag

Figure 6.18: The fake factors for the EW components, $FF^{\mathrm{EW}}_{\tau\to\tau}$ as a function of visible-τ p_{T} for 1-prong (blue) and 3-prong (red). Plots (a,b) and (c,d) shows the fake factors of 2015 and 2016 data-taking period respectively. The fake factors are splitted events with *b*-veto (a,c) and *b*-tag (b,d) respectively. In each plot, points with marker present a center value and its statistical uncertainty, while filled regions present total uncertainty including all systematic uncertainties.

uncertainties. The acceptance uncertainty does not change a shape of final discriminating variable. It changes only event weights[12]. While a shape uncertainty changes its kinematic distributions, so it is propagated to the final discriminating distributions[13]. Further grouping is done with respect to source of uncertainty, an experimental and theoretical uncertainties. The various systematic uncertainties are summarised in this section. Their inclusion into the combined likelihood fit and their impact on the final analysis result is discussed in Section 7.1. Description of the experimental systematic uncertainties are given in Section 6.6.1. The theoretical systematic uncertainties are briefly described in Section 6.6.2. Detailed values of each systematic uncertainties for all relevant background and signal processes are shown in Appendix E.

[12] for example a analysis scale factor of the hadronic-τ identification efficiency.
[13] for example a transverse momenta of lepton or hadronic-τ.

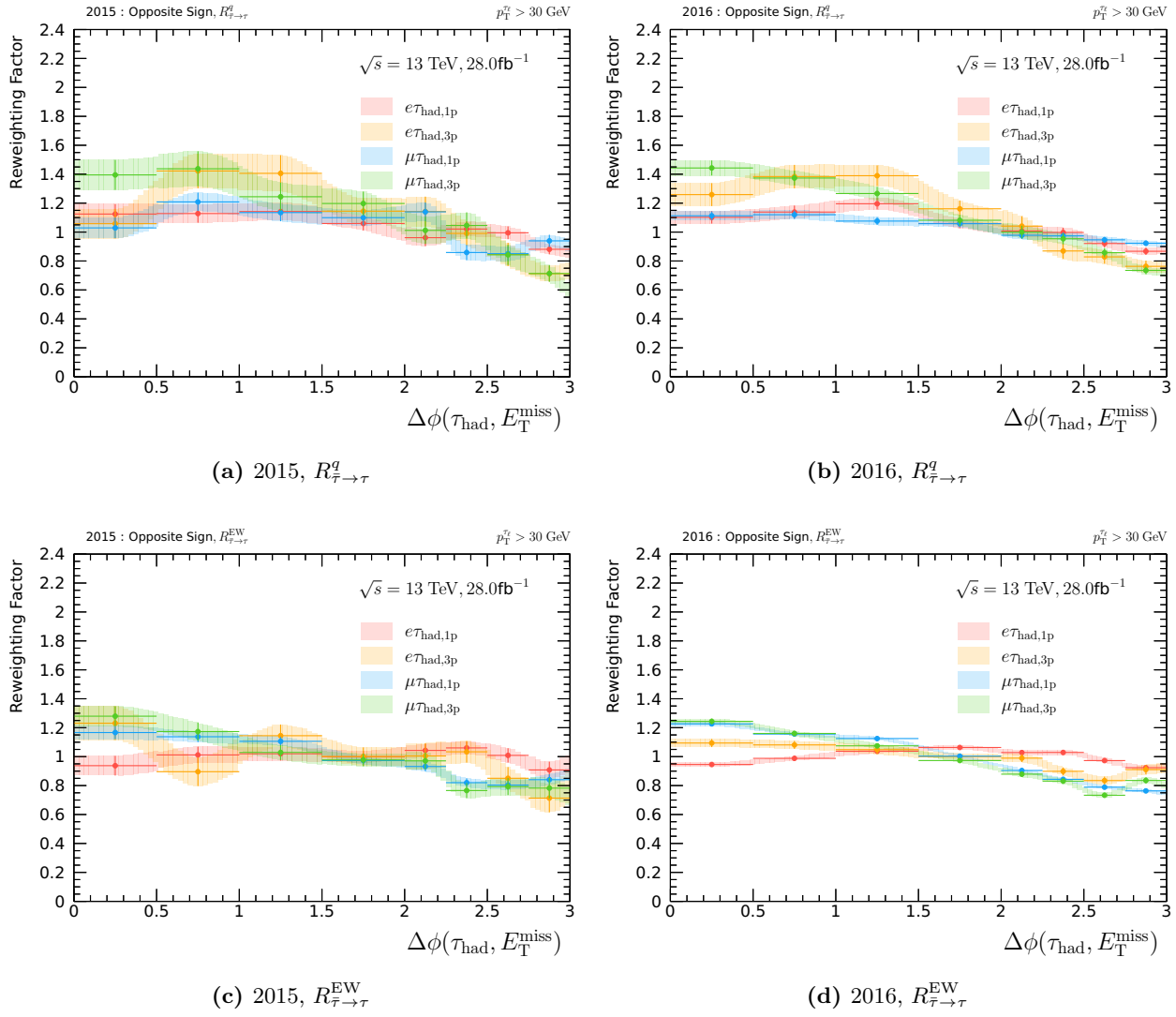

(a) 2015, $R^{q}_{\tau\to\tau}$ **(b)** 2016, $R^{q}_{\tau\to\tau}$

(c) 2015, $R^{\mathrm{EW}}_{\tau\to\tau}$ **(d)** 2016, $R^{\mathrm{EW}}_{\tau\to\tau}$

Figure 6.19: The correction factor $R^{q}_{\tau\to\tau}, R^{\mathrm{EW}}_{\tau\to\tau}$ for two data-taking period with four decay mode channels. Filled regions represent uncertainty bands, which applied interpolation with the PCHIP technique to perform stable smoothing from original points with filled circle.

6.6.1 Experimental Uncertainties

The performance of the particle reconstruction, calibration, identification and the trigger performance is measured in real data. The respective uncertainties are discussed in Chapter 5. All such uncertainties are propagated and compared to the nominal expectation. Such uncertainties affect only simulated events. The experimental systematic uncertainties are summarised correspondingly the physics objects in the following. The systematic uncertainty of data-driven background modelling is also described.

Missing Transverse Energy, $E_{\mathrm{T}}^{\mathrm{miss}}$

Since the $E_{\mathrm{T}}^{\mathrm{miss}}$ is reconstructed from several physics objects, the energy resolution and scale are taken into account from each physical objects uncertainties. The soft-term is enough for the systematic uncertainties. Two systematic uncertainties is defined as the soft-term systematic uncertainties. A measurement of resolution is performed using Z+jets event samples, and it is defined as in direction

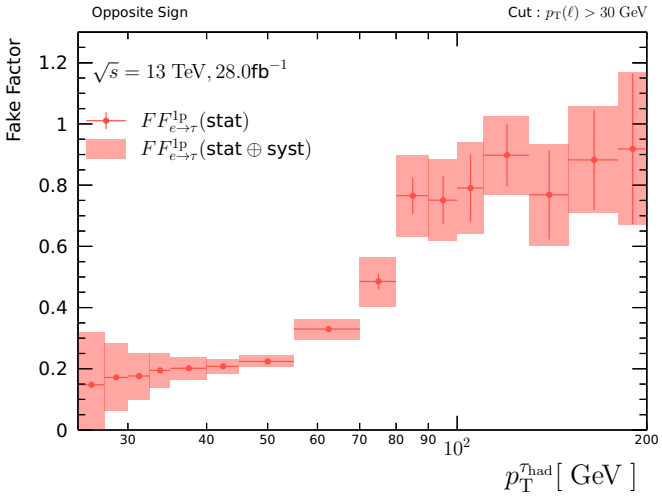

Figure 6.20: The $e \to \tau_{\text{had}}$ fake factor for the $e\tau_{\text{had}}$ 1prong channel as a function of the visible-τ p_{T}. Each points with marker present center values and statistical uncertainty, while filled regions present total uncertainty including systematic uncertainty.

of p_{T}^{Z}. An absolute and accidental effect of is measured in the parallel direction of p_{T}^{Z}. While in perpendicular direction it slightly depends on p_{T}^{Z} accuracy and it is affected by muons or electrons momentum resolution. The soft-term resolution uncertainty is evaluated using the vector sum of all soft tracks. It is splitted into the parallel and perpendicular direction. The uncertainty on the soft-term scale is calculated using track parameters. In addition to the soft-term systematic uncertainties, the $E_{\text{T}}^{\text{miss}}$ trigger efficiency uncertainty is also assigned.

Electrons

The electron object has four acceptance uncertainties related to efficiency of the reconstruction, identification, isolation and trigger. In addition to acceptance uncertainties, several shape uncertainties are evaluated, one energy resolution and six energy calibration scale uncertainties. All uncertainties are summarised in Table D.13. The uncertainty of the LAr calorimeter simulation is evaluated by 2015 and 2016 data-taking conditions separately. The four acceptance uncertainties are measured using the $Z \to ee$ tag-&-probe method as described in Section 5.4.

Muons

The muon object has four acceptance uncertainties related to the efficiency of the reconstruction, TTVA (Track-to-vertex-association), isolation and trigger. One energy resolution and six energy calibration scale uncertainties are evaluated as the shape uncertainty. All uncertainties are summarised in Table D.13. The four acceptance uncertainties are measured using the $Z \to \mu\mu$ tag-&-probe method as described in Section 5.5. All acceptance uncertainties have two type of uncertainties correspond to statistical and systematic uncertainties on its efficiency measurements.

Jets

There are one acceptance and several energy scale and resolution shape uncertainties in the jet objects. The jet vertex tagging (JVT), jet energy scale (JES), resolution (JER) and flavour tagging (FT) is summarised in Table D.13 . The FT Eigen uncertainties are statistically determined by smoothing algorithm of transverse momentum of b-,c- and light-quark using the Kernel density estimator with the local polynomial function. This technique performs a smoothing of input distributions using locally optimised polynomial functions which has the same number of functions as input data points. The systematic uncertainties which has same or similar shape of the Kernel density are merged into one combined systematic uncertainty with certain threshold of merging. The JES has similar grouping, but this is performed by some assumptions depending on its measurement procedures. The JER is measured by several physics processes and its uncertainty is evaluated by taking difference between

measurements.

Hadronic-τ

Uncertainties on the hadronic-τ object are one of important systematic uncertainties in this analysis. There are six acceptance uncertainties and three shape uncertainties corresponds to the tau energy scale (TES). Table D.13 summarises their uncertainties and its type. For the identification uncertainties, an extrapolation is performed from low p_{T} into higher p_{T} events ($p_{\mathrm{T}} > 250$ GeV) due to a lack of data with high p_{T} τ. High-p_{T} systematic uncertainties have additional $10 \sim 20\%$ uncertainties including sample dependence and extrapolation procedure difference. Uncertainty of TES is one of important systematic uncertainties in this analysis. It directly changes the $m_{\tau\tau}$ shape, so it is assigned as the shape nuisance parameter as described in Section 7.2.

Background Modelling Uncertainties

As shown in Section 6.5.1, several uncertainties are assigned corresponding background estimations. Besides the fake τ_{had} background, uncertainties on correction for $t\bar{t} \to \ell\tau_{\mathrm{had}}$ and $Z \to \tau\tau$ process, as well as fake τ_{had} non-closer should be taken into account.

Luminosity and Pile-up

The luminosity uncertainty is determined by the forward detector and with the var-der-Meer scan as described in Section 4.2.5. The Luminosity uncertainty depends on the data-taking period, for the 2015 and 2016 data-taking it is estimated as 2.8% and 5% respectively. The pile-up reweighting as described in Section 3.1.6, the uncertainty on this technique is derived by an error of fitting to observed correlation between ($\langle\mu\rangle$, nPV).

6.6.2 Theoretical Uncertainties

As uncertainties on theoretical calculation, modelling and assumption are estimated by changing its tuning parameters or different calculation model. The parton distribution function, the factorisation and renormalization scale and the MC tuning is considered in this analysis. In addition to these uncertainties, the difference between alternative MC generator is also taken into account for the background processes.

PDF Uncertainties

The PDF fit contains inherent uncertainties due to the fitting procedure. These uncertainties are propagated to the final observable. As sundry PDF sets are provided from different collaborations, there are The difference of center values among alternative PDF sets is taken into account as a systematic uncertainty. `CT10(CT14)`, `MMHT2014`, `NNPDF3.0` are commonly used for this purpose. For signal processes, the `CT10` is used, so two other PDF sets are used to take variations[14]. This variation is performed by reweighting scheme, this makes the assumption that to change the PDF used in the matrix element is negligible in the parton shower evolution. Secondary effect is dependency of the initial state radiation and underlying event, it is also treated by following approach.

$$w = \frac{pdf_{\mathrm{new}}(x_1, f_1, Q) \times pdf_{\mathrm{new}}(x_2, f_2, Q)}{pdf_{\mathrm{old}}(x_1, f_1, Q) \times pdf_{\mathrm{old}}(x_2, f_2, Q)}, \tag{6.16}$$

where x_1, x_2 is parton density, pdf_{old} and pdf_{new} is the original and compared value of the PDF. Totally 101 variations exist in each PDF set, so the maximum variation is symmetries and taken as

[14] These PDF sets agree well on the gluon-gluon initiated process, while disagrees on the valence PDF and also the quark-gluon process.

the total PDF uncertainty.

Factorisation and Renormalization Scale Uncertainties

Since the factorisation and renormalization scale are not physical parameters, but parameters for calculating physical observable and its cross sections. In principle, it is not expected that the observable depends on the factorisation and renormalization scale, to ensure this dedicated test is performed. The factorisation and renormalization $\mu_{F,R}$ is varied by factor 0.5 to 2.0, and its deviation is taken into account as a systematic uncertainty.

MC Tuning Uncertainties

The final to consider are the uncertainties corresponding the Monte Carlo tuning. For this purpose, there are established methodology. Since two signal processes are made by different MC generators with different PDF set and tuning. Table F.13 and F.13 summarise internal parameter variations for the MC tuning variation based on Reference [185]. For both signal processes, there are different variation sets, the gluon-fusion samples has three variations, while the bottom-annihilation samples has five variations.

Uncertainties on Signal Modelling

The uncertainties on the signal acceptance which are considered as normalisation uncertainties It is evaluated by alternative samples with truth particle information. In addition to use truth samples, it is not realistic to generate truth event samples for all signal process including different mass hypothesis. It is compromised to use three different mass hypothesis, the 200, 500, 1000 GeV are choices. The results are shown in below Eq. (6.17).

$$f_{\mathrm{ggH}} = 18.4654 - 0.0027954 \times m_{\mathrm{A}}\ (\%) \tag{6.17}$$

$$f_{\mathrm{bbA}} = 17.6896 + 0.0059865 \times m_{\mathrm{A}}\ (\%) \tag{6.18}$$

In order to use for all mass samples, a linear fit is performed for total uncertainties by results summarised in Table D.13.

Uncertainties on Background Modelling

Theoretical cross-section uncertainties for Z+jets and diboson process is assigned as 5% and 6% respectively based on Reference [**Butterworth:1287902**]. For the $t\bar{t}$ process, five variation is evaluated. Table F.13 summerizes various systematic uncertainties for $t\bar{t}$ processes. Figure 6.21 shows variations for three dedicated uncertainties on $t\bar{t}$ sample using alternative simulated samples. For $Z \to \tau\tau$ background process, an addtional uncertainty is evaluated using the ZCR events as shown in Figure 6.21 (b).

6.7 Results

The results as described in the preceding sections is given in this section.

Several important variables are shown in Figure 6.22 - Figure 6.24. For di-τ mass distributions, the total transverse mass is chosen as a final discriminant.

Table 6.4 shows event yields for three signal regions with statistical uncertainty only, the systematic uncertinties are described in Section 6.6.

Process	$e\tau_{\text{had}}$		$\mu\tau_{\text{had}}$	
	1-prong	3-prong	1-prong	3-prong
		high-$E_{\text{T}}^{\text{miss}}$		
Diboson	5.1 ± 1.0	1.3 ± 0.5	34 ± 3.1	10 ± 2.1
$j \to \tau_{\text{had}}$	126 ± 4.5	29 ± 0.9	901 ± 11	208 ± 2.3
$t\bar{t} \to \ell\tau_{\text{had}}$	49 ± 3.5	19 ± 2.2	323 ± 9	117 ± 5.6
$Z \to \tau\tau$	25 ± 6.2	18 ± 7.2	171 ± 19	62 ± 10
Total	205 ± 8.5	67 ± 7.6	$1\,429 \pm 24$	397 ± 12
Signal	10 ± 3.1	3.5 ± 1.1	40 ± 10	14 ± 3.4
Data	194	57	1451	387
		b-tag		
Diboson	8.0 ± 1.7	2.8 ± 1.0	6.2 ± 1.6	0.6 ± 0.8
$\ell \to \tau_{\text{had}}$	126 ± 6.6	1.7 ± 0.8	77 ± 17	< 0.1
$j \to \tau_{\text{had}}$	$1\,344 \pm 15$	309 ± 3.3	$1\,277 \pm 13$	335 ± 3.4
$t\bar{t} \to \ell\tau_{\text{had}}$	708 ± 14	261 ± 8.5	676 ± 14	232 ± 8.0
$Z \to \tau\tau$	301 ± 29	135 ± 22	381 ± 34	138 ± 18
Total	$2\,487 \pm 36$	710 ± 24	$2\,417 \pm 43$	706 ± 20
Signal	9.3 ± 2.5	3.6 ± 1.0	3.8 ± 1.1	1.3 ± 0.4
Data	2286	709	2668	818
		b-veto		
Diboson	338 ± 11	113 ± 6.4	467 ± 12	134 ± 6.4
$\ell \to \tau_{\text{had}}$	$5\,612 \pm 39$	36 ± 2.9	$9\,292 \pm 182$	60 ± 16
$j \to \tau_{\text{had}}$	$30\,692 \pm 70$	$9\,669 \pm 20$	$29\,227 \pm 70$	$8\,365 \pm 19$
$t\bar{t} \to \ell\tau_{\text{had}}$	177 ± 6.9	60 ± 4.1	161 ± 6.4	61 ± 3.9
$Z \to \tau\tau$	$22\,725 \pm 224$	$8\,411 \pm 136$	$32\,061 \pm 264$	$12\,312 \pm 162$
Total	$59\,545 \pm 239$	$18\,290 \pm 138$	$71\,208 \pm 328$	$20\,932 \pm 164$
Signal	18 ± 4.2	5.8 ± 1.4	8.0 ± 2.0	2.0 ± 0.5
Data	59729	17434	68182	20272

Table 6.4: Events yields for three signal regions with four decay channels. As a signal $m_{\text{A}} = 600\,\text{GeV}$ and $\tan\beta = 15$ is assumed.

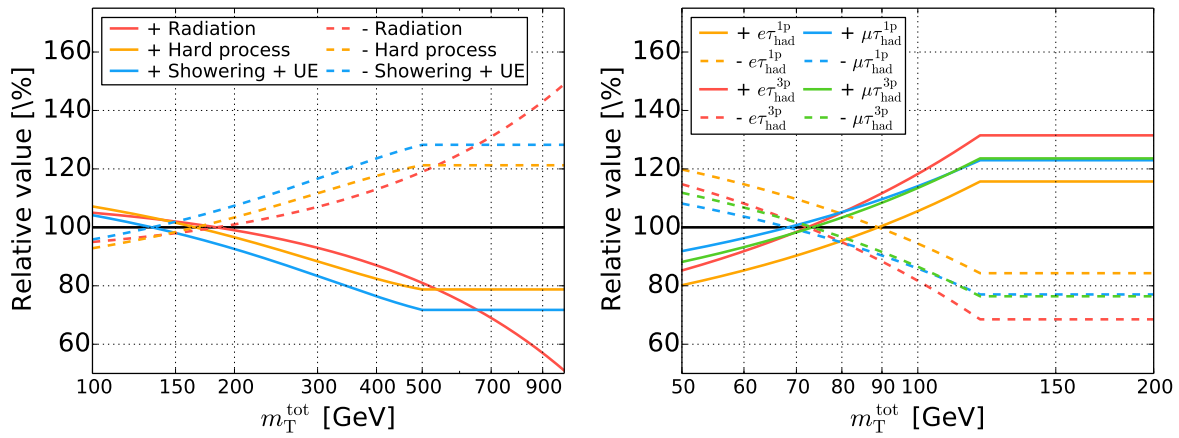

(a) $t\bar{t}$ **(b)** $Z \to \tau\tau$

Figure 6.21: Systematic uncertainties for $t\bar{t}$ process (a) with variation of radiation (red lines), hard process (blue line) and showering + underlying uncertainties as a function of final discriminant variable ($m_{\mathrm{T}}^{\mathrm{tot}}$). From 500 GeV, it is not relevant to estimated them due to a lack of event statistics, so an extrapolation is performed. And hard process uncertainty for $Z \to \tau\tau$ process (b) with + and - variation from comparison between nominal and alternative simulated sample.

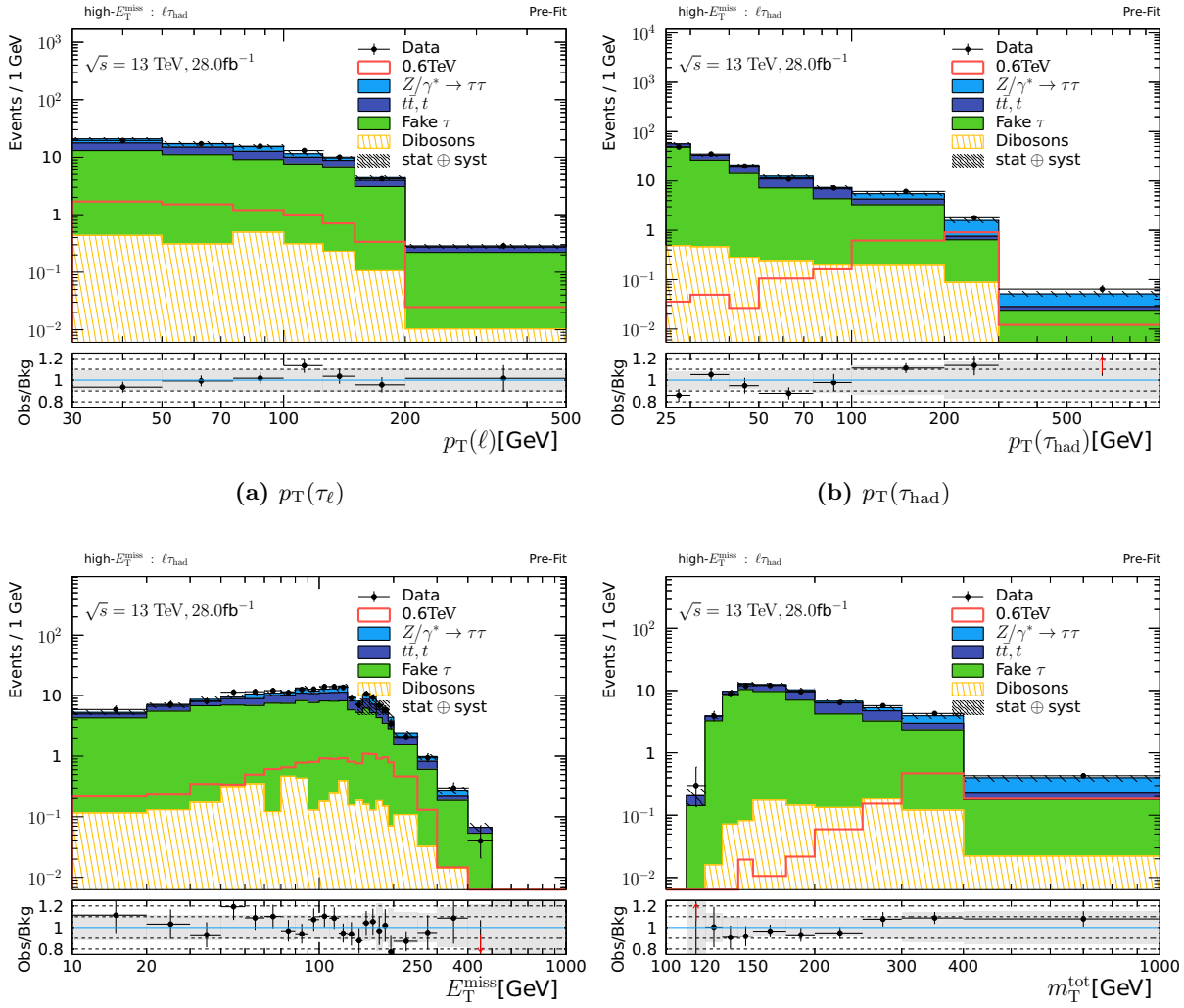

(a) $p_{\mathrm{T}}(\tau_\ell)$ **(b)** $p_{\mathrm{T}}(\tau_{\mathrm{had}})$

(c) $E_{\mathrm{T}}^{\mathrm{miss}}$ **(d)** $m_{\tau\tau}$

Figure 6.22: Distributions for several variables in the high-$E_{\mathrm{T}}^{\mathrm{miss}}$ category. In the bottom panels a ratio of data and expected background model and the uncertainties correspond to the statistical uncertainties are shown. The signal process is assumed $m_{\mathrm{A}} = 600\,\mathrm{GeV}$ and $\tan\beta = 15$ with the gluon-fusion and bottom-annihilation production processes.

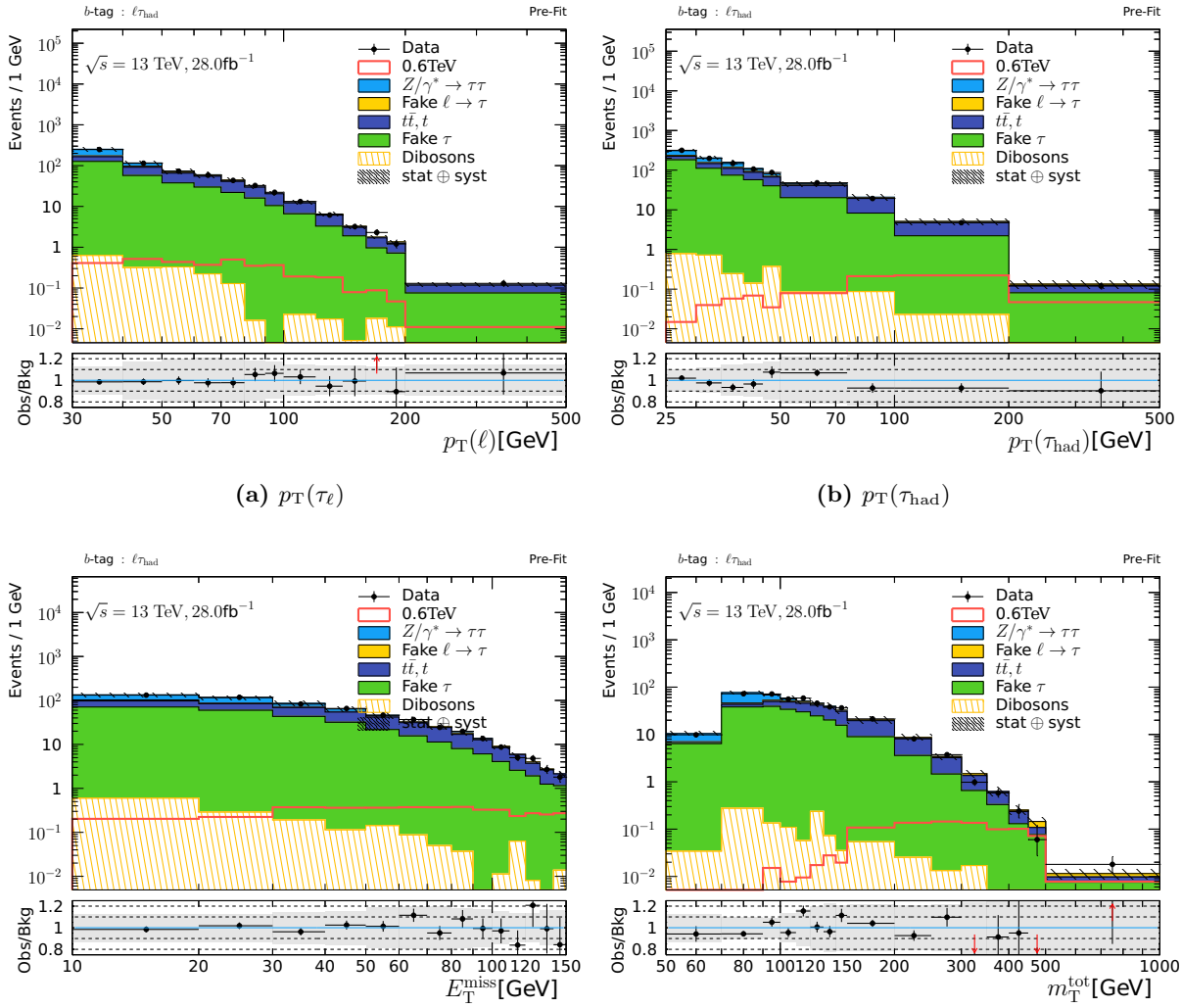

(a) $p_{\mathrm{T}}(\tau_\ell)$ **(b)** $p_{\mathrm{T}}(\tau_{\mathrm{had}})$

(c) $E_{\mathrm{T}}^{\mathrm{miss}}$ **(d)** $m_{\tau\tau}$

Figure 6.23: Distributions for several variables in the b-tag category. In the bottom panels a ratio of data and expected background model and the uncertainties correspond to the statistical uncertainties are shown. The signal process is assumed $m_{\mathrm{A}} = 600\,\mathrm{GeV}$ and $\tan\beta = 15$ with the gluon-fusion and bottom-annihilation production processes.

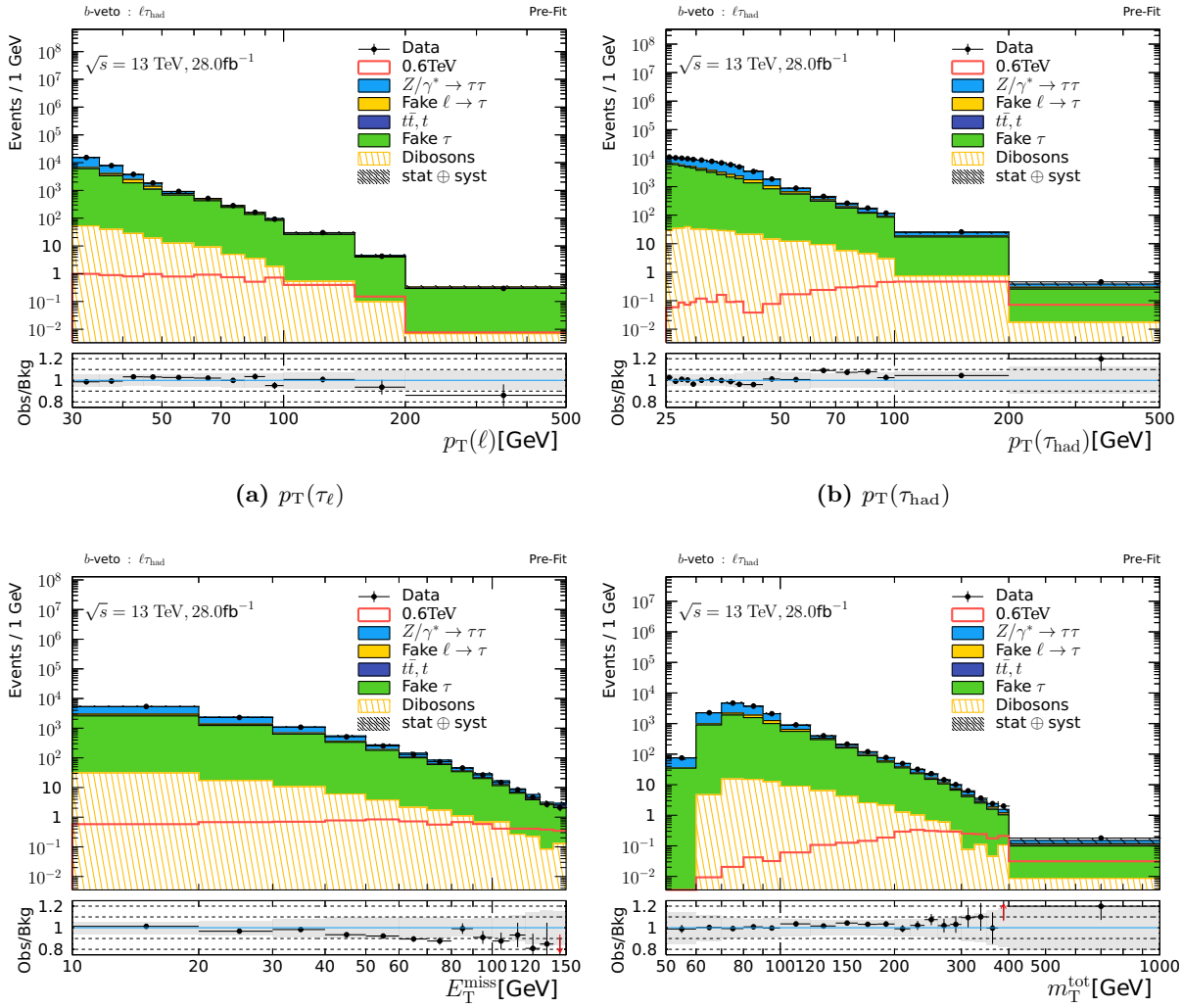

(a) $p_{\text{T}}(\tau_\ell)$ **(b)** $p_{\text{T}}(\tau_{\text{had}})$

(c) $E_{\text{T}}^{\text{miss}}$ **(d)** $m_{\tau\tau}$

Figure 6.24: Distributions for several variables in the b-veto category. In the bottom panels a ratio of data and expected background model and the uncertainties correspond to the statistical uncertainties are shown. The signal process is assumed $m_{\text{A}} = 600\,\text{GeV}$ and $\tan\beta = 15$ with the gluon-fusion and bottom-annihilation production processes.

7 Statistical Analysis of the Search for $H/A \to \tau_\ell \tau_{\mathrm{had}}$ Decays

The combined likelihood fit is described in this chapter. The general concept of the maximum likelihood fit and likelihood function is introduced in Section 7.1. The likelihood function needs to reflect the various statistical and systematic uncertinties of the background and signal expectation. The parameterization of the signal event rate and the compatibility of the data with the background-only-hypothesis is quantified using a hypothesis test described in Section 7.3. The statistical result and an interpretation of signal hypothesis is presented in Section 7.4

7.1 The Profile Likelihood Function

An extended maximum-likelihood fit to the observed data is used to estimate the parameters of the combined signal and background model, including the signal strength parameter μ. The probability-density-function (PDFs) of the background and signal model are denoted as $f_B(x;\boldsymbol{\theta})$ and $f_S(x;\boldsymbol{\theta})$ respectively. It is a function of an observable x and normalised to unity. A set of parameter $\boldsymbol{\theta}$, nuisance parameters (NP), reflects PDFs. The NPs reflects several systematic uncertainties, but it is not the primary goal of the analysis. The PDFs will consists of several contributions from various physics processes as discussed above chapters. The probability to observed N events in data with the expected number of signal and background events S and B can be written as

$$\mathcal{P}(x;\mu,\boldsymbol{\theta}) = \frac{e^{-(\mu S+B)}(\mu S+B)^N}{N!}\left[\prod_e^N \frac{\mu S f_S(x_e;\boldsymbol{\theta}) + B f_B(x_e;\boldsymbol{\theta})}{\mu S + B}\right]. \tag{7.1}$$

The first term describes the Poisson probability to observed N events while expecting and the number of signal plus background events of $(\mu S + B)$. The second term describes the probability to observed the N events at values x_e of the observable x. When the data can be considered as a constant value, this probability is regarded as a function of only the parameters. The likelihood function is usually denoted as $\mathcal{L}(\mu,\boldsymbol{\theta}|x)$. A maximum-likelihood fit is used to estimate the parameters. This is performed by maximising the likelihood function given the observed data. As it is shown several analysis categories is used to enhance the analys sensitivity. This property can be incorporated by multiplying the likelihood functions defined in each categories. Eq.(7.1) is transformed as following if the input data is binned distribution, as in this analysis performs :

$$\mathcal{P}'(\boldsymbol{n_i};\mu,\boldsymbol{\theta}) = C\left[\prod_i \frac{(\mu s_i(\boldsymbol{\theta}) + b_i(\boldsymbol{\theta}))^{n_i}}{n_i!} e^{-(\mu s_i(\boldsymbol{\theta})+b_i(\boldsymbol{\theta}))}\right], \tag{7.2}$$

where n_i denotes the number of data events in i-th bin, $s_i(\boldsymbol{\theta})$ and $b_i(\boldsymbol{\theta})$ are the expected number of signal and background events in the bin and C is combinatorial constant which can be neglected in the maximisation procedure as it is constant. The various bins in the combined likelihood function may describes different categories, including those which consider the shape of an observable and other which just consider the event count.

To simplify the maximisation procedure, it is useful to consider to take logarithm of the likelihood function, since the product then decouples into a sum. It is also considered as the negative logarithm of the likelihood function (NLL) instead. `MINUIT` [200] is to solve minimisation problems, which is very common and fast. The estimators $(\hat{\mu}, \hat{\boldsymbol{\theta}})$ or best-fit values are defined as values minimising the NLL, it follows $\min(-\ln \mathcal{L}(\mu, \boldsymbol{\theta})) = -\ln \mathcal{L}(\hat{\mu}, \hat{\boldsymbol{\theta}})$. The variance of the estimators $(\hat{\mu}, \hat{\boldsymbol{\theta}})$ is defined by considering the change in the "profile" of the likelihood function. The likelihood profile is defined by $\Delta(-\ln \mathcal{L}(\theta_0, \hat{\hat{\theta}}'))$. This equation describes the absolute change of the likelihood as a function of a variable θ_0, while the likelihood is minimised with respect to all other dependencies θ' pointwise. The notation of $\mathcal{L}(\theta_0, \hat{\hat{\theta}}')$ refers to the conditional minimum of the likelihood with respect to θ' and fixed parameter θ_0. So one NP is fixed at the profiling process and other NPs are profiled to minimise the NLL. A simple likelihood depending on only one parameter θ_0 are described as :

$$\mathcal{L}(\theta_0) = \mathcal{L}_{\max} \exp\left(-\frac{(\theta_0 - \hat{\theta_0})}{2\sigma^2}\right), \tag{7.3}$$

$$-\ln \mathcal{L}(\theta_0) = -\ln \mathcal{L}_{\max} + \frac{(\theta_0 - \hat{\theta_0})}{2\sigma^2}, \tag{7.4}$$

$$\Delta\text{NLL} = \ln \mathcal{L}_{\max} + -\ln \mathcal{L}(\hat{\theta_0} + \sigma). \tag{7.5}$$

This leads that the uncertainty of a parameter θ_0 can be obtained from value which the NLL differ by 1/2 from the its minimum. This procedure can be generalised for multidimensional likelihood functions.

7.2 Treatment of Systematic Uncertainties

The systematic uncertinties are propagated into the analysis by taking same analysis after changing the corresponding parameter of uncertinties by one standard deviation. To take into account such effects, the systematic uncertinties is treated as additional measurements into the likelihood function. The likelihood function is modified by terms, assuming a Gaussian form of $P_i(\theta_i) = G(\theta_i|0,1)$ where normalised sigma by its $\pm 1\sigma$ deviation.

$$\mathcal{L}(\mu, \boldsymbol{\theta}) = \prod_{i \in \text{bins}} \mathcal{P}'(\boldsymbol{n_i}; \mu, \boldsymbol{\theta}) \times \prod_j G\left(\theta_j|0,1\right), \tag{7.6}$$

To incorporate into the likelihood function, a smooth parameterization is considered. The $\pm 1\sigma$ values of events yields corresponding systematic uncertainty is measured in this analysis. The systematic uncertinties can have an impact on both the absolute normalisation and its differential distribution so different interpolation procedures are necessary. The number of expected events can be written as following:

$$n_{p,c,i}\left(\boldsymbol{\theta}\right) = \eta_{p,c}\left(\boldsymbol{\theta}\right) \times \sigma^{p,c,i}\left(\boldsymbol{\theta}\right) \times \nu_{p,c,i}, \tag{7.7}$$

where $\nu_{p,c,i}$ is the number of events of process p in channel c at i-th bin of parametric histogram, and η and σ denote acceptance and shape effects corresponding to nuisance parameters reflecting the

systematic uncertainties. The negative number of event is considered by an interpolation of such η and σ. A piecewise exponential and linear technique is used for acceptance and shape nuisance parameter respectively. The η and σ can be written by

$$\eta_{p,c}\ (\boldsymbol{\theta}) = 1 + \sum_{j=\text{syst}} I_{\text{exp.}}\ (\theta_j; 1, \eta^{+}_{p,c,j}, \eta^{-}_{p,c,j}), \tag{7.8}$$

$$\sigma_{p,c,i}\ (\boldsymbol{\theta}) = \sigma^{0}_{p,c,i} \prod_{j=\text{syst}} I_{\text{lin.}}\ (\theta_j; \sigma^{0}_{p,c,i}, \sigma^{+}_{p,c,i,j}, \eta^{-}_{p,c,i,j}), \tag{7.9}$$

where, $I_{\text{lin.}}$ and $I_{\text{exp.}}$ describe a piecewise linear and exponential interpolation defined as following:

$$I_{\text{lin.}}(\theta; I^0, I^+, I^-) = \begin{cases} \theta \times (I^+ - I^0) \text{ for } \theta \geq 0 \\ \theta \times (I^0 - I^-) \text{ for } \theta \leq 0 \end{cases}, \tag{7.10}$$

$$I_{\text{exp.}}(\theta; I^0, I^+, I^-) = \begin{cases} (I^+/I^0)^{+\theta} \text{ for } \theta \geq 0 \\ (I^-/I^0)^{-\theta} \text{ for } \theta \leq 0 \end{cases}. \tag{7.11}$$

The piecewise exponential interpolation does not reach at $\eta \leq 0$, this is the reason why an acceptance nuisance parameter is made up by this interpolation. While a shape nuisance parameter is constructs by i-th bin of a histogram. The likelihood function is built using the `HistFactory` [201] and `RooFit/RooStats` [202, 203] software package within `ROOT` [204] framework. `HistFactory` constructs the likelihood function based on histograms of expected event yields for all background and signal processes with all systematic uncertainties. An acceptance and shape Uncertainties is taken as `OverAllSys` and `HistoSys`, and it can be separated with different systematic uncertainties, analysis categories and physical processes.

7.2.1 Symmetrization and Smoothing

A smoothing procedure is exploited to flatten statistical fluctuations in the systematically varied histograms to avoid a statistical fluctuation. The smoothing algorithm denoted as `353QH` algorithm [205] is based on a computation of subsequent medians of the bin contents[1] To keep a track of an exact identifier of events present in each individual bin, a fraction of a nominal to varied histogram is smoothed instead of varied histogram directly. It is often happened that an upward and downward variation deviates from the nominal expectation in the same direction. Such case of one-sided systematic variation might lead multiple minima in the likelihood minimisation procedure and disturb to find true minima. The most of such one-sided variations are caused by statistical fluctuation, to avoid this situation it is set to lower variation to nominal expectation.

7.2.2 Pruning and Systematic Uncertainties Type

A lot of systematic variation is introduced in the likelihood function, but there might be variations which does not have any impact on the result. As the complexity of the likelihood function takes longer processing time with the number of shape degrees of freedom, it is desirable to reduce their number. For this purpose, a number of tests is applied to each systematic variation in order to reduce them. All tests are performed before the smoothing and symmetrization, and it is not done for theoretical uncertinties. The test is denoted as "pruning" in the following. Figure 7.1 shows relative differences on the expected significance as a function of a pruning threshold for shape (red) and overall (blue) variations. The pruning criteria is described in following. Applying the Symmetrization

[1] It computes two medians which constructed by three bins and five bins around the bin and checks its difference.The algorithm is implemented in the `ROOT` framework.

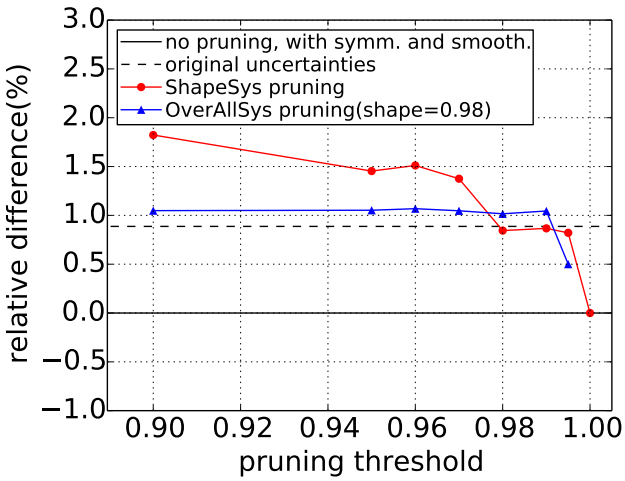

Figure 7.1: Relative difference in the expected discovery significance at $m_{\mathrm{A}} = 600$ GeV mass point. Points with red circle represent a pruning criteria on shape variations, while blue triangles show on overall variations. Solid line is uncertinties with symmetrization and smoothing, but not applied pruning criteria. Broken line is uncertinties from original variations.

and smoothing procedure effectively increases the systematic uncertinties and lowers the significance by about 0.9%. It is relevant to compare with this 0.9% for a shape and overall systematic pruning. About the shape pruning, relative differences increase significantly, the pruning threshold of 0.98 is obtained. While the overall pruning rapidly increases after threshold of 0.995, so that the pruning threshold of 0.995 (0.5%) is obtained.

χ^2 Test

The compatibility between the nominal and varied histograms is tested using following χ^2 definition :

$$\chi^2_{\mathrm{u,d}} = \sum_{i \in \mathrm{bins}} \frac{(N^{\mathrm{tot}}_{\mathrm{nom}} N^i_{\mathrm{nom}} - N^{\mathrm{tot}}_{\mathrm{u,d}} N^i_{\mathrm{u,d}})^2}{(N^{\mathrm{tot}}_{\mathrm{nom}} \sigma^i_{\mathrm{nom}})^2 + (N^{\mathrm{tot}}_{\mathrm{u,d}} \sigma^i_{\mathrm{u,d}})^2} \tag{7.12}$$

where $N^{i,\mathrm{tot}}_{\mathrm{nom}}$ and $N^{i,\mathrm{tot}}_{\mathrm{u,d}}$ refer to the bin content and total of the nominal and up/down varied histogram, and σ_{nom} and $\sigma_{\mathrm{u,d}}$ is the statistical uncertainties of the bin content among nominal and varied histogram. The p-values under a χ^2 distribution with the degrees of freedom given by the number of histogram bins are obtained for up/down variation respectively and its minimum among up and down variation: $p = \min\{P_{\chi^2}\ (\chi^2_u), P_{\chi^2}\ (\chi^2_d)\}$. If the p-values are greater than 0.98, then corresponding variations are taken into account only an acceptance uncertainty (`OverAllSys`). Besides a shape of variation, its acceptance variation is tested by checking same χ^2 but with only event yields. If it is greater than 0.5%, then it is assigned as an acceptance variation. These two tests are independently checked.

Kolmogorov-Smirov Test

The pruning using a "Kolmogorov-Smirov" test is considered as well as the χ^2 based test described above. A normalisation is not considered, only a difference of shape is considered.

Maximum Deviation Test

If the maximum relative deviation of the varied histogram to the nominal histogram among all bins is smaller than 0.5%, it is considered as only an acceptance uncertainty.

7.3 Hypothesis Testing

Definitions of several quantity are given based on Reference [206, 207]. The maximum likelihood (ML) estimates $\hat{\mu}$ and $\hat{\boldsymbol{\theta}}$, the values of the parameters that maximise the likelihood function $\mathcal{L}(\mu\boldsymbol{\theta})$ and equivalently, minimise $-\ln\mathcal{L}(\mu,\boldsymbol{\theta})$. The first to consider is the test statistic and the profile likelihood ratio as given in following:

$$\lambda(\mu) = \frac{\mathcal{L}\ (\mu, \hat{\hat{\boldsymbol{\theta}}}(\mu))}{\mathcal{L}\ (\hat{\mu}, \hat{\boldsymbol{\theta}})}, \tag{7.13}$$

where $\hat{\hat{\boldsymbol{\theta}}}$ is the conditional maximum likelihood estimate, which maximises the likelihood function with fixed μ, it is often called "the profiled value of $\boldsymbol{\theta}$". The profile likelihood ratio $\lambda(\mu)$ depends on the parameter of interest μ, but not on the nuisance parameters $\boldsymbol{\theta}$ which have been eliminated via "'profiling'. In any physical theory the rate of signal events would have non-negative values, this leads a constraint of $\mu > 0$. It is convenient to allow $\mu < 0$ in minimisation step, so a trick is used to avoid complication at the boundary of $\mu = 0$ in Reference [206]. The profile likelihood ratio follows this modification as :

$$\tilde{\lambda}(\mu) = \begin{cases} \frac{\mathcal{L}\ (\mu, \hat{\hat{\boldsymbol{\theta}}}(\mu))}{\mathcal{L}\ (\hat{\mu}, \hat{\boldsymbol{\theta}})} & \text{for } \hat{\mu} \geq 0 \\ \frac{\mathcal{L}\ (\mu, \hat{\hat{\boldsymbol{\theta}}}(\mu))}{\mathcal{L}\ (0, \hat{\boldsymbol{\theta}}(0))} & \text{for } \hat{\mu} < 0 \end{cases}. \tag{7.14}$$

This is not necessary if ensembles of pseudo-experiments are performed with "toy-Monte Carlo" techniques, But the toy-MC always takes extremely long computation time and power, so the asymptotic formulas [206] is used for all calculation as described later section. For the test statistic of discovery $\tilde{q}_0$ is used to distinguish the background-only-hypothesis, i.e. $\mu = 0$ from the alternative hypothesis $\mu > 0$:

$$\tilde{q}_0 = \begin{cases} -2\ln\tilde{\lambda}(\mu) & \text{for } \hat{\mu} > 0 \\ 0 & \text{for } \hat{\mu} \leq 0 \end{cases}. \tag{7.15}$$

For the test statistic of limiting setting $\tilde{q}_\mu$ is used to distinguish the signal produced at signal strength μ from the alternative hypothesis of signal events product at less- or more signal strength $\mu' \leq \mu$:

$$\tilde{q}_\mu = \begin{cases} -2\ln\tilde{\lambda}(\mu) & \text{for } \hat{\mu} \leq \mu \\ 0 & \text{for } \hat{\mu} > \mu \end{cases} = \begin{cases} -2\ln\dfrac{\mathcal{L}\ (\mu, \hat{\hat{\boldsymbol{\theta}}}(\mu))}{\mathcal{L}\ (0, \hat{\hat{\theta}}(0))} & \text{for } \hat{\mu} \leq 0 \\ -2\ln\dfrac{\mathcal{L}\ (\mu, \hat{\hat{\boldsymbol{\theta}}}(\mu))}{\mathcal{L}\ (\hat{\mu}, \hat{\boldsymbol{\theta}})} & \text{for } 0 \leq \hat{\mu} \leq \mu \\ 0 & \text{for } \hat{\mu} > \mu \end{cases} \tag{7.16}$$

The test statistic $\tilde{t}_\mu$ is used to similar definition as $\tilde{q}_\mu$ but with $\mu' \neq \mu$ of $\tilde{t}_\mu = -2\ln\tilde{\lambda}\ (\mu)$.

7.3.1 The Test Statistic Distribution and p-values

The observed test statistic has a given value of $\tilde{q}_\mu^{\text{obs}}$ and when the experiment repeat many times, the test statistic would take on different values. Thus, the test statistic achieves a distribution and it is denoted as $f\ (\tilde{q}_\mu|\mu,\boldsymbol{\theta})$. The p-value for a given observation under a hypothesis $(\mu,\boldsymbol{\theta})$ is the

probability defined as :

$$p_{\mu,\boldsymbol{\theta}} = \int_{\tilde{q}_\mu^{\rm obs}}^{\infty} f\ (\tilde{q}_\mu|\mu,\boldsymbol{\theta}) d\tilde{q}_\mu. \tag{7.17}$$

The important reason for using the test statistic on the profile likelihood ratio is the distribution of the profile likelihood ratio is asymptotically independent of the values of the nuisance parameters. Above definition of the p-value depends on the nuisance parameters, so the p-value are modified as following :

$$p_{\mu,\boldsymbol{\theta}} = \int_{\tilde{q}_\mu^{\rm obs}}^{\infty} f\ (\tilde{q}_\mu|\mu,\hat{\hat{\boldsymbol{\theta}}}(\mu,{\rm obs})) d\tilde{q}_\mu. \tag{7.18}$$

This is based on assumption on Wilk's theorem and Hybrid Resampling method as discussed in Reference [207, 208] (as also known in "profile construction"). To construct two-sided confidence interval, the modified frequentest method called "$\rm CL_S$" [209, 210] is introduced. A ratio of p-values, p'_μ is defined as $p'_\mu = \frac{p_\mu}{1-p_b}$ where p_b is the p-value under the background-only-hypothesis.

$$p_b = 1 - \int_{\tilde{q}_\mu^{\rm obs}}^{\infty} f\ (\tilde{q}_\mu|0,\hat{\hat{\boldsymbol{\theta}}}(\mu=0,{\rm obs})) d\tilde{q}_\mu. \tag{7.19}$$

The upper-limit on μ $\rm CL_S$ is obtained by solving for $p'_\mu = 5\%$ for 95% confidence-level, which is denoted by μ_{95} Statistically, a discovery means that to reject the background-only hypothesis, this is calculated by p_0 as defined following:

$$p_0 = \int_{\tilde{q}_0^{\rm obs}}^{\infty} f\ (\tilde{q}_0|0,\hat{\hat{\boldsymbol{\theta}}}(\mu=0,{\rm obs})) d\tilde{q}_0. \tag{7.20}$$

Based on the p_0 the significance of the result can be written as $Z = \Phi^{-1}(1-p_0)$, where Φ^{-1} is the inverse of the cumulative distribution for a Gaussian with unit parameters. Conventionally the standard discovery significance is 5σ corresponding to $p_0 = 2.87 \cdot 10^{-7}$ in the particle physics.

Other important quantities are introduced, the expected sensitivity for limits and discovery and its uncertainty bands are calculated by similar way. The expected limit is the upper limit which would expect to obtain if the background-only hypothesis is true. In order to find the expected limit and significance, a distribution of $f(\mu_{\rm up}|\mu=0,\boldsymbol{\theta})$ and $f(p_0|\mu=1,\boldsymbol{\theta})$ are necessary respectively. These distributions depend on the nuisance parameters which are unknown without measuring observed data. So that the nuisance parameters need is profiled based on observed data, this leads that two distributions are re-written as $f(\mu_{\rm up}|0,\hat{\hat{\boldsymbol{\theta}}}(\mu=0,{\rm obs}))$ and $f(p_0|1,\hat{\hat{\boldsymbol{\theta}}}(\mu=1,{\rm obs}))$ respectively. Using above definition, $\pm1,2\sigma$ bands around the median upper limit is defined as following :

$$\int_0^{\mu_{\pm1,2}} f(\mu_{\rm up}|0,\hat{\hat{\boldsymbol{\theta}}}(\mu=0,{\rm obs})) d\mu_{\rm up} = \Phi^{-1}(\pm1,2), \tag{7.21}$$

where $\mu_{\pm1,2}$ present $\hat{\mu} \pm 1\Delta\mu, 2\Delta\mu$.

7.3.2 Asymptotic Formulas and Asimov Data

Integration of the test statistic is performed using the asymptotic formulas introduced on Reference [206] instead of performing the toy-MC. As a result of Wald's theorem [211], the test statistic is

approximated as :

$$-2\ln\lambda(\mu) = \frac{(\mu-\hat{\mu})^2}{\sigma^2} + \mathcal{O}(1/\sqrt{N}), \tag{7.22}$$

where N represents the data sample size. Here, $\hat{\mu}$ follows a Gaussian distribution with a standard deviation σ and mean μ'. If V denotes the covariance matrix of the estimation for all the parameter including the parameter of interests μ, the standard deviation σ of $\hat{\mu}$ is obtained by $V_{ij} = \mathrm{cov}[\hat{\theta}_i], \hat{\theta}_j$ and take $\theta_0 = \mu, \sigma^2 = V_{00}$. In the limit of large data sample, the bias term of the maximum likelihood estimators can be neglected, so the inverse of the covariance matrix is written as :

$$V_{ij}^{-1} = -E\left[\frac{\partial^2\mathcal{L}}{\partial\theta_i\partial\theta_j}\right], \tag{7.23}$$

where the expectation value assumes a signal strength parameter μ'. The asymptotic formulae needs this σ, for this purpose the "Asimov" dataset is constructed by sum of the number of expected events. By using the Asimov dataset, a mean value of μ' gives $\hat{\mu} = \mu'$ and the test statistic is approximated as:

$$-2\ln\lambda_A(\mu) \approx \frac{(\mu-\mu')^2}{\sigma^2}, \quad \text{with} \quad \sigma = \frac{\mu-\mu'}{\sqrt{q_{\mu,A}}} \tag{7.24}$$

where the test statistic under the Asimov dataset satisfies $q_{\mu,A} = \lambda_A(\mu)$. For the hypothesis assuming μ, it becomes $\mu' = 0$, a mean value is obtained as $\sigma \sim \mu/\sqrt{q_{\mu,A}}$.

By using the asymptotic formulae the probability density function $f(\tilde{q}_0|\mu')$ is approximated by

$$f(\tilde{q}_0|\mu') = \left(1-\Phi\left(\frac{\mu'}{\sigma}\right)\right)\delta(q_0) + \frac{1}{2}\frac{1}{\sqrt{2\pi}}\frac{1}{\sqrt{q_0}}\exp\left[-\frac{1}{2}\left(\sqrt{q_0}-\frac{\mu'}{\sigma}\right)\right], \tag{7.25}$$

$$f(\tilde{q}_0|0) = \frac{1}{2}\delta(q_0) + \frac{1}{2}\frac{1}{\sqrt{2\pi}}\frac{1}{\sqrt{q_0}}\exp\left(-\frac{q_0}{2}\right) \tag{7.26}$$

where the PDF consists of a mixture of a delta function at zero and a χ^2 distribution for one degree of freedom which has a weight of 1/2. The corresponding cumulative distribution is obtained as :

$$F(\tilde{q}_0|\mu') = \Phi\left(\sqrt{q_0}-\frac{\mu'}{\sigma}\right), \tag{7.27}$$

$$F(\tilde{q}_0|0) = \Phi\left(\sqrt{q_0}\right). \tag{7.28}$$

As a result of this approach, the p-value of the null hypothesis $\mu = 0$ and the significance is

$$p_0 = 1 - F(q_0|0) \tag{7.29}$$

$$Z = \Phi^{-1}(1-p_0) = \sqrt{q_0}. \tag{7.30}$$

For the $f(\tilde{q}_\mu|\mu)$ as well, same approximation can be applied and one obtains $p_\mu = 1 - F(\tilde{q}_\mu|\mu)$. The upper limit on μ at confidence level $1-\alpha$ is found as $\mu_{\mathrm{up}} = \hat{\mu} + \sigma\Phi^{-1}(1-\alpha)$ by solving $p_\mu = \alpha$. where this should be solved numerically. The expected limit and its bands is calculated by the CL_S method. It needs distributions of $\tilde{q}_\mu$ at the hypothesis at μ and $\mu = 0$, The p-value is found as :

$$p'_\mu = \frac{1-\Phi(\sqrt{q_\mu})}{\Phi(\sqrt{q_{\mu,A}}-\sqrt{q_\mu})}, \tag{7.31}$$

So the median and expected bands become :

$$\mu_{\text{up}+n} = \sigma(\Phi^{-1}(1-\alpha\Phi(n))+n), \quad \text{with} \quad \sigma = \frac{\mu}{\sqrt{q_{\mu,A}}}, \tag{7.32}$$

where n represents values at $n\sigma$. Usually it takes $\alpha = 0.05$ (95% confidence level), μ can be taken in the calculation of σ. For the case of the median limit, i.e. $n = 0$, is written as:

$$\mu_{\text{up}}^{\text{med}} = \sigma\Phi^{-1}\left(1-\frac{1}{2}\alpha\right). \tag{7.33}$$

7.4 Statistical Results and Interpretation

Exclusion at the 95% confidence level are obtained with the frequentest method described in Section 7.3. Results assuming background-only hypothesis are shown in Section 7.4.1. Model independent results are given in Section 7.4.2. Results based on the hMSSM benchmark scenario are given in Section 7.4.3. A validation of the likelihood fit is described in Appendix G.

7.4.1 Results on Null Hypothesis

Firstly results assuming the null hypothesis is obtained by the combined likelihood fit with $\mu = 0$. The events yields and the $m_{\tau\tau}$ distributions are shown in Table 7.1 and Figure 7.2 after the fit("post-fit"). As shown in table and figures, the background expectation agrees well with observed data within the uncertinties. Other important variable with the post-fit are shown in Appendix H.

Process	b-tag		b-veto		high-$E_{\text{T}}^{\text{miss}}$	
	$e\tau_{\text{had}}$	$\mu\tau_{\text{had}}$	$e\tau_{\text{had}}$	$\mu\tau_{\text{had}}$	$e\tau_{\text{had}}$	$\mu\tau_{\text{had}}$
Diboson	9.7 ± 2.2	6.1 ± 1.9	453 ± 41	605 ± 57	6.6 ± 1.1	45 ± 7
$\ell \to \tau_{\text{had}}$	135 ± 29	83 ± 18	$2\,709 \pm 600$	$9\,034 \pm 850$	< 0.1	< 0.1
$t\bar{t}$, single-t	859 ± 100	$1\,223 \pm 480$	209 ± 30	227 ± 32	53 ± 11	354 ± 58
$Z \to \tau\tau$	333 ± 65	610 ± 115	$31\,702 \pm 6\,207$	$38\,767 \pm 6\,256$	44 ± 12	286 ± 53
$j \to \tau_{\text{had}}$	$1\,634 \pm 221$	$1\,575 \pm 161$	$42\,144 \pm 2\,705$	$39\,742 \pm 2\,420$	158 ± 15	$1\,149 \pm 107$
Total	$2\,970 \pm 257$	$3\,497 \pm 548$	$77\,216 \pm 6\,807$	$88\,375 \pm 7\,033$	262 ± 23	$1\,834 \pm 140$
data	2 986	3 486	77 162	88 454	250	1 834

Table 7.1: Events yields after the $\mu = 0$ fit. The uncertinties on the total background yields reflect the full statistical and systematic uncertainty, while the uncertinties on the individual background components reflect the statistical uncertainty only.

7.4.2 Result on Model Independent Cross Section

The search are interpreted in the more generic case of a single scalar boson ϕ that is produced in either the gluon-fusion or the bottom-annihilation production mode. A model independent results considering only single signal production process is important . The combined likelihood fit is performed and its results based on only the bottom-annihilation and gluon-fusion signal hypothesis are shown in Figure 7.3 (a) and (b) as a function of signal mass m_{A} respectively. The expected sensitivity

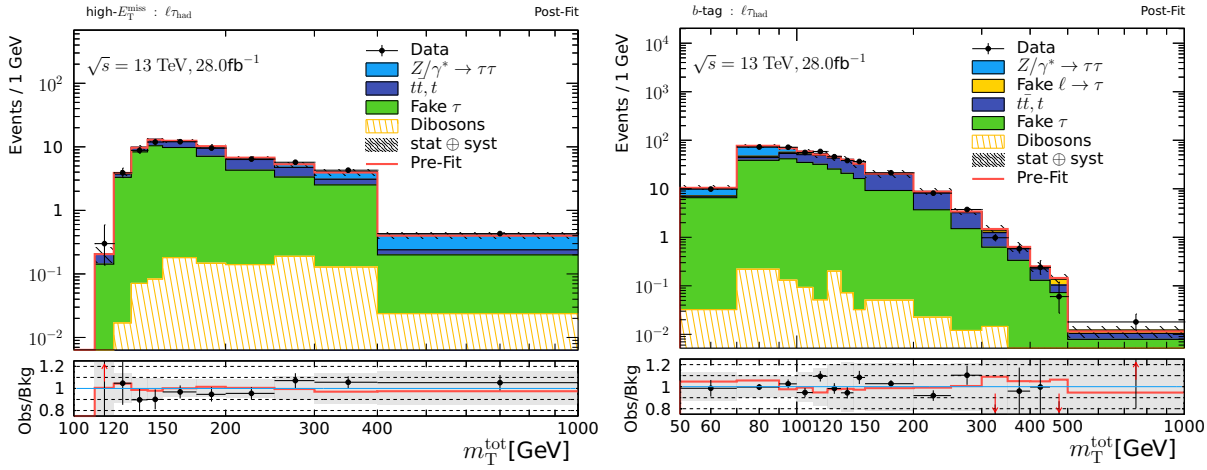

(a) high-$E_{\mathrm{T}}^{\mathrm{miss}}$ **(b)** b-tag

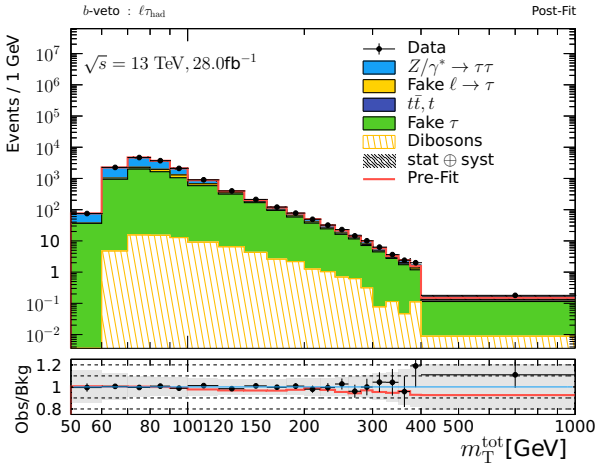

(c) b-veto

Figure 7.2: Post-fit $m_{\tau\tau}$ distributions for three signal regions assuming $\mu = 0$ hypothesis. In the ratio plots, gray filled regions represent the full statistical systematic uncertainty, the red lines show the total expected background before the combined likelihood fit (so-called, "pre-fit").

for each analysis category is shown in Figure 7.3 (c) and (d). An important comparison between this analysis and past strategy is shown. The pas strategy consists of only events fired the single-lepton-trigger and it is inclusive in terms of the $E_{\mathrm{T}}^{\mathrm{miss}}$, but with b-tag or b-veto event categorisation. The gluon-fusion production limit improves about 25% of its sensitivity at m_{A}= 1 TeVby including the high-$E_{\mathrm{T}}^{\mathrm{miss}}$ category While the bottom-annihilation production limit improves about 50% at m_{A}= 1 TeV. Figure 7.4 shows the observed local p-value with the gluon-fusion and bottom-annihilation production hypothesis.

In addition to this improvement, the high-$E_{\mathrm{T}}^{\mathrm{miss}}$ signal region significantly contributes in both production processes. This is important feature in terms of analysis robustness for "other" processes, like a non-Higgs resonance signal. Besides one-dimensional limits, the fit on the gluon-fusion and bottom-annihilation process corss section times the branching ratios of $H/A \to \tau\tau$ is obtained using two-dimensional fit. Figure 7.5 shows the bset fit point on the cross-section times the branching fraction plane of the gluon-fusion and bottom-annihilation production process with several mass

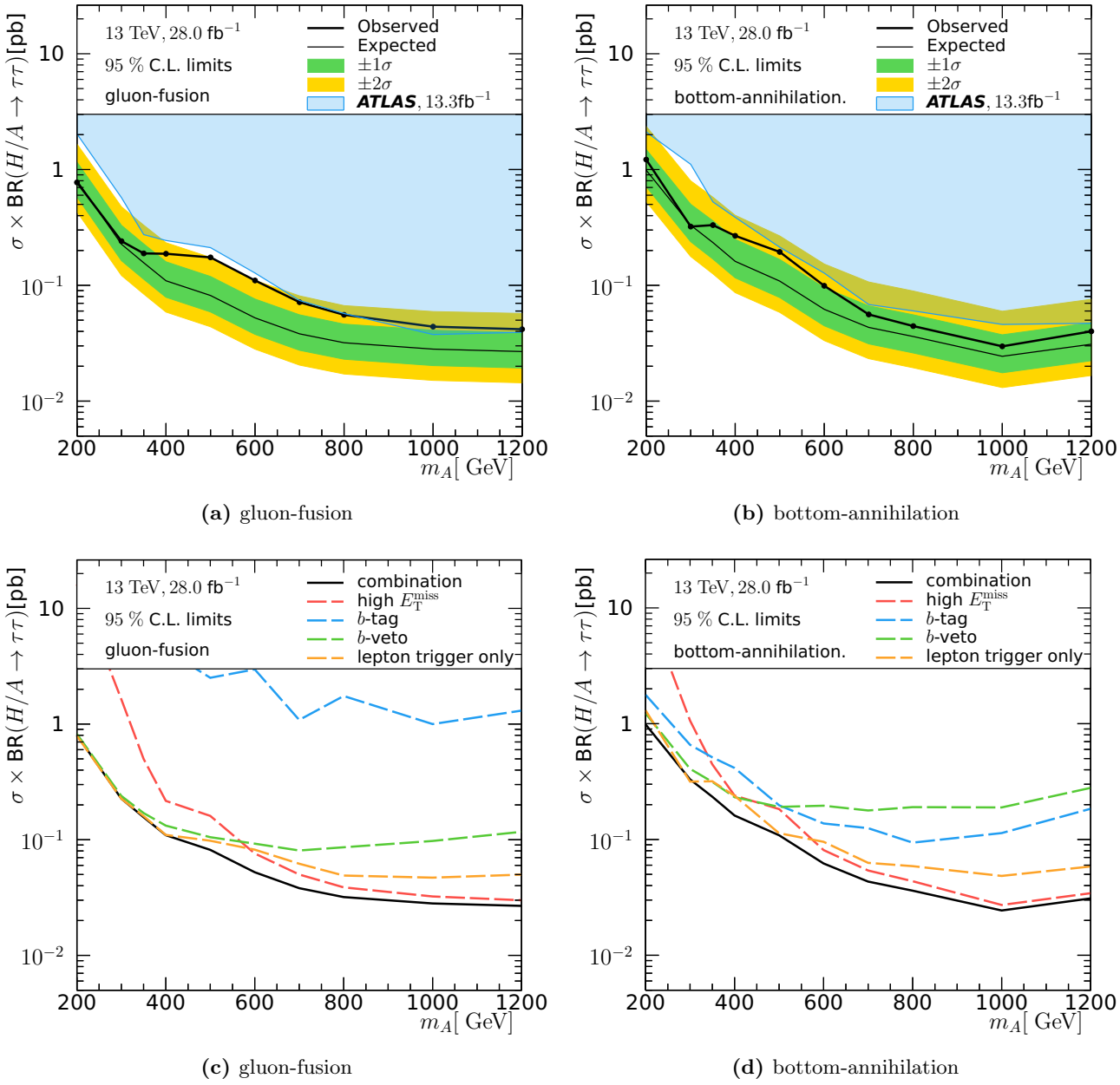

(a) gluon-fusion

(b) bottom-annihilation

(c) gluon-fusion

(d) bottom-annihilation

Figure 7.3: Expected (dashed line) and observed (solid line), 95% confidence level limits on the cross-section for Higgs boson production in gluon-fusion (a) and bottom-annihilation (b) times the branching ratio into a pair of τ leptons, along with $\pm1\sigma$ (green) and $\pm2\sigma$ (yellow) uncertainty bands for the expected limit in upper column. The region filled with blue represents the exclusion limit of search for heavy Higgs boson decaying into τ leptons with 13.3 fb^{-1} (from Reference [212]) In bottom column, expected limit for the combination (solid black line), high-$E_{\mathrm{T}}^{\mathrm{miss}}$ (red broken line), b-tag (blue broken line), b,-veto (green broken line) and the lepton-trigger-only results (orange broken line) are shown. limits on the cross section for Higgs boson production in gluon-fusion (a) and bottom-annihilation (b) times the branching ratio into a pair of τ leptons.

hypotheses. Each plots has the best fit point and 68(95)% confidence interval contours. The limits represents the best sensitivity up until now with corresponding decay mode search.

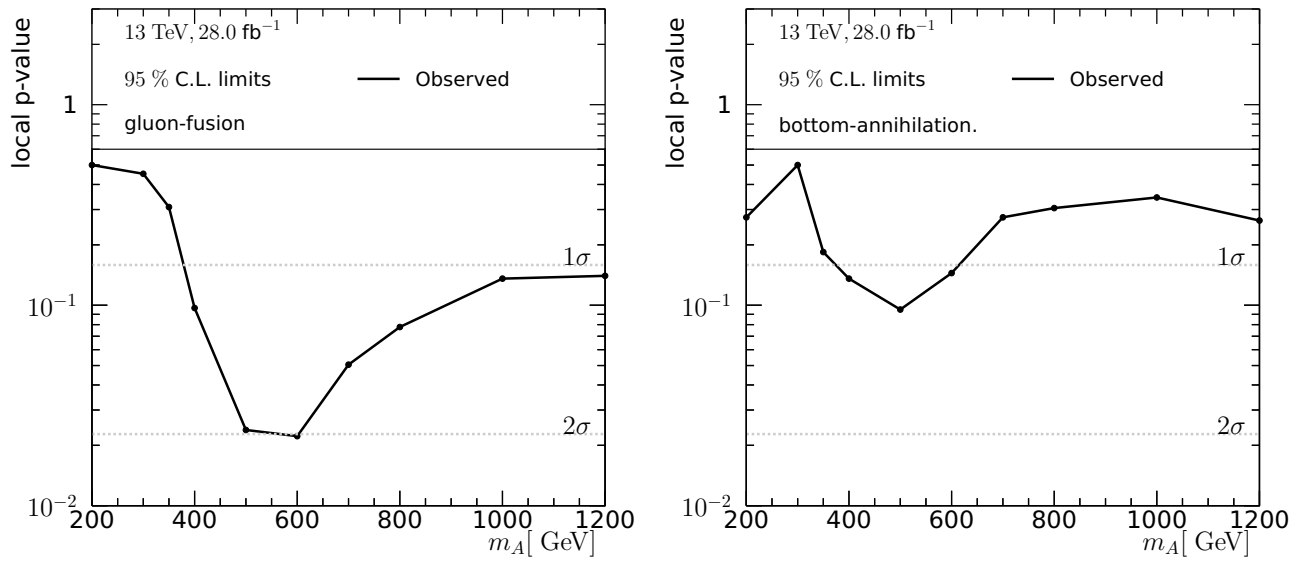

(a) gluon-fusion **(b)** bottom-annihilation

Figure 7.4: Observed local p-value with hypotheses of the gluon-fusion (a) and bottom-annihilation (b) production process.

7.4.3 Result on Benchmark Scenario

The limits on the parameter space of the MSSM is obtained by using the hMSSM benchmark scenario. For given m_{A} and various $\tan\beta$ hypotheses the excluded signal strength $\mu_{95\%}$ is calculated. Figure 7.6 shows the exclusion limit for the hMSSM scenario in the (m_{A}, $\tan\beta$) parameter space. The value of $\tan\beta$ excluded at the 95% confidence level is obtained by interpolating between the values of m_{A}. The limits represents the best sensitivity up until now with corresponding decay mode search.

7.4.4 Disscusion of Obtained Results

In collision data 165616 events are observed in the b-veto event category, where 165000±460 (stat.)± 9800 (syst.) background events are expected. For the b-tag event category 6472 events are observed, while for background process 6700 ± 64 (stat.) ± 610 (syst.) events are expected. In the high-$E_{\mathrm{T}}^{\mathrm{miss}}$ category 2084 events are observed, where 2095 ± 30 (stat.) ± 140 (syst.) background events are expected. The distribution of the di-τ mass of three categories exhibit no significant excess of data events compared with the background expectation.

Several interpretations are shown in this section using above results. There is approximately 2σ excess in the gluon-fusion only hypothesis. The excess comes from the high-$E_{\mathrm{T}}^{\mathrm{miss}}$ category excess, especially last three bins in Figure 7.2 (a). These three bins surplus looks consistent with signal shape, but such excess does not appear in the b-tag and b-veto categories. The $Z \to \tau\tau$ background process dominates in such region, if $Z \to \tau\tau$ has a mis-modelling on its shape, it follows this excess. The reason why the $Z \to \tau\tau$ has a shape mis-modelling would be expected from the TES mis-modelling. The TES is currently estimated by the simulated samples, because the integrated luminosity of data is not enough to precisely measure the TES. The in-situ TES measurement is also important in terms of reducing its uncertainty, because the TES is the highest ranked systematic uncertainty in terms of an impact on the likelihood fit. The largest source of the TES systematic uncertainty is the signle-partile-responce, it is a responce of a charged pion energy scale. This uncertainty is estimated by Run1 data and asigned with two times higer safe factor, so that it will be approximately half size of

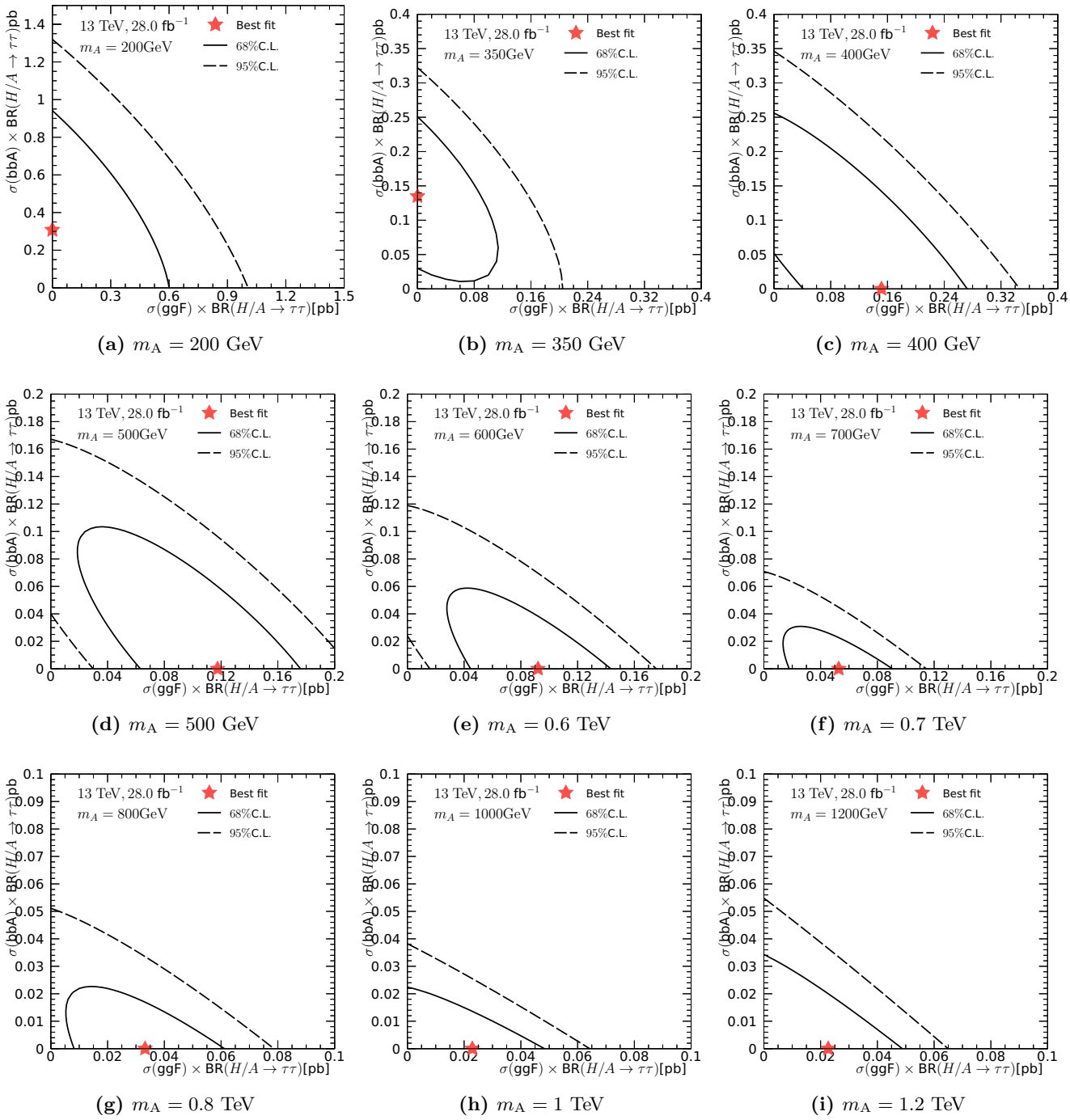

(a) $m_{\mathrm{A}} = 200$ GeV **(b)** $m_{\mathrm{A}} = 350$ GeV **(c)** $m_{\mathrm{A}} = 400$ GeV

(d) $m_{\mathrm{A}} = 500$ GeV **(e)** $m_{\mathrm{A}} = 0.6$ TeV **(f)** $m_{\mathrm{A}} = 0.7$ TeV

(g) $m_{\mathrm{A}} = 0.8$ TeV **(h)** $m_{\mathrm{A}} = 1$ TeV **(i)** $m_{\mathrm{A}} = 1.2$ TeV

Figure 7.5: Observed limit on the gluon-fusion production and bottom-annihilation production processes in each m_{A} hypotheses. The 68% (95%) confidence level contour is presented as solid (broken) line in each plot. A red star shows the best fit value on the two dimensional plane.

current uncertainty if more data is available to estimate by the tag-&-probe method.

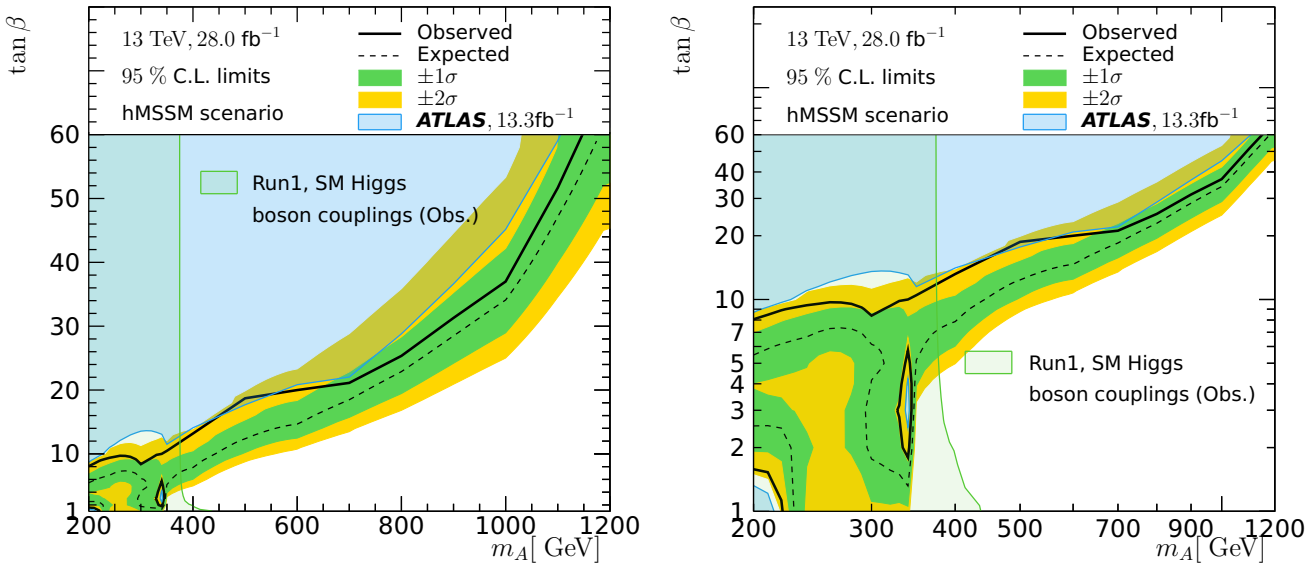

(a) linear scale **(b)** log scale

Figure 7.6: Expected (dashed line) and observed (solid line), 95% confidence level limits on the cross section for Higgs boson production in gluon-fusion (a) and bottom-annihilation (b) times the branching ratio into a pair of τ leptons, along with $\pm 1\sigma$ (green) and $\pm 2\sigma$ (yellow) uncertainty bands for the expected limit. The region filled with blue represents the exclusion limit of search for heavy Higgs boson decaying into τ leptons with 13.3 fb^{-1} (from Reference [212]). The region filled with green shows the indirect exclusion limit using the SM Higgs boson coupling measurements of the ATLAS Run1 results.

8 Conclusions

The LHC proton-proton collisions leads the high-energy frontier at a center-of-mass energy $\sqrt{s}$ = 13 TeV. A new boson was found by ATLAS [31] and CMS [32] collaboration in July 2012. The measurements of the cross-section for the different production processes and the spin are consistent with the Standard Model Higgs boson hypothesis. It is still possible that the observed boson stems from an extended Higgs sector, such as the two-Higgs-doublets of the Minimal Supersymmetric Standard Model (MSSM). The MSSM leads to five physical Higgs bosons, the electrically neutral Higgs boson h, A and H and the electrically charged Higgs bosons $H^{\pm}$.

A search for the neutral heavy Higgs boson H and A in the decay channel with a electron or muon and hadronically decaying τ lepton is documented in this thesis. The search exploits events with a large missing transverse energy produced from an imbalance decay of a pair of τ leptons. An enhancement of down-type fermions is important property of the two-Higgs-doublets model to enhance analysis sensitivity. The hMSSM scenario is considered as a benchmark model of the MSSM Higgs boson mechanism. The hMSSM scenario considers the new boson with m_h = 125 GeV as the neutral Higgs boson h. Invariant mass of remaining two neutral Higgs boson H and A are degenerated at the pseudoscalar Higgs boson mass m_{A} due to the decoupling limit. Two production mechanisms are considered as the signal process in the MSSM Higgs sector. The bottom-annihilation process produces at least one b-quark and their cross-section is enhanced from the down-type fermions enhancement in higher-tan β parameter space. The gluon-fusion process produces only the Higgs bosons at leading order of strong coupling constant and their corss-section dominates in lower-tan β parameter space. The search is based on proton-proton collisions at a center-of-mass energy $\sqrt{s}$ = 13 TeV. The collisions have been recorded with the ATLAS detector at the LHC in 2015 and 2016 correspond to the integrated luminosity of 3.2 fb^{-1} and 24.8 fb^{-1} respectively.

Three analysis categories are defined to distinguish signals and backgrounds expected from the Standard Model particle productions. A region with large missing transverse energy is developed and optimised in this analysis for the first time (high-$E_{\mathrm{T}}^{\mathrm{miss}}$ category). Events with the large missing transverse energy are collected by triggers based on a signature of the missing transverse energy. While events with the small missing transverse energy are collected by trigger based on electron or muon and events are categorised by requiring at least one identified b-jet for the b-tag signal region and for no b-jet for the b-veto signal region. The heavy Higgs boson cannot be highly boosted and a topology where two decay products kinetically lie back-to-back is selected. In order to suppress background processes, event selection criteria based on final states particle topology are performed to three analysis categories.

A variety of background processes contributes to the selected final state. Besides events with true τ-leptons, events with mis-identified hadronic-τ objects is an important source of background. The mis-identified hadronic-τ background consists of several physics processes. It is divided two components with the QCD multijets and the W+jets/$t\bar{t}$ processes. It is necessary to model both components and a dedicated method to estimate the mis-identified hadronic-τ background is established. The

QCD multijets component is estimated by the data-driven technique as well and its estimates are propagated in the combined mis-identified background estimation. $Z \to \tau\tau$ background is irreducible, because it has exactly same final states as signals. The simulated event samples are used and it is validated in the dedicated control regions. $t\bar{t} \to \ell\tau_{\text{had}}$ process is an important background in the b-tagged signal topology. It is modelled by simulated event samples and it is cross-checked together with the mis-identified hadronic-τ background. A smaller contribution to the background events is expected from the diboson and Z+jets production process and it is estimated by the simulated event samples.

The statistical interpretation of the search based on two classes of signal hypotheses and more model-independent case of a single scalar boson produced in eigher the gluon-fusion or bottom-annihilation process is presented. Based on the reconstructed invariant mass distributions, 95% confidence level exclusion limits are derived with the frequentest CL_S procedure using the profile likelihood ratio as a test statistic. In the single production hypothesis of the gluon-fusion the exclusion limit is 0.043 pb at $m_\text{A} = 1\,\text{TeV}$. The exclusion limit is 0.029 pb at $m_\text{A} = 1\,\text{TeV}$ in the bottom-annihilation only hypothesis. A two dimensional likelihood scan of the cross-section times the branching fraction for the gluon-fusion and bottom-annihilation process is provided. The best fit point of $m_\text{A} = 1\,\text{TeV}$ hypothesis is $(0.02, < 0.001)$ for the gluon-fusion and bottom-annihilation, it is still consistent to null hypothesis within $\pm 1\sigma$ uncertainty. The exclusion limit is given in m_A and $\tan\beta$ parameter space assuming the hMSSM scenario. $\tan\beta > 36.8$ are excluded at $m_\text{A} = 1\,\text{TeV}$, while the expected exclusion is $\tan\beta > 34.1$.

The search presented in this thesis is published together with the other decay channel. Recently the new result by the CMS [213] with all decay channels including $e\mu$ final state is published with 13.3 fb^{-1}. The sensitivity of $e\mu$ decay channel shows non-negligible contribution at extremely high mass hypotheses in the CMS result. This channel would help improving the search sensitivity as well as in the feature result of the ATLAS. It might be useful to split a large missing transverse energy event category into two categories correspondingly the number of b-tagged jets when more dataset is recorded. The dataset incoming next two years and recorded in 2016 helps getting further sensitivity and understanding important systematic uncertainties.

After the discovery of a boson with a mass near 125 GeV, the search for the MSSM Higgs bosons provides important insight into whether the discovered boson can be a Higgs boson that is described by the two-Higgs-double model also the MSSM. Even though a large region of the parameter space of the hMSSM scenario is excluded and no obvious excess of data is observed, a significant part of the parameter space is still compatible with the results of the performed searches for Higgs bosons from extended Higgs sectors. Additional information could be obtained from the two-Higgs-doublet benchmark models like a parameterization mixing angle of the h and H bosons, α. Such information will provide the possibility to determine the nature of the electroweak symmetry breaking.

Appendix

Auxiliary Material

A $E_{\mathrm{T}}^{\mathrm{miss}}$ Trigger Efficiency

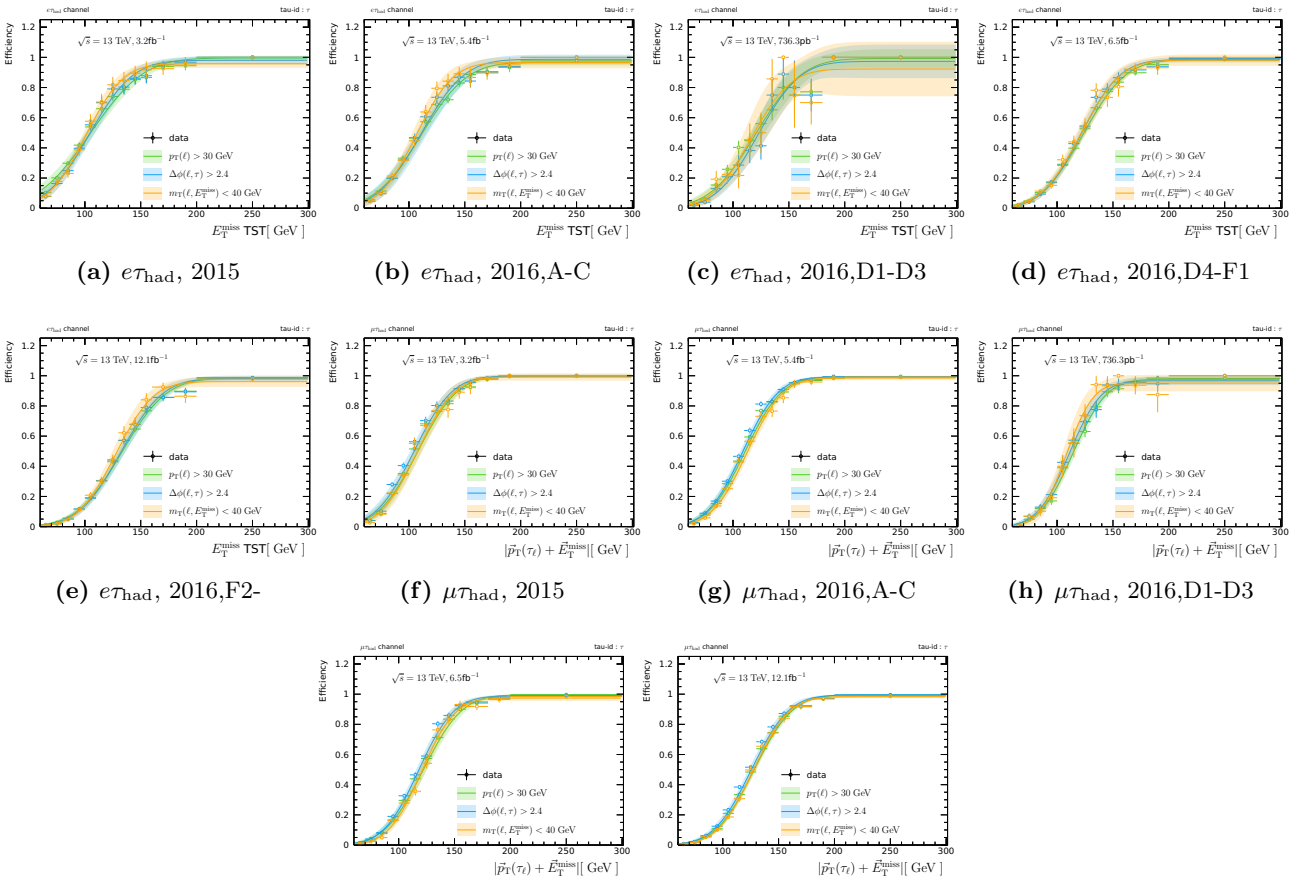

(a) $e\tau_{\mathrm{had}}$, 2015 **(b)** $e\tau_{\mathrm{had}}$, 2016,A-C **(c)** $e\tau_{\mathrm{had}}$, 2016,D1-D3 **(d)** $e\tau_{\mathrm{had}}$, 2016,D4-F1

(e) $e\tau_{\mathrm{had}}$, 2016,F2- **(f)** $\mu\tau_{\mathrm{had}}$, 2015 **(g)** $\mu\tau_{\mathrm{had}}$, 2016,A-C **(h)** $\mu\tau_{\mathrm{had}}$, 2016,D1-D3

(i) $\mu\tau_{\mathrm{had}}$, 2016,D4-F1 **(j)** $\mu\tau_{\mathrm{had}}$, 2016,F2-

Figure A.1: Efficiency for the $E_{\mathrm{T}}^{\mathrm{miss}}$ trigger of $e\tau_{\mathrm{had}}$ (a-e) and $\mu\tau_{\mathrm{had}}$ (f-j) channel with dedicated data-taking periods as a function $E_{\mathrm{T}}^{\mathrm{miss}}$ and $|\vec{E}_{\mathrm{T}}^{\mathrm{miss}} + \vec{p}_{\mathrm{T}}(\mu)|$. Each plots have three different curves, after the preselection ($p_{\mathrm{T}}(\ell) > 30$ GeV), $\Delta\phi(\ell, \tau_{\mathrm{vis}}) > 2.4$ and $m_{\mathrm{T}}(\ell, E_{\mathrm{T}}^{\mathrm{miss}}) < 40$ GeV.

B Validation of Event Selection Variables

Figure B.2 shows the angle difference between lepton and hadronic-τ in the transverse plane for three signal regions.

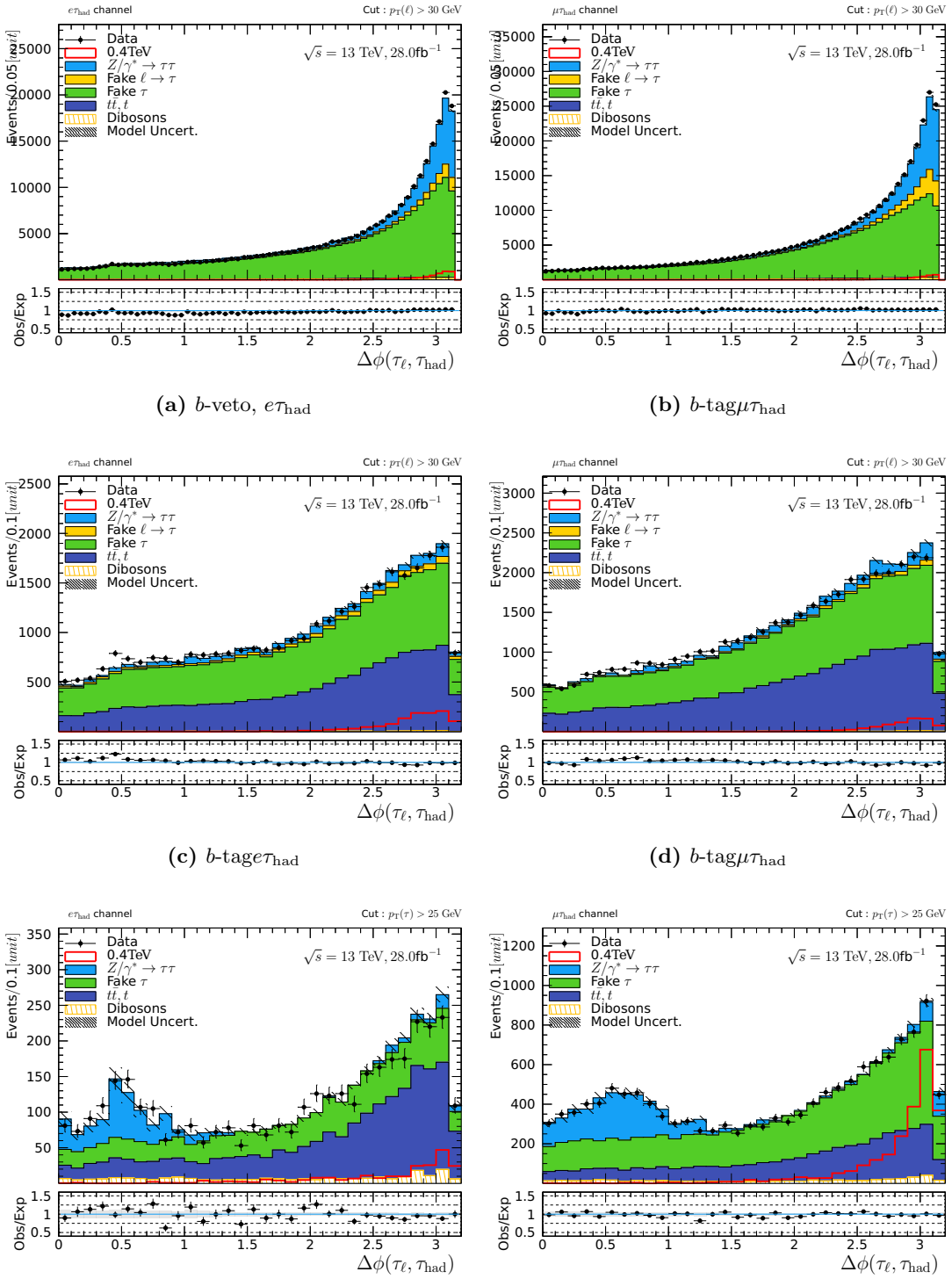

(a) b-veto, $e\tau_{\text{had}}$ **(b)** b-tag$\mu\tau_{\text{had}}$

(c) b-tag$e\tau_{\text{had}}$ **(d)** b-tag$\mu\tau_{\text{had}}$

(e) high-$E_{\text{T}}^{\text{miss}}$, $e\tau_{\text{had}}$ **(f)** high-$E_{\text{T}}^{\text{miss}}$, $\mu\tau_{\text{had}}$

Figure B.2: $\Delta\phi(\ell, \tau_{\text{had}})$ distributions for all signal regions and channels.

Figure B.3 shows the transverse mass between lepton and the missing transverse energy for three signal regions.

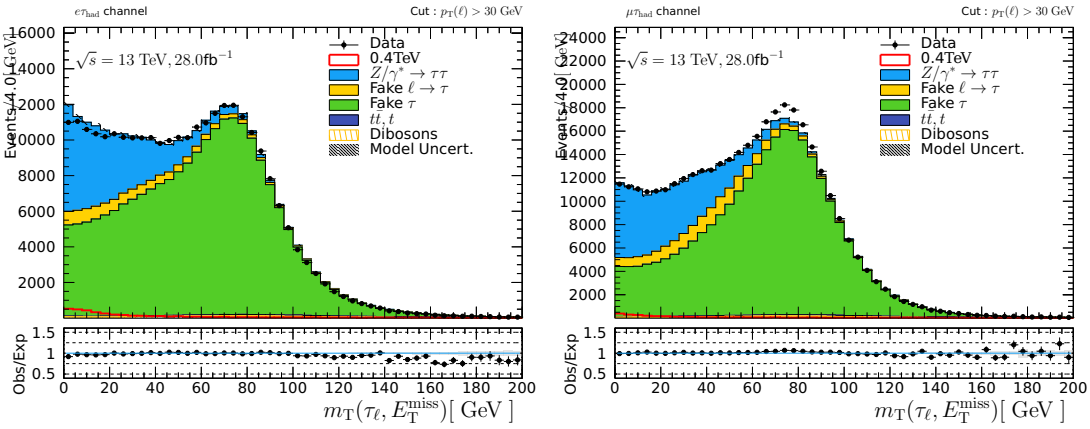

(a) b-veto, $e\tau_{\text{had}}$

(b) b-tag$\mu\tau_{\text{had}}$

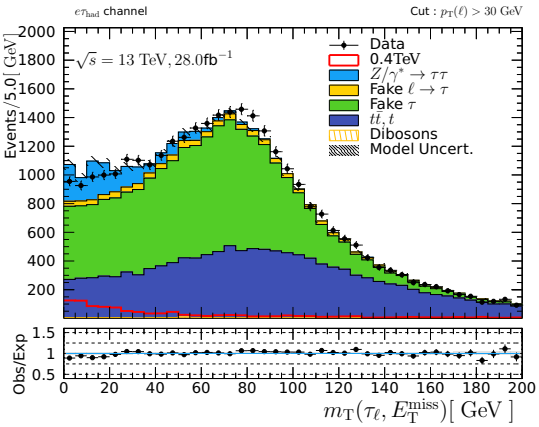

(c) b-tag$e\tau_{\text{had}}$

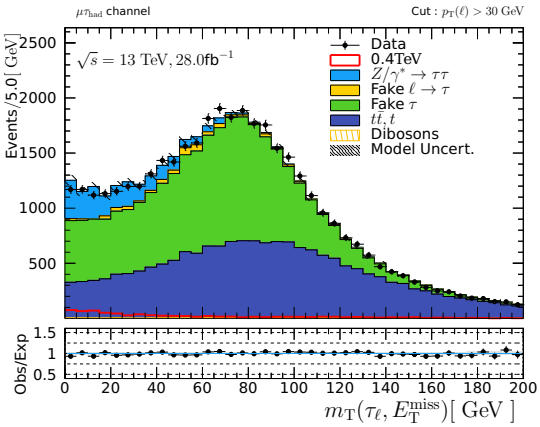

(d) b-tag$\mu\tau_{\text{had}}$

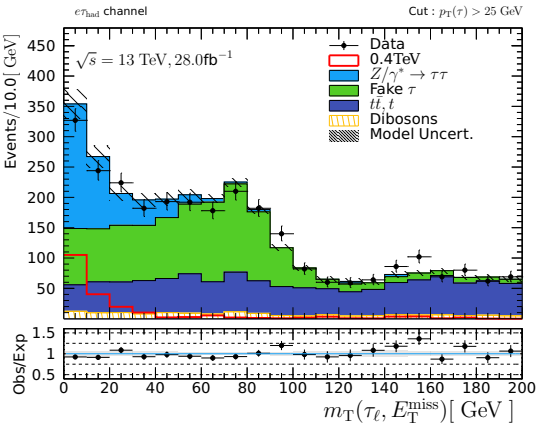

(e) high-$E_{\text{T}}^{\text{miss}}$, $e\tau_{\text{had}}$

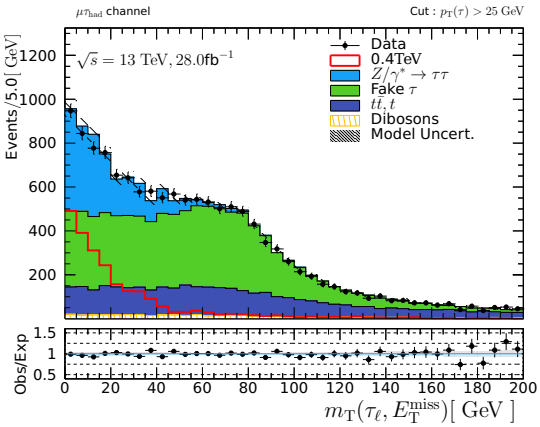

(f) high-$E_{\text{T}}^{\text{miss}}$, $\mu\tau_{\text{had}}$

Figure B.3: $m_{\text{T}}(\ell, E_{\text{T}}^{\text{miss}})$ distributions for all signal regions and channels.

C Plots of Control Regions

Figure C.4 – C.7 shows validation plots in the WCR, TCR, ZCR and SSCR for the high-$E_{\mathrm{T}}^{\mathrm{miss}}$ category respectively.

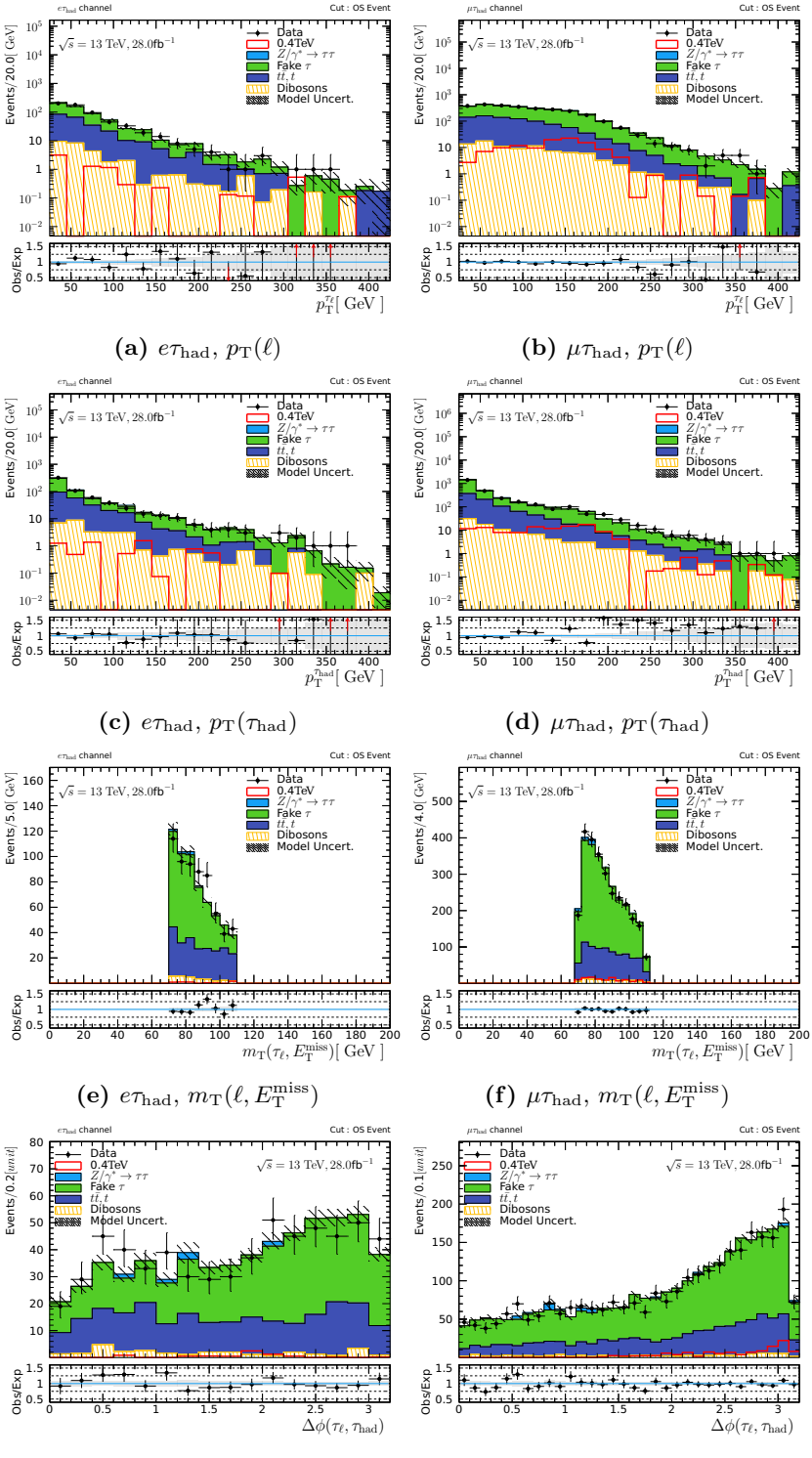

(a) $e\tau_{\mathrm{had}}$, $p_{\mathrm{T}}(\ell)$ **(b)** $\mu\tau_{\mathrm{had}}$, $p_{\mathrm{T}}(\ell)$

(c) $e\tau_{\mathrm{had}}$, $p_{\mathrm{T}}(\tau_{\mathrm{had}})$ **(d)** $\mu\tau_{\mathrm{had}}$, $p_{\mathrm{T}}(\tau_{\mathrm{had}})$

(e) $e\tau_{\mathrm{had}}$, $m_{\mathrm{T}}(\ell, E_{\mathrm{T}}^{\mathrm{miss}})$ **(f)** $\mu\tau_{\mathrm{had}}$, $m_{\mathrm{T}}(\ell, E_{\mathrm{T}}^{\mathrm{miss}})$

(g) $e\tau_{\mathrm{had}}$, $\Delta\phi(\ell, \tau_{\mathrm{had}})$ **(h)** $\mu\tau_{\mathrm{had}}$, $\Delta\phi(\ell, \tau_{\mathrm{had}})$

Figure C.4: Comparisons of data and background in the high-$E_{\mathrm{T}}^{\mathrm{miss}}$ WCR for $e\tau_{\mathrm{had}}$ and $\mu\tau_{\mathrm{had}}$ channel with four important variables.

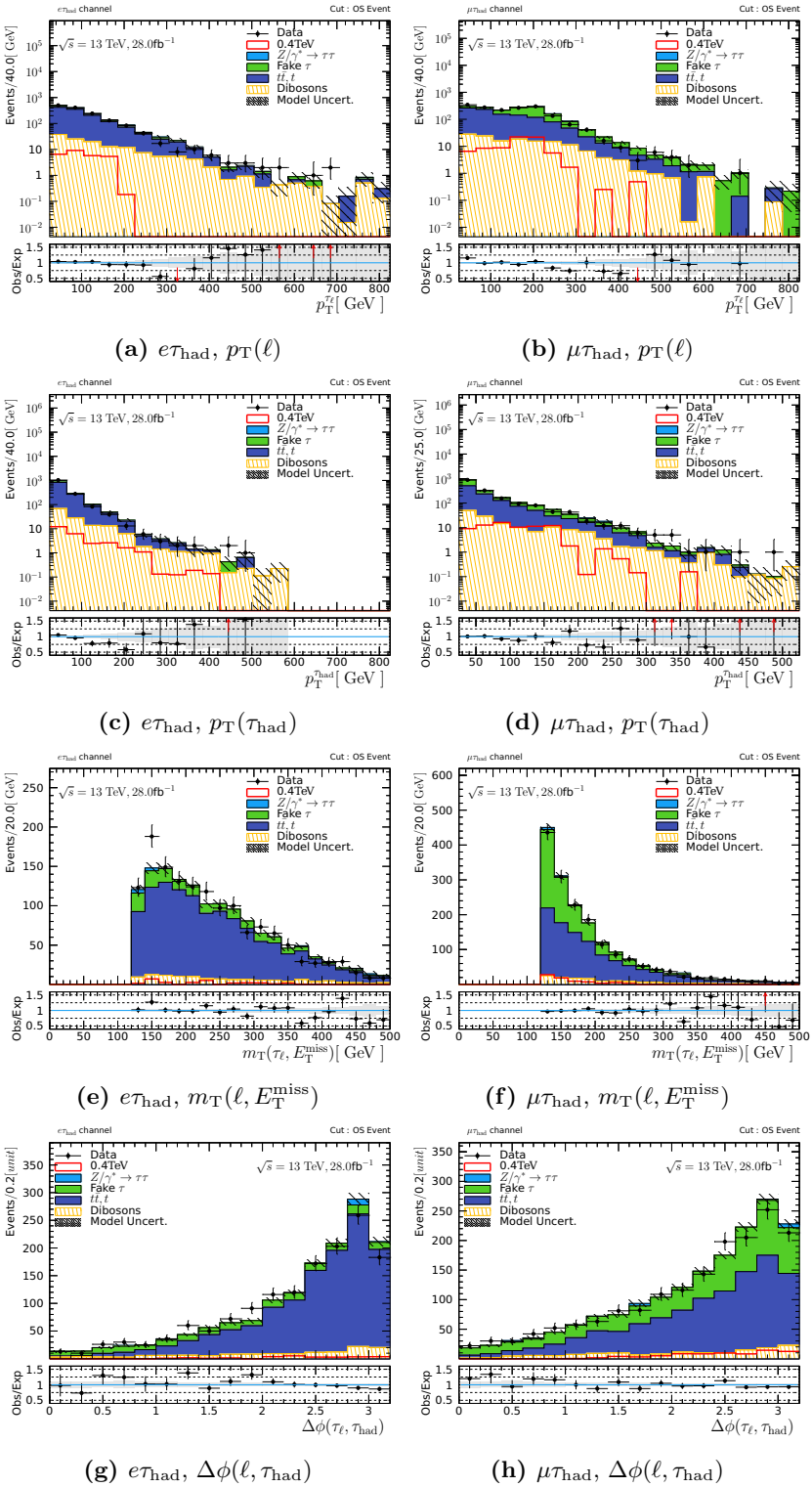

(a) $e\tau_{\text{had}}$, $p_{\text{T}}(\ell)$ **(b)** $\mu\tau_{\text{had}}$, $p_{\text{T}}(\ell)$

(c) $e\tau_{\text{had}}$, $p_{\text{T}}(\tau_{\text{had}})$ **(d)** $\mu\tau_{\text{had}}$, $p_{\text{T}}(\tau_{\text{had}})$

(e) $e\tau_{\text{had}}$, $m_{\text{T}}(\ell, E_{\text{T}}^{\text{miss}})$ **(f)** $\mu\tau_{\text{had}}$, $m_{\text{T}}(\ell, E_{\text{T}}^{\text{miss}})$

(g) $e\tau_{\text{had}}$, $\Delta\phi(\ell, \tau_{\text{had}})$ **(h)** $\mu\tau_{\text{had}}$, $\Delta\phi(\ell, \tau_{\text{had}})$

Figure C.5: Comparisons of data and background in the high-$E_{\text{T}}^{\text{miss}}$ TCR for $e\tau_{\text{had}}$ and $\mu\tau_{\text{had}}$ channel with four important variables.

Figure C.8 – C.10 shows validation plots in the TCR, ZCR and SSCR for the b-tag category respectively.

Figure C.11 – C.13 shows validation plots in the WCR, ZCR and SSCR for the b-veto category

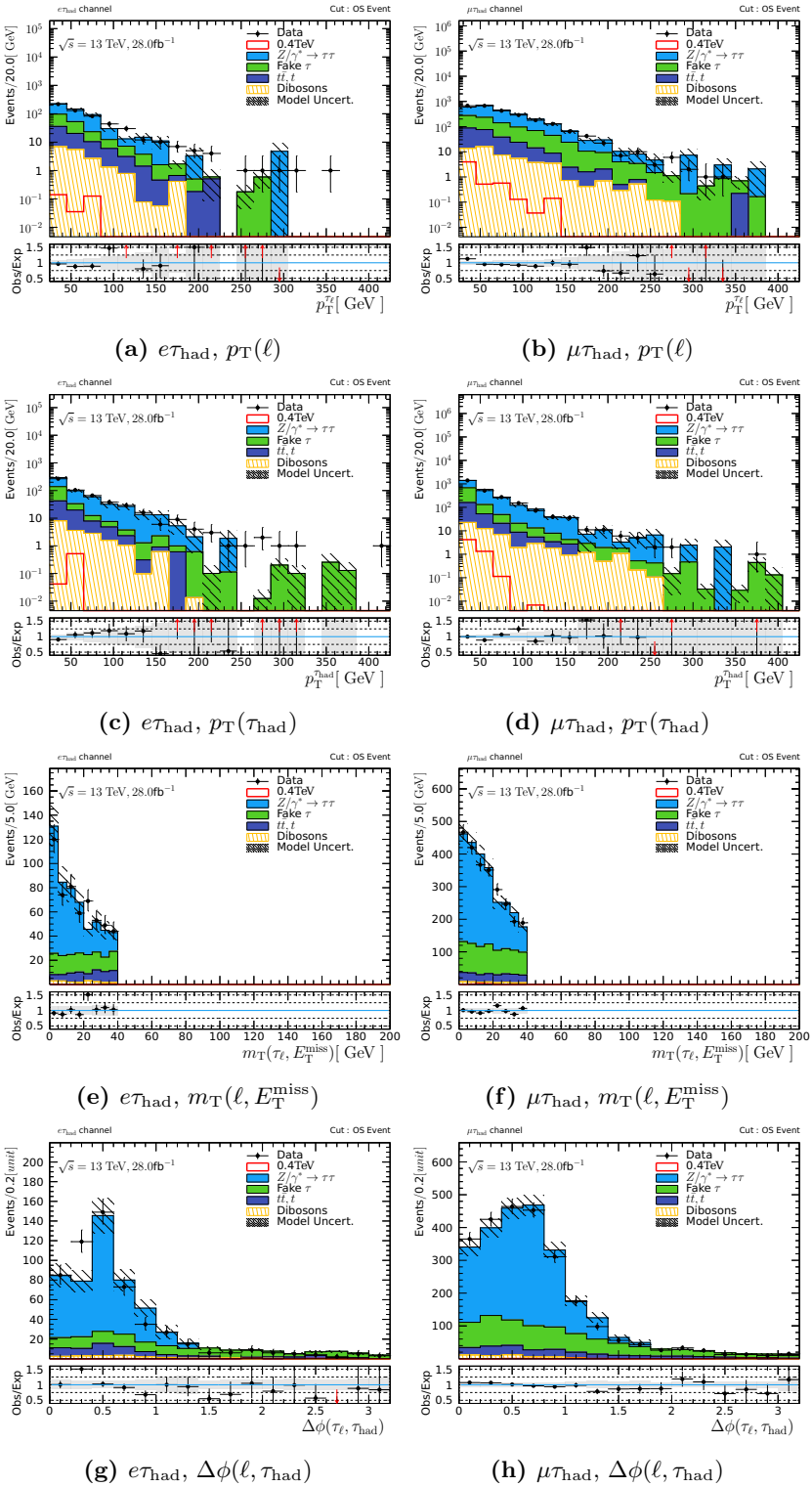

(a) $e\tau_{\text{had}}$, $p_{\text{T}}(\ell)$ **(b)** $\mu\tau_{\text{had}}$, $p_{\text{T}}(\ell)$

(c) $e\tau_{\text{had}}$, $p_{\text{T}}(\tau_{\text{had}})$ **(d)** $\mu\tau_{\text{had}}$, $p_{\text{T}}(\tau_{\text{had}})$

(e) $e\tau_{\text{had}}$, $m_{\text{T}}(\ell, E_{\text{T}}^{\text{miss}})$ **(f)** $\mu\tau_{\text{had}}$, $m_{\text{T}}(\ell, E_{\text{T}}^{\text{miss}})$

(g) $e\tau_{\text{had}}$, $\Delta\phi(\ell, \tau_{\text{had}})$ **(h)** $\mu\tau_{\text{had}}$, $\Delta\phi(\ell, \tau_{\text{had}})$

Figure C.6: Comparisons of data and background in the high-$E_{\text{T}}^{\text{miss}}$ ZCR for $e\tau_{\text{had}}$ and $\mu\tau_{\text{had}}$ channel with four important variables.

respectively.

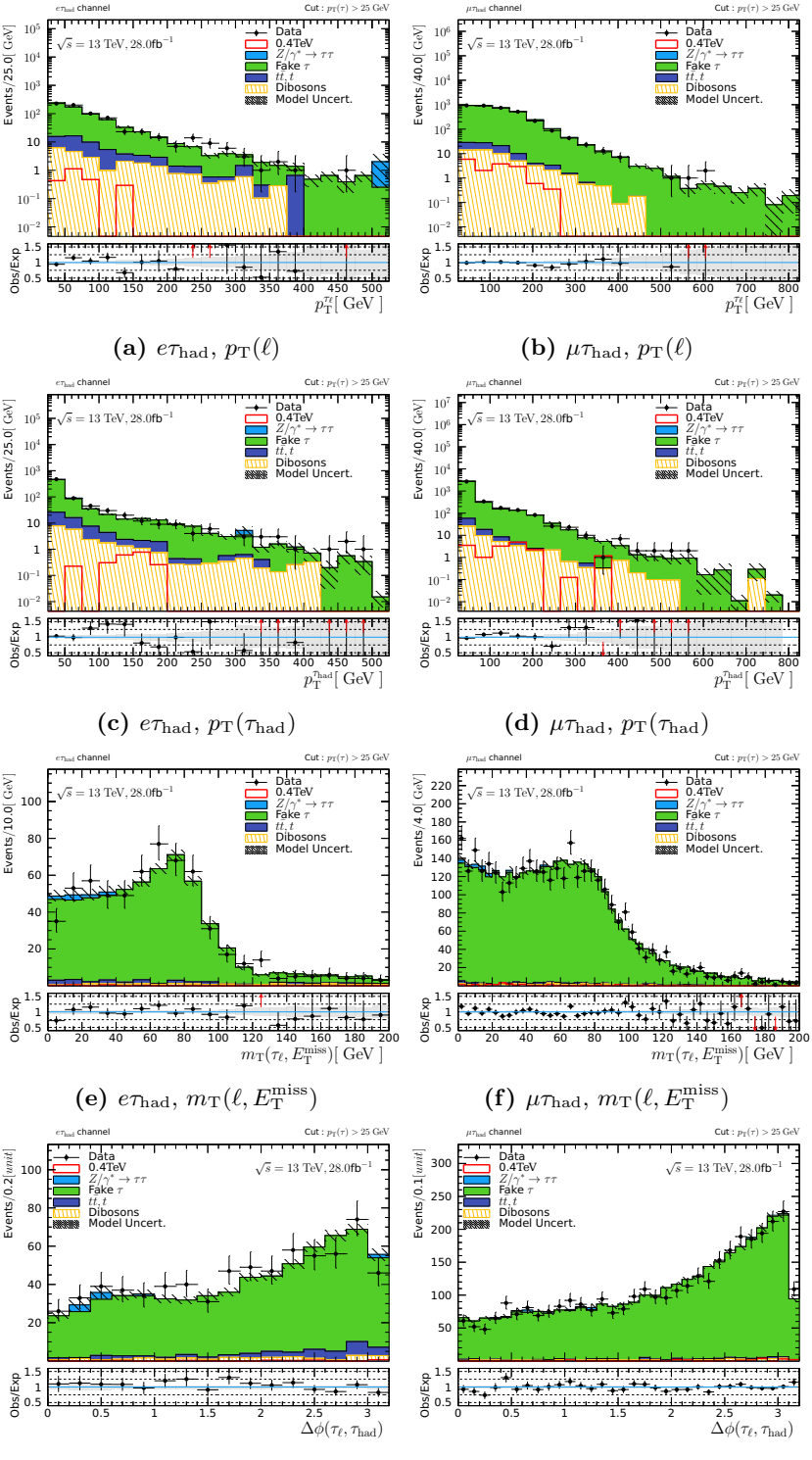

(a) $e\tau_{\text{had}}$, $p_{\text{T}}(\ell)$ **(b)** $\mu\tau_{\text{had}}$, $p_{\text{T}}(\ell)$

(c) $e\tau_{\text{had}}$, $p_{\text{T}}(\tau_{\text{had}})$ **(d)** $\mu\tau_{\text{had}}$, $p_{\text{T}}(\tau_{\text{had}})$

(e) $e\tau_{\text{had}}$, $m_{\text{T}}(\ell, E_{\text{T}}^{\text{miss}})$ **(f)** $\mu\tau_{\text{had}}$, $m_{\text{T}}(\ell, E_{\text{T}}^{\text{miss}})$

(g) $e\tau_{\text{had}}$, $\Delta\phi(\ell, \tau_{\text{had}})$ **(h)** $\mu\tau_{\text{had}}$, $\Delta\phi(\ell, \tau_{\text{had}})$

Figure C.7: Comparisons of data and background in the high-$E_{\text{T}}^{\text{miss}}$ SSCR for $e\tau_{\text{had}}$ and $\mu\tau_{\text{had}}$ channel with four important variables.

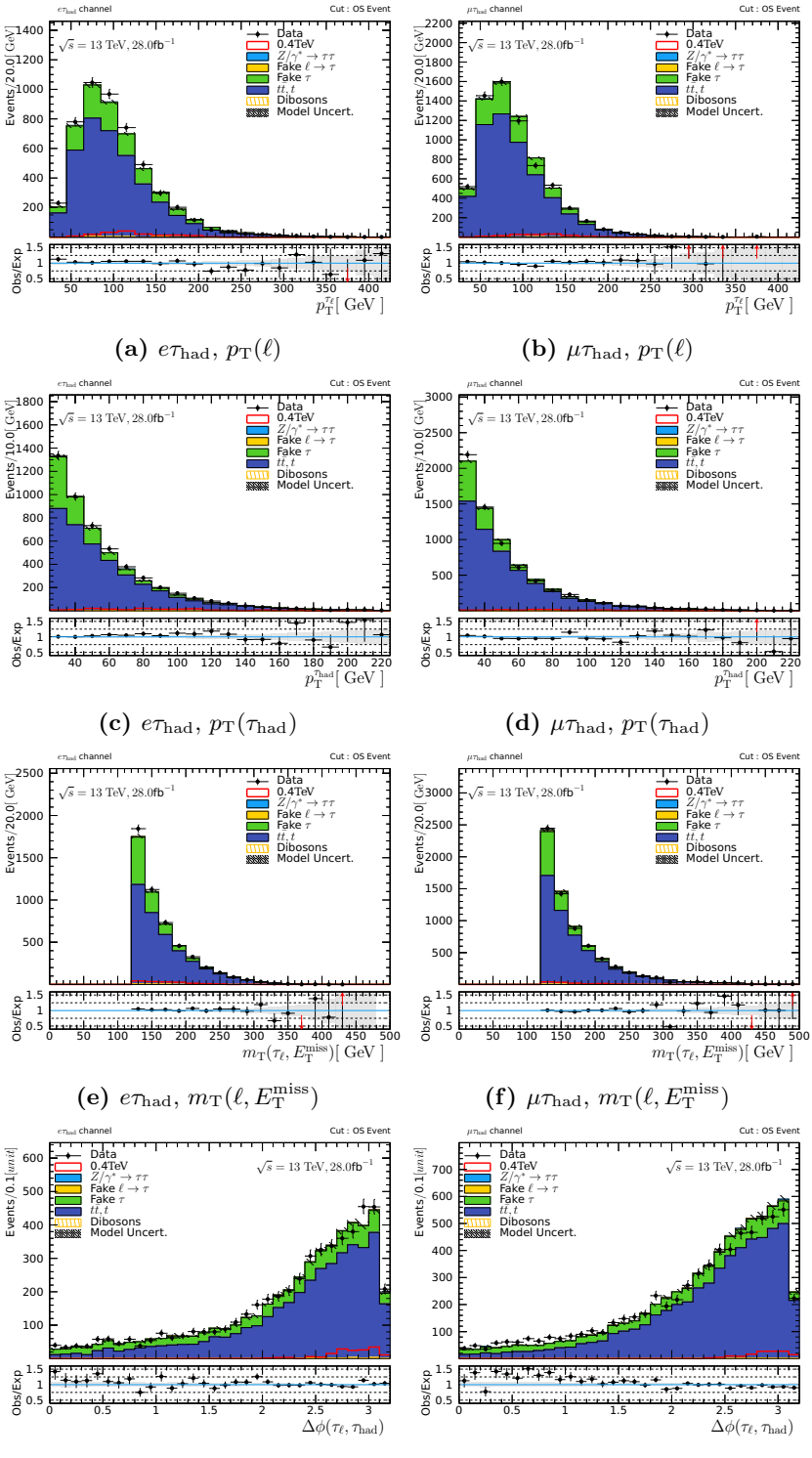

(a) $e\tau_{\text{had}}$, $p_{\text{T}}(\ell)$ **(b)** $\mu\tau_{\text{had}}$, $p_{\text{T}}(\ell)$

(c) $e\tau_{\text{had}}$, $p_{\text{T}}(\tau_{\text{had}})$ **(d)** $\mu\tau_{\text{had}}$, $p_{\text{T}}(\tau_{\text{had}})$

(e) $e\tau_{\text{had}}$, $m_{\text{T}}(\ell, E_{\text{T}}^{\text{miss}})$ **(f)** $\mu\tau_{\text{had}}$, $m_{\text{T}}(\ell, E_{\text{T}}^{\text{miss}})$

(g) $e\tau_{\text{had}}$, $\Delta\phi(\ell, \tau_{\text{had}})$ **(h)** $\mu\tau_{\text{had}}$, $\Delta\phi(\ell, \tau_{\text{had}})$

Figure C.8: Comparisons of data and background in the b-tag TCR for $e\tau_{\text{had}}$ and $\mu\tau_{\text{had}}$ channel with four important variables.

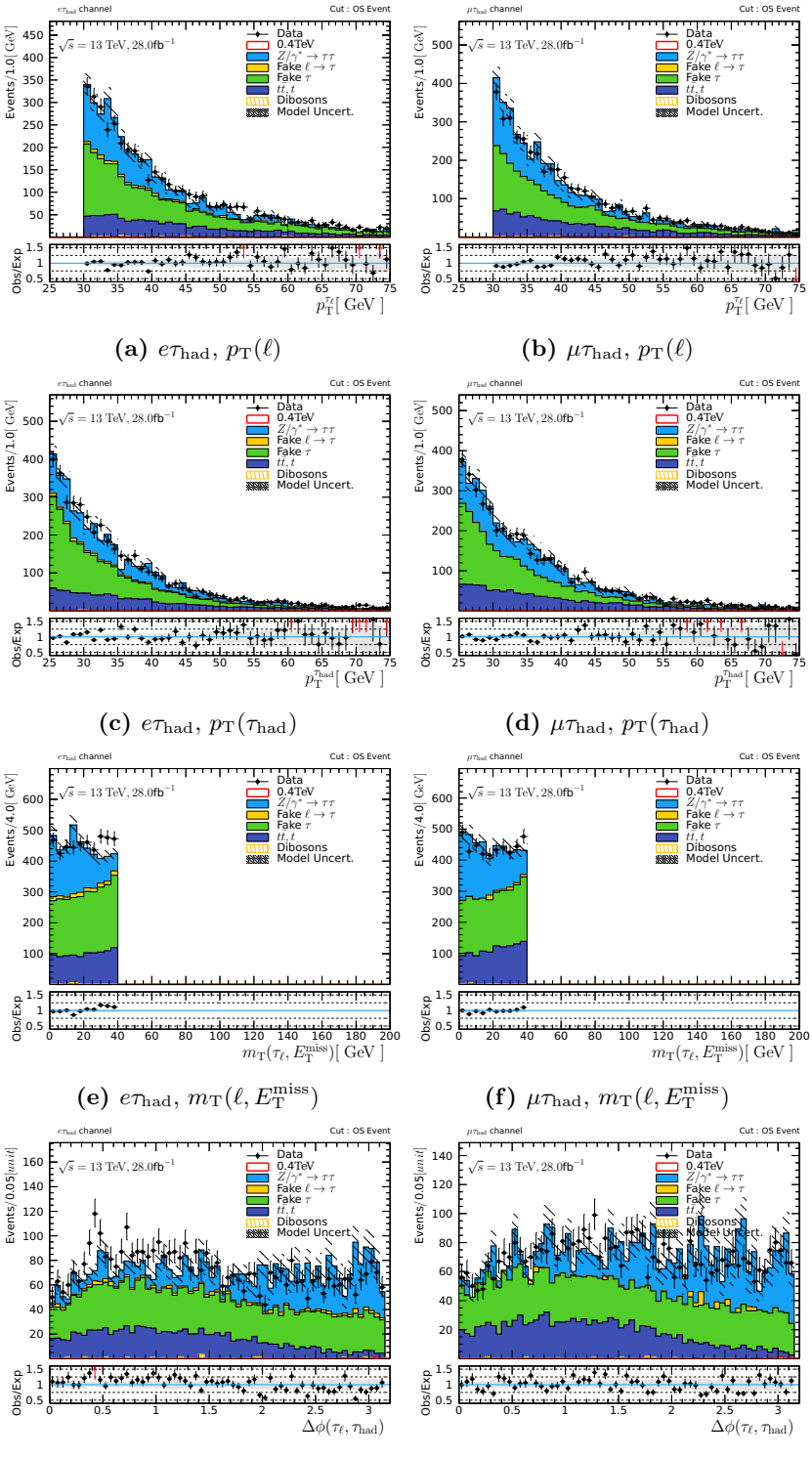

(a) $e\tau_{\mathrm{had}}$, $p_{\mathrm{T}}(\ell)$ **(b)** $\mu\tau_{\mathrm{had}}$, $p_{\mathrm{T}}(\ell)$

(c) $e\tau_{\mathrm{had}}$, $p_{\mathrm{T}}(\tau_{\mathrm{had}})$ **(d)** $\mu\tau_{\mathrm{had}}$, $p_{\mathrm{T}}(\tau_{\mathrm{had}})$

(e) $e\tau_{\mathrm{had}}$, $m_{\mathrm{T}}(\ell, E_{\mathrm{T}}^{\mathrm{miss}})$ **(f)** $\mu\tau_{\mathrm{had}}$, $m_{\mathrm{T}}(\ell, E_{\mathrm{T}}^{\mathrm{miss}})$

(g) $e\tau_{\mathrm{had}}$, $\Delta\phi(\ell, \tau_{\mathrm{had}})$ **(h)** $\mu\tau_{\mathrm{had}}$, $\Delta\phi(\ell, \tau_{\mathrm{had}})$

Figure C.9: Comparisons of data and background in the b-tag ZCR for $e\tau_{\mathrm{had}}$ and $\mu\tau_{\mathrm{had}}$ channel with four important variables.

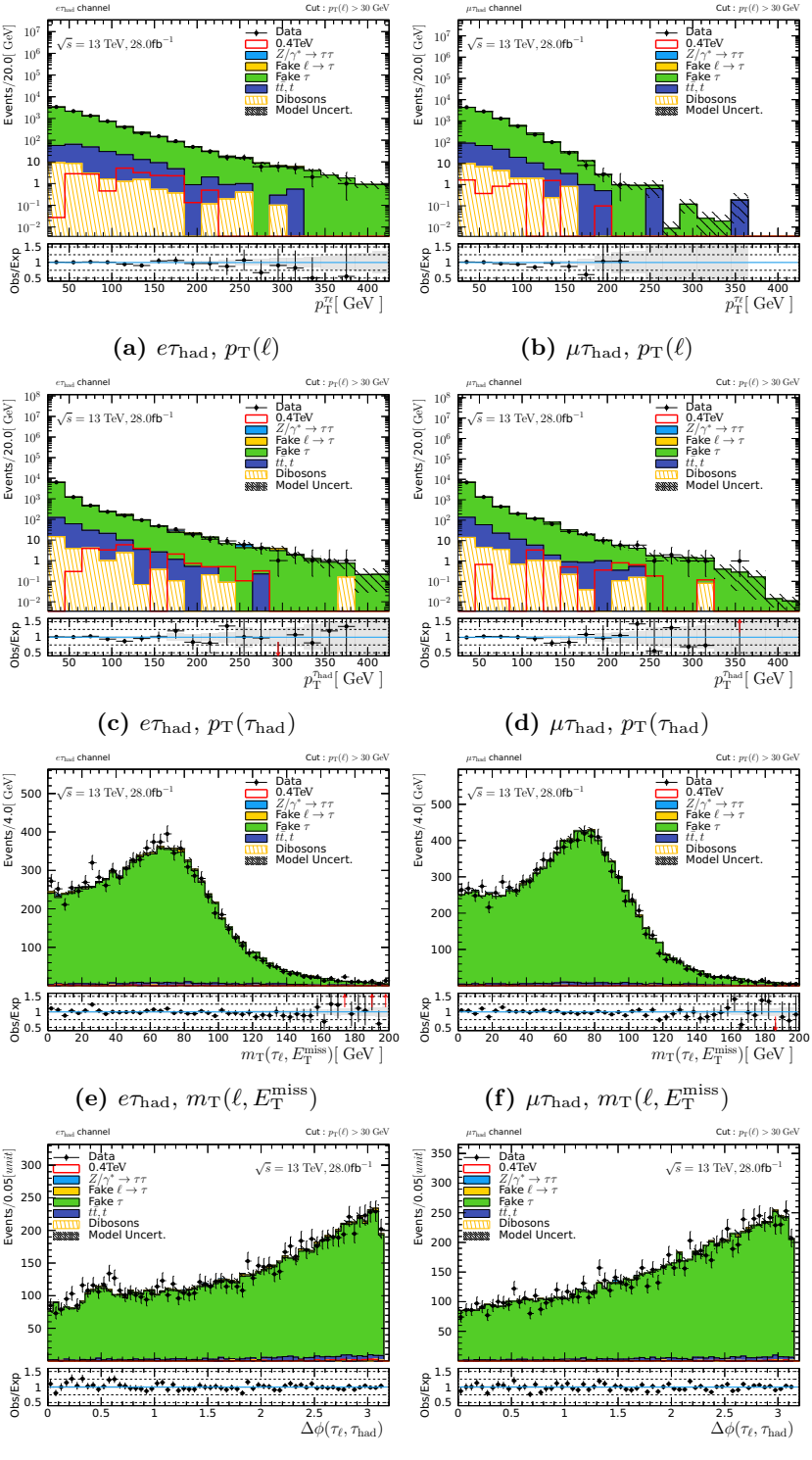

(a) $e\tau_{\text{had}}$, $p_{\text{T}}(\ell)$ **(b)** $\mu\tau_{\text{had}}$, $p_{\text{T}}(\ell)$

(c) $e\tau_{\text{had}}$, $p_{\text{T}}(\tau_{\text{had}})$ **(d)** $\mu\tau_{\text{had}}$, $p_{\text{T}}(\tau_{\text{had}})$

(e) $e\tau_{\text{had}}$, $m_{\text{T}}(\ell, E_{\text{T}}^{\text{miss}})$ **(f)** $\mu\tau_{\text{had}}$, $m_{\text{T}}(\ell, E_{\text{T}}^{\text{miss}})$

(g) $e\tau_{\text{had}}$, $\Delta\phi(\ell, \tau_{\text{had}})$ **(h)** $\mu\tau_{\text{had}}$, $\Delta\phi(\ell, \tau_{\text{had}})$

Figure C.10: Comparisons of data and background in the b-tag SSCR for $e\tau_{\text{had}}$ and $\mu\tau_{\text{had}}$ channel with four important variables.

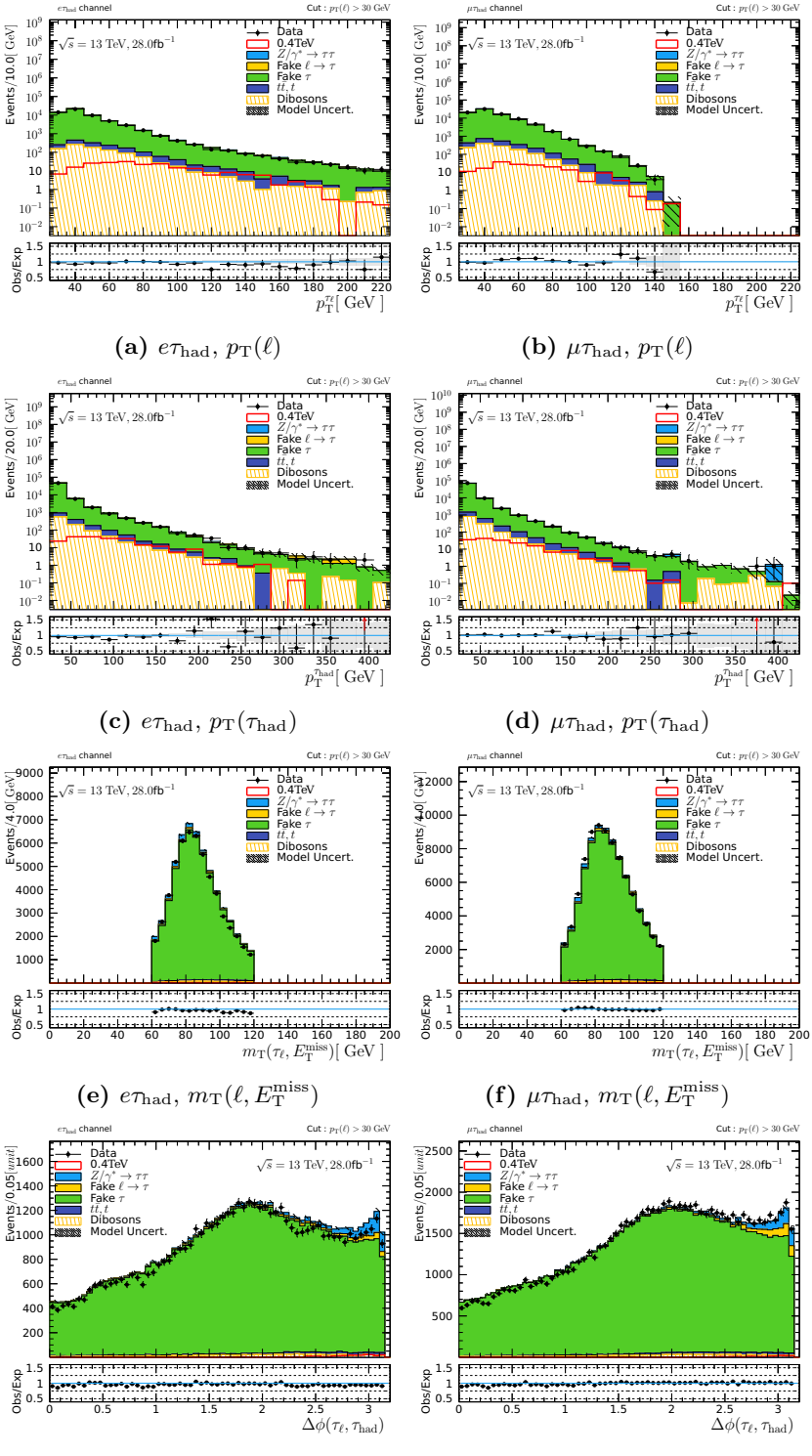

(a) $e\tau_{\text{had}}$, $p_{\text{T}}(\ell)$ **(b)** $\mu\tau_{\text{had}}$, $p_{\text{T}}(\ell)$

(c) $e\tau_{\text{had}}$, $p_{\text{T}}(\tau_{\text{had}})$ **(d)** $\mu\tau_{\text{had}}$, $p_{\text{T}}(\tau_{\text{had}})$

(e) $e\tau_{\text{had}}$, $m_{\text{T}}(\ell, E_{\text{T}}^{\text{miss}})$ **(f)** $\mu\tau_{\text{had}}$, $m_{\text{T}}(\ell, E_{\text{T}}^{\text{miss}})$

(g) $e\tau_{\text{had}}$, $\Delta\phi(\ell, \tau_{\text{had}})$ **(h)** $\mu\tau_{\text{had}}$, $\Delta\phi(\ell, \tau_{\text{had}})$

Figure C.11: Comparisons of data and background in the b-veto WCR for $e\tau_{\text{had}}$ and $\mu\tau_{\text{had}}$ channel with four important variables.

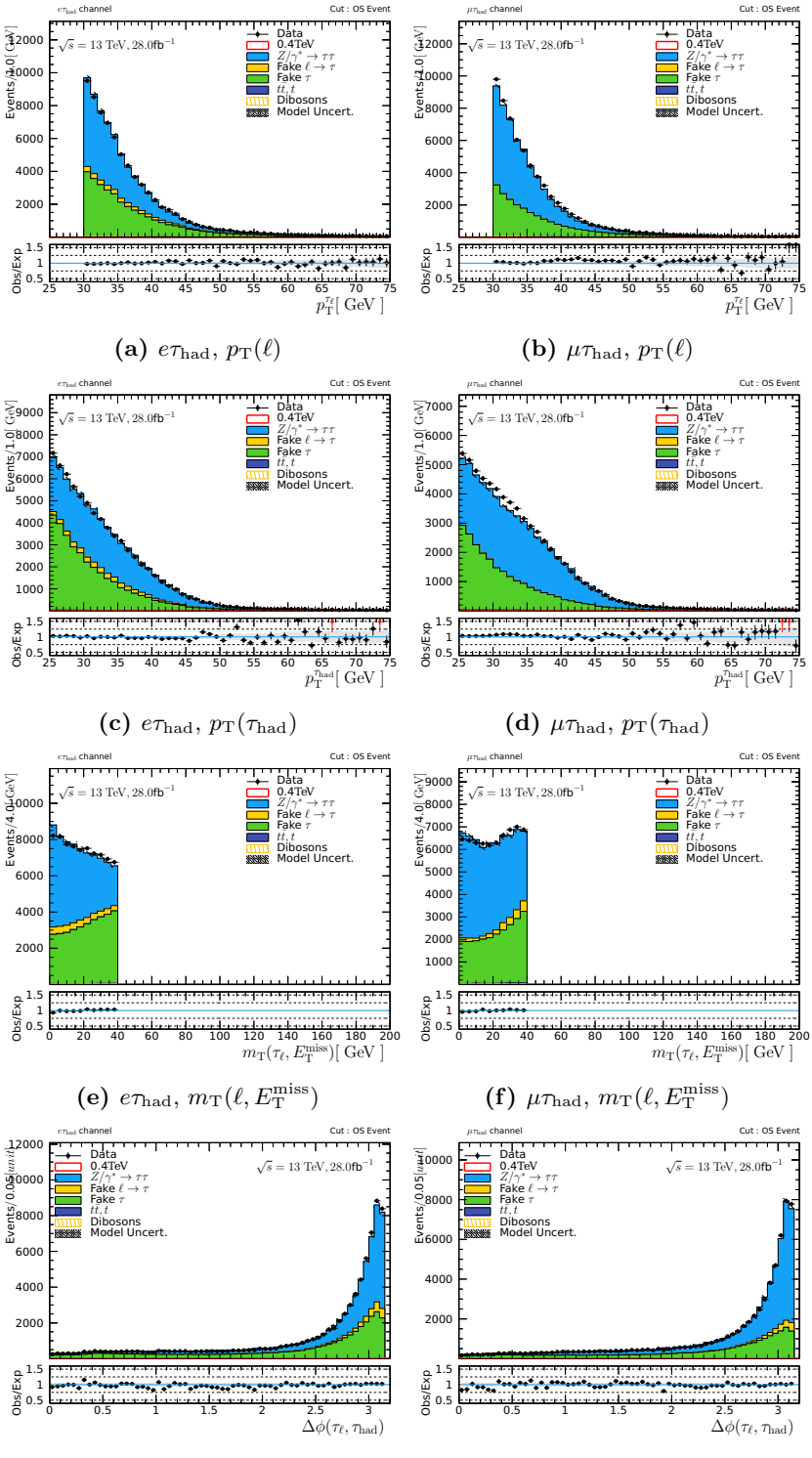

(a) $e\tau_{\mathrm{had}}$, $p_{\mathrm{T}}(\ell)$ **(b)** $\mu\tau_{\mathrm{had}}$, $p_{\mathrm{T}}(\ell)$

(c) $e\tau_{\mathrm{had}}$, $p_{\mathrm{T}}(\tau_{\mathrm{had}})$ **(d)** $\mu\tau_{\mathrm{had}}$, $p_{\mathrm{T}}(\tau_{\mathrm{had}})$

(e) $e\tau_{\mathrm{had}}$, $m_{\mathrm{T}}(\ell, E_{\mathrm{T}}^{\mathrm{miss}})$ **(f)** $\mu\tau_{\mathrm{had}}$, $m_{\mathrm{T}}(\ell, E_{\mathrm{T}}^{\mathrm{miss}})$

(g) $e\tau_{\mathrm{had}}$, $\Delta\phi(\ell, \tau_{\mathrm{had}})$ **(h)** $\mu\tau_{\mathrm{had}}$, $\Delta\phi(\ell, \tau_{\mathrm{had}})$

Figure C.12: Comparisons of data and background in the b-veto ZCR for $e\tau_{\mathrm{had}}$ and $\mu\tau_{\mathrm{had}}$ channel with four important variables.

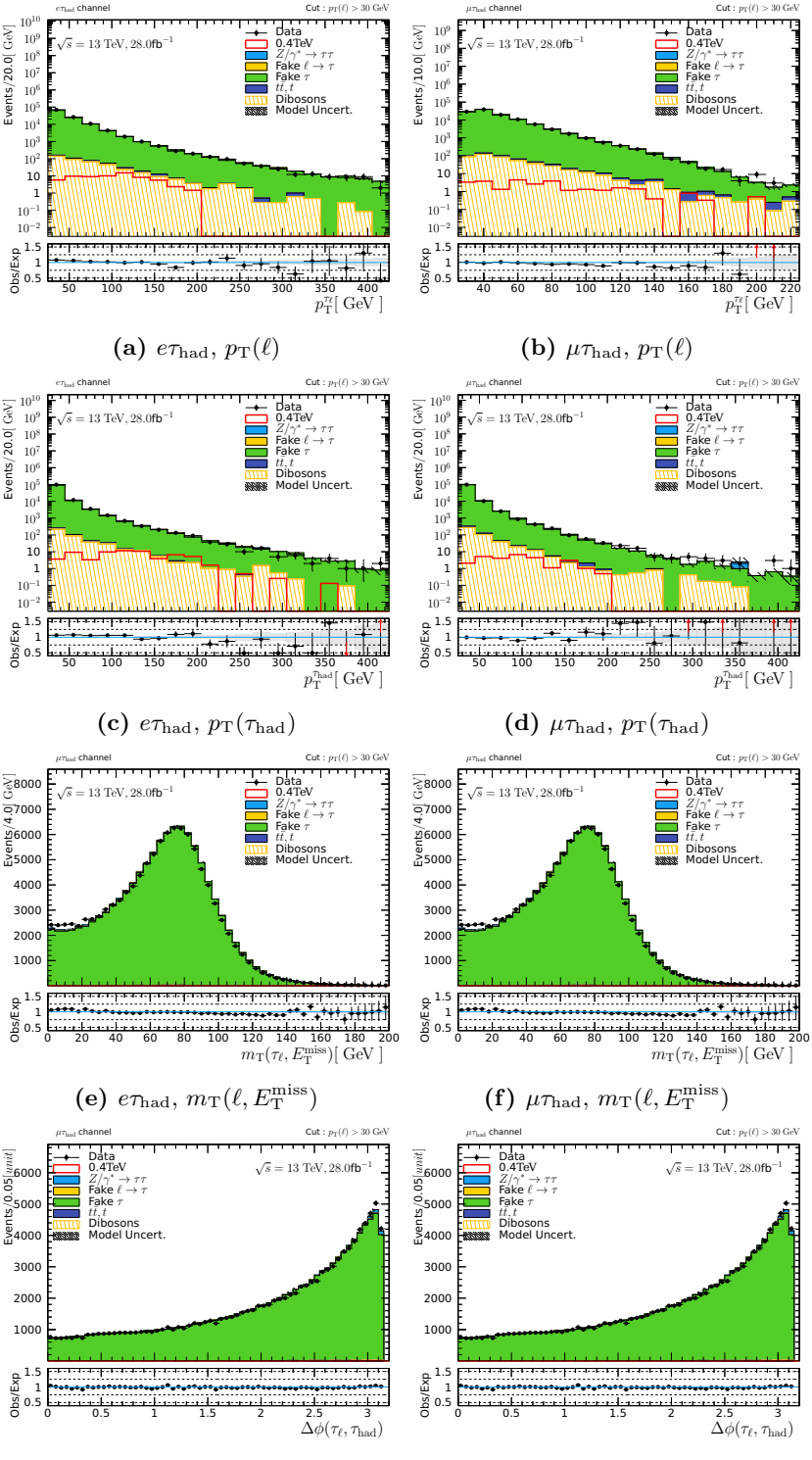

(a) $e\tau_{\mathrm{had}}$, $p_{\mathrm{T}}(\ell)$ **(b)** $\mu\tau_{\mathrm{had}}$, $p_{\mathrm{T}}(\ell)$

(c) $e\tau_{\mathrm{had}}$, $p_{\mathrm{T}}(\tau_{\mathrm{had}})$ **(d)** $\mu\tau_{\mathrm{had}}$, $p_{\mathrm{T}}(\tau_{\mathrm{had}})$

(e) $e\tau_{\mathrm{had}}$, $m_{\mathrm{T}}(\ell, E_{\mathrm{T}}^{\mathrm{miss}})$ **(f)** $\mu\tau_{\mathrm{had}}$, $m_{\mathrm{T}}(\ell, E_{\mathrm{T}}^{\mathrm{miss}})$

(g) $e\tau_{\mathrm{had}}$, $\Delta\phi(\ell, \tau_{\mathrm{had}})$ **(h)** $\mu\tau_{\mathrm{had}}$, $\Delta\phi(\ell, \tau_{\mathrm{had}})$

Figure C.13: Comparisons of data and background in the b-veto SSCR for $e\tau_{\mathrm{had}}$ and $\mu\tau_{\mathrm{had}}$ channel with four important variables.

D Definition of Experimental Systematic Uncertainties

Uncertainty	Alias	Type	Description
Resolution	MET_SoftTrk_ResoPara	shape	soft term resol. in parallel direction
	MET_SoftTrk_ResoPerp	shape	soft term resol. in perpendicular direction
Scale	MET_SoftTrk_Scale	shape	soft term scale
Trigger	MET_TrigEff_elhad	accep.	trig. eff. for $e\tau_{\text{had}}$ channel
	MET_TrigEff_muhad	accep.	trig. eff. for $\mu\tau_{\text{had}}$ channel

Table D.13: Systematic uncertainties for $E_{\text{T}}^{\text{miss}}$ with alias in the final fit and its type.

Uncertainty	Alias	Type	Description
Reconstruction	EL_Reco	accep.	reco. eff. measurement
Identification	EL_Id	accep.	id eff. measurement
Isolation	EL_Iso	accep.	iso. eff. measurement
Trigger	EL_Trig	accep.	trig. eff. measurement
Energy resolution	EG_RESOLUTION_ALL	shape	MC energy resolution
Energy scale	EG_SCALE_ALLCORR	shape	energy calib. correction
	EG_SCALE_E4SCINTILLATOR	shape	LAr calo. 4th layer simulation
	EG_SCALE_LARCALIB_EXTRA2015PRE	shape	LAr calo. calib. for 2015
	EG_SCALE_LARCALIB_EXTRA2016PRE	shape	LAr calo. calib. for 2016
	EG_SCALE_LARTEMP_EXTRA2015PRE	shape	LAr calo. temperture for 2015
	EG_SCALE_LARTEMP_EXTRA2016PRE	shape	LAr calo. temperture for 2016

Table D.13: Systematic uncertainties for electron objects with alias in the final fit and its type.

Uncertainty	Alias	Type	Description
Reconstruction	MU_Reco_Stat/Syst	accep.	reco. eff. stat/syst term
TTVA	MU_TTVA_Stat/Syst	accep.	TTVA eff. stat/syst term
Isolation	MU_Iso_Stat/Syst	accep.	iso. eff. stat/syst term
Trigger	MU_Trig_Stat/Syst	accep.	trig. eff. stat/syst term
Momentum scale	MU_Scale	shape.	MC momentum scale
Momentum resolution	MU_ID	shape	MC momentum resol. at ID
	MU_MS	shape	MC momentum resol. at MS

Table D.13: Systematic uncertainties for muon objects with alias in the final fit and its type.

E Variation of Systematic Uncertainty

As the results of evaluation of systematic uncertinties, Table E.13 and E.13 show variations for the high-$E_{\text{T}}^{\text{miss}}$ category with each decay channels. Each systematic uncertinties are taken as quadrature sum. For signal processes, both production processes are assumed $m_{\text{A}} = 600\,\text{GeV}$ mass hypothesis.

Table E.13 and E.13 show variations for the b-veto category with each decay channels.

Uncertainty	Alias	Type	Description
JVT	JET_JVT	accep.	JVT eff.
Energy scale	JET_GroupedNP_1,2,3	shape	JES groped as 1,2,3
	JET_EtaIntercalib_NonClosure	shape	non closer for inter calib. η binning
Energy resolution	JET_JER_SINGLE_NP	shape	energy resolution
b-tagging	FT_Eigen_B_00∼01	accep.	eigne vector for real b-quark
	FT_Eigen_C_00∼02	accep.	eigne vector for real c-quark
	FT_Eigen_L_00∼03	accep.	eigne vector for other light-quark
	FT_Extra	accep.	extrapolation
	FT_ExtraC	accep.	extrapolation for c-quark

Table D.13: Systematic uncertainties for jet objects with alias in the final fit and its type.

Uncertainty	Alias	Type	Description
Reconstruction	TAU_Reco_LowPt/HighPt	accep.	reco. eff. for low-p_{T}/high-p_{T}
	TAU_Reco_TrueEleEleOLR	accep.	eVeto eff. for real electron
	TAU_Reco_TrueTauEleOLR	accep.	eVeto eff. for real hadronic-τ
Identification	TAU_Id_LowPt/HighPt	accep.	id.. eff. for low-p_{T}/high-p_{T}
Energy Scale	TAUS_SME_TES_DETECTOR	shape	TES on detector simulation
	TAUS_SME_TES_MODEL	shape	TES on simulation model
	TAUS_SME_TES_INSITU	shape	TES on in-situ measurement

Table D.13: Systematic uncertainties for hadronic-τ objects with alias in the final fit and its type.

Uncertainty	Alias	Type	Description
$FF^{q}_{\bar{\tau}\to\tau}$	FFQ_Btag/Bveto	shape	QCD Fake factor for b-tagged/-veto event
$FF^{\mathrm{EW}}_{\bar{\tau}\to\tau}$	FFW_Btag/Bveto	shape	EW Fake factor for b-tagged/-veto event
W+jets non-closer	Fake_HM_el/muhad	accep.	fake non-closer for the high-$E_{\mathrm{T}}^{\mathrm{miss}}$ $e/\mu\tau_{\mathrm{had}}$ SR
	Fake_Btag_el/muhad	accep.	fake non-closer for the b-tag $e/\mu\tau_{\mathrm{had}}$ SR
	Fake_Bveto_el/muhad	accep.	fake non-closer for the b-veto $e/\mu\tau_{\mathrm{had}}$ SR
r_q	rQ_HM_el/muhad	shape	r_q for the high-$E_{\mathrm{T}}^{\mathrm{miss}}$ $e/\mu\tau_{\mathrm{had}}$ SR
	rQ_Btag_el/muhad	shape	r_q for the b-tag $e/\mu\tau_{\mathrm{had}}$ SR
	rQ_Bveto_el/muhad	shape	r_q for the b-veto $e/\mu\tau_{\mathrm{had}}$ SR
$Z\to\tau\tau$ SF	SFZ_HM_el/muhad	accep.	SF for $Z\to\tau\tau$ in the high-$E_{\mathrm{T}}^{\mathrm{miss}}$ $e/\mu\tau_{\mathrm{had}}$ SR
	SFZ_Btag_el/muhad	accep.	SF for $Z\to\tau\tau$ in the b-tag $e/\mu\tau_{\mathrm{had}}$ SR
	SFZ_Bveto_el/muhad	accep.	SF for $Z\to\tau\tau$ in the b-veto $e/\mu\tau_{\mathrm{had}}$ SR
$t\bar{t}\to\ell\tau_{\mathrm{had}}$ SF	SFT_HM_el/muhad	accep.	SF for $t\bar{t}\to\ell\tau_{\mathrm{had}}$ in the high-$E_{\mathrm{T}}^{\mathrm{miss}}$ $e/\mu\tau_{\mathrm{had}}$ SR
	SFT_Btag_el/muhad	accep.	SF for $t\bar{t}\to\ell\tau_{\mathrm{had}}$ in the b-tag $e/\mu\tau_{\mathrm{had}}$ SR
	SFT_Bveto_el/muhad	accep.	SF for $t\bar{t}\to\ell\tau_{\mathrm{had}}$ in the b-veto $e/\mu\tau_{\mathrm{had}}$ SR

Table D.13: Systematic uncertainties for background modelling.

Table E.13 and E.13 show variations for the b-tag category with each decay channels.

Uncertainty	ggF			bbA		
	200 GeV	500 GeV	1 TeV	200 GeV	500 GeV	1 TeV
PDF	4.100	4.800	4.300	5.978	6.529	12.356
$\mu_{F,R}$	17.400	15.500	15.100	17.569	18.755	20.043
MC tuning	3.835	2.795	2.488	4.744	3.983	3.718
total	18.283	16.465	15.896	19.155	20.254	23.837

Table D.13: Systematic uncertainties for signal samples. MC tuning values are quadratic sum of each MC tuning variations. All values are denoted by %.

Uncertainty	ggF	bbA	Diboson	$j \to \tau_{\text{had}}$	$t\bar{t}, t$	$Z \to \tau\tau$
			$e\tau_{\text{had}}^{\text{1p}}$			
Electron	±1.5%	±1.2%	±1.9%	-	±1.7%	±1.3%
Jet	±3.5%	±2.4%	±9.5%	-	±9.4%	±18.7%
MET	±0.6%	±1.2%	±4.8%	-	±1.8%	±1.1%
TES	±16.6%	±16.8%	±8.6%	-	±6.2%	±32.7%
Tau	±6.0%	±6.0%	±5.3%	-	±6.1%	±5.5%
Theory	±15.1%	±24.9%	±6.0%	-	±17.0%	±16.5%
Total	±23.5%	±30.7%	±15.9%	±13.5%	±23.6%	±41.5%
			$e\tau_{\text{had}}^{\text{3p}}$			
Electron	±1.1%	±1.8%	±1.0%	-	±1.2%	±23.2%
Jet	±1.3%	±3.2%	±16.8%	-	±8.5%	±0.4%
MET	±0.5%	±1.9%	±17.5%	-	±2.7%	±0.3%
TES	±23.3%	±24.6%	±14.6%	-	±8.3%	±2.4%
Tau	±6.4%	±6.4%	±5.7%	-	±6.0%	±6.5%
Theory	±15.1%	±24.9%	±6.0%	-	±16.5%	±31.9%
Total	±28.5%	±35.8%	±29.5%	±10.6%	±23.6%	±40.0%

Table E.13: Values of systematic uncertainty variation to nominal expectation for the high-$E_{\text{T}}^{\text{miss}}$ category $e\tau_{\text{had}}$ channel.

Uncertainty	ggF	bbA	Diboson	$j \to \tau_{\text{had}}$	$t\bar{t}, t$	$Z \to \tau\tau$
			$\mu\tau_{\text{had}}^{\text{1p}}$			
Muon	±0.7%	±0.7%	±1.1%	-	±0.9%	±4.3%
Jet	±2.0%	±2.9%	±11.0%	-	±4.1%	±1.7%
MET	±1.3%	±0.7%	±2.0%	-	±1.7%	±0.3%
TES	±8.9%	±7.9%	±10.3%	-	±7.5%	±8.7%
Tau	±5.9%	±5.9%	±4.9%	-	±6.1%	±5.8%
Theory	±15.1%	±24.9%	±6.0%	-	±12.0%	±23.5%
Total	±18.7%	±26.9%	±17.1%	±11.5%	±18.9%	±26.2%
			$\mu\tau_{\text{had}}^{\text{3p}}$			
Muon	±1.0%	±0.7%	±1.3%	-	±0.7%	±2.0%
Jet	±3.3%	±4.1%	±15.8%	-	±4.8%	±10.3%
MET	±1.0%	±0.8%	±5.3%	-	±2.0%	±8.7%
TES	±9.8%	±10.8%	±10.8%	-	±12.5%	±26.8%
Tau	±6.3%	±6.3%	±5.6%	-	±6.0%	±6.1%
Theory	±15.1%	±24.9%	±6.0%	-	±12.3%	±24.1%
Total	±19.4%	±28.2%	±21.5%	±10.4%	±21.8%	±39.0%

Table E.13: Values of systematic uncertainty variation to nominal expectation for the high-$E_{\text{T}}^{\text{miss}}$ category $\mu\tau_{\text{had}}$ channel.

Uncertainty	ggF	bbA	Diboson	$j \to \tau_{\text{had}}$	$\ell \to \tau_{\text{had}}$	$t\bar{t}, t$	$Z \to \tau\tau$
			$e\tau_{\text{had}}^{\text{1p}}$				
Electron	±1.6%	±1.6%	±5.3%	-	-	±1.3%	±3.5%
Jet	±20.4%	±4.3%	±14.6%	-	-	±4.0%	±19.4%
FT	±25.0%	±4.3%	±18.0%	-	-	±2.7%	±10.9%
MET	±3.6%	±2.5%	±5.3%	-	-	±0.7%	±5.4%
TES	±11.3%	±1.2%	±7.2%	-	-	±6.0%	±6.4%
Tau	±6.6%	±6.3%	±6.0%	-	-	±6.4%	±6.9%
Theory	±15.1%	±24.9%	±6.0%	-	-	±6.9%	±5.4%
Total	±38.2%	±26.6%	±26.8%	±15.9%	±21.0%	±15.8%	±25.6%
			$e\tau_{\text{had}}^{\text{3p}}$				
Electron	±1.3%	±1.9%	±1.1%	-	-	±1.7%	±2.1%
Jet	±21.3%	±4.9%	±14.5%	-	-	±4.4%	±11.6%
FT	±37.1%	±4.6%	±10.3%	-	-	±2.8%	±16.3%
MET	$< 0.01\%$	±2.7%	±3.9%	-	-	±0.9%	±25.9%
TES	±18.2%	±3.1%	±19.2%	-	-	±7.6%	±8.3%
Tau	±6.0%	±6.2%	±6.1%	-	-	±6.0%	±6.4%
Theory	±15.1%	±24.9%	±6.0%	-	-	±7.2%	±10.7%
Total	±49.2%	±26.9%	±27.8%	±20.5%	±21.0%	±16.6%	±36.0%

Table E.13: Values of systematic uncertainty variation to nominal expectation for the b-tag category $e\tau_{\text{had}}$ channel.

Uncertainty	ggF	bbA	$j \to \tau_{\text{had}}$	$Z \to \ell\ell(\to\tau)$	$t\bar{t}, t(\ell \to \tau)$	$t\bar{t}, t$	Diboson	$Z \to \tau\tau$
			$\mu\tau_{\text{had}}^{\text{1p}}$					
Muon	±7.0%	±2.0%	-	±1.6%	±2.8%	±1.7%	±2.8%	±1.8%
Jet	±23.9%	±13.0%	-	±20.7%	±9.9%	±21.0%	±24.0%	±15.6%
FT	±18.8%	±5.1%	-	±8.7%	±4.1%	±2.6%	±15.0%	±13.5%
MET	±7.0%	±2.0%	-	±7.7%	±5.1%	±17.3%	±8.2%	±20.9%
TES	±16.3%	±3.0%	-	< 0.01%	< 0.01%	±5.3%	±12.3%	±8.5%
Tau	±5.9%	±5.8%	-	< 0.01%	< 0.01%	±6.3%	±5.0%	±6.8%
Theory	±15.1%	±24.9%	-	±5.0%	±6.7%	±7.1%	±6.0%	±9.6%
Total	±39.4%	±29.4%	±12.2%	±24.4%	±14.0%	±29.5%	±33.0%	±32.8%
			$\mu\tau_{\text{had}}^{\text{3p}}$					
Muon	±28.2%	±1.9%	-	< 0.01%	±1.6%	±1.7%	±1.1%	±3.8%
Jet	±25.6%	±10.2%	-	< 0.01%	±30.9%	±19.5%	±18.4%	±23.3%
FT	±16.7%	±4.4%	-	< 0.01%	±5.5%	±2.8%	±13.4%	±9.7%
MET	±24.4%	±3.9%	-	< 0.01%	±11.8%	±16.6%	±10.2%	±17.7%
TES	±25.4%	±21.3%	-	< 0.01%	< 0.01%	±8.6%	±10.6%	±9.4%
Tau	±6.0%	±6.0%	-	< 0.01%	< 0.01%	±6.0%	±5.2%	±6.3%
Theory	±15.1%	±24.9%	-	±5.0%	±10.0%	±6.8%	±6.0%	±10.6%
Total	±56.9%	±35.4%	±16.9%	±5.0%	±35.0%	±28.9%	±27.8%	±34.7%

Table E.13: Values of systematic uncertainty variation to nominal expectation for the b-tag category $\mu\tau_{\text{had}}$ channel.

Uncertainty	ggF	bbA	Diboson	$j \to \tau_{\text{had}}$	$\ell \to \tau_{\text{had}}$	$t\bar{t}, t$	$Z \to \tau\tau$
			$e\tau_{\text{had}}^{\text{1p}}$				
Electron	±1.5%	±1.5%	±1.5%	-	-	±1.3%	±1.4%
Jet	±4.1%	±5.9%	±2.3%	-	-	±6.3%	±13.1%
FT	±0.4%	±3.3%	±0.3%	-	-	±11.3%	±0.2%
MET	±1.4%	±1.7%	±1.1%	-	-	±1.1%	±15.0%
TES	±0.3%	±2.0%	±5.1%	-	-	±3.4%	±2.6%
Tau	±6.3%	±6.3%	±6.5%	-	-	±6.4%	±6.9%
Theory	±15.1%	±24.9%	±6.0%	-	-	±6.8%	±6.6%
Total	±17.0%	±26.7%	±10.7%	±8.6%	±21.0%	±19.2%	±22.3%
			$e\tau_{\text{had}}^{\text{3p}}$				
Electron	±1.6%	±1.7%	±2.0%	-	-	±1.5%	±1.5%
Jet	±2.5%	±7.1%	±1.9%	-	-	±5.9%	±5.2%
FT	±0.5%	±2.6%	±0.4%	-	-	±10.7%	±0.2%
MET	±1.8%	±2.9%	±2.1%	-	-	±2.0%	±11.0%
TES	±3.1%	±3.6%	±7.2%	-	-	±6.4%	±1.1%
Tau	±6.1%	±6.0%	±5.7%	-	-	±6.0%	±6.4%
Theory	±15.1%	±24.9%	±6.0%	-	-	±7.2%	±7.7%
Total	±16.9%	±27.1%	±11.5%	±8.6%	±21.0%	±19.6%	±15.8%

Table E.13: Values of systematic uncertainty variation to nominal expectation for the b-veto category $e\tau_{\text{had}}$ channel.

Uncertainty	ggF	bbA	$j \to \tau_{\text{had}}$	$Z \to \ell\ell(\to\tau)$	$t\bar{t}, t(\ell \to \tau)$	$t\bar{t}, t$	Diboson	$Z \to \tau\tau$
			$\mu\tau_{\text{had}}^{\text{1p}}$					
Muon	±1.9%	±1.9%	-	±1.0%	±1.3%	±1.6%	±1.4%	±1.1%
Jet	±6.3%	±9.7%	-	±2.9%	±13.1%	±7.0%	±2.5%	±8.5%
FT	±0.4%	±2.4%	-	±0.1%	±5.0%	±10.3%	±0.3%	±0.2%
MET	±2.8%	±0.8%	-	±5.1%	±3.8%	±1.2%	±0.7%	±14.8%
TES	±6.6%	±8.1%	-	< 0.01%	< 0.01%	±4.4%	±5.6%	±5.6%
Tau	±5.9%	±5.8%	-	< 0.01%	< 0.01%	±6.2%	±5.3%	±6.7%
Theory	±15.1%	±24.9%	-	±5.0%	±8.3%	±7.1%	±6.0%	±8.1%
Total	±18.9%	±28.7%	±8.1%	±7.8%	±16.8%	±19.2%	±10.2%	±20.9%
			$\mu\tau_{\text{had}}^{\text{3p}}$					
Muon	±1.8%	±2.2%	-	±5.7%	±4.7%	±1.8%	±1.9%	±1.1%
Jet	±7.2%	±8.8%	-	±4.4%	±11.4%	±7.6%	±8.2%	±7.1%
FT	±0.4%	±4.7%	-	±0.4%	±1.3%	±9.6%	±0.3%	±0.1%
MET	±1.8%	±0.9%	-	±7.0%	±6.4%	±1.5%	±2.5%	±11.9%
TES	±10.0%	±10.8%	-	< 0.01%	< 0.01%	±6.4%	±11.3%	±6.3%
Tau	±6.0%	±5.9%	-	< 0.01%	< 0.01%	±6.0%	±5.9%	±6.3%
Theory	±15.1%	±24.9%	-	±5.0%	±9.3%	±6.8%	±6.0%	±7.4%
Total	±20.6%	±29.6%	±8.2%	±11.3%	±16.8%	±19.5%	±16.6%	±18.1%

Table E.13: Values of systematic uncertainty variation to nominal expectation for the b-veto category $\mu\tau_{\text{had}}$ channel.

F Theoretical Systematic Uncertainties

Parameter	default	vari, 1	vari. 2	MPI
Hard interaction primordial $k_\perp$	1.74948	1.719/1.780	1.762/1.737	-
ISR α_S	0.118	-	-	-
ISR p_{T} cutoff	1.923589	1.919/1.928	1.844/2.004	-
MPI p_{T} cutoff	2.002887	-	-	2.05/1.97

Table F.13: Parameters of MC tuning variation for ggH signal samples.

Parameter	default	vari. 1	vari. 2	vari. 3a	vari. 3b	vari. 3c
ISR p_{T} cutoff	1.56	-	1.60/1.50	1.67/1.51	-	-
f max ISR evol. scale	0.91	-	1.05/0.91	0.98/0.88	1.00/0.83	-
$\mu_{F,R}$ dampling	1.05	-	1.04/1.08	1.36/0.93	1.04/1.07	-
ISR α_S	0.127	-	-	-	0.129/0.126	0.140/0.115
FSR α_S	0.127	-	0.139/0.111	0.136/0.124	0.114/0.138	-
MPI α_S	0.126	0.131/0.121	-	0.125/0.127	-	-
Colour reconn. strengh	1.71	1.73/1.69	-	-	-	-

Table F.13: Parameters of MC tuning variation for ggH signal samples.

Source	description	variation (%)
Scale	it is considered varying $\mu_{F,R}$ by factor of 0.5 and 2.0.	$+2.37/-3.51$
PDF + α_S	PDF uncertinties are evaluated by above way, α_S uncertinty is evaluated by takning 68% C.L. on its uncertinty.	± 4.21
m_{top}	m_{top} variation of ± 1.0 GeV.	$+2.77/-2.70$
Radiation	By taking enriched or reduced initial state radiation conditions.	shape plus ± 0.92
Hard process	Diff. between nom. and samples generated by `aMC@NLO+Herwig`.	shape plus ± 0.51
Showering and UE	Diff. between nom. and samples generated by `Powheg+HerwigUE`.	shape plus ± 1.98

Table F.13: Systematic uncertainties for $t\bar{t}$ process. For radiation, hadronisation and parton showering uncertinty, it is changed event rates and its shape on the final discriminant. It is shown in Figure 6.21 as a ratio to nominal sample.

G Validation of Maximum Likelihood Fit

For the validation of the values of the nuisance parameters obtained in the minimisation procedure have been performed. Figure G.14 shows the fitted values of the nuisance parameters in the combined likelihood fit using the benchmark scenario of $m_{\mathrm{A}} = 600\,\mathrm{GeV}$, $\tan\beta = 20$. The impact of individual

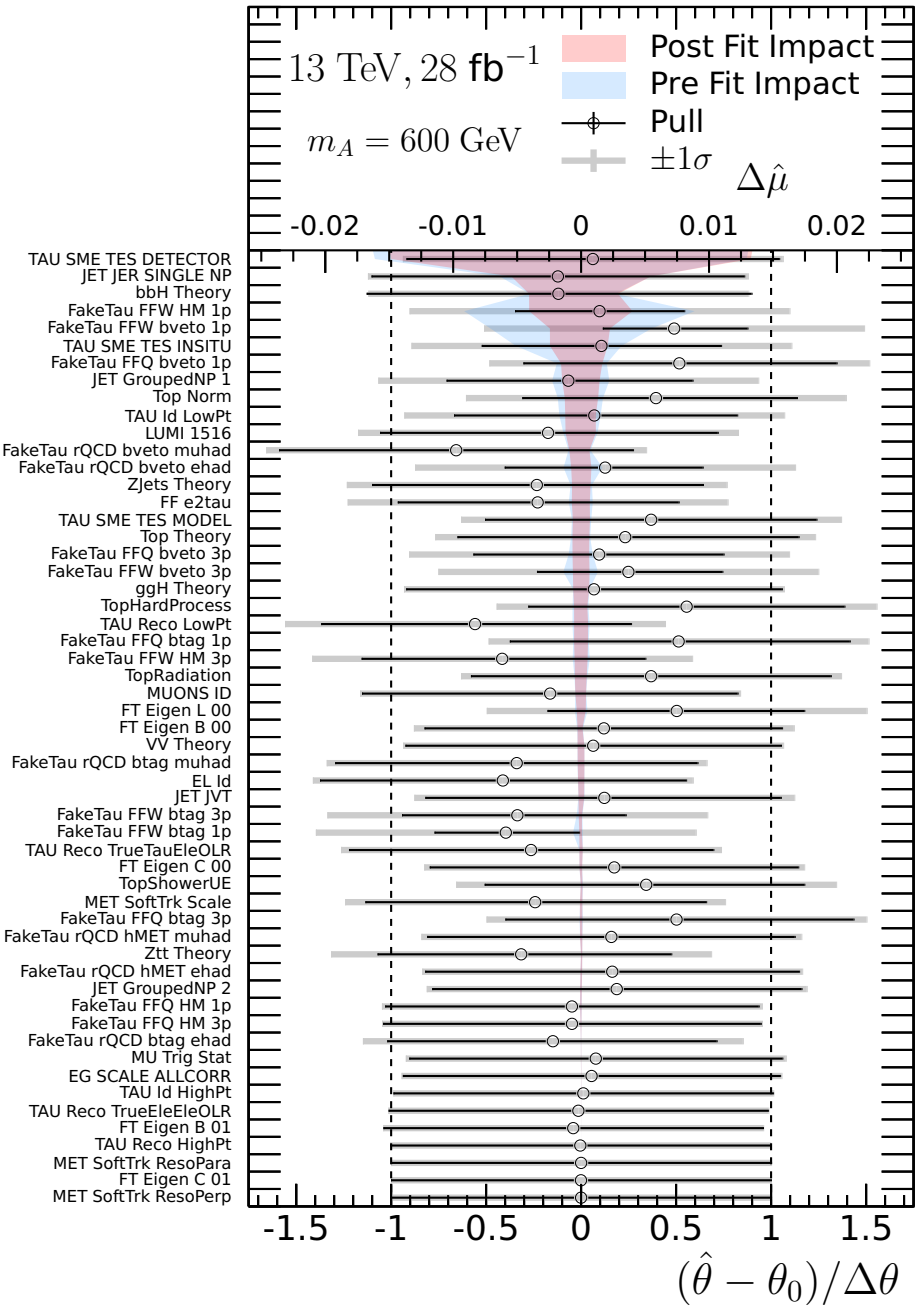

Figure G.14: Fitted values of the nuisance parameters obtained in the combined likelihood fit with $m_{\mathrm{A}} = 600\,\mathrm{GeV}$ and $\tan\beta = 20$ hypothesis. Each nuisance parameters show fitted value (opend circle) and its $\pm1\sigma$ (black line), original $\pm1\sigma$ is given as gray line. The nuisance parameters are listed by ordering its post-fit impact on the signal strength, it is shown in red filled region, while a pre-fit impact is shown in blue regions.

uncertainties on the results is defined as following. Each nuisance parameter is is fixed to its $\pm1\sigma$ estimates and the impact on $\hat{\mu}$ is evaluated after re-minimising the combined likelihood with respect

to all other nuisance paramters of the fit model. The absolute change in the fitted signal strength $\Delta\hat{\mu}$ with respect to the default estimate is used as the impact on the model for the pre-fit and post-fit. The highest ranked nuisance parameter is the uncertinty of the hadronic-τ energy scale on a detector sumulation. This systematic uncertinty dramatically changes the $m_{\tau\tau}$ shape. The second highest ranked nuisance paramter is the energy resolution of jet objects, in this analysis jet is not directly used. The $E_{\mathrm{T}}^{\mathrm{miss}}$, however, strongly depends on inputs from jet objects, so that this systematic uncertinty has strong impact on the $m_{\tau\tau}$ shape. In general, the uncertinties on the fake background are constrained by the combined likelihood fit. Because the fake backgrund is leading background in all signal region and its property can be measured. This feature is confirmed using the Asimov data result, the uncertinties related to the fake backgrund can potentially be constrained.

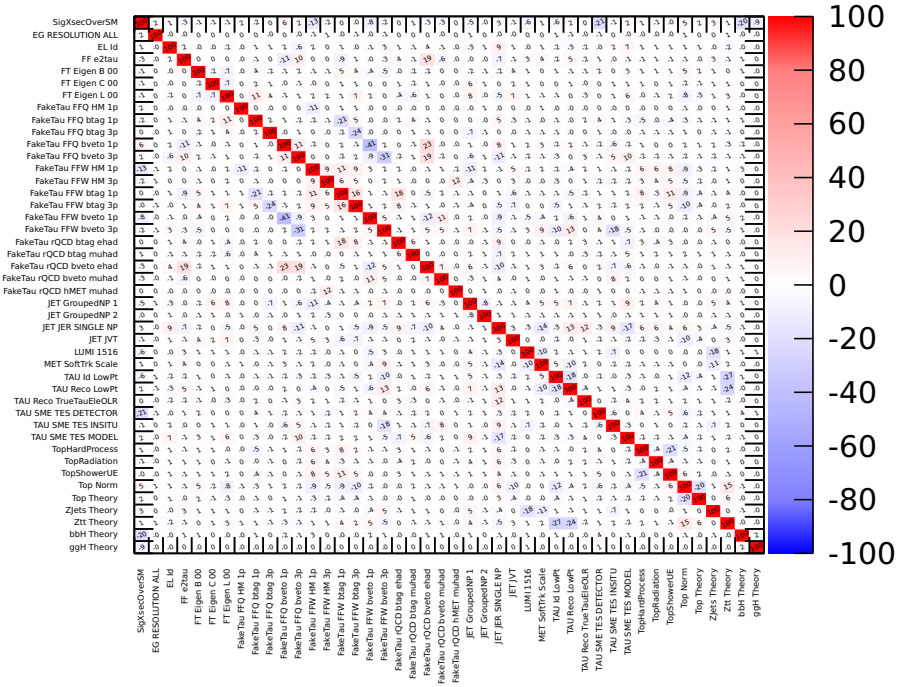

Figure G.15: Mutual correlation coffieents of the nuisance paramters in percentage, only with the highly correlated nuisance parameter pairs.

Figure G.15 shows the mutual correlation coffieents of the nuisance parameters with only highly correlated nuisance parameter pairs. Large correlation cofficients would indicate potential degeneracies between parameters. The largest correlations are of the order of -40% and are found between the fake factor systematic uncertinties. These uncertinties, in principle, should be separated in the 1- or 3-prong hadronic-τ decay channels, but the combined likelihood fit is perfromed together with only $e\tau_{\mathrm{had}}$ or $\mu\tau_{\mathrm{had}}$, so this behaviour is expected. The second largest correlations are of the order of $-20 \sim -30\%$ between the $Z \to \tau\tau$ theory and the hadronic-τ reconstruction and identification uncertinties for the low-p_{T} candidates. Since this signal hypotesis has higher-p_{T} compared with one from $Z \to \tau\tau$ background, so these systematic uncertinties dominate from $Z \to \tau\tau$ background, it is expected behaviour.

H Plots for the Post-Fit

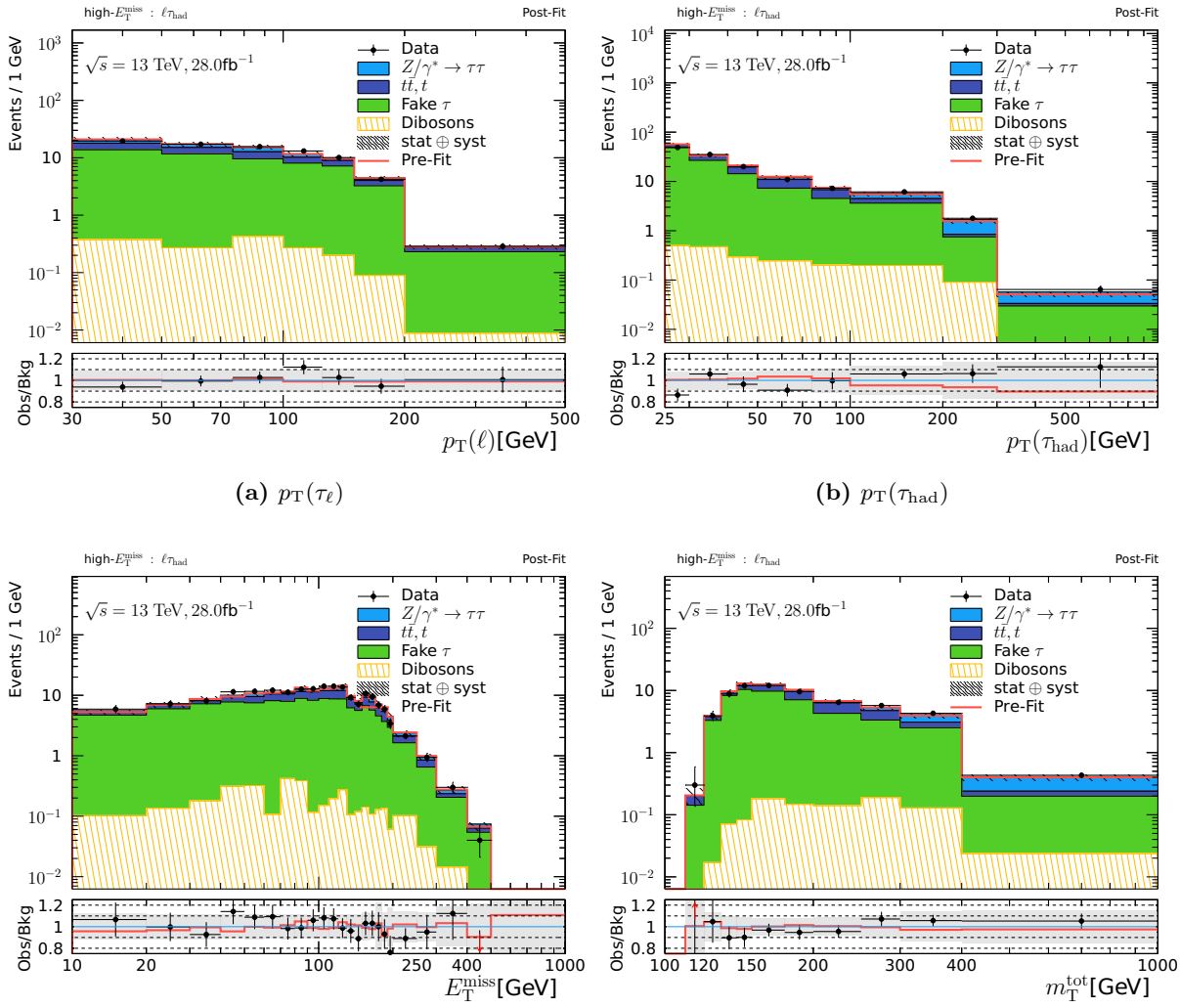

(a) $p_{\mathrm{T}}(\tau_\ell)$ **(b)** $p_{\mathrm{T}}(\tau_{\mathrm{had}})$

(c) $E_{\mathrm{T}}^{\mathrm{miss}}$ **(d)** $m_{\tau\tau}$

Figure H.16: Distributions for several variables in the high-$E_{\mathrm{T}}^{\mathrm{miss}}$ category after the combined likelihood fit. In the bottom panels a ratio of data and expected background model and the uncertainties correspond to the systematic and statistical uncertainties are shown. All plots are in logarithmic scale in x- and y-axis. Red line in the ratio shows the ratio of pre-fit expectation.

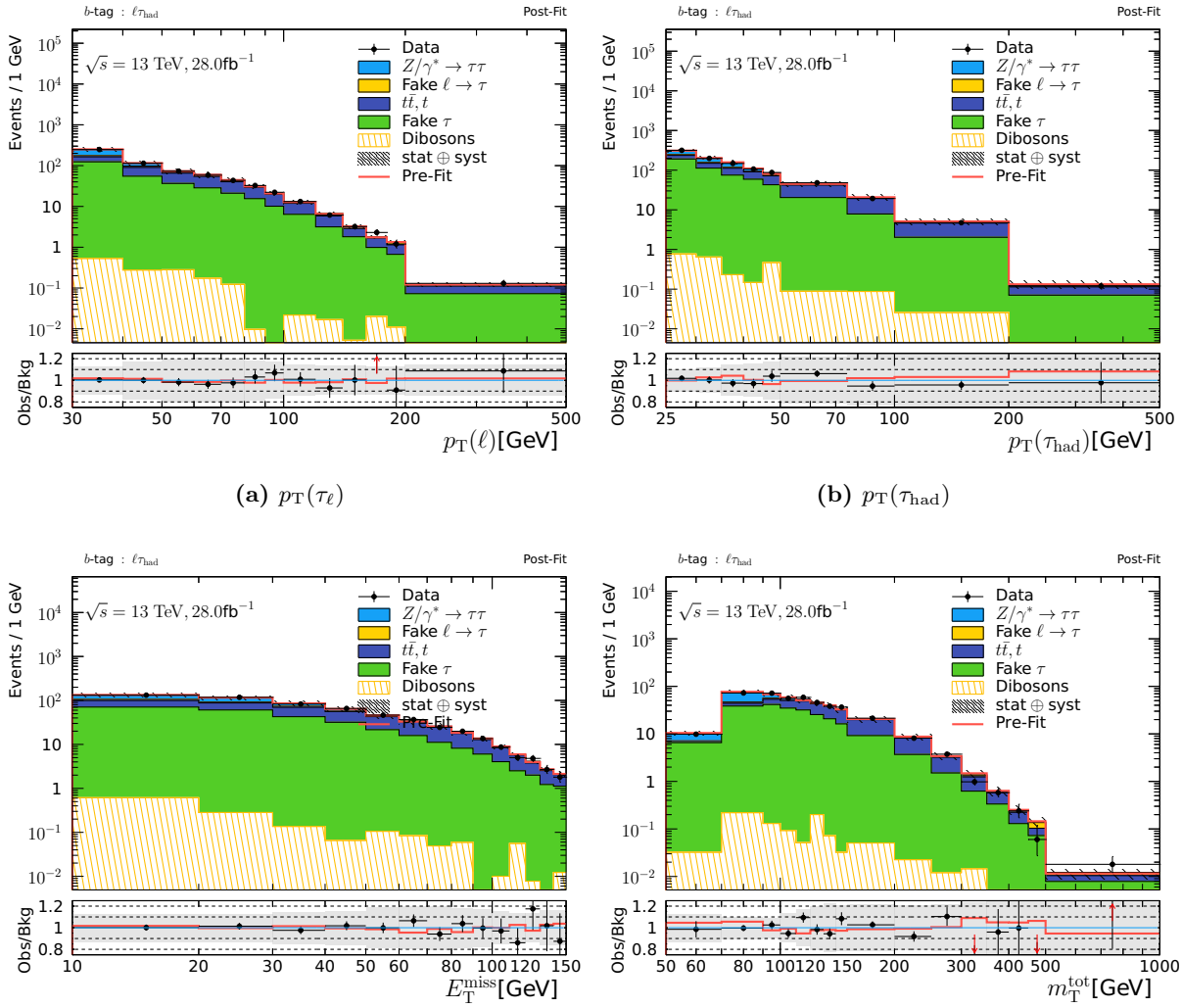

(a) $p_{\text{T}}(\tau_\ell)$ **(b)** $p_{\text{T}}(\tau_{\text{had}})$

(c) $E_{\text{T}}^{\text{miss}}$ **(d)** $m_{\tau\tau}$

Figure H.17: Distributions for several variables in the b-tag category after the combined likelihood fit. In the bottom panels a ratio of data and expected background model and the uncertainties correspond to the systematic and statistical uncertainties are shown. All plots are in logarithmic scale in x- and y-axis. Red line in the ratio shows the ratio of pre-fit expectation.

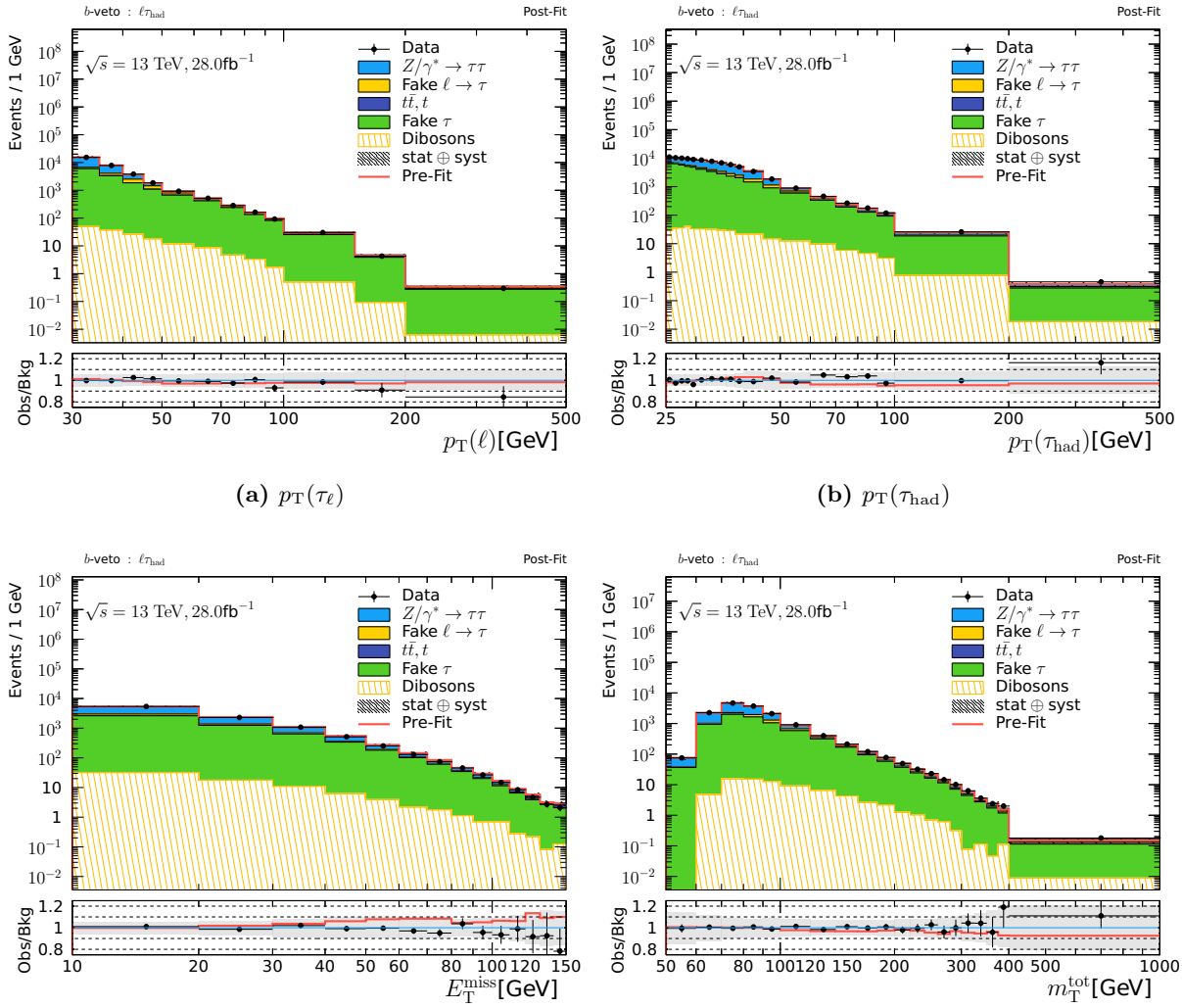

(a) $p_{\text{T}}(\tau_\ell)$ **(b)** $p_{\text{T}}(\tau_{\text{had}})$

(c) $E_{\text{T}}^{\text{miss}}$ **(d)** $m_{\tau\tau}$

Figure H.18: Distributions for several variables in the b-veto category after the combined likelihood fit. In the bottom panels a ratio of data and expected background model and the uncertainties correspond to the systematic and statistical uncertainties are shown. All plots are in logarithmic scale in x- and y-axis. Red line in the ratio shows the ratio of pre-fit expectation.

Bibliography

[1] G. Altarelli, *Collider Physics within the Standard Model: a Primer* (2013), arXiv: 1303.2842 [hep-ph].

[2] S. P. Martin, *A Supersymmetry primer* (1997), [Adv. Ser. Direct. High Energy Phys.18,1(1998)], arXiv: hep-ph/9709356 [hep-ph].

[3] A. Djouadi, *The anatomy of electroweak symmetry breaking Tome II: The Higgs bosons in the Minimal Supersymmetric Model*, Phys. Rep. **459** (2008) 1, and references therein.

[4] ATLAS Collaboration, *Observation of a new particle in the search for the Standard Model Higgs boson with the ATLAS detector at the LHC*, Phys. Lett. B **716** (2012) 1, arXiv: 1207.7214 [hep-ex].

[5] CMS Collaboration, *Observation of a new boson at a mass of 125 GeV with the CMS experiment at the LHC*, Phys. Lett. B **716** (2012) 30, arXiv: 1207.7235 [hep-ex].

[6] M. E. Peskin and D. V. Schroeder, *An Introduction to Quantum Field Theory; 1995 ed.* Includes exercises, Boulder, CO: Westview, 1995, URL: https://cds.cern.ch/record/257493.

[7] S. L. Glashow, *Partial Symmetries of Weak Interactions*, Nucl. Phys. **22** (1961) 579.

[8] A. Salam, *Weak and Electromagnetic Interactions*, Conf. Proc. **C680519** (1968) 367.

[9] S. Weinberg, *A Model of Leptons*, Phys. Rev. Lett. **19** (1967) 1264.

[10] H. Fritzsch, M. Gell-Mann and H. Leutwyler, *Advantages of the Color Octet Gluon Picture*, Phys. Lett. **B47** (1973) 365.

[11] F. Englert and R. Brout, *Broken symmetry and the mass of gauge vector mesons*, Phys. Rev. Lett. **13** (1964) 321.

[12] P. W. Higgs, *Broken symmetries, massless particles and gauge fields*, Phys. Lett. **12** (1964) 132.

[13] P. W. Higgs, *Broken symmetries and the masses of gauge bosons*, Phys. Rev. Lett. **13** (1964) 508.

[14] P. W. Higgs, *Spontaneous symmetry breakdown without massless bosons*, Phys. Rev. **145** (1966) 1156.

[15] K. A. Olive et al., *Review of Particle Physics*, Chin. Phys. **C38** (2014) 090001.

[16] H. Yukawa, *On the Interaction of Elementary Particles I*, Proc. Phys. Math. Soc. Jap. **17** (1935) 48, [Prog. Theor. Phys. Suppl.1,1(1935)].

[17] C. L. Bennett et al., *Nine-Year Wilkinson Microwave Anisotropy Probe (WMAP) Observations: Final Maps and Results*, Astrophys. J. Suppl. **208** (2013) 20, arXiv: 1212.5225 [astro-ph.CO].

[18] P. A. R. Ade et al., *Planck 2013 results. I. Overview of products and scientific results*, Astron. Astrophys. **571** (2014) A1, arXiv: 1303.5062 [astro-ph.CO].

[19] H. Kurki-Suonio, *Physics of the Cosmic Microwave Background and the Planck Mission* (2010), arXiv: 1012.5204 [astro-ph.CO].

[20] A. D. Sakharov, *Violation of CP Invariance, c Asymmetry, and Baryon Asymmetry of the Universe*, Pisma Zh. Eksp. Teor. Fiz. **5** (1967) 32, [Usp. Fiz. Nauk161,61(1991)].

[21] B. T. Cleveland et al., *Measurement of the solar electron neutrino flux with the Homestake chlorine detector*, Astrophys. J. **496** (1998) 505.

[22] M. Altmann et al., *Complete results for five years of GNO solar neutrino observations*, Phys. Lett. **B616** (2005) 174, arXiv: hep-ex/0504037 [hep-ex].

[23] K. Eguchi et al., *First results from KamLAND: Evidence for reactor anti-neutrino disappearance*, Phys. Rev. Lett. **90** (2003) 021802, arXiv: hep-ex/0212021 [hep-ex].

[24] Y. Fukuda et al., *Evidence for oscillation of atmospheric neutrinos*, Phys. Rev. Lett. **81** (1998) 1562, arXiv: hep-ex/9807003 [hep-ex].

[25] K. Abe et al., *Evidence for the Appearance of Atmospheric Tau Neutrinos in Super-Kamiokande*, Phys. Rev. Lett. **110** (2013) 181802, arXiv: 1206.0328 [hep-ex].

[26] P. Fayet, *Supersymmetry and Weak, Electromagnetic and Strong Interactions*, Phys. Lett. B **64** (1976) 159.

[27] P. Fayet, *Spontaneously Broken Supersymmetric Theories of Weak, Electromagnetic and Strong Interactions*, Phys. Lett. B **69** (1977) 489.

[28] G. R. Farrar and P. Fayet, *Phenomenology of the Production, Decay, and Detection of New Hadronic States Associated with Supersymmetry*, Phys. Lett. B **76** (1978) 575.

[29] H. P. Nilles, *Supersymmetry, Supergravity and Particle Physics*, Phys. Rept. **110** (1984) 1.

[30] E. Bagnaschi et al., *Benchmark scenarios for low* $\tan\beta$ *in the MSSM*, LHCHXSWG-2015-002, 2015, URL: http://cdsweb.cern.ch/record/2039911.

[31] T. A. Collaboration, *Observation of a new particle in the search for the Standard Model Higgs boson with the ATLAS detector at the LHC*, Physics Letters B **716** (2012) 1.

[32] T. C. Collatoration, *Observation of a new boson at a mass of 125 GeV with the CMS experiment at the LHC*, Physics Letters B **716** (2012) 30.

[33] ATLAS, and CMS Collaborations, *Combined Measurement of the Higgs Boson Mass in pp Collisions at* $\sqrt{s} = 7$ *and 8 TeV with the ATLAS and CMS Experiments*, Phys. Rev. Lett. **114** (2015) 191803, arXiv: 1503.07589 [hep-ex].

[34] CMS Collaboration, *Precise determination of the mass of the Higgs boson and tests of compatibility of its couplings with the standard model predictions using proton collisions at 7 and 8 TeV*, Eur. Phys. J. C **75** (2015) 212, arXiv: 1412.8662 [hep-ex].

[35] ATLAS Collaboration, *Measurements of the Higgs boson production and decay rates and coupling strengths using pp collision data at $\sqrt{s} = 7$ and 8 TeV in the ATLAS experiment*, Eur. Phys. J. C **76** (2016) 6, arXiv: 1507.04548 [hep-ex].

[36] CMS Collaboration,
Search for neutral MSSM Higgs bosons decaying to a pair of tau leptons in pp collisions, JHEP **10** (2014) 160, arXiv: 1408.3316 [hep-ex].

[37] ATLAS Collaboration, *Search for neutral Higgs bosons of the minimal supersymmetric standard model in pp collisions at $\sqrt{s} = 8$ TeV with the ATLAS detector*, JHEP **11** (2014) 056, arXiv: 1409.6064 [hep-ex].

[38] 'Search for charged Higgs bosons with the H+ to tau nu decay channel in the fully hadronic final state at sqrt s = 8 TeV', tech. rep. CMS-PAS-HIG-14-020, CERN, 2014,
URL: https://cds.cern.ch/record/1950346.

[39] G. Aad et al., *Search for charged Higgs bosons decaying via $H^{\pm} \to \tau^{\pm}\nu$ in fully hadronic final states using pp collision data at $\sqrt{s} = 8$ TeV with the ATLAS detector*, JHEP **03** (2015) 088, arXiv: 1412.6663 [hep-ex].

[40] G. Degrassi et al., *Towards high precision predictions for the MSSM Higgs sector*, Eur. Phys. J. C **28** (2003) 133, arXiv: hep-ph/0212020.

[41] B. C. Allanach et al., *Precise determination of the neutral Higgs boson masses in the MSSM*, JHEP **09** (2004) 044, arXiv: hep-ph/0406166 [hep-ph].

[42] L Maiani, A. D. Polosa and V Riquer,
Bounds to the Higgs Sector Masses in Minimal Supersymmetry from LHC Data, Phys. Lett. **B724** (2013) 274, arXiv: 1305.2172 [hep-ph].

[43] A. Djouadi et al., *The post-Higgs MSSM scenario: Habemus MSSM?*, Eur. Phys. J. C **73** (2013) 2650, arXiv: 1307.5205 [hep-ph].

[44] A. Djouadi et al., *Fully covering the MSSM Higgs sector at the LHC*, JHEP **06** (2015) 168, arXiv: 1502.05653 [hep-ph].

[45] A. Djouadi, J.-L. Kneur and G. Moultaka,
SuSpect: A Fortran code for the supersymmetric and Higgs particle spectrum in the MSSM, Comput. Phys. Commun. **176** (2007) 426, arXiv: hep-ph/0211331 [hep-ph].

[46] S. Heinemeyer, W. Hollik and G. Weiglein, *FeynHiggs: A Program for the calculation of the masses of the neutral CP even Higgs bosons in the MSSM*, Comput. Phys. Commun. **124** (2000) 76, arXiv: hep-ph/9812320.

[47] S. Heinemeyer, W. Hollik and G. Weiglein, *The Masses of the neutral CP - even Higgs bosons in the MSSM: Accurate analysis at the two loop level*, Eur. Phys. J. C **9** (1999) 343, arXiv: hep-ph/9812472.

[48] M. Frank et al., *The Higgs Boson Masses and Mixings of the Complex MSSM in the Feynman-Diagrammatic Approach*, JHEP **02** (2007) 047, arXiv: hep-ph/0611326.

[49] T. Hahn et al., *High-Precision Predictions for the Light CP -Even Higgs Boson Mass of the Minimal Supersymmetric Standard Model*, Phys. Rev. Lett. **112** (2014) 141801, arXiv: 1312.4937 [hep-ph].

[50] ALEPH, DELPHI, L3, and OPAL Collaborations, G. Abbiendi et al.,
Search for neutral MSSM Higgs bosons at LEP, Eur. Phys. J. C **47** (2006) 547, arXiv: hep-ex/0602042 [hep-ex].

[51] V. M. Abazov et al., *Search for Higgs bosons of the minimal supersymmetric standard model in $p\bar{p}$ collisions at $\sqrt(s) = 1.96$ TeV*, Phys. Lett. **B710** (2012) 569, arXiv: 1112.5431 [hep-ex].

[52] The CDF Collaboration, the D0 Collaboration, the Tevatron New Physics Higgs Working Group (TEVNPHWG), *Combined CDF and D0 upper limits on MSSM Higgs boson production in $\tau - \tau$ final states with up to 2.2 fb^{-1}* (2010), arXiv: {1003.3363} [hep-ex].

[53] A. Elagin et al., *A New Mass Reconstruction Technique for Resonances Decaying to di-tau* (2010), arXiv: 1012.4686 [hep-ex].

[54] ATLAS Collaboration, *Constraints on new phenomena via Higgs boson couplings and invisible decays with the ATLAS detector*, JHEP **11** (2015) 206, arXiv: 1509.00672 [hep-ex].

[55] F. Halzen and A. D. Martin, *QUARKS AND LEPTONS: AN INTRODUCTORY COURSE IN MODERN PARTICLE PHYSICS*, 1984, ISBN: 0471887412, 9780471887416.

[56] M. E. Peskin and D. V. Schroeder, *An Introduction to quantum field theory*, 1995, ISBN: 9780201503975, 0201503972, URL: http://www.slac.stanford.edu/spires/find/books/www?cl=QC174.45%3AP4.

[57] A. Buckley et al., *General-purpose event generators for LHC physics*, Phys. Rept. **504** (2011) 145, arXiv: 1101.2599 [hep-ph].

[58] LHC Higgs Cross Section Working Group, *Handbook of LHC Higgs Cross Sections: 3. Higgs Properties*, CERN-2013-004 (CERN, Geneva, 2013), arXiv: 1307.1347 [hep-ph].

[59] G. Aad et al., *Improved luminosity determination in pp collisions at sqrt(s) = 7 TeV using the ATLAS detector at the LHC*, Eur. Phys. J. **C73** (2013) 2518, arXiv: 1302.4393 [hep-ex].

[60] P. Z. Skands, 'QCD for Collider Physics', *Proceedings, High-energy Physics. Proceedings, 18th European School (ESHEP 2010): Raseborg, Finland, June 20 - July 3, 2010*, 2011, arXiv: 1104.2863 [hep-ph], URL: https://inspirehep.net/record/896215/files/arXiv:1104.2863.pdf.

[61] A. Martin et al., *Heavy-quark mass dependence in global PDF analyses and 3- and 4-flavour parton distributions*, Eur. Phys. J. C **70** (2010) 51, arXiv: 1007.2624 [hep-ph].

[62] Y. L. Dokshitzer, *Calculation of the Structure Functions for Deep Inelastic Scattering and e+ e- Annihilation by Perturbation Theory in Quantum Chromodynamics.*, Sov. Phys. JETP **46** (1977) 641, [Zh. Eksp. Teor. Fiz.73,1216(1977)].

[63] V. N. Gribov and L. N. Lipatov, *Deep inelastic e p scattering in perturbation theory*, Sov. J. Nucl. Phys. **15** (1972) 438, [Yad. Fiz.15,781(1972)].

[64] G. Altarelli and G. Parisi, *Asymptotic Freedom in Parton Language*, Nucl. Phys. **B126** (1977) 298.

[65] J. Butterworth et al., *PDF4LHC recommendations for LHC Run II* (2015), arXiv: 1510.03865 [hep-ph].

[66] R. D. Ball et al., *Parton distributions for the LHC Run II*, JHEP **04** (2015) 040, arXiv: 1410.8849 [hep-ph].

[67] S. Dulat et al., *New parton distribution functions from a global analysis of quantum chromodynamics*, Phys. Rev. D **93** (2016) 033006, arXiv: 1506.07443 [hep-ph].

[68] ATLAS Collaboration, *Measurement of the Z/γ^* boson transverse momentum distribution in pp collisions at $\sqrt{s} = 7$ TeV with the ATLAS detector*, JHEP **09** (2014) 145, arXiv: 1406.3660 [hep-ex].

[69] T. Gleisberg et al., *Event generation with SHERPA 1.1*, JHEP **02** (2009) 007, arXiv: 0811.4622 [hep-ph].

[70] T. Sjöstrand et al., *An Introduction to PYTHIA 8.2*, Comput. Phys. Commun. **191** (2015) 159, arXiv: 1410.3012 [hep-ph].

[71] S. Schumann and F. Krauss, *A Parton shower algorithm based on Catani-Seymour dipole factorisation*, JHEP **03** (2008) 038, arXiv: 0709.1027 [hep-ph].

[72] S. Catani et al., *QCD matrix elements + parton showers*, JHEP **11** (2001) 063, arXiv: hep-ph/0109231 [hep-ph].

[73] F. Krauss, *Matrix elements and parton showers in hadronic interactions*, JHEP **08** (2002) 015, arXiv: hep-ph/0205283 [hep-ph].

[74] S. Catani et al., *New clustering algorithm for multi - jet cross-sections in e+ e- annihilation*, Phys. Lett. **B269** (1991) 432.

[75] B. Andersson et al., *Parton Fragmentation and String Dynamics*, Phys. Rept. **97** (1983) 31.

[76] V. V. Sudakov, *Vertex parts at very high-energies in quantum electrodynamics*, Sov. Phys. JETP **3** (1956) 65, [Zh. Eksp. Teor. Fiz.30,87(1956)].

[77] J. Alwall et al., *Comparative study of various algorithms for the merging of parton showers and matrix elements in hadronic collisions*, Eur. Phys. J. **C53** (2008) 473, arXiv: 0706.2569 [hep-ph].

[78] P. Skands, *Tuning Monte Carlo Generators: The Perugia Tunes*, Phys. Rev. D **82** (2010) 074018, arXiv: 1005.3457 [hep-ph].

[79] D. Kar, A. Buckley and S. von Buddenbrock, 'A study of the Pythia 8 description of ATLAS minimum bias measurements with the Donnachie-Landshoff diffractive model', tech. rep. ATL-COM-PHYS-2016-580, CERN, 2016, URL: https://cds.cern.ch/record/2154449.

[80] ATLAS Collaboration, *The ATLAS simulation infrastructure*, Eur. Phys. J. C **70** (2010) 823, arXiv: 1005.4568 [physics.ins-det].

[81] *ATLAS Computing: technical design report*, Technical Design Report ATLAS, Geneva: CERN, 2005, URL: http://cds.cern.ch/record/837738.

[82] S. Agostinelli et al., GEANT4 Collaboration, *GEANT4 - a simulation toolkit*, Nucl. Instrum. Meth. A **506** (2003) 250.

[83] R. V. Harlander, S. Liebler and H. Mantler, *SusHi: A program for the calculation of Higgs production in gluon fusion and bottom-quark annihilation in the Standard Model and the MSSM*, Comp. Phys. Commun. **184** (2013) 1605, arXiv: 1212.3249 [hep-ph].

[84] M. Spira et al., *Higgs boson production at the LHC*, Nucl. Phys. B **453** (1995) 17, arXiv: hep-ph/9504378.

[85] R. Harlander and P. Kant, *Higgs production and decay: Analytic results at next-to-leading order QCD*, JHEP **12** (2005) 015, arXiv: hep-ph/0509189.

[86] R. V. Harlander and W. B. Kilgore,
Next-to-next-to-leading order Higgs production at hadron colliders,
Phys. Rev. Lett. **88** (2002) 201801, arXiv: hep-ph/0201206 [hep-ph].

[87] R. Harlander and W. B. Kilgore,
Production of a pseudoscalar Higgs boson at hadron colliders at next-to-next-to leading order,
JHEP **10** (2002) 017, arXiv: hep-ph/0208096.

[88] C. Anastasiou and K. Melnikov, *Higgs boson production at hadron colliders in NNLO QCD*,
Nucl. Phys. B **646** (2002) 220, arXiv: hep-ph/0207004.

[89] C. Anastasiou and K. Melnikov,
Pseudoscalar Higgs boson production at hadron colliders in NNLO QCD,
Phys. Rev. D **67** (2003) 037501, arXiv: hep-ph/0208115.

[90] V. Ravindran, J. Smith and W. L. van Neerven, *NNLO corrections to the total cross-section for Higgs boson production in hadron hadron collisions*, Nucl. Phys. B **665** (2003) 325,
arXiv: hep-ph/0302135.

[91] U. Aglietti et al., *Two loop light fermion contribution to Higgs production and decays*,
Phys. Lett. B **595** (2004) 432, arXiv: hep-ph/0404071.

[92] R. Bonciani, G. Degrassi and A. Vicini,
On the Generalized Harmonic Polylogarithms of One Complex Variable,
Comput. Phys. Commun. **182** (2011) 1253, arXiv: 1007.1891 [hep-ph].

[93] R. V. Harlander and W. B. Kilgore,
Higgs boson production in bottom quark fusion at next-to-next-to leading order,
Phys. Rev. **D68** (2003) 013001, arXiv: hep-ph/0304035 [hep-ph].

[94] S. Dittmaier, M. Krämer and M. Spira,
Higgs radiation off bottom quarks at the Tevatron and the LHC,
Phys. Rev. D **70** (2004) 074010, arXiv: hep-ph/0309204.

[95] S. Dawson, C. B. Jackson, L. Reina and D. Wackeroth,
Exclusive Higgs boson production with bottom quarks at hadron colliders,
Phys. Rev. D **69** (2004) 074027, arXiv: hep-ph/0311067.

[96] R. Harlander, M. Krämer and M. Schumacher, *Bottom-quark associated Higgs-boson production: reconciling the four- and five-flavour scheme approach* (2011),
arXiv: 1112.3478 [hep-ph].

[97] A. Djouadi, J. Kalinowski and M. Spira, *HDECAY: A Program for Higgs boson decays in the standard model and its supersymmetric extension*, Comput. Phys. Commun. **108** (1998) 56,
arXiv: hep-ph/9704448.

[98] A. Djouadi, M. M. Muhlleitner and M. Spira, *Decays of supersymmetric particles: The Program SUSY-HIT (SUspect-SdecaY-Hdecay-InTerface)*, Acta Phys. Polon. **B38** (2007) 635,
arXiv: hep-ph/0609292 [hep-ph].

[99] E. Braaten and J. P. Leveille, *Higgs Boson Decay and the Running Mass*,
Phys. Rev. **D22** (1980) 715.

[100] N. Sakai, *Perturbative quantum-chromodynamic corrections to the hadronic decay width of the Higgs boson*, Phys. Rev. D **22** (9 1980) 2220,
URL: http://link.aps.org/doi/10.1103/PhysRevD.22.2220.

[101] T. Inami and T. Kubota,
Renormalization group estimate of the hadronic decay width of the Higgs boson,
Nuclear Physics B **179** (1981) 171 , ISSN: 0550-3213,
URL: http://www.sciencedirect.com/science/article/pii/0550321381902534.

[102] M. Drees and K.-i. Hikasa, *Heavy-quark thresholds in Higgs-boson physics*,
Phys. Rev. D **41** (5 1990) 1547,
URL: http://link.aps.org/doi/10.1103/PhysRevD.41.1547.

[103] M. Drees and K. ichi Hikasa, *Note on QCD corrections to hadronic Higgs decay*,
Physics Letters B **240** (1990) 455 , ISSN: 0370-2693,
URL: http://www.sciencedirect.com/science/article/pii/0370269390911304.

[104] S. G. GORISHNY et al., *THREE-LOOP QCD CORRECTION TO THE CORRELATOR OF THE QUARK SCALAR CURRENTS AND* $\Gamma tot(H^0 \to HADRONS)$,
Modern Physics Letters A **05** (1990) 2703,
eprint: http://www.worldscientific.com/doi/pdf/10.1142/S0217732390003152,
URL: http://www.worldscientific.com/doi/abs/10.1142/S0217732390003152.

[105] A. L. KATAEV and V. T. KIM,
THE EFFECTS OF THE QCD CORRECTIONS TO $\Gamma\left(H^0 \to b\bar{b}\right)$,
Modern Physics Letters A **09** (1994) 1309,
eprint: http://www.worldscientific.com/doi/pdf/10.1142/S0217732394001131,
URL: http://www.worldscientific.com/doi/abs/10.1142/S0217732394001131.

[106] S. G. Gorishnii, A. L. Kataev and S. A. Larin, *The Width of Higgs Boson Decay Into Hadrons: Three Loop Corrections of Strong Interactions*,
Sov. J. Nucl. Phys. **40** (1984) 329, [Yad. Fiz.40,517(1984)].

[107] L. R. Surguladze, *Quark mass effects in fermionic decays of the Higgs boson in O (alpha-s**2) perturbative QCD*, Phys. Lett. **B341** (1994) 60,
arXiv: hep-ph/9405325 [hep-ph].

[108] S. A. Larin, T. van Ritbergen and J. A. M. Vermaseren, *The Large top quark mass expansion for Higgs boson decays into bottom quarks and into gluons*, Phys. Lett. **B362** (1995) 134,
arXiv: hep-ph/9506465 [hep-ph].

[109] K. G. Chetyrkin and A. Kwiatkowski, *Second order QCD corrections to scalar and pseudoscalar Higgs decays into massive bottom quarks*, Nucl. Phys. **B461** (1996) 3,
arXiv: hep-ph/9505358 [hep-ph].

[110] K. G. Chetyrkin, *Correlator of the quark scalar currents and Gamma(tot) (H —¿ hadrons) at O (alpha-s**3) in pQCD*, Phys. Lett. **B390** (1997) 309,
arXiv: hep-ph/9608318 [hep-ph].

[111] P. A. Baikov, K. G. Chetyrkin and J. H. Kuhn, *Scalar correlator at O(alpha(s)**4), Higgs decay into b-quarks and bounds on the light quark masses*, Phys. Rev. Lett. **96** (2006) 012003,
arXiv: hep-ph/0511063 [hep-ph].

[112] G. Aad et al., *Searches for Higgs boson pair production in the* $hh \to bb\tau\tau, \gamma\gamma WW^*, \gamma\gamma bb, bbbb$ *channels with the ATLAS detector*, Phys. Rev. **D92** (2015) 092004,
arXiv: 1509.04670 [hep-ex].

[113] 'Search for heavy Higgs bosons A/H decaying to a top-quark pair in pp collisions at $\sqrt{s} = 8$ TeV with the ATLAS detector', tech. rep. ATLAS-CONF-2016-073, CERN, 2016,
URL: https://cds.cern.ch/record/2206229.

[114] *The ATLAS Experiment at the CERN Large Hadron Collider*, JINST **3** (2008) S08003.

[115] L. Evans and P. Bryant, *LHC Machine*, JINST **3** (2008) S08001.

[116] S. Chatrchyan et al., *The CMS experiment at the CERN LHC*, JINST **3** (2008) S08004.

[117] K. Aamodt et al., *The ALICE experiment at the CERN LHC*, JINST **3** (2008) S08002.

[118] A. A. Alves Jr. et al., *The LHCb Detector at the LHC*, JINST **3** (2008) S08005.

[119] O. Adriani et al., *The LHCf detector at the CERN Large Hadron Collider*, JINST **3** (2008) S08006.

[120] G. Anelli et al., *The TOTEM experiment at the CERN Large Hadron Collider*, JINST **3** (2008) S08007.

[121] J. Pinfold et al., 'Technical Design Report of the MoEDAL Experiment', tech. rep. CERN-LHCC-2009-006. MoEDAL-TDR-001, 2009, URL: https://cds.cern.ch/record/1181486.

[122] A. Airapetian et al., *ATLAS: Detector and physics performance technical design report. Volume 1* (1999).

[123] A. Airapetian et al., *ATLAS: Detector and physics performance technical design report. Volume 2* (1999).

[124] S van der Meer, 'Calibration of the effective beam height in the ISR', tech. rep. CERN-ISR-PO-68-31. ISR-PO-68-31, CERN, 1968, URL: https://cds.cern.ch/record/296752.

[125] ATLAS Collaboration, *Improved luminosity determination in pp collisions at $\sqrt{s}$ = 7 TeV using the ATLAS detector at the LHC*, Eur. Phys. J. C **73** (2013) 2518, arXiv: 1302.4393 [hep-ex].

[126] ATLAS Collaboration, *The ATLAS experiment at the CERN Large Hadron Collider*, JINST **3** (2008) S08003.

[127] E. Simioni et al., *Upgrade of the ATLAS Level-1 Trigger with event topology information*, Journal of Physics: Conference Series **664** (2015) 082052, URL: http://stacks.iop.org/1742-6596/664/i=8/a=082052.

[128] Y. Nakahama, *The ATLAS Trigger System: Ready for Run-2*, Journal of Physics: Conference Series **664** (2015) 082037, URL: http://stacks.iop.org/1742-6596/664/i=8/a=082037.

[129] G. Duckeck et al., *ATLAS computing: Technical design report* (2005).

[130] 'The Optimization of ATLAS Track Reconstruction in Dense Environments', tech. rep. ATL-PHYS-PUB-2015-006, CERN, 2015, URL: https://cds.cern.ch/record/2002609.

[131] A. Rosenfeld and J. L. Pfaltz, *Sequential Operations in Digital Picture Processing*, J. ACM **13** (1966) 471, ISSN: 0004-5411, URL: http://doi.acm.org/10.1145/321356.321357.

[132] G. Aad et al., *A neural network clustering algorithm for the ATLAS silicon pixel detector*, JINST **9** (2014) P09009, arXiv: 1406.7690 [hep-ex].

[133] R. Fruhwirth, *Application of Kalman filtering to track and vertex fitting*, Nucl. Instrum. Meth. **A262** (1987) 444.

[134] *Performance of primary vertex reconstruction in proton-proton collisions at $\sqrt{s}$ =7 TeV in the ATLAS experiment* (2010).

[135] *Performance of the ATLAS Inner Detector Track and Vertex Reconstruction in the High Pile-Up LHC Environment* (2012).

[136] R. Fruhwirth, W. Waltenberger and P. Vanlaer, *Adaptive vertex fitting*, J. Phys. **G34** (2007) N343.

[137] P. Speckmayer, T. Carli and C. W. Fabjan, 'Energy Measurement of Hadrons with the CERN ATLAS Calorimeter', Presented on 18 Jun 2008, PhD thesis: Vienna, Tech. U., 2008, URL: https://cds.cern.ch/record/1112036.

[138] ATLAS Collaboration, *Topological cell clustering in the ATLAS calorimeters and its performance in LHC Run 1* (2016), arXiv: 1603.02934 [hep-ex].

[139] T Barillari et al., 'Local Hadronic Calibration', tech. rep. ATL-LARG-PUB-2009-001-2. ATL-COM-LARG-2008-006. ATL-LARG-PUB-2009-001, Due to a report-number conflict with another document, the report-number ATL-LARG-PUB-2009-001-2 has been assigned.: CERN, 2008, URL: https://cds.cern.ch/record/1112035.

[140] G. Aad et al., *Jet energy measurement with the ATLAS detector in proton-proton collisions at* $\sqrt{s} = 7$ *TeV*, Eur. Phys. J. **C73** (2013) 2304, arXiv: 1112.6426 [hep-ex].

[141] M. Cacciari, G. P. Salam and G. Soyez, *The anti-k_t jet clustering algorithm*, JHEP **04** (2008) 063, arXiv: 0802.1189 [hep-ph].

[142] M. Cacciari, G. P. Salam and G. Soyez, *FastJet User Manual*, Eur. Phys. J. C **72** (2012) 1896, arXiv: 1111.6097 [hep-ph].

[143] G. P. Salam, *Towards Jetography*, Eur. Phys. J. **C67** (2010) 637, arXiv: 0906.1833 [hep-ph].

[144] 'Jet Calibration and Systematic Uncertainties for Jets Reconstructed in the ATLAS Detector at $\sqrt{s} = 13$ TeV', tech. rep. ATL-PHYS-PUB-2015-015, CERN, 2015, URL: https://cds.cern.ch/record/2037613.

[145] M. Cacciari and G. P. Salam, *Pileup subtraction using jet areas*, Phys. Lett. B **659** (2008) 119, arXiv: 0707.1378 [hep-ph].

[146] 'Pile-up subtraction and suppression for jets in ATLAS', tech. rep. ATLAS-CONF-2013-083, CERN, 2013, URL: https://cds.cern.ch/record/1570994.

[147] M. Cacciari, G. P. Salam and G. Soyez, *The Catchment Area of Jets*, JHEP **04** (2008) 005, arXiv: 0802.1188 [hep-ph].

[148] S. D. Ellis and D. E. Soper, *Successive combination jet algorithm for hadron collisions*, Phys. Rev. **D48** (1993) 3160, arXiv: hep-ph/9305266 [hep-ph].

[149] S. Catani et al., *Longitudinally invariant K_t clustering algorithms for hadron hadron collisions*, Nucl. Phys. **B406** (1993) 187.

[150] ATLAS Collaboration, *Expected performance of the ATLAS b-tagging algorithms in Run-2*, ATL-PHYS-PUB-2015-022, 2015, URL: http://cdsweb.cern.ch/record/2037697.

[151] 'Optimisation of the ATLAS *b*-tagging performance for the 2016 LHC Run', tech. rep. ATL-PHYS-PUB-2016-012, CERN, 2016, URL: https://cds.cern.ch/record/2160731.

[152] *Commissioning of the ATLAS high-performance b-tagging algorithms in the 7 TeV collision data* (2011), URL: https://cds.cern.ch/record/1369219.

[153] G Piacquadio and C Weiser,
A new inclusive secondary vertex algorithm for b-jet tagging in ATLAS,
Journal of Physics: Conference Series **119** (2008) 032032,
URL: http://stacks.iop.org/1742-6596/119/i=3/a=032032.

[154] ATLAS Collaboration, *Tagging and suppression of pileup jets with the ATLAS detector*,
ATLAS-CONF-2014-018, 2014, URL: http://cdsweb.cern.ch/record/1700870.

[155] 'Tagging and suppression of pileup jets with the ATLAS detector',
tech. rep. ATLAS-CONF-2014-018, CERN, 2014,
URL: https://cds.cern.ch/record/1700870.

[156] ATLAS Collaboration, *Electron efficiency measurements with the ATLAS detector using the 2015 LHC proton-proton collision data*, ATLAS-CONF-2016-024, 2016,
URL: http://cdsweb.cern.ch/record/2157687.

[157] T. G. Cornelissen et al., *The global χ^2 fitter in ATLAS*,
Journal of Physics: Conference Series **119** (2008) 032013,
URL: http://stacks.iop.org/1742-6596/119/i=3/a=032013.

[158] 'Improved electron reconstruction in ATLAS using the Gaussian Sum Filter-based model for bremsstrahlung', tech. rep. ATLAS-CONF-2012-047, CERN, 2012,
URL: https://cds.cern.ch/record/1449796.

[159] ATLAS Collaboration, *Electron efficiency measurements with the ATLAS detector using the 2012 LHC proton-proton collision data* (2014),
URL: http://cdsweb.cern.ch/record/1706245.

[160] ATLAS Collaboration,
Electron and photon energy calibration with the ATLAS detector using LHC Run 1 data,
Eur. Phys. J. C **74** (2014) 3071, arXiv: 1407.5063 [hep-ex].

[161] ATLAS Collaboration,
Electron and photon energy calibration with the ATLAS detector using LHC Run 1 data (2014), arXiv: 1407.5063 [hep-ex].

[162] M. Aharrouche and A. E. B. C. Collaboration, **568** (2006) 601.

[163] M. Backes et al., 'Electron/photon trigger efficiency plots for ICHEP2016',
tech. rep. ATL-COM-DAQ-2016-086, CERN, 2016,
URL: https://cds.cern.ch/record/2200359.

[164] J. Illingworth and J. Kittler, *A survey of the hough transform*,
Computer Vision, Graphics, and Image Processing **44** (1988) 87 , ISSN: 0734-189X,
URL: http://www.sciencedirect.com/science/article/pii/S0734189X88800331.

[165] ATLAS Collaboration, *Measurement of the muon reconstruction performance of the ATLAS detector using 2011 and 2012 LHC proton-proton collision data* (2014),
arXiv: 1407.3935 [hep-ex].

[166] ATLAS Collaboration, *Muon reconstruction performance of the ATLAS detector in proton–proton collision data at $\sqrt{s}$=13 TeV*, Eur. Phys. J. C **76** (2016) 292,
arXiv: 1603.05598 [hep-ex].

[167] The ATLAS Collaborations, 'Muon trigger performances in 2015 25ns data-taking period',
https://twiki.cern.ch/twiki/bin/view/AtlasPublic/MuonTriggerPublicResults.

[168] C. Patrignani, *Review of Particle Physics*, Chin. Phys. **C40** (2016) 100001.

[169] G. Aad et al.,
Reconstruction of hadronic decay products of tau leptons with the ATLAS experiment,
Eur. Phys. J. **C76** (2016) 295, arXiv: 1512.05955 [hep-ex].

[170] 'Reconstruction, Energy Calibration, and Identification of Hadronically Decaying Tau Leptons', tech. rep. ATLAS-CONF-2011-077, CERN, 2011,
URL: https://cds.cern.ch/record/1353226.

[171] *Performance of the Reconstruction and Identification of Hadronic Tau Decays in ATLAS with 2011 Data* (2012), URL: https://cds.cern.ch/record/1485531.

[172] *Determination of the tau energy scale and the associated systematic uncertainty in proton-proton collisions at $\sqrt{s} = 8$ TeV with the ATLAS detector at the LHC in 2012* (2013), URL: https://cds.cern.ch/record/1544036.

[173] ATLAS Collaboration, *Identification and energy calibration of hadronically decaying tau leptons with the ATLAS experiment in pp collisions at $\sqrt{s}$=8 TeV*,
Eur. Phys. J. C **75** (2015) 303, arXiv: 1412.7086 [hep-ex].

[174] ATLAS Collaboration, *Reconstruction, Energy Calibration, and Identification of Hadronically Decaying Tau Leptons in the ATLAS Experiment for Run-2 of the LHC*,
ATL-PHYS-PUB-2015-045, 2015, URL: http://cdsweb.cern.ch/record/2064383.

[175] ATLAS Collaboration, *Performance of missing transverse momentum reconstruction for the ATLAS detector in the first proton-proton collisions at $\sqrt{s}$= 13 TeV*,
ATL-PHYS-PUB-2015-027, 2015, URL: http://cdsweb.cern.ch/record/2037904.

[176] 'Expected performance of missing transverse momentum reconstruction for the ATLAS detector at $\sqrt{s} = 13$ TeV', tech. rep. ATL-PHYS-PUB-2015-023, CERN, 2015,
URL: https://cds.cern.ch/record/2037700.

[177] *Missing Transverse Momentum Distribution and Performance in 2016 data* (2016),
URL: https://atlas.web.cern.ch/Atlas/GROUPS/PHYSICS/PLOTS/JETM-2016-008.

[178] A. Collaboration, 'Performance of the ATLAS Trigger System in 2015',
tech. rep. ATL-COM-DAQ-2016-034, CERN, 2016,
URL: https://cds.cern.ch/record/2140103.

[179] P. Nason, *A New method for combining NLO QCD with shower Monte Carlo algorithms*,
JHEP **11** (2004) 040, arXiv: hep-ph/0409146 [hep-ph].

[180] S. Frixione, P. Nason and C. Oleari,
Matching NLO QCD computations with parton shower simulations: the POWHEG method,
JHEP **11** (2007) 070, arXiv: 0709.2092 [hep-ph].

[181] S. Alioli et al., *A general framework for implementing NLO calculations in shower Monte Carlo programs: the POWHEG BOX*, JHEP **06** (2010) 043, arXiv: 1002.2581 [hep-ph].

[182] J. Alwall et al., *The automated computation of tree-level and next-to-leading order differential cross sections, and their matching to parton shower simulations*,
JHEP **07** (2014) 079, arXiv: 1405.0301 [hep-ph].

[183] M. Wiesemann et al., *Higgs production in association with bottom quarks*,
JHEP **02** (2015) 132, arXiv: 1409.5301 [hep-ph].

[184] H.-L. Lai et al., *New parton distributions for collider physics*,
Phys. Rev. D **82** (2010) 074024, arXiv: 1007.2241 [hep-ph].

[185] *ATLAS Run 1 Pythia8 tunes* (2014), URL: http://cds.cern.ch/record/1966419.

[186] D. J. Lange, *The EvtGen particle decay simulation package*, Nucl. Instrum. Meth. A **462** (2001) 152.

[187] ATLAS Collaboration, *Summary of ATLAS Pythia 8 tunes*, ATL-PHYS-PUB-2012-003, 2012, URL: http://cdsweb.cern.ch/record/1474107.

[188] E. Barberio, B. V. Eijk and Z. Was, *PHOTOS - a universal Monte Carlo for QED radiative corrections in decays*, Comput. Phys. Commun. **66** (1991) 115.

[189] N. Davidson, T. Przedzinski and Z. Was, *PHOTOS Interface in C++: Technical and Physics Documentation*, Comput. Phys. Commun. **199** (2016) 86, arXiv: 1011.0937 [hep-ph].

[190] C. Anastasiou et al., *High precision QCD at hadron colliders: Electroweak gauge boson rapidity distributions at NNLO*, Phys. Rev. D **69** (2004) 094008, arXiv: hep-ph/0312266.

[191] K. Melnikov and F. Petriello, *Electroweak gauge boson production at hadron colliders through O(alpha(s)**2)*, Phys. Rev. D **74** (2006) 114017, arXiv: hep-ph/0609070.

[192] R. Gavin et al., *FEWZ 2.0: A code for hadronic Z production at next-to-next-to-leading order*, Comput. Phys. Commun. **182** (2011) 2388, arXiv: 1011.3540 [hep-ph].

[193] P. Artoisenet et al., *Automatic spin-entangled decays of heavy resonances in Monte Carlo simulations*, JHEP **03** (2013) 015, arXiv: 1212.3460 [hep-ph].

[194] T. Sjöstrand, S. Mrenna and P. Skands, *PYTHIA 6.4 physics and manual*, JHEP **05** (2006) 026, arXiv: hep-ph/0603175.

[195] M. Czakon and A. Mitov, *Top++: A Program for the Calculation of the Top-Pair Cross-Section at Hadron Colliders*, Comput. Phys. Commun. **185** (2014) 2930, arXiv: 1112.5675 [hep-ph].

[196] N. Kidonakis, *Next-to-next-to-leading-order collinear and soft gluon corrections for t-channel single top quark production*, Phys. Rev. D **83** (2011) 091503, arXiv: 1103.2792 [hep-ph].

[197] N. Kidonakis, *NNLL resummation for s-channel single top quark production*, Phys. Rev. D **81** (2010) 054028, arXiv: 1001.5034 [hep-ph].

[198] N. Kidonakis, *Two-loop soft anomalous dimensions for single top quark associated production with a W- or H-*, Phys. Rev. D **82** (2010) 054018, arXiv: 1005.4451 [hep-ph].

[199] *Evidence for Higgs Boson Decays to the $\tau^+\tau^-$ Final State with the ATLAS Detector* (2013), URL: http://cds.cern.ch/record/1632191.

[200] F. James and M. Roos, *Minuit: A System for Function Minimization and Analysis of the Parameter Errors and Correlations*, Comput.Phys.Commun. **10** (1975) 343.

[201] K. Cranmer et al., 'HistFactory: A tool for creating statistical models for use with RooFit and RooStats', tech. rep. CERN-OPEN-2012-016, New York U., 2012, URL: https://cds.cern.ch/record/1456844.

[202] W. Verkerke and D. Kirkby, *The RooFit toolkit for data modeling*, ArXiv Physics e-prints (2003), eprint: physics/0306116.

[203] L. Moneta et al., 'The RooStats project',
Proceedings of the 13th International Workshop on Advanced Computing and Analysis Techniques in Physics Research. February 22-27, 2010, Jaipur, India. 2010 57,
arXiv: 1009.1003 [physics.data-an].

[204] R. Brun and F. Rademakers, *ROOT — An object oriented data analysis framework*,
Nuclear Instruments and Methods in Physics Research Section A: Accelerators, Spectrometers, Detectors and Associated Equipment **389** (1997) 81 , ISSN: 0168-9002,
URL: http://www.sciencedirect.com/science/article/pii/S016890029700048X.

[205] J. Friedman, 'Data Analysis Techniques for High Energy Particle Physics', 1974.

[206] G. Cowan et al., *Asymptotic formulae for likelihood-based tests of new physics*,
Eur. Phys. J. C **71** (2011) 1554, [Erratum: Eur. Phys. J. C 73 (2013) 2501],
arXiv: 1007.1727 [physics.data-an].

[207] K. Cranmer, *Practical Statistics for the LHC* (2015) 41 p, Comments: presented at the 2011 European School of High-Energy Physics, Cheile Gradistei, Romania, 7-20 September 2011 I expect to release updated versions of this document in the future,
URL: https://cds.cern.ch/record/2004587.

[208] K. S. Cranmer, *Statistics for the LHC: Progress, Challenges, and Future* (2008),
URL: https://cds.cern.ch/record/1099969.

[209] A. L. Read, *Presentation of search results: the CL_s technique*, J. Phys. G **28** (2002) 2693.

[210] G. Cowan et al., *Power-Constrained Limits* (2011), arXiv: 1105.3166 [physics.data-an].

[211] A. Wald, *Tests of Statistical Hypotheses Concerning Several Parameters When the Number of Observations is Large*, Transactions of the American Mathematical Society **54** (1943) 426,
ISSN: 00029947, URL: http://www.jstor.org/stable/1990256.

[212] 'Search for Minimal Supersymmetric Standard Model Higgs Bosons H/A in the $\tau\tau$ final state in up to 13.3 fb^{-1} of pp collisions at $\sqrt{s} = 13$TeV with the ATLAS Detector',
tech. rep. ATLAS-CONF-2016-085, CERN, 2016,
URL: https://cds.cern.ch/record/2206278.

[213] 'Search for a neutral MSSM Higgs boson decaying into $\tau\tau$ with 12.9 fb^{-1} of data at $\sqrt{s} = 13$ TeV', tech. rep. CMS-PAS-HIG-16-037, CERN, 2016,
URL: https://cds.cern.ch/record/2231507.